Polish Academy of Sciences
Institute of Fundamental Technological Research

Archives of Mechanics

Archiwum Mechaniki Stosowanej

volume 55 issue 5-6

DRUKARNIA
BRACI GRODZICKICH

SUBSCRIPTIONS

Address of the Editorial Office: Archives of Mechanics
Institute of Fundamental Technological Research, Świętokrzyska 21
PL 00-049 Warsaw, Poland
Tel. 48 (*prefix*) 22 826 60 22, Fax 48 (*prefix*) 22 826 98 15,
e-mail:publikac@ippt.gov.pl

Subscription orders for all journals edited by IFTR may be sent directly to the Editorial Office of the Institute of Fundamental Technological Research

Subscription rates

Annual subscription rate (2003) including postage is US $ 240.
Please transfer the subscription fee to our bank account: Payee: IPPT PAN,
Bank: PKO SA. IV O/Warszawa,
Account number 12401053-40054492-3000-401112-001.

All journals edited by IFTR are available also through:

- Foreign Trade Enterprise ARS POLONA Krakowskie Przedmieście 7,
  00-068 Warszawa, Poland fax 48 (*prefix*) 22 826 86 73
- RUCH S.A. ul. Towarowa 28,
  00-958 Warszawa, Poland fax 48 (*prefix*) 22 620 17 62
- International Publishing Service Sp. z o.o. ul. Noakowskiego 10 lok. 38
  00-664 Warszawa, Poland tel./fax 48 (*prefix*) 22 625 16 53, 625 49 55

Warunki prenumeraty

Redakcja przyjmuje prenumeratę na wszystkie czasopisma wydawane przez IPPT PAN. Bieżące numery można nabyć, a także zaprenumerować roczne wydanie Archiwum Mechaniki Stosowanej bezpośrednio w Dziale Wydawnictw IPPT PAN, Świętokrzyska 21, 00-049 Warszawa, Tel. 48 (*prefix*) 22 826 60 22; Fax 48 (*prefix*) 22 826 98 15.
Cena rocznej prenumeraty z bonifikatą (na rok 2003) dla krajowego odbiorcy wynosi 300 PLN

Również można je nabyć, a także zamówić (przesyłka za zaliczeniem pocztowym) we Wzorcowni Ośrodka Rozpowszechniania Wydawnictw Naukowych PAN,
00-818 Warszawa, ul. Twarda 51/55, tel. 48 (*prefix*) 22 697 88 35.
Wpłaty na prenumeratę przyjmują także jednostki kolportażowe RUCH S.A. Oddział Krajowej Dystrybucji Prasy, 00-958 Warszawa, ul. Towarowa 28. Konto: PBK. S.A. XIII Oddział Warszawa nr 11101053-16551-2700-1-67. Dostawa odbywa się pocztą lotniczą, której koszt w pełni pokrywa zleceniodawca. Tel. 48 (*prefix*) 22 620 10 39, Fax 48 (*prefix*) 22 620 17 62

Arkuszy wydawniczych 14. Arkuszy drukarskich 10,5.
Papier offset. kl III 70g. B1.
Druk ukończono w listopadzie 2003 r.
Skład w systemie TEX: E. Jaczyńska.
Druk i oprawa: Drukarnia Braci Grodzickich, Piaseczno ul. Geodetów 47A.

Arch. Mech., **55**, 5–6, p. 391, Warszawa 2003

Preface

This issue of the Archives of Mechanics contains a selection of papers presented at the **34th Solid Mechanics Conference**, 2–7 September, 2002 (Zakopane, Poland).

Following a long tradition going back to the first Polish Solid Mechanics Conference in 1953, the objective of the 34th Conference SolMech (like many previous ones – being an international conference) was to bring together researchers engaged in all major areas of contemporary mechanics of solids and structures. The program of the Conference included 8 invited plenary (keynote) lectures (40 min), several invited sectional lectures (30 min), and contributed presentations (20 min) in thematic sessions.

The main subjects included into the program of the Conference were the following:

- Mechanics and Thermodynamics of Solids with Microstructure
- Inelastic Response of Materials and Structures
- Geomechanics
- Structural Mechanics, Sensitivity and Optimization
- Instability and Localization Phenomena
- Fracture Mechanics, Damage, Fatigue
- Dynamics of Solids and Structures
- Composites, Porous Media
- Biomechanics
- Stochastic Methods
- Computational Methods
- Experimental Methods

The Editorial Board of the Archives of Mechanics kindly offered a possibility of publishing a special Conference issue of the journal to commemorate the 34th Solid Mechanics Conference and at the same time, to allow some papers presented (and not published yet) a quick editorial processing. On behalf of the Scientific and Organizing Committees of the Conference, I express our grateful acknowledgment to the Editorial Board. Also, I wish to thank the authors who have contributed to this special Conference issue.

Warsaw, November 18, 2003

Kazimierz Sobczyk

Chairman of the 34th Solid Mechanics Conference

Arch. Mech., **55**, 5–6, pp. 393–406, Warszawa 2003

Numerical simulation of atomic positions in quantum dot by means of molecular statics

P. DŁUŻEWSKI, P. TRACZYKOWSKI

Institute of Fundamental Technological Research, PAS
Świętokrzyska 21, 00-049 Warsaw
e-mail:pdluzew@ippt.gov.pl
e-mail:ptracz@ippt.gov.pl

DEFORMATION OF A CRYSTAL structure is considered here in terms of constitutive modelling based upon both the atomistic and continuum approaches. Atomistic calculations are made by using the Stillinger–Weber potential for the GaAs and CdTe structures. The stress-strain behaviour of the best-known anisotropic hyperelastic models are compared with the behaviour of the atomistic one in the uniaxial deformation test.

Key words: molecular simulations, stress analysis, nonlinear elasticity, molecular potential, Stillinger–Weber potential, finite element analysis.

1. Introduction

RECENTLY MANY MOLECULAR models of crystal behaviour have been used in modelling of the crystal lattice deformation. Many constitutive models based on the continuum thermodynamics are also available. Hence the question arises about the relation between the nonlinear behaviour of these two types of models. For instance, it is well known that the stress-strain behaviour of nonlinear continuum elastic models depends very heavily on the strain measure applied, [1, 4]. Namely, the linear stress-strain constitutive relation rewritten for the stress conjugate to the Almansi strain makes the extension softer than compression, while the analogical linear stress-strain constitutive relation for the second Piola–Kirchhoff stress conjugate by work with the Green strain measure makes the extension harder than compression. It is easy to show on the third order elastic constants obtained by reducing these nonlinear constitutive equation to the common strain measures, e.g. to the logarithmic strain [4].

Atomistic modelling of crystal deformation can be divided into the computational methods based upon the fundamental and empirical potentials. The fundamental potentials are based upon the quantum theory and Schrödinger wave equation, while the empirical potentials predict the dependence of strain energy directly on the basis of atomic positions. It can be shown that the quasi-classical

treatment of atomic interaction in terms of interatomic potentials and the classical momentum equation are consistent in certain limits with the solution of the Schrödinger wave equation [8, 3]. The analogy results from the decomposition of the analytical solution into the time-dependent and time-independent parts. The time-independent wave function corresponds to the spatial arrangement of particles. Generally, the empirical potentials can be divided into two and more modern many-body potentials. In the simple pair potentials (like the Morse, Lennard–Jones, Madelung ones) only the direct interaction of two atoms is considered and added up for a certain sphere with the radius of about four atoms. In the multi-atom potentials not only two-atoms but also the influence of the neighbouring atoms is taken into account; for example, in the Stillinger–Weber potentials applied here noncentral atomic interactions are taken into account by adding three-atoms interaction terms.

Continuum models of elastic behaviour of crystal lattice can be divided generally into the linear models based on the linear theory of elasticity, and nonlinear constitutive models where the differentiation of displacement field over the current and initial configurations are distinguished. In the linear theory, by writing $\varepsilon_{ij} = \frac{1}{2}(\nabla_i u_j + \nabla_j u_i)$ we do not specify precisely over which configuration the differentiation is made, i.e. over the current or the initial configuration. Generally, we assume then that it does not matter because the configuration changes are very small. In the nonlinear theory, before the displacement gradient is written, we have to answer precisely over which configuration the differentiation is done.

Anisotropic hyperelastic models compose a very narrow group among numerous continuum models describing elastic behaviour of materials. Let us emphasize that the most familiar *anisotropic* hyperelastic models, like the St.-Venant–Kirchhoff and Biot models, change heavily their instantaneous stiffness under large strains. Moreover, the stiffness evolution often differs significantly from the behaviour of real materials. Neglecting an anomalous behaviour we can expect that with respect to molecular effects *the instantaneous stiffness of crystalline solids increases under compression and decreases under tension.* This nonlinear elastic effect is responsible for many phenomena observed experimentally. For instance due to the different stress-strain response of the extension and compression regions, a single edge dislocation causes the volume expansion of crystal lattice [6, 11]. The asymmetry in the stress–strain response appears also in the form of negative values of third-order elastic constants measured experimentally for many real crystal structures [13, 15, 16]. Thus, applying elastic constitutive models which behave just conversely (St.-Venant–Kirchhoff, Biot) to the real material, can be the cause of many undesirable effects such as improper proportion between stress values and sizes of extension and compression regions around

a single edge dislocation which causes positive or negative volume expansion induced by edge dislocations in elastic continuum. Therefore, the use of new elastic and elastic-plastic constitutive models, whose behaviour could be more adapted to the nonlinear behaviour of real crystal structures, is desired.

2. Nonlinear continuum elasticity

According to the polar decomposition theorem, the deformation gradient $\mathbf{F}$ can be decomposed into the rotation tensor $\mathbf{R}$ and the left or right stretch tensor, $\mathbf{U}$ or $\mathbf{V}$, respectively, $\mathbf{F} = \mathbf{RU} = \mathbf{VR}$.

DEFINITION 1. *By general Lagrangian and Eulerian strain tensors we mean two tensor functions*

$$\widehat{\boldsymbol{\varepsilon}} \stackrel{\text{df}}{=} \mathcal{A} f(u_i)\, \mathbf{u}_i \otimes \mathbf{u}_i \qquad \text{and} \qquad \boldsymbol{\varepsilon} \stackrel{\text{df}}{=} f(v_i)\, \mathbf{v}_i \otimes \mathbf{v}_i, \tag{2.1}$$

where $u_i, \mathbf{u}_i, v_i, \mathbf{v}_i$ denote respectively i-th eigenvalues and eigenvectors of the right and left stretch tensors, while $f(x) : R^+ \ni x \to f \in R$ denotes an arbitrarily chosen C^1 monotonically increasing function which satisfies the conditions $f(x)|_{x=1} = 0$ and $\left.\dfrac{df(x)}{dx}\right|_{x=1} = 1$.

This definition includes the well-known family of strain measures noted first in [10]

$$\widehat{\boldsymbol{\varepsilon}} = \frac{1}{m}(\mathbf{U}^m - \mathbf{1}) \qquad \text{and} \qquad \boldsymbol{\varepsilon} = \frac{1}{m}(\mathbf{V}^m - \mathbf{1}), \tag{2.2}$$

and many others. It can be proved that to balance the energy for an arbitrarily chosen deformation process, the Cauchy stress has to be governed by the following equation:

$$\boxed{\boldsymbol{\sigma} = \mathbf{R}\left(\widehat{\mathcal{A}} : \hat{\rho}\frac{\partial \psi}{\partial \widehat{\boldsymbol{\varepsilon}}}\right)\mathbf{R}^T \det \mathbf{F}^{-1},} \tag{2.3}$$

where the fourth-order tensor $\widehat{\mathcal{A}}$ decomposed in the vector basis $\{\mathbf{u}_K\}$ consisting of the eigenvectors of right stretch tensor is represented by the following non-vanishing components:

$$\widehat{\mathcal{A}}_{IJIJ} = \widehat{\mathcal{A}}_{IJJI} = \begin{cases} \delta_{IJ}\, u_I f'(u_I) & \text{for } u_I = u_J, \\ \dfrac{u_I u_J [f(u_I) - f(u_J)]}{u_I^2 - u_J^2} & \text{for } u_I \neq u_J, \end{cases} \tag{2.4}$$

where $\widehat{\rho} = \rho \det \mathbf{F}$, $f'(u_1) = \left.\dfrac{df(u)}{du}\right|_{u=u_1}$, [4]. Let us consider the hyperelastic material governed by the following constitutive equation stated for the specific strain energy

$$\psi = \frac{1}{2\widehat{\rho}} \widehat{\boldsymbol{\varepsilon}} : \widehat{\mathbf{c}} : \widehat{\boldsymbol{\varepsilon}} \tag{2.5}$$

where $\widehat{\mathbf{c}}$ is the fourth-order tensor of elastic stiffness. Substitution into (2.3) leads to

$$\boldsymbol{\sigma} = \mathbf{R}(\widehat{\mathcal{A}} : \widehat{\mathbf{c}} : \widehat{\boldsymbol{\varepsilon}})\mathbf{R}^T \det \mathbf{F}^{-1}. \tag{2.6}$$

This constitutive model based on the generalized strain measure takes into account the most of the well-known anisotropic elastic models. Obviously, the models which do not satisfy the energy conservation law, like hypoelastic models, are out of our consideration.

3. Interatomic potentials

Recently a wide group of interatomic potentials are used in the computation materials science. Below, we present in brief the mathematical foundation of a few empirical potentials.

Embedded Atom Method. The Embedded Atom Method has been proposed by M. I. BASKES and M. S. DAW in 1984 [3]. The EAM is using the density functional theory. In this model, the energy required to place an atom in crystal lattice is a function of electron density in the desired place. This method is using two-body interactions so it is a central a forces method. This allows to calculate lattice relaxation and many properties of large sets of atoms. The fundamental equations for EAM are

$$E_{\text{tot}} = \sum_i F_i(\rho_{h,i}) + \frac{1}{2}\sum_{i,j} \phi_{i,j}(R_{i,j}), \tag{3.1}$$

$$\rho_{h,i} = \sum_{j(\neq i)} \rho_j^a(R_{ij}), \tag{3.2}$$

where E_{tot} is total internal energy, $\rho_{h,i}$ is closely approximated by a sum of atomic densities ρ^a of the constituents [i.e. $\rho_{h,i,}$], f_i is electron density of atom j as a function of distance from its center, R_{ij} is distance between atoms i and j, $F_i(\rho_{h,i})$ is energy of embedded atom i for electron density $\rho_{h,i}$ and $\phi_{i,j}$ is the short range (doubly screened) pair potential. This potential looks quite simple but the results obtained using it are very close to those obtained experimentally [3, 5].

All parameters are more precisely discussed by authors of this potential. The numerical problem in applying this potential is that it requires to calculate the interactions of all atoms with each other – that gives a huge number of equations to process. Two other presented potentials have a cut-off parameter which allows to limit the number of interacting atoms to those within cut-off range.

Tersoff potential is more advanced than two-body potentials. The Tersoff potential depends not only on atomic distances but also on the angle between three atoms (two bindings) [8]. That makes this potential more flexible and accurate in calculations, but it makes it harder to adapt to numerical calculations. The geometric term which contains information about the angle θ between two bindings is very important. This angle limits the number of atomic positions – without this term the number of possible positions is almost unlimited and does not correlate with physical reality (the angle between e.g. Ga–As and As–Ga in a crystal is known exactly). The energy function

$$E = \sum_i \frac{1}{2} \sum_{j \neq i} V_{ij}, \tag{3.3}$$

where V_{ij} is the energy of bindings between i-atom and j-atom in a crystal,

$$V_{ij} = f_C(r_{ij})[f_B(r_{ij}) + b_{ij} f_A(r_{ij})]. \tag{3.4}$$

Functions f_A and f_B are the attractive and repulsive parts of potentials for a pair of atoms. The function f_C is responsible for limiting the length of bond and is a smooth cut-off function. The parameters R and D are chosen in order to limit the interactions to first-neighbour shell only. The functions are described below:

$$f_A(r) = -Be^{-\lambda_2 r}, \tag{3.5}$$

$$f_B(r) = Ae^{-\lambda_1 r}, \tag{3.6}$$

$$f_C(r) = \begin{cases} 1 & \text{for} \quad r < R - D, \\ \frac{1}{2} - \frac{1}{2} \sin \frac{\pi(r-R)}{2D} & \text{for} \quad R - D < r < R + D, \\ 0 & \text{for} \quad r > R + D, \end{cases} \tag{3.7}$$

$$b_{ij} = (1 + \beta^n \xi_{ij}{}^n)^{-1/2n}, \tag{3.8}$$

$$\xi_{ij} = \sum_{k \neq (i,j)} f_C(r_{ik}) g(\theta_{ijk}) e^{\lambda_3{}^3 (r_{ij} - r_{ik})^3}. \tag{3.9}$$

The b_{ij} term is responsible for the strength of bonds. In this case the bond strength depends on local environment and is lower when the number of neighbours is relatively high. This potential is based on the Morse interactions.

The parameters should be chosen to fit the theoretical and experimental data obtained for realistic and hypothetical crystal configurations, e.g. the cohesive energy of several high-symmetry bulk structures, the lattice constant and bulk modulus of the researched crystal lattice [14].

Stillinger–Weber potential [12], its energy function comprises both two- and three-atom contributions which make it possible to describe complex deformations in crystals more accurately than in the case of potentials based only on two-atomic interactions. Any interatomic energy function describing interactions between N atoms can be simplified to one-body, two-body, three-body etc. interactions as it is presented in the following equation:

$$\Psi(1,\ldots,N) = \sum_{i} v_1(i) + \sum_{\substack{i,j \\ i<j}} v_2(i,j) + \sum_{\substack{i,j,k \\ i<j<k}} v_3(i,j,k) + \ldots + v_N(1,\ldots,N). \tag{3.10}$$

The potential v_1 stands for a single particle in the system. This part will be neglected because it is not considered in our discussion. It is important that the component functions v_n should quickly tend to zero with increasing value of n. To this end the Stillinger–Weber potential is approximated only by v_2 and v_3 functions, that is two-body and three-body interactions. The potential is based on the well-known Lennard–Jones potential, which was assumed for noble gases description; however, it is unusable for semiconductors due to the lack of fitting parameters. The partial energy functions v_2 and v_3 are introduced as follows

$$v_2(r_{ij}) = \epsilon f_2(r_{ij}/\sigma) \quad \text{and} \quad v_3(\mathbf{r}_i,\mathbf{r}_j,\mathbf{r}_k) = \epsilon f_3(\mathbf{r}_i/\sigma,\mathbf{r}_j/\sigma,\mathbf{r}_k/\sigma), \tag{3.11}$$

where ϵ is chosen to give f_2 depth -1, and σ is chosen to make $f_2(2^{1/6})$ vanish. The f_2 is a function only of the scalar distance, but f_3 must possess full translational and rotational symmetry.

Finally the two-body part of Stillinger–Weber potential takes the following form:

$$f_2(r) = \begin{cases} A(Br^{-p} - r^{-q})e^{\frac{1}{r-a}} & \text{for} \quad r < a, \\ 0 & \text{for} \quad r \geq a, \end{cases} \tag{3.12}$$

where the constants A, B, p have to be positive. This potential is also automatically cut off when $r = a$, without any discontinuities in any r derivative, which makes it very useful in any molecular dynamics simulations.

The same cut-off condition has to be held in the three-body interactions

$$f_3(\mathbf{r}_i,\mathbf{r}_j,\mathbf{r}_k) = h(\mathbf{r}_{ij},\mathbf{r}_{ik},\Theta_{jik}) + h(\mathbf{r}_{ji},\mathbf{r}_{jk},\Theta_{ijk}) + h(\mathbf{r}_{ki},\mathbf{r}_{kj},\Theta_{ikj}), \tag{3.13}$$

where Θ_{ijk} denotes the angle between r_i and r_k subtended at vertex i. The function h has two parameters $(\lambda, \gamma > 0)$, it takes the form

$$h(\mathbf{r}_{ij}, \mathbf{r}_{ik}, \Theta_{jik}) = \begin{cases} \lambda e^{\frac{\gamma}{r_{ij}-a}+\frac{\gamma}{r_{ik}-a}}\left(\cos\Theta_{jik} + \frac{1}{3}\right) & \text{for} \quad r_{ij}, r_{ik} < a, \\ 0 & \text{for} \quad r \geq a. \end{cases}$$

For this part the Θ parameter is very important; it gives us information about the crystal deformation. When Θ is such that $\cos\Theta = -1/3$, then the three-body potential vanishes, which is because of the perfect tetrahedral angle $\cos\Theta = -1/3$. This shows that in an undeformed state this potential is based only on two-body interactions.

Table 1. Parameters assumed for the Stillinger–Weber potential.

	ε (eV)	σ (nm)	a	A	B	λ	υ
GaAs	1.409	0.210	1.794	8.513	0.782	27.0	1.0
CdTe	1.088	0.228	1.863	8.582	0.993	27.0	1.20

We have used parameters determined in [2] for GaAs. The parameters $A, B, p, q, a, \lambda, \gamma$ have been determined on the basis of many conditions. One of them is crystal's minimal energy in undeformed state. The second condition arises from experimental values of the elastic constants and the third one from the temperature of melting point and other similar constants. Some constants are calculated using the *ab initio* methods for determining physical properties of atomic bonds. In addition we compared the crystal's energy, calculated with the Stillinger–Weber potential, response on stretching with hyperelastic models based on generalized strain models which is shown in Fig. 1.

To find the stress-strain response of atomic structure the energy of which is governed by a given interatomic potential, we have applied the following relation yielding from the strain energy balance:

$$\widehat{\boldsymbol{\sigma}}_I = \widehat{\rho}\frac{\partial \Psi}{\partial \mathbf{F}}, \tag{3.14}$$

where $\widehat{\boldsymbol{\sigma}}_I$ denotes the first Piola–Kirchhoff stress tensor while Ψ means the crystal's specific free energy (per unit mass). The energy depends on distances and positions between all the atoms in the crystal, i.e. $\Psi = \Psi(\mathbf{r}_1, \ldots, \mathbf{r}_N)$. Assuming that the current position vector $\mathbf{r}_i$ depends on the deformation gradient $\mathbf{F}$ and on the reference position vector $\mathbf{R}_i$, we find

$$\frac{\partial \Psi}{\partial \mathbf{F}} = \sum_i \left(\frac{\partial \Psi}{\partial \mathbf{r}_i}\frac{\partial(\mathbf{F}\mathbf{R}_i)}{\partial \mathbf{F}}\right) = \sum_i \left(\frac{\partial \Psi}{\partial \mathbf{r}_i} \otimes \mathbf{R}_i\right), \tag{3.15}$$

where $\mathbf{r}_i = \mathbf{F}\mathbf{R}_i$. Substituting (3.15) into (3.14) we find the Cauchy stress tensor corresponding to the Stillinger–Weber potential

$$\boldsymbol{\sigma} = \widehat{\rho}\frac{\partial \Psi}{\partial \mathbf{F}}\mathbf{F}^T \det \mathbf{F}^{-1}. \tag{3.16}$$

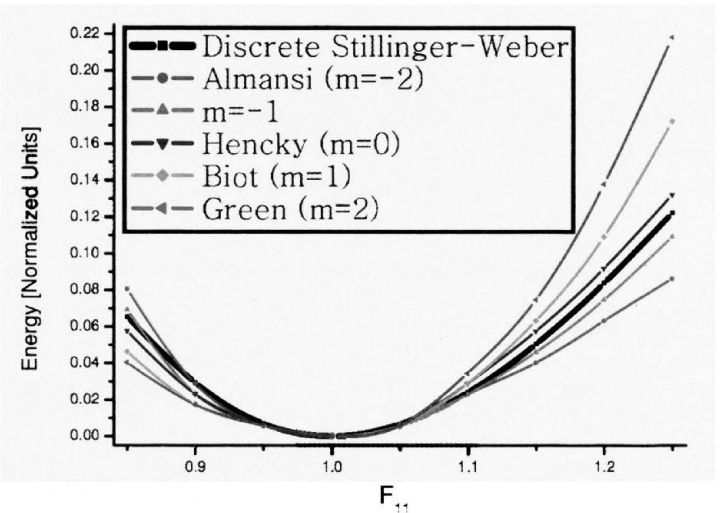

FIG. 1. Energy of hyperelastic models based on generalized strain models versus discrete Stillinger–Weber potential model in uniaxial stretch test.

The method described above is very similar to the method used by [17]. Because the calculation of stress on the basis of numerical differentiation of all two- and three-atomic terms over the deformation process turned out to be very time-consuming, the Stillinger–Weber potential model was replaced by a nonlinear hyperelastic constitutive model based upon a non-monotonic (pseudo-strain) functions. Finally, the functions below will describe the continuized Stillinger–Weber model.

$$\widehat{\boldsymbol{\varepsilon}} = \sum_{i=1}^{3} \ln u_i \; e^{-\frac{n}{2}(u_i^2-1)} \; \mathbf{u}_i \otimes \mathbf{u}_i, \tag{3.17}$$

$$\boldsymbol{\varepsilon} = \sum_{i=1}^{3} \ln v_i \; e^{-\frac{n}{2}(v_i^2-1)} \; \mathbf{v}_i \otimes \mathbf{v}_i, \tag{3.18}$$

where n is a strain parameter. In our research we have found parameter n by fitting the above functions to discrete Stillinger–Weber potential. The fitting procedure shows that the parameter n should be 0.57 for GaAs crystal lattice. We didn't fit the n parameter for CdTe or ZnTe. The results of using such a

continuized potential function for GaAs are presented in Fig. 2. This fitted model differs from the discrete Stillinger–Weber potential, the difference is about 3%. The stretching test was performed with atoms able to reorganize themselves.

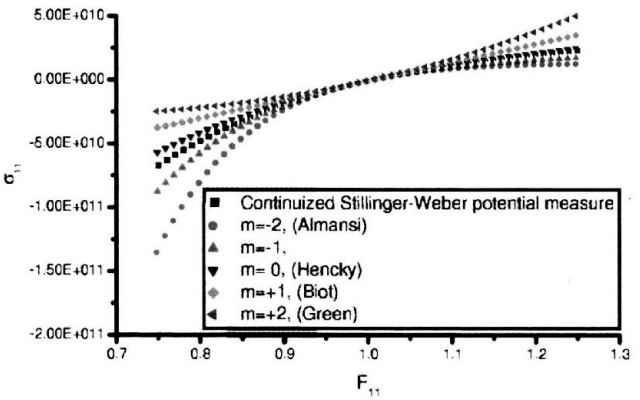

FIG. 2. Stress of hyperelastic models based on generalized strain models versus continuized Stillinger–Weber potential model in uniaxial stretch test.

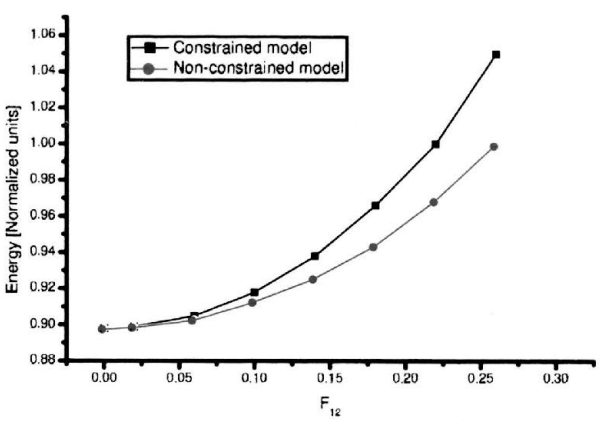

FIG. 3. Stress-strain comparison of the considered constrained and non-constrained model for the simple shear test.

We made also a shearing test for the Stillinger–Weber potential model. The shear test plot is a comparison between a model with atoms allowed to reorganize and find their local energy minima and another one where atoms are placed with no possibility to move.

4. Quantum dot calculations example

We have applied the discrete Stillinger–Weber potential with special subroutines to FEM solver, namely FEAP [18]. Here we must explain that although the algorithm is using a FEM solver, it is not the Finite Element Method – there are no finite elements.

In our approach we have used subroutines describing two- and three-body interaction terms. The fundamental difference between our method and FEM is that our, let's say, pseudo-elements do not contain continuous distributions of mass and stress/forces within elements, but they are based on the energy balance of discrete atoms situated in the mesh nodes, which satisfy the motion equation

$$m_n \ddot{r}_n = f_n, \tag{4.1}$$

where the nodal forces f_n are determined as a superposition of elemental forces

$$f_n^2 = \frac{\partial v_2}{\partial r_n} \qquad \text{and} \qquad f_n^3 = \frac{\partial v_3}{\partial r_n} \tag{4.2}$$

corresponding directly to the two- and three-body terms of energy, v_2 and v_3, according to (17). In other words, in the classical FEM the energy, mass and forces are continuously distributed within elements, while in our approach there are no continuous distributions over the two- and three-body pseudo-elements. Such approach allows us to link these pseudo-elements with the classical solver of FEM. Such attempt doesn't require any changes in the FEAP solver.

The mesh, similar to the FE mesh, is only a graphic representation of all possible connections and data needed to calculate the interaction between atoms. The algorithm is capable of calculating dynamic (time-dependent) or static problems. The material distribution is assumed for quantum dot structures observed on HRTEM experimental images [7]. In this example we applied CdTe in ZnTe quantum dot atoms positions to the prepared program which generates mesh of pseudo-elements. The generator produces a block of sphallerite structure of desired size and shape or uses an input file where the atoms position were stored (e.g. Zn, Te or Cd). The Stillinger–Weber potential which is applied in our pseudo-elements recognizes the bond type and the atoms by recognizing the material number (e.g. Cd–Te material has the number "1" and Zn–Te has the number "2"). The quantum dot was composed of 40 300 atoms – to limit the calculation time and conserve the computer memory we applied the so-called multipoint displacement boundary conditions on each boundary plane of our block chosen for calculation. These conditions correspond to the assumption that the quantum dot is not alone in the bulk material but is surrounded by other quantum dots of the same shape and size what also required setting the boundary

condtions on external walls of our material. Finally the problem was limited to only 10 075 atoms. In the presented example we have calculated the static problem - time-independent. The assumed quantum dot material decomposition is shown in Fig. 4.

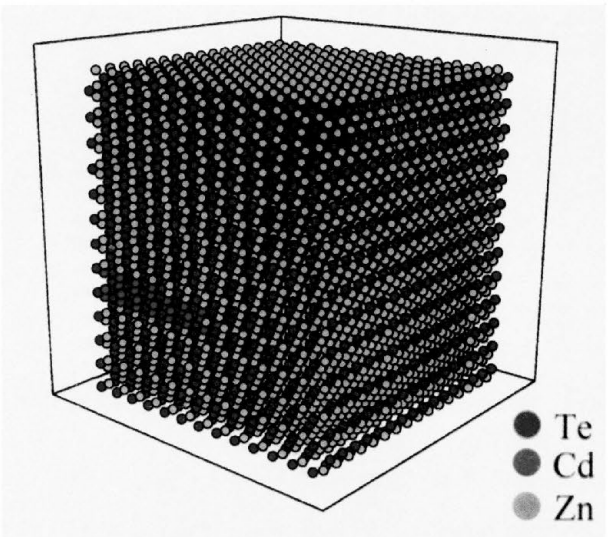

FIG. 4. Assumed material decomposition in quantum dot quarter.

The obtained atom displacements, Fig. 5, were compared with similar quantumdot calculated with FEM, and they were very similar both in the shape and the displacements. In initial state of the performed simulation both structures of quantum dot and the surrounding region have the same lattice constant – ZnTe lattice constant. Because CdTe has a larger lattice constant than ZnTe, we expected that the quantum dot region will extend to reach the CdTe lattice constant. Such extension can be noticed in Fig. 5 presenting the directions of extension X, Y and Z. We can notice that the largest displacements are in pictures presenting X plane (almost 0.22 nm) and Z plane (0.28 nm), what is caused by periodic boundary conditions. The block of crystal presented here is a simulation of an infinite line of quantum dots in Y direction, so the last row of atoms in Y direction has been disabled to move along the Y axis – in real structure just behind the last row of atoms begins the next similar quantum dot which interacts in opposite direction [7]. These results can be later easily applied to the HRTEM image simulation program allowing to verify and reconstruct the quantum structures observed in laboratory conditions. Parameters for the Stillinger–Weber potential used in these calculation were taken from [9, 4].

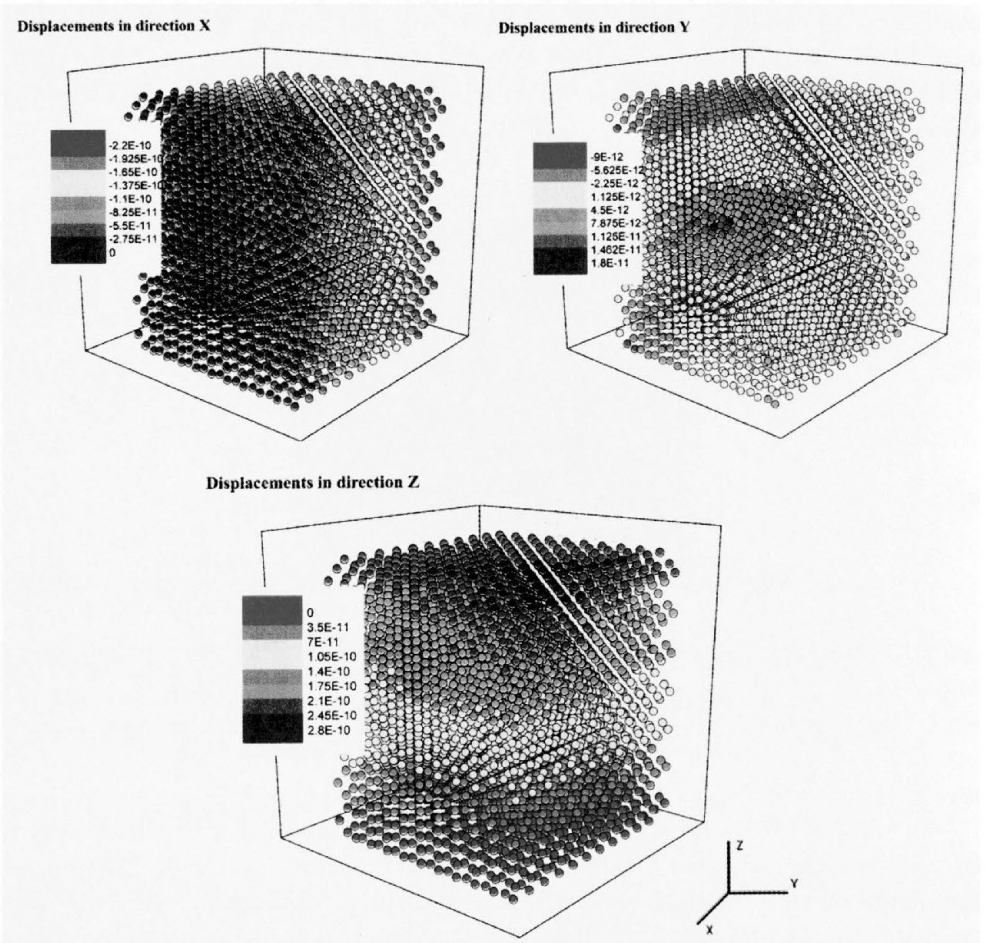

FIG. 5. Displacements resulting from the performed calculations.

5. Conclusion

In the hyperelasticity based upon general strain measure, the fundamental question arises: which of the finite strain measures is the best one? The choice of the given measure is responsible for the higher order elastic effects. For example, the third-order elastic constants depend very strongly on the strain measure choice, see [4]. In this paper, we have shown that the nonlinear elastic behaviour of one of the most popular interatomic potentials used in MD simulations, namely the behaviour of the Stillinger–Weber potential, is closest to the behaviour of the first-order hyperelastic models based upon the strains corresponding to the strain parameter between -1 and 0. This means that the first-order anisotropic

hyperelasticity based upon the strain $\boldsymbol{\varepsilon} = \ln \mathbf{U}$ or $\boldsymbol{\varepsilon} = -\mathbf{U}^{-1} + \mathbf{1}$ gives approximately the same extension/compression asymmetry in elastic behaviour as that obtained by physicists with the use of interatomic potential like the Stillinger–Weber one. Recently, it has been used in the majority of MD simulations carried out for semiconductor nanostructures. Obviously, our comparison concerned only the elastic behaviour in the uniaxial deformation range in which the interatomic potential was able to hold a stable GaAs atomic structure in the approximately uniform deformation state.

Acknowledgment

This work was supported by the State Committee for Scientific Research (KBN) in Poland under Grants No. 7 T07A 004 16 and 7 T07A 01517.

References

1. L. ANAND, *On H. Hencky's approximate strain-energy function for moderate deformations*, Transactions of ASME, **46**, 78–82, 1979.
2. J. E. ANGELO and M. J. MILLS, *Investigations of the misfit dislocation structure at a CdTe(001)/GaAs(001) interface using Stillinger-Weber potentials and high-resolution transmission electron microscopy,* Philosophical Magazine A, **72**, 3, 635–649, 1995.
3. M. I BASKES and M. S. DAW, *Embedded-atom-method: Derivation and application to impurities, surfaces, and other defects in metals*, Phys. Rev. B, **29**, 6443, 1984.
4. P. DŁUŻEWSKI, *Anisotropic hyperelasticity based upon general strain measures*, Journal of Elasticity, **60**, 2, 119–129, 2000.
5. M. I. FOILES, S. M. BASKES and M. S. DAW, *Embedded-atom-method functions for the fcc metals Cu, Ag, Au, ni, Pd, Pt, and their alloys*, Phys. Rev. B., **33**, 7983, 1986.
6. M. J. HORODON and B. L. AVERBACH, Acta Metallurgica, 9, 247, 1961.
7. E. SOBCZAK, A. SZCZEPANSKA, S. MACKOWSKI, T. WOJTOWICZ, G. KARCZEWSKI, J. KOSSUT, S. KRET, P. DLUZEWSKI and P. RUTERANA, *Electron microscopy study of ZnTe/CdTe superlattice with high density of quantum dots*, Mat. Res. Soc. Symp. Proc., 642, 2001.
8. D. RAABE, *Computational material science. The simulations of materials and properties*, Wiley-VCH, Weinheim 1998.
9. D. KIRMSE, H. SCHNEIDER, R. SCHEERSCHMIDT, K. CONRAD and W. NEUMANN, *Electron microscope characterization of CdSe/ZnSe quantum dots based on molecular dynamics structure relaxations*, Ultramicroscopy, **81**, 289–300, 200.
10. B. R. SETH, *Generalized strain measure with applications to physical problems*, [in:] M. REINER and D. ABIR [Eds.], *Second-order effects in elasticity, Plasticity and Fluid Dynamics*, Pergamon Press Oxford 1964. Proc. Int. Symp., April 23–27, Haifa 1962.
11. F. SPAEPEN, *Interfaces and stresses in thin films*, Acta Materialia, **48**, 31–42, 2000.

12. F. H STILLINGER and T. A. WEBER, *Computer simulation of local order in condensed phases of silicon*, Physical Review B, **31**, 8, April 15 1985.

13. C TEODOSIU, *Elastic models of crystal defects*, Springer-Verlag and Editura Academiei, Berlin and Bucureşti 1982.

14. J. TERSOFF, *Empirical interatomic potential for carbon, with applications to amorphous carbon*, Phys. Rev. Lett., **61**, 2879, 1988.

15. S. N. VAIDYA and G. C. KENNEDY, *Compressibility of 18 metals to 45kb*, J. Phys. Chem. Solids, **31**, 2329–2345, 1970.

16. S. N. VAIDYA and G. C. KENNEDY, *Compressibility of 22 elemental solids to 45kb*, J. Phys. Chem. Solids, **33**, 1377–1389, 1972.

17. K. YASHIRO and Y. TOMITA, *Local lattice instability at dislocation nucleation and motion*, J. Phys. IV France, 11, PR5–3, 2001.

18. O. C. ZIENKIEWICZ and R. J. TAYLOR, *The finite element method*, McGraw-Hill, London 1991.

Received January 22, 2003.

Arch. Mech., **55**, 5–6, pp. 407–430, Warszawa 2003

The process zone around the tip of cracks in metal matrix composites

S. K. KOURKOULIS

National Technical University of Athens,
School of Applied Sciences, Department of Mechanics,
Theocaris Building, Zografou Campus, GR 157-73 Athens, Hellas
e-mail:stakkour@central.ntua.gr

SOME CHARACTERISTICS of the process zone developed around the tips of cracks as well as the fractography of the fracture surfaces constitute the subject of the present paper. The study was carried out using Scanning Electron Microscopy for the determination of the Crack Tip Opening Displacement, while numerical analysis and experimental results were combined for the determination of the J-integral. A modern particulate Metal Matrix Composite and its matrix alloy were used for the fabrication of relatively thin tensile specimens of two different types, i.e. single- and double-edge-notched. Dependence of the above quantities on the thickness of the specimen is detected: both the critical Crack Tip Opening Displacement and the critical J-integral are found to increase in an almost linear manner with thickness. For comparison, intact prismatic specimens were considered, in order to study the dependence of ductility and fracture on the thickness of the specimen. It is observed that they depend also on the specimen thickness in a similar manner. Variation of these two properties with the direction of the specimen with respect to the rolling axis is also detected, indicating the importance of the plastically induced anisotropy due to the manufacturing process. Concerning the mechanisms leading to failure, it is concluded that void coalescence is active although void nucleation due to the presence of particles appears to be unavoidable.

1. Introduction

THE QUANTIFICATION of the characteristics of the process zone developed around the tip of a crack is among the most important tasks of Fracture Mechanics since this zone governs the further development and propagation of the crack. However, in spite of the fact that the definition of a single-parameter mechanical quantity, which could serve as a failure criterion in case of pre-cracked specimens or structural members, has been the subject of an enormous number of research papers, already since the very early steps of the development of Fracture Mechanics, the problem is not yet closed.

The introduction of the concept of the stress intensity factor, K, by WESTERGAARD [1] and IRWIN [2] as well as of the concept of the critical stress intensity factor or fracture toughness, K_C, gave the impression that an acceptable solution

of the problem was achieved. The initial enthusiasm was shadowed, however, by a long series of experimental findings, which indicated that K_C depends on the thickness of the specimen [3]. Indeed, experiments have shown that only above a certain specimen thickness, beyond which the material is under predominantly plane strain, K_C tends to a constant value, which is usually considered as a material property. Below this limit K_C depends in a sigmoid manner on the thickness of the specimen exhibiting a well-defined maximum value. For very thin specimens the dependence is not exactly known.

The above behaviour is usually attributed to the fact that for very thin plates, the fracture toughness results from the plastic energy spent in the neck in front of the crack tip, which in general is significantly larger in comparison to the energy spent for the overall damage of the material. The work of necking, however, depends directly on the thickness of the specimen. As a consequence, the fracture toughness varies also with thickness, as pointed out by BLUHM [4] and SWEDLOW [5] already from the early sixties and for purely plane stress the variation is almost linear.

Unfortunately, experimental results concerning the dependence of fracture toughness on thickness for very thin specimens are rather scarce and as a result, the relation between the resistance to cracking initiation and plate thickness remains insufficiently understood until today [6] even for conventional metallic materials and alloys. The situation is worse in case of modern composite materials and especially for the class of them described under the term particulate Metal Matrix Composites (MMCs), since the study of their behaviour from the Fracture Mechanics point of view is still in progress all over the world. These materials were only developed during the last two or three decades to meet the increased demands of aerospace industry for optimized mechanical properties combined with low specific weight.

In general, the principal concept of the technology of composite materials is to combine certain assets of their constituents in order to give to the newly synthesized material unique and useful properties. The reinforcement may be either of one- (fibrous) or two- (laminar) or even three-dimensional shape (particulates). The last class includes composites with more than 20% of the hard reinforcing dispersed phase. The particulate composites are non-homogeneous materials and their properties appear to be very sensitive to the constituent properties as well as to the geometric shapes of the array. The strength of particulate composites depends on the diameter of the particles, the interparticle spacing as well as on the volume fraction of the reinforcement.

Among particulate composite materials Metal Matrix Composites (MMCs) are advantageous as structural materials since in their virgin state they are isotropic materials without any kind of texture anisotropy. Also, they combine metallic with ceramic properties, such as high strength, high modulus of elastic-

ity, high toughness, relatively low sensitivity to thermal shocks and temperature changes, high surface durability, low sensitivity to surface flaws, high thermal and electrical conductivity. Additionally, the ductile metal matrices, such as aluminum (used in the present work), titanium or nickel-chromium alloys, undergo energy absorbing plastic deformation under impact, which is very important in many dynamic structural applications [7].

On the other hand, the ductile matrix permits the blunting of cracks and relieves stress concentrations by plastic deformation. It is thus expected that the composite materials should be characterized by improved fracture toughness. However, it has been pointed out [8] that the presence of cracks strongly deteriorates the fracture strength of MMCs, in comparison to the uncracked materials, rendering the use of the matrix material more advantageous in case of presence of macro-cracks. Indeed, pairs of matrix alloys and MMCs are reported for which under specific loading conditions the fracture toughness of the matrix alloy is higher compared to that of the composite material [8, 9].

Thus it can be said that the target of the paper is twofold: The determination of the characteristics of the process zone and their dependence on the thickness of the specimen in case of MMCs and, on the other hand, the study of the mechanisms leading to failure, in an attempt to understand the deterioration of the mechanical characteristics of MMCs in the presence of macro-cracks.

2. Some theoretical considerations

It is accepted that in Linear Elastic Fracture Mechanics, a single parameter can characterize in a satisfactory manner the singular stress and strain fields around a crack tip. This parameter is usually described in terms of a balance of energy rates, which leads to the energy release rate concept, uniquely related to the stress intensity factor. Following a similar procedure for the case of nonlinear materials, the J-contour integral (or simply the J-integral) was introduced [10], which describes the flow of energy into the tip region. With respect to a point s on the crack front in a nonlinear elastic material, the J-integral is defined by the formula:

$$J(s) = \int_{\Gamma} \left(W\delta_{1j} - P_{ji}\frac{\partial u_i}{\partial X_1} \right) n_j d\Gamma - \int_{A_\Gamma} \frac{\partial}{\partial X_3}\left(P_{3i}\frac{\partial u_i}{\partial X_1} \right) dA. \tag{2.1}$$

In the above Eq. (2.1) Γ is an arbitrary curve enclosing the crack front at the position given by s, in the plane $X_3 = 0$, A_Γ is the surface area defined by Γ, W is the deformation work per unit volume, u is the displacement vector, P_{ij} denotes the Piola–Kirchhoff stress tensor, X_i is a component of the position

vector of a material point in the undeformed configuration and n_j is a component of a unit vector perpendicular to Γ.

For the Double Edge Notched Tensile (DENT) specimen, used for the determination of the J-integral in the experimental program of the present work, RICE [11] introduced the following simplified formula for J-integral:

$$J_R = \frac{K_I^2}{E} + \frac{1}{\ell_0 t_0}\left(2\int P du_P - P u_P\right). \tag{2.2}$$

Here K_I is the stress intensity factor, E the Young's modulus, P the applied load and u_p the plastic displacement. For this type of specimen the stress intensity factor, K_I, is given as [12]:

$$K_I = \frac{P}{t_0}\sqrt{\frac{\pi\lambda}{2w_0(1-\lambda)}}\left(1.122 - 0.561\lambda - 0.205\lambda^2 + 0.471\lambda^3 + 0.190\lambda^4\right). \tag{2.3}$$

In Eq. (2.3) w_0 is the half-width of the plate while $\lambda = a_0/w_0$, where a_0 is the initial crack length.

The validity of the J-integral approach was the subject of a long series of papers. The point most intensively criticized was related to the fact that it is strictly founded exclusively for nonlinear elastic materials, which are of reversible nature concerning the loading-unloading path. It appears thus that using the J-integral for elastic-plastic materials is illegitimate and the concept is applicable only until no unloading occurs in any part of the material, or in other words until crack propagation starts. Other points related to the difficulties encountered during the practical determination of the critical value of J-integral and the necessity to combine the experimental results with finite element analysis are of rather minor importance.

The consensus reached today is that the J-integral can be calculated at the tip of a crack even for an elastic-plastic solid until the crack starts propagating subject to the additional condition that the crack tip finite strain zone, in which damage occurs, is sufficiently confined. Indeed, the loss of constraint, appearing with large scale yielding, is directly related to the deviation of the relationship between the J-integral and the Crack Tip Opening Displacement (δ_t) from the one proposed by SHIH [13], even for a stationary crack:

$$J = \frac{\sigma_0 \delta_t}{d_n}. \tag{2.4}$$

The above Eq. (2.4) was obtained by Shih using the HRR solution for the stress and strain fields, which is valid within the framework of the deformation theory of plasticity, assuming that no unloading occurs. The flow behaviour of the material

is simulated by a power law, generalized as follows:

$$\varepsilon_{ij} = \frac{3}{2}\alpha \left(\frac{\sigma_e}{\sigma_0}\right)^{n-1} \frac{S_{ij}}{E}, \tag{2.5}$$

where ε_{ij} and S_{ij} are the components of the strain- and of the deviatoric stress-tensor, respectively, σ_e is the effective stress, defined as $\sigma_e=[3/2(S_{ij}S_{ij})]^{1/2}$, σ_0 is a reference value for the stress (usually defined as the 0.2% offset yield strength) and α, n are experimentally defined constants. Assuming then that the above restrictions are fulfilled, the stress field components, σ_{ij}, can be described according to Shih's approach by the following equation:

$$\sigma_{ij} = \sigma_0 \left(\frac{EJ}{\alpha\sigma_0^2 I_n r}\right)^{1/(n+1)} \tilde{\sigma}_{ij}(n,\theta), \tag{2.6}$$

where r is the radial distance from the crack tip, I_n is a dimensionless constant which depends on strain hardening and $\tilde{\sigma}_{ij}$ is, also, a dimensionless constant depending on strain hardening and angle θ from the crack plane. Concerning the function $d_n = d_n(n, \varepsilon_0)$ of Eq. (2.4), which was given by Shih as a nomogramme, OMIDVAR'S *et al.* [14] approximate solution was adopted in the present study, according to which it holds that:

$$d_n\,(n, \varepsilon_0) = \frac{\sigma_0}{E}^{1.05/(n-0.1)} \left(1 + \frac{3}{n}\right). \tag{2.7}$$

It is to be emphasized at this point that the previous analysis is valid as long as each material point experiences proportional loading. For cracked bodies this is not the case, since an intense strain region exists, within $\sim 2\delta_t$ of the tip, that experiences highly non-proportional loading. In such a case the analysis is only valid as far as the intense strain region is surrounded by a region in which the HRR model assumptions still prevail. This is true as long as δ_t is relatively small compared to both the crack size and the uncracked ligament length. Otherwise fracture toughness becomes strongly geometry-dependent [15]. The validity of the above assumption will be checked experimentally in the next paragraphs.

3. Experimental procedure

3.1. The material

The material used in the present study is the BP-2124 Al-Cu particulate MMC, produced by a powder metallurgy process. According to this process, aluminum alloys are reinforced with extremely fine silicon carbide (SiC) particles. The chemical composition of the matrix alloy is listed in Table 1. The respective

Table 1. The chemical composition of the BP-2124 Al-Cu alloy.

Element	Wt [%]
Copper	4.0–4.4
Magnesium	1.3–1.6
Manganese	0.4–0.7
Iron	0.3 max
Zinc	0.25
Silicon	0.2
Chromium	0.1
Titanium & Zirconium	0.2
Others (each)	0.05 max
Others (total)	0.2 max
Aluminum	Balance

composite is obtained by adding to the matrix alloy about 20% wt of SiC particles of average diameter 3 μm [16].

The BP-2124 Al-Cu particulate MMC has very good specific properties (specific stiffness and high specific strength). Its absolute mechanical properties are considerably improved in comparison to the matrix alloy. As it can be seen from Table 2, in which the values of the modulus of elasticity, tension strength, torsion strength and ductility are recorded, the improvement varies between 37% for the modulus of elasticity and 50% for the strength under torsion. Of course as it is expected, the ductility of the composite material is about 27% lower compared to that of the matrix alloy [17].

Table 2. The average mechanical properties of the BP-2124 Al-Cu MMC and of the respective matrix alloy (properties measured along the rolling direction).

	Elastic Modulus [GPa]	Tensile Strength [MPa]	Torsional Strength [MPa]	Ductility [%]
2124 Alloy	80.0	435	505	6.7
2124 MMC	109.9	622	760	4.9
Change [%]	(37)	(43)	(50)	(–27)

According to the manufacturing process, the raw materials, i.e. the atomized aluminum alloy powder and the silicon carbide microgrit, are bought-in to an internal specification covering chemistry and size. The powders are then processed and blended to a homogeneous mixture. The mixed powders are then canned, degassed and hot isostatically pressed to full density using conventional aluminum powder metallurgy practices. The hot pressed billets are decanned and converted to wrought product using standard metal working equipment.

The material was available in rolled plates of thickness equal to $t = 12$ mm and rolled sheets of thickness $t = 1.2$ mm. After the specimens were cut from the plate and machined in their standardized shape (by removing away material in the thickness direction), they were subjected to heat treatment as it was suggested by the manufacturer. The procedure included solution treatment for ninety minutes at 505°C and then immediately cold-water quench. No visible distortion or surface cracking of the specimens was observed due to the quenching. Finally, the specimens were carefully polished in order to eliminate any scratches and similar irregularities from their surface.

However, it should be mentioned at this point that the above heat treatment procedure might be the reason for the generation of residual stresses, which are suspected to be responsible for many mechanical changes including anisotropy, especially in case of particulate reinforced MMCs. Although the analysis of the residual stresses is beyond the scope of the present paper, it is mentioned here that extensive study of the BP-2124 Al-Cu MMC with the aid of SEM and TEM techniques verifies the above option: The rupture of it is generally initiated in the matrix alloy in the immediate vicinity of the SiC particles. The dislocation density is much higher in the grains in contact with the particles. The cracks are initiated in this region because there are high residual stresses due to the coefficient of thermal expansion mismatch and the heat treatment procedure adopted [18].

3.2. Specimens and testing procedure

Three different types of specimens were employed:

- The first one included miniature Single Edge Notched (SEN) used for the determination of the Crack Tip Opening Displacement (CTOD) with the aid of the Scanning Electron Microscopy (SEM) technique. They were cut out from the rolled sheet and plates along the rolling direction. After they were machined to the required thickness, which varied between 1.2 and 3.5 mm (by removing away material in the thickness direction very slowly by mechanical milling), they were formed to the familiar dog-bone – like standardized geometry. Edge cracks were machined on one side of the specimens by means of a rotating slow cutting diamond disc of thickness 100 μm. The specific cutting procedure was chosen

since it creates cracks with minimal mechanical damage at their root. The width of the specimens was $w = 6.5$ mm, their thickness varied between $t = 1.2$ mm and $t = 3.5$ mm, while their gauge length varied between 65 and 70 mm. The initial length of the cracks, a_0, varied between 1 mm and 3 mm, yielding f values (ratio of width of the specimen over the length of the crack) in the range from about 0.15 to 0.45. The cracks were cut either perpendicular to the rolling and loading direction ($\beta = 90°$) or inclined at 60° with respect to it ($\beta = 60°$).

These miniature specimens were subjected to in-situ, monotonically increasing tensile loading in the Scanning Electron Microscope (SEM), Cambridge S4-10 type, available at the Laboratory of Testing and Materials of the National Technical University of Athens. The level of the tensile loading is servo-controlled (patent of the Institute of Physics, London, UK). The maximum capacity of the loading device is 2.2 kN. Following the above procedure it becomes possible to measure *in situ*, with the maximum possible accuracy, the current CTOD. However, it is emphasized that if the exact shape of the crack tip were taken into account, the term describing better the quantity measured would be "Notch Root Opening Displacement" (NROD).

As far as it concerns the method for the measurement of CTOD, a procedure similar to the one described in ref. [8] was adopted, based on continuous monitoring and successive photograph of the specimen at various stages of the testing procedure. The measurements were carried out by means of a Gruman-type visioscopic fringe analyzer, equipped with a digital electronic micro-positioning system, of maximum error ± 0.5 μm.

- The second type included Double Edge Notched Tensile (DENT) specimens of length 150 mm and width 60 mm, the thickness of which varied again between 1.2 and 3.5 mm. They were cut from the rolled plates along the rolling direction and the load was induced along the same direction. The width of the ligament was kept constant equal to 20 mm since it was not among the purposes of the paper to study the influence of the length of the ligament on the process. The edge cracks of initial length $a_0 = 20$ mm were machined using the above described procedure for the same reasons. During the numerical analysis of the experimental results it was verified that path-independence at cracking initiation was secured and no case was detected for which the whole ligament length underwent finite strains.

The specimens were subjected to static tensile loading with the aid of a very stiff hydraulic frame. The crosshead speed did not exceed 0.02 mm/min. The load-displacement curve was recorded by means of very sensitive extensometers. The onset of fracture was detected by the appearance of thumbnails on the crack front at the center of the plates.

- The third type included prismatic specimens with orthogonal cross-section of constant width $w = 9$ mm and thickness varying from $t = 1.2$ mm to $t = 9$ mm,

for the determination of the dependence of fracture strength and ductility on the specimen thickness. They were cut either along the rolling direction or perpendicular to it or inclined 45° with respect to it, in order to study, also, the influence of the plastically induced anisotropy on the ductility and fracture stress. They were prepared very carefully to ensure parallel gauge length and faces that were orthogonal to the plane of the sheet.

A system of 8 strain gauges bonded in the mid-section of the specimens was used to measure in real time the transverse and the through-thickness strains as well as the longitudinal ones, which are necessary for the determination of the constitutive law. Gauges were bonded on all four sides of the specimens to monitor possible bending parasitic effects. A series of successive loading-unloading loops was executed in each experiment, in order to measure the pure elastic constants of the material as well as the plastic portion of strains. It is to be mentioned at this point that considerable difficulties were encountered during the measurement of strain in the case of very thin specimens, the maximum thickness of which did not exceed in any case 1.2 mm. Bonding gauges on such thin surfaces is not possible and uncertainties appear concerning the validity of the results. For these specimens the strains were measured using two alternative methods, one based on laser technology and a purely mechanical one based on conventional extensometers. The differences recorded between the two methods were insignificant.

4. Experimental results

4.1. SEN specimens and the critical COD

In Figures 1 (a, b) characteristic SEM photographs are displayed showing the unloaded tip of a crack (Fig. 1a) and the same tip immediately before final failure (Fig. 1b), for a crack oriented perpendicularly to the loading direction ($\beta = 90°$), with a crack length-to-width ratio $f = 0.3$. On the other hand, in Figs. 2 (a–c) characteristic SEM photographs are displayed showing the unloaded tip of a crack (Fig. 2a) and the same tip immediately before final failure (Fig. 2b), for a crack oriented at a direction $\beta = 60°$ with respect to the loading axis and $f = 0.3$ again. The photographs in Figs. 1 (a, b) and 2 (a, b) correspond to a magnification ratio equal to 500, while that in Fig. 2c corresponds to a magnification equal to 1000 giving a better view of the damaged zone around the tip.

From the series of SEM photographs taken during the loading process the CTOD was measured, adopting the procedure indicated in Figs. 3 (a, b), where 1 and 2 indicate characteristic material features on the specimens. Characteristic results are shown in Fig. 4, in which the CTOD is plotted versus the exter-

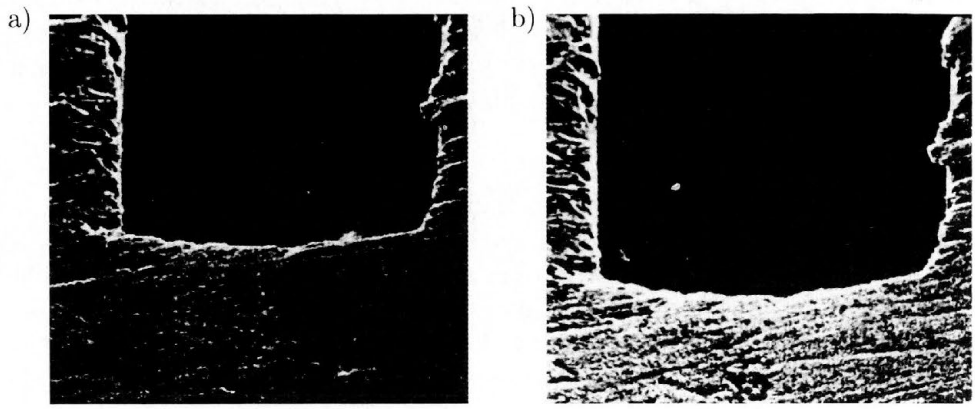

FIG. 1. SEM photographs of a crack with $\beta = 90^0$ (magnification 500×): a) Zero loading step. b) Final loading step.

nally applied net stress reduced over its corresponding maximum value, for the thinnest specimens, i.e. the ones with thickness $w = 1.2$ mm. In this figure filled symbols correspond to specimens with $\beta = 90°$ while empty symbols correspond to specimens with $b = 60°$. It is seen from this figure that the evolution of CTOD is almost negligible for load levels lower than half the final net fracture stress and then it increases in an exponential manner until the fracture stress is reached.

The above behaviour is qualitatively identical with the respective one described by KOURKOULIS in ref. [8] where a different technique for the measurement of COD was adopted, based on a modified δ_5 technique. In Fig. 5 results taken from [8] are shown concerning the COD values reduced over the initial width of the crack, for a crack with $\beta = 90°$, for both the composite material and the matrix alloy, for comparison reasons. Considering the initial width of the crack in [8] ($\delta_0 = 0.2$ mm), the absolute COD values reported there are of the order of 80 μm. Extrapolating these results at the tip of the crack the values of CTOD obtained vary in the range between 15 μm and 25 μm, in very good agreement with the results of the present study, for specimens of the same thickness.

As far as it concerns the dependence of the critical CTOD on the thickness of the specimen, it was concluded that an almost linear relationship exists, for the range of thickness studied in the present series of experiments. This linear relationship is clearly depicted in Fig. 6, in which the values of the critical CTOD are plotted versus the thickness of the specimen, for both the composite material and its respective alloy. As it can be seen from this figure, the critical CTOD increases linearly with increasing thickness from an initial value of 18 μm for

$t = 1.2$ mm to a final value of about 30 μm for $t = 3.5$ mm for the composite material. On the other hand, for the matrix alloy the respective values vary between 72 μm and 97 μm.

Finally, it was concluded that the average values of the critical CTOD appear to be independent of the value of f, for all specimen thicknesses, at least for the values of f used in the present study.

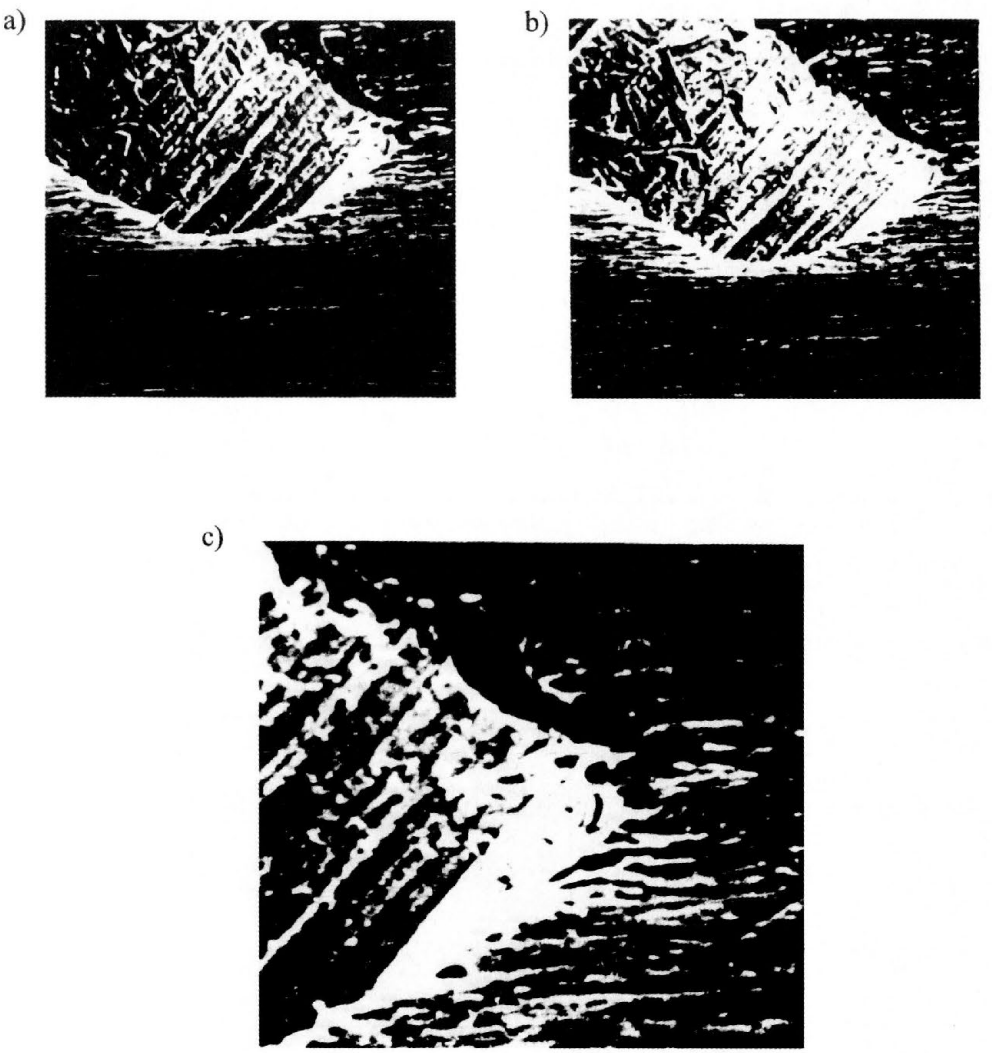

FIG. 2. SEM photographs of a crack with $\beta = 60°$: a) Zero loading step (magnification 500×). b) Final loading step (magnification 500×). c) Detailed view of the crack-tip area at the final loading step (magnification 1000×). Localized damage at the "corner" of the notch root is clearly visible.

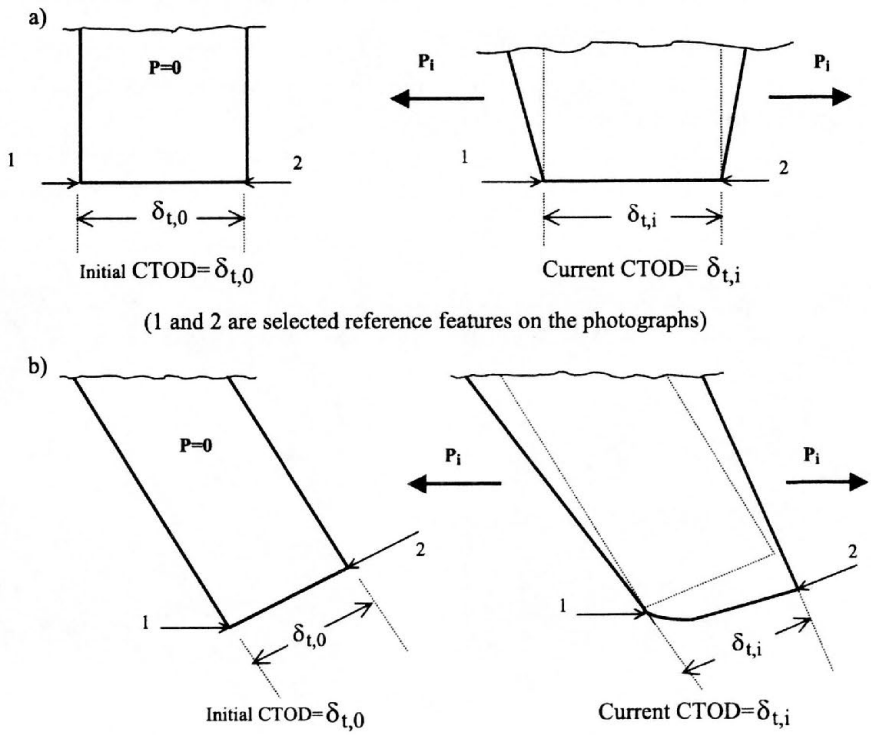

FIG. 3. The procedure followed for the measurement of the CTOD from the SEM photographs.

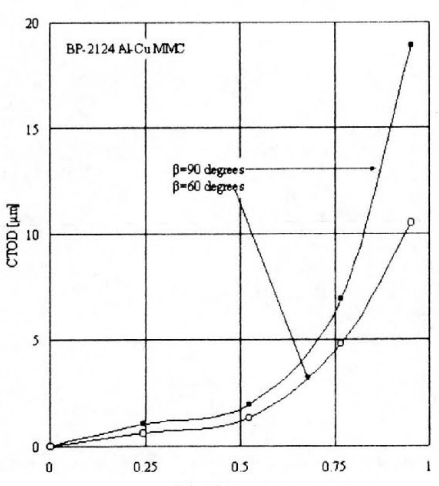

FIG. 4. CTOD versus the net remote stress for cracks with $\beta = 90°$ (filled symbols) and $\beta = 60°$ (empty symbols).

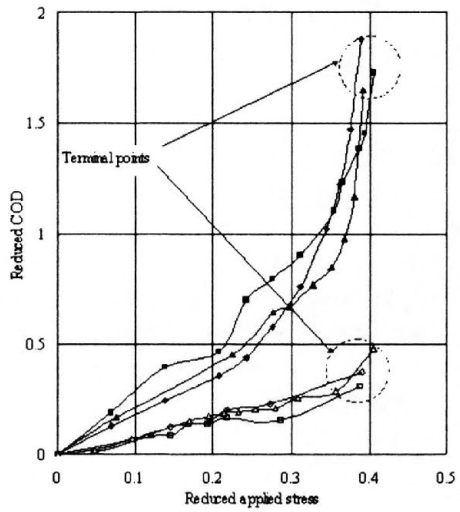

FIG. 5. COD vs. applied stress for $\beta = 90°$. Empty symbols represent the 2124 MMC and filled ones the respective alloy [8].

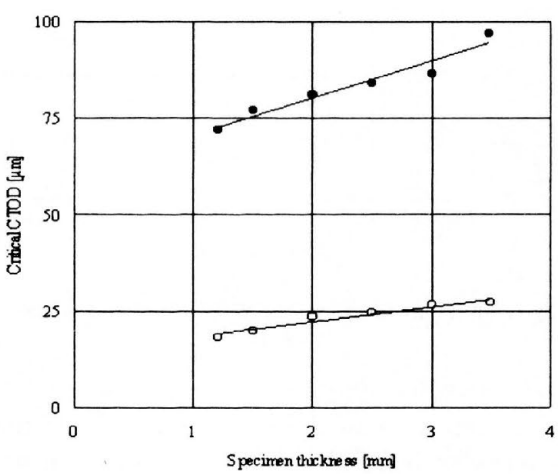

FIG. 6. The dependence of the critical Crack Tip Opening Displacement on the thickness of the specimens. Empty symbols correspond to the 2124 MMC and filled ones to the respective alloy.

4.2. DENT specimens and the critical J-integral

In order to determine the critical values of the J-integral, the DENT specimen configuration was used since the symmetry characterizing it renders numerical simulations easier. The numerical analysis employed is similar to the one followed

by PARDOEN *et al.* [6], based on the 3D domain integration technique introduced by SHIH *et al.* [19]. According to it $J(s)$ is computed from various contours in order to check the path-independence and a mean value is obtained by averaging the local values on the entire thickness. However, it is to be mentioned that the differences detected between these local values were relatively small for all specimens. As it was mentioned earlier, path-independence at the moment of crack propagation onset was observed for all geometries tested. Alternatively, the J-integral was determined using Eq. (2.2) together with the experimental results for the load – displacement curves. It is encouraging for the validity of the numerical analysis that the differences detected between the values obtained from the two alternative methods were very small and the maximum discrepancy did not exceed 4% in any case.

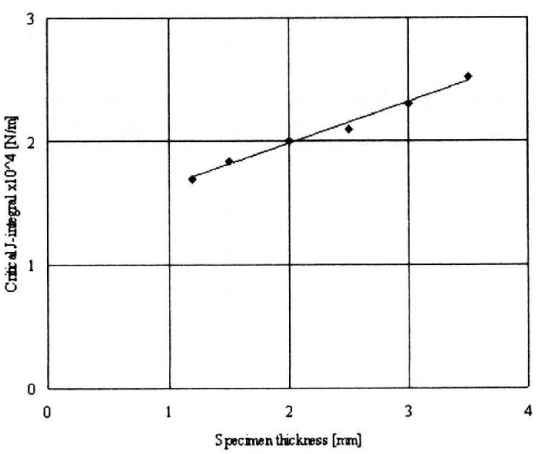

FIG. 7. Numerically calculated critical values of the J-integral versus the thickness of the specimen.

The results of the numerical analysis for the composite material are plotted in Fig. 7. As it can be seen from this figure, the critical values of J-integral increase linearly with increasing thickness, in a manner similar to Crack Tip Opening Displacement. However, it is to be mentioned that the line is of rather abrupt inclination although the material is rather brittle. Indeed the values vary from about 1.7×10^4 N/m for the specimens with $t = 1.2$ mm to about 2.5×10^4 N/m for the specimens with $t = 3.5$ mm. Such a behaviour is rather unexpected since the material studied here is less ductile compared to the one studied by PARDOEN *et al.* [6] for which the maximum value was reached for a thickness of about 5–6 mm. Such a trend is not detected for the material studied in the present work. However, it could be explained on the basis of the different

failure modes activated in case of pure metallic materials and composite ones, as it will be discussed in the next paragraph. In any case it is obvious that additional analysis is required (including also the tests with thicker specimens) in order to determine the exact form of the relation between J_C and specimen thickness.

The conclusions for the matrix alloy are of the same qualitative nature, however the slope of the $J_C = J_C(t)$ function is much higher.

4.3. Intact specimens

As a first experimental observation it should be mentioned that the axial strains measured in the rolling plane, $\varepsilon_{\text{axial},rp}$, diverge slightly, but systematically, from the axial strains measured in the thickness plane, $\varepsilon_{\text{axial},tp}$, for the same load level. The divergence becomes higher with increasing width-to-thickness ratio, as it can be seen from Fig. 8, in which the ratio $\varepsilon_{\text{axial},rp}/\varepsilon_{\text{axial},tp}$ has been plotted versus the axial stress, for a series of characteristic experiments with prismatic specimens cut and loaded along the rolling direction. Also, it is observed from the same figure that while $\varepsilon_{\text{axial},rp}$ exceeds $\varepsilon_{\text{axial},tp}$ during the initial loading steps, however, as the load increases, the phenomenon is inversed and tends to be eliminated as the load approaches the failure limit. The above observations indicate a non-uniformity of the deformation along the thickness of the plates, which becomes more pronounced as the thickness of the specimens increases. The conclusions for the other two types of prismatic specimens, namely the ones cut perpendicular to the rolling direction and diagonal to it, are of similar qualitative nature.

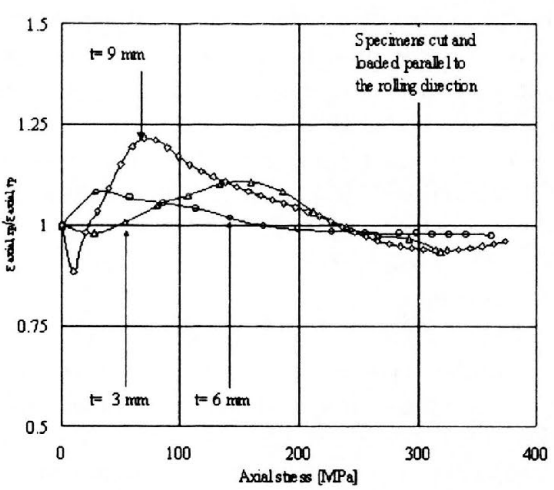

FIG. 8. The divergence between the axial strains measured in the rolling- and in the thickness-plane for specimens cut and loaded along the rolling direction.

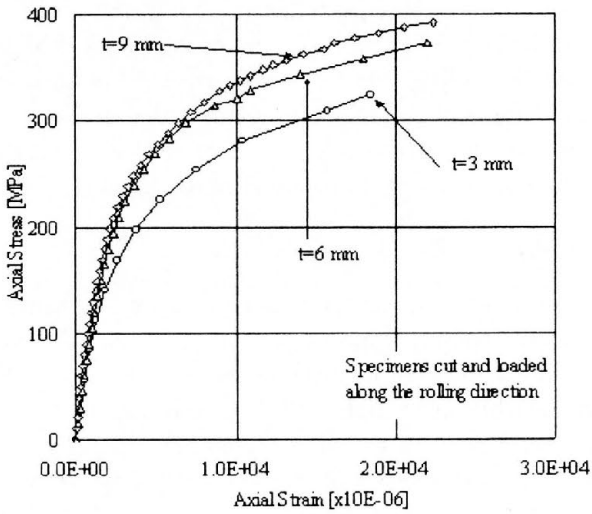

FIG. 9. The axial stress versus the axial strain measured in the rolling plane for prismatic specimens cut and loaded along the rolling direction.

As far as it concerns the variation of the fracture strength and ductility with specimen thickness it was concluded that both quantities increase with increasing thickness. In Fig. 9 characteristic axial stress – axial strain curves are plotted for the specimens cut and loaded parallel to the rolling direction. The axial strains were measured in the rolling plane. It can be seen from this figure that, contrary to the observations by ASSERIN–LEBERT *et al.* [20], the deviation between the graphs starts relatively early, namely almost immediately after surpassing the linearity limit. Such a behaviour seems to contradict common sense, however it can be explained if one takes into account that the material studied here is not a homogeneous continuum medium due to the presence of the reinforcing dispersed phase of the silicon carbide particles. The conclusions for the specimens cut and loaded perpendicular and inclined at 45° with respect to the rolling axis are almost identical. The respective results are summarized in next Figs. 10 and 11 for all types of specimens.

In Fig. 10 the fracture stress is plotted versus the specimen thickness for all three types of prismatic specimens. It is seen from this figure that the fracture stress–specimen thickness curve is almost linearly increasing with increasing thickness for thicknesses between $t = 1.2$ mm and $t = 5$ mm. From this point on the linearity is lost and the curve reaches its maximum value for specimens with thickness about 9 mm. The absolute differences between the fracture strength of the thinnest and thickest specimens was about 40% for all three types of specimens.

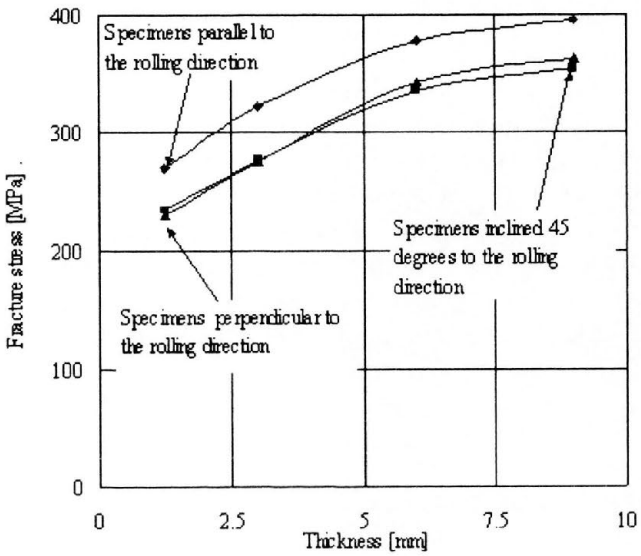

FIG. 10. The dependence of fracture stress on the specimen thickness.

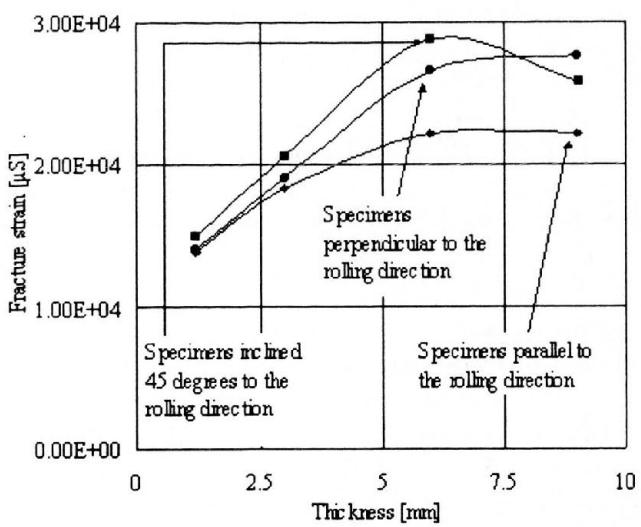

FIG. 11. The dependence of the ductility on the specimen thickness.

Concerning the influence of plastically induced anisotropy it is seen from Fig. 10 that the rolling direction is the strongest one while the differences between the other two directions are negligible no matter what the thickness of the specimen is.

In the next Fig. 11 the dependence of the fracture strain on the specimen thickness is plotted for all types of prismatic specimens. Although the qualitative behaviour of the graph is similar to that of the fracture stress, it is worth to be mentioned here that the specimens cut along the direction inclined 45° with respect to the rolling one appear to be the most ductile, especially for small thickness and they reach their respective maximum value of ductility already for a thickness equal to about 6 mm. Concerning the absolute differences they vary from about 80% for the specimens cut perpendicular to the rolling direction to about 50% for the ones cut parallel to it.

5. The fracture surfaces and the fracture mode

In Figs. 12 and 13 microfractographs are shown taken from two different locations of the fracture surface of a typical specimen with $\beta = 90°$ and $f = 0.3$. Indeed, in Fig. 14, in which the specific specimen is shown, the plane-stress "macromode" of fracture ahead of the crack tip (inclined plane of fracture) can be clearly detected. This failure mode is a combination of a shear component (distinguished by the shear lips) and a normal one (normal cone). The shear component prevails close to the surface layers whereas the normal one prevails at the mid-thickness layers of the specimen. The microfractograph of Fig. 12 corresponds to points of the shear failure area while the one of Fig. 13 to points of the normal failure one. From these figures it is safely concluded that the overall failure process is a ductile plane-stress one with an additional feature: The "dimple microfailure mode" is active. This is attributed to the microvoid coalescence mechanism, on which the ductile macrofracture of metals [21] is based.

Figures 12 b and 13 b were taken with the aid of the signal differentiation processing mode, by which contour enhancement or edge sharpening of the dimples is achieved. In this way one can better distinguish the differences in the morphology between the two areas of the failure surface (shear lips and normal cone). It can be observed from them that the shear prevailing area is characterized by an elongated dimple pattern, in contrast to the normal cone area which is characterized by a more or less "quasi-equiaxed" dimple pattern. Such a behaviour is attributed to the loss of severity of the triaxiality of the stress state near the surface layers of the material [22].

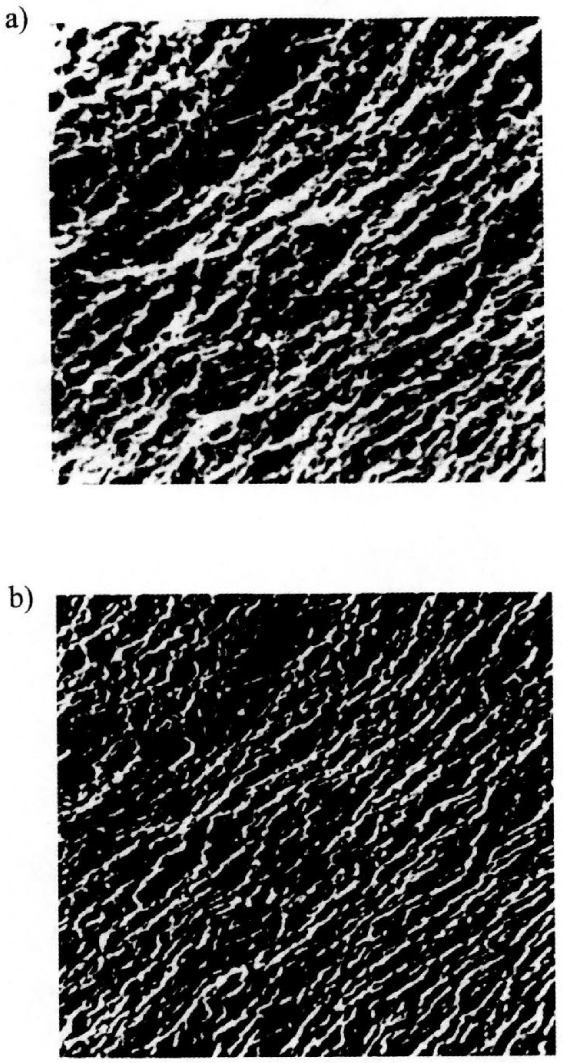

FIG. 12. SEM micro-fractographs (magnification 500×): a) Elongated shear dimpled surface. b) Signal processed image for the enhancement of elongated pattern.

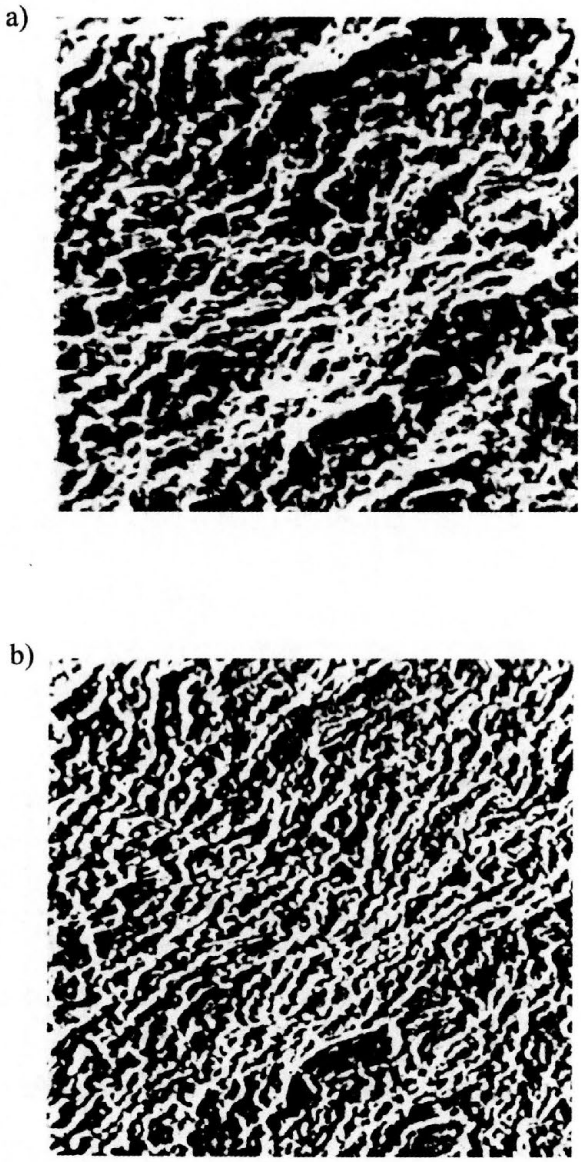

FIG. 13. SEM micro-fractographs magnification 500×): a) "Quasi-equiaxed" dimpled surface. b) Signal processed image for the enhancement of "quasi-equiaxed" pattern.

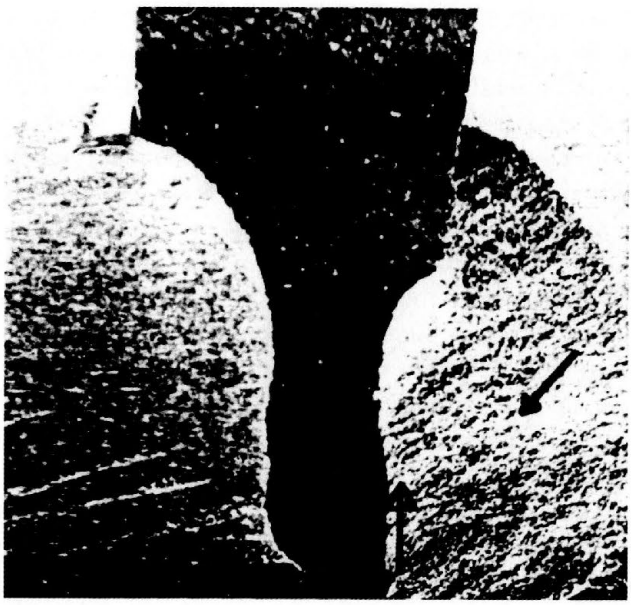

FIG. 14. SEM photograph of the fractured specimen. The arrows indicate the exact points at which the photographs of Fig. 12 (filled arrow) and Fig. 13 (empty arrow) were taken.

6. Conclusions

Some characteristics of the process zone developed around the tip of cracks as well as the fracture strength and ductility of the 2124 Al-Cu MMC were studied in the present work. The fractography of the fracture surfaces was used in order to determine the failure mechanisms activated.

The values of the critical CTOD recorded were less than 30 μm for the composite material and less than 100 μm for the matrix alloy. It is thus concluded that the intensively damaged zone surrounding the tip is restricted to less than about 2% of a_0 for the SEN specimens, for both the composite material and the respective alloy. Hence the HRR model appears to be valid, at least for the range of f values tested, although the failure mode detected is a ductile one. It means that Eqs. (2.6), (2.7) can be safely used for the description of the stress field for both materials.

It was also concluded that both the critical CTOD and the critical J-integral depend almost linearly on the thickness of the specimen. However, the experimental study did not employed specimens of increased thickness in order to determine the above quantities under plane strain conditions since it is not possible to apply the loads required to cause failure *in situ* on the Scanning Electron

Microscope. This was possible only for the fracture strength and ductility since the respective tests were executed using conventional hydraulic loading frames. For these quantities it was verified that after an initial linear portion of the respective graph, the increasing tendency was eliminated and a maximum value was reached for specimens with thickness about 9 mm for the fracture stress and of about 6 mm for the ductility. Additionally it is mentioned that the above quantities strongly depend on the orientation of the specimen with respect to the rolling direction, indicating the importance of the plastically induced anisotropy due to the manufacturing process adopted for the production of the composite material. The dependence for the matrix alloy is almost insignificant. This behaviour should be expected since in the case of the composite material, the plastically induced anisotropy is caused by the fact that the initially spherical reinforcing particles are transformed gradually into elliptic-paraboloidal ones [23]. Such a transformation does not take place in the matrix alloy and thus the plastically induced anisotropy is much weaker.

On the other hand, the analysis of the SEM images pointed out that the fracture process is still controlled by the void coalescence mechanism despite the presence of the reinforcing SiC particles. On the other hand, SEM analysis of the fracture surface of uncracked specimens indicated that the micro-cracks are initiated in the matrix rather than at the particle-matrix interface. This peculiar, at least for MMCs, phenomenon can be explained by the fineness of the reinforcement phase as well as by the process used for the production of the specific MMC (powder metallurgy) which is responsible for some porosity. Thus, in the case of uncracked specimens void nucleation than void coalescence is the critical step for failure. When the local plastic relaxation that relieves stress concentration becomes difficult, as in the case of pre-cracked specimens, where it is concentrated in the vicinity of the tip of the macroscopic crack, then the final failure occurs at rather low strains. It seems thus that the presence of macro-cracks changes the failure mechanism, explaining in this way the deterioration of the mechanical properties of cracked MMCs.

References

1. H. M. WESTERGAARD, *Bearing pressures and cracks*, Transactions of the ASME, **61**, A49–A53, 1939.

2. G. R. IRWIN, *Analysis of stresses and strains near the end of a crack transversing a plate*, J. Appl. Mech., **24**, 361–364, 1957.

3. H. L. EWALDS, R. J. H. WANHILL, *Fracture mechanics*, Edward Arnold Publishers, London, 1985.

4. J. L. BLUHM, *A model for the effect of thickness on fracture toughness*, ASTM Proc., **61**, 1324–1331, 1961.

5. J. L. SWEDLOW, *The thickness effect and plastic flow in cracked plates. Aerospace Research Laboratories*, Office of Aerospace Research, U.S. Air Force, Wright-Patterson Air Force Base, OH, 1965.

6. T. PARDOEN, Y. MARCHALL, F. DELLANNAY, *Thickness dependence of cracking resistance in thin aluminium plates*, J. Mech. Phys. Solids, **47**, 2093–2123, 1999.

7. K. G. KREIDER, *Introduction to metal matrix composites*, [in:] Composite Materials, L. J. BROUTMAN and R. H. CROCK [Eds.], vol. **4**, chap. 1, Academic Press, New York, 1974.

8. S. K. KOURKOULIS, *The influence of cracks on the mechanical behaviour of particulate MMCs: an experimental study*, Arch. Mech., **53**, 439–456, 2001.

9. G. HENESS, L. GAN, Y. W. MAI, *Effect of particle morphology on matrix constraint in metal matrix composites*, 9th Int. Conf. of Fracture, Sydney, Australia, B. L. KARIHALOO [Ed.], Pergamon Press, **1**, 759–765, New York 1997.

10. J. R. RICE, *A path independent integral and approximate analysis of strain concentration by notches and cracks*, J. of Appl. Mech., **35**, 379–386, 1968.

11. J. R. RICE, *Elastic – plastic models for stable crack growth*, Proc. of the Conference on Mechanics and Mechanisms of Crack Growth, Churchill College, Cambridge, England, 14–39, 1973.

12. T. L ANDERSON, *Fracture mechanics – fundamentals and applications*, CRC Press, Boca Raton, 1995.

13. C. F. SHIH, *Relationships between the J-integral and the COD for stationary and extending cracks*, J. Mech. Phys. of Solids, **29**, 305–326, 1981.

14. B. OMIDVAR, M. P. WNUK, M. CHOROSZYNSKI, *Relationship between the CTOD and the J-integral for stationary and growing cracks*, Int. J. of Fracture, **87**, 331–343, 1997.

15. A. SCHAPERY, *Report MM5762-88-1*, Texas A&M University, College Station TX, 1988.

16. Particulate Metal Matrix Composite Processing Handbook, Issue 1, BP Metal Composites, Farnborough, England, 1991.

17. S. K. KOURKOULIS, N. P. ANDRIANOPOULOS, *Some Critical Aspects of the Mechanical Behaviour of Metal Matrix Composites*, Proc. 1st Nat. Conf. on Composite Materials and Structures, 57–71, S. A. PAIPETIS and E. E.GDOUTOS [Eds.], Kyriakidis Brothers S.A., Xanthi, Greece, 1997.

18. B. DODD, *Workability of metals and MMCs, in particular Al-Li alloys and Al-based composites*, Final technical Report of the EU project BREU-CT91-0398: BE4500-90, 50–51, 1994.

19. C. F. SHIH, B. MORAN, T. NAKAMURA, *Energy release rate along a three dimensional crack front in a thermally stressed body*, Int. J. Fract., **30**, 79–102, 1986.

20. A. ASSERIN-LEBERT, F. BRON, J. BESSON, A. F. GOURGUES, *Rupture of 6056 aluminum sheet materials: Effect of sheet thickness on strain localization and toughness*, Proc. ECF-14: Fracture Mechanics Beyond 2000, EMAS Publishing, Sheffield, England, **1**, 97–103, 2002.

21. Fractography and materials science, ASTM-STP 733, 1981.

22. S. K. KOURKOULIS, V. KYTOPOULOS, *Experimental quantification of crack tip parameters for particulate metal matrix composites*, Proc. of the 6th Congress of the Hellenic Association of Theoretical and Applied Mechanics, Thessaloniki, Hellas, **1**, 339–347, 2001.

23. S. K. KOURKOULIS, *Quantifying the plastic anisotropy for particulate Metal Matrix Composites,* Advanced Composites Letters, **11**, 153–163, 2002.

Received December 13, 2002.

Arch. Mech., **55**, 5–6, pp. 431–448, Warszawa 2003

An energy-based yield criterion for solids of cubic elasticity and orthotropic limit state

K. KOWALCZYK, J. OSTROWSKA-MACIEJEWSKA,
R. B. PĘCHERSKI

Institute of Fundamental Technological Research, PAS
Świętokrzyska 21, 00-049 Warsaw

THE AIM OF THE PAPER is to formulate a particular case of the J. Rychlewski yield condition for anisotropic linear elastic solids with Hooke's law and the limit tensor representing elastic range in the Mises yield condition under the assumption that different symmetry of elasticity tensors and the limit tensor appears. The elasticity tensor $\mathbf{C}$ is assumed to have cubic symmetry. The yield condition is based on the concept of stored elastic energy density, the theory of proper elastic states and energy orthogonal stress states developed by J. RYCHLEWSKI [1–3]. Three possible specifications of energy-based yield condition for cubic crystals are considered: the criterion based on the total distortion energy, the criterion based on the energy accumulated in the three proper states pertinent to cubic symmetry and the energy based criterion for cubic symmetry in elastic range and orthotropic symmetry in the limit state. Physical motivation, comparison with available experimental results and possible applications in mechanics of anisotropic solids as well as in nanomechanics are discussed.

1. Introduction

THE AIM OF THE PAPER is to study some particular cases of the RYCHLEWSKI yield condition [2, 3] for anisotropic linear elastic solids with Hooke's law

$$\boldsymbol{\sigma} = \mathbf{S} \cdot \boldsymbol{\varepsilon} \leftrightarrow \sigma_{ij} = S_{ijkl}\varepsilon_{kl}\,, \quad \boldsymbol{\varepsilon} = \mathbf{C} \cdot \boldsymbol{\sigma} \leftrightarrow \varepsilon_{mn} = C_{mnij}\sigma_{ij} \tag{1.1}$$

such that

$$\mathbf{C} \circ \mathbf{S} = \mathbf{S} \circ \mathbf{C} = \mathbf{I}_S \leftrightarrow S_{ijkl}C_{klmn} = \frac{1}{2}\left(\delta_{im}\delta_{jn} + \delta_{in}\delta_{jm}\right) \tag{1.2}$$

and the limit tensor $\mathbf{H}$ representing elastic range in the Mises yield condition

$$\boldsymbol{\sigma} \cdot \mathbf{H} \cdot \boldsymbol{\sigma} = H_{ijkl}\sigma_{ij}\sigma_{kl} \leq 1, \tag{1.3}$$

under the assumption that different symmetry of elasticity tensors of stiffness $\mathbf{S}$ and compliance $\mathbf{C}$ vis-à-vis the limit tensor $\mathbf{H}$ appears. The elasticity tensor $\mathbf{C}$ is assumed to have cubic symmetry, while at the limit the state material becomes

cubic or tetragonal or in general orthotropic. Three possible formulations of the energy-based yield condition are considered.

In the simplest case, the energy of distortion, which can be separated from the total elastic energy density, is taken as a measure of material effort. This is a direct extension of the approach proposed independently by J. C. MAXWELL [4], M. T. HUBER [5] and H. HENCKY [6] for isotropic solids, which is based on the assumption that only a part of the density of elastic energy – energy of distortion – is responsible for reaching a limit state. In this case, only one critical value of the limit state exists, e.g. yield strength. Such an approach can be applied only for solids of isotropic or cubic symmetry because only in such a case the part of elastic energy related with volumetric change corresponds to proper elastic state and the assumption of material incompressibility is admissible. For other symmetries, a volumetric change does not correspond to proper elastic state and W. BURZYŃSKI condition [7] should be assumed in order to extract the density of elastic energy related with spherical part of stress from the total one. This confines the considerations to the class of solids with volumetric (spherical) isotropy and enables introduction of the simplifying constraint of incompressibility (cf. [8]).

The second case is related with the elastic energy densities corresponding to three proper elastic states, as derived in [9, 10]. In such a case three critical values of limit state (e.g. yield constants) can appear in the limit condition. Under incompressibility assumption the number of critical values reduces to two. The advantage of J. RYCHLEWSKI approach [2, 3] lays in the possibility of consideration of different symmetries of a solid body in the elastic range and in the limit state. This enriches the spectrum of possible applications. Therefore, in the third case, the energy-based yield criterion is derived for the situation when a body is of cubic symmetry in elastic range and becomes orthotropic in the limit state. Physical motivation is presented and possible experimental verification of the proposed energy based criteria is discussed.

2. Physical motivation

The well-known examples of solids with cubic symmetry are metal single crystals of FCC and BCC lattice. Since early investigations of E. SCHMID [11, 12], the assumption that single crystal starts to yield, if the shear stress resolved onto the crystallographically defined slip plane and in the slip direction reached a critical value, is commonly used in plasticity of single crystals and polycrystalline aggregates. Such a criterion, known as the Schmid rule, can be expressed in the case of a single crystal subjected to tensile load P in the form:

$$\frac{P}{A}\cos\varphi\cos\lambda = \tau_{\mathrm{cr}}, \tag{2.1}$$

where φ and λ are, respectively, the inclination angle of the normal to the slip plane $\mathbf{n}$ with respect to the tensile axis and the inclination angle of the slip direction $\mathbf{b}$ with respect to the tensile axis, while τ_{cr} denotes critical value of shear stress once plastic glide starts to operate. In general, for arbitrary Cauchy stress tensor $\boldsymbol{\sigma}$ the criterion reads

$$\mathbf{b}\boldsymbol{\sigma}\mathbf{n} = \tau_{cr}. \tag{2.2}$$

The experimental investigations reveal a good confirmation of this criterion for HCP and FCC single crystals in situations, when only a single slip system operates. Remarkable deviations have been observed, however, in cases when multiple slip occurs, e.g. for the orientations of tensile axis lying near to the corners of the fundamental triangle of stereographic projection. The plastic yield in BCC single crystals also does not conform to the Schmid criterion. These facts have been already reported in [12, 13]. The studies concerning localization of plastic deformation in single crystals [14, 15] also show that modification of the Schmid condition accounting for other components of stress tensor provides better prediction of localization phenomena. The atomistic study based on molecular dynamics simulations and examining the effect of crystal orientation on the stress-strain relationship of Ni single crystal shows large deviations from the Schmid criterion [16]. The recent investigations of [17, 18] related with atomistic calculations of the behaviour of dislocation core and the so-called non-Schmid effects in the plastic yielding of BCC single crystals led the authors to the yield criterion including non-glide components of stress. Although the mentioned applications of molecular dynamics simulations provide deeper insight into the phenomenon of the onset of plastic glide and the core structure of a dislocation in BCC metals, the criterion accounting for non-glide components bears an empirical character. Therefore, such an approach cannot be generalized for other situations, which might be related with other crystalline structures, e.g.: nanostructures, thin layers or interfaces. In the case of nanocrystals the difference in the interatomic distances, with resulting change of symmetry of the bulk material and strained surface layer becomes essential (cf. e.g. [19]). The strained surface layer is often a site, where a limit state can appear first. Under the limit state, we can understand in such a situation breaking of atomic bonds, which may lead to formation of a point defect or a dislocation. Evaluation of the critical energy of breaking of atomic bonds with application of a quantum-mechanical model of an ideal Cu crystal was presented in [20]. The question arises then, how to formulate the limit criteria for solids exhibiting different symmetry in elastic range and in limit state.

The problem was studied afresh in [21], where a new approach has been proposed. It is based on the fundamental concept of density of elastic energy of distortion accumulated in a strained solid, anticipated in 1856 by J. C. Maxwell

in his private letter to W. Thompson [4] and discovered, independently, by M. T. Huber [5]. This pivotal idea, proposed originally for isotropic solids, was further extended for elastic anisotropic solids in the studies of W. BURZYŃSKI [7], W. OLSZAK, W. URBANOWSKI [22], W. OLSZAK, J. OSTROWSKA-MACIEJEWSKA [23] J. OSTROWSKA-MACIEJEWSKA, J. RYCHLEWSKI [9] and J. RYCHLEWSKI [2].

3. Formulation of the problem

The yield conditions are based on the concept of stored elastic energy, the theory of proper elastic states and energy orthogonal stress states developed by J. RYCHLEWSKI [1–3], who proved that the Mises limit criterion bounds the weighted sum of stored elastic energies of uniquely defined, energy orthogonal states of stress

$$\boldsymbol{\sigma}\cdot\mathbf{H}\cdot\boldsymbol{\sigma}=\frac{1}{h_1}\Phi(\boldsymbol{\sigma}_1)+\cdots+\frac{1}{h_p}\Phi(\boldsymbol{\sigma}_p),\qquad p\leq 6, \tag{3.1}$$

where $\boldsymbol{\sigma}=\boldsymbol{\sigma}_1+\boldsymbol{\sigma}_2+\cdots+\boldsymbol{\sigma}_p$ is the unique decomposition of stress tensor $\boldsymbol{\sigma}$ into energy orthogonal states, $\boldsymbol{\sigma}_k\cdot\mathbf{C}\cdot\boldsymbol{\sigma}_l=0$ for $k\neq l$, and $h_1,\ldots,h_p$ are the pertinent energy limits of elasticity, which we called in [20] the Rychlewski moduli.

If the compliance tensor $\mathbf{C}$ possesses cubic symmetry, three elastic proper states exist. The spectral decomposition of the compliance tensor for cubic symmetry has the form [9, 10]:

$$\mathbf{C}=\frac{1}{\lambda_{\mathrm{I}}}\mathbf{P}_{\mathrm{I}}+\frac{1}{\lambda_{\mathrm{II}}}\mathbf{P}_{\mathrm{II}}+\frac{1}{\lambda_{\mathrm{III}}}\mathbf{P}_{\mathrm{III}}, \tag{3.2}$$

where the projectors $\mathbf{P}_K$, $K=\mathrm{I},\mathrm{II},\mathrm{III}$ are given by

$$\begin{aligned}\mathbf{P}_{\mathrm{I}}&=\frac{1}{3}\mathbf{1}\otimes\mathbf{1},\\ \mathbf{P}_{\mathrm{II}}&=\left(\mathbf{K}-\frac{1}{3}\mathbf{1}\otimes\mathbf{1}\right),\\ \mathbf{P}_{\mathrm{III}}&=(\mathbf{I}_S-\mathbf{K})\end{aligned} \tag{3.3}$$

and λ_{I}, λ_{II} and λ_{III} are the Kelvin moduli, which can be expressed by elasticity constants representing the components of stiffness tensor (cf. [24], where the opposite notation for the tensors of compliance – $\mathbf{S}$ and stiffness – $\mathbf{C}$ in comparison with our work was assumed):

$$\begin{aligned}\lambda_{\mathrm{I}}&=\lambda_1=S_{1111}+2S_{1122},\\ \lambda_{\mathrm{II}}&=\lambda_2=\lambda_3=\lambda_4=S_{1111}-S_{1122},\\ \lambda_{\mathrm{III}}&=\lambda_5=\lambda_6=2S_{2323},\end{aligned} \tag{3.4}$$

whereas the fourth-order tensor $\mathbf{K}$ is defined by unit vectors lying along the edges of the elementary cube $(\mathbf{m}_1, \mathbf{m}_2, \mathbf{m}_3)$

$$\mathbf{K} = \mathbf{m}_1 \otimes \mathbf{m}_1 \otimes \mathbf{m}_1 \otimes \mathbf{m}_1 + \mathbf{m}_2 \otimes \mathbf{m}_2 \otimes \mathbf{m}_2 \otimes \mathbf{m}_2 + \mathbf{m}_3 \otimes \mathbf{m}_3 \otimes \mathbf{m}_3 \otimes \mathbf{m}_3. \tag{3.5}$$

The stored elastic energy for unit volume is composed in such a case of three parts [9, 10]

$$\begin{aligned} \Phi(\boldsymbol{\sigma}) &= \frac{1}{2}\boldsymbol{\sigma} \cdot \mathbf{C} \cdot \boldsymbol{\sigma} = \Phi_v^{\mathrm{I}}(\boldsymbol{\sigma}) + \Phi_f^{\mathrm{II}}(\boldsymbol{\sigma}) + \Phi_f^{\mathrm{III}}(\boldsymbol{\sigma}) \\ &= \frac{1}{6}\frac{1}{\lambda_{\mathrm{I}}}(\mathrm{tr}\boldsymbol{\sigma})^2 + \frac{1}{2\lambda_{\mathrm{II}}}\left[\boldsymbol{\sigma} \cdot \mathbf{K} \cdot \boldsymbol{\sigma} - \frac{1}{3}(\mathrm{tr}\boldsymbol{\sigma})^2\right] + \frac{1}{2\lambda_{\mathrm{III}}}\left(\mathrm{tr}\boldsymbol{\sigma}^2 - \boldsymbol{\sigma} \cdot \mathbf{K} \cdot \boldsymbol{\sigma}\right), \end{aligned} \tag{3.6}$$

the energy of hydrostatic states $\Phi_v^{\mathrm{I}}(\boldsymbol{\sigma})$ and the energy of distortion $\Phi_f(\boldsymbol{\sigma}) = \Phi_f^{\mathrm{II}}(\boldsymbol{\sigma}) + \Phi_f^{\mathrm{III}}(\boldsymbol{\sigma})$ related with two deviatoric states, respectively.

4. Criterion based on the energy of distortion

In the first approach, the energy of distortion $\Phi_f(\boldsymbol{\sigma})$ that can be separated from the total elastic energy density is taken as a measure of material effort:

$$\begin{aligned} \Phi_f(\boldsymbol{\sigma}) &= \Phi_f^{\mathrm{II}}(\boldsymbol{\sigma}) + \Phi_f^{\mathrm{III}}(\boldsymbol{\sigma}) \\ &= \frac{(\mathbf{m}_1\boldsymbol{\sigma}\mathbf{m}_1)^2 + (\mathbf{m}_2\boldsymbol{\sigma}\mathbf{m}_2)^2 + (\mathbf{m}_3\boldsymbol{\sigma}\mathbf{m}_3)^2 - \frac{1}{3}(\mathrm{tr}\boldsymbol{\sigma})^2}{2\lambda_{\mathrm{II}}} \\ &\quad + \frac{\boldsymbol{\sigma} \cdot \boldsymbol{\sigma} - (\mathbf{m}_1\boldsymbol{\sigma}\mathbf{m}_1)^2 + (\mathbf{m}_2\boldsymbol{\sigma}\mathbf{m}_2)^2 + (\mathbf{m}_3\boldsymbol{\sigma}\mathbf{m}_3)^2}{2\lambda_{\mathrm{III}}}. \end{aligned} \tag{4.1}$$

The criterion of energy of distortion for solids of cubic symmetry, in particular for crystals of cubic lattice, can be stated as follows [21]:

The yield condition is satisfied, if the density of energy of distortion accumulated in a body of cubic symmetry attains certain critical value Φ_{cr}

$$\Phi_f(\boldsymbol{\sigma}) = \Phi_{\mathrm{cr}}. \tag{4.2}$$

The critical value of energy of distortion can be determined experimentally in a tensile test of a single crystal along the direction of unit vector $\mathbf{n} = l\mathbf{m}_1 + m\mathbf{m}_2 + n\mathbf{m}_3$ with stress $\boldsymbol{\sigma} = \sigma_n \mathbf{n} \otimes \mathbf{n}$. The energy of distortion takes in such a case the form [10]:

$$\Phi_f(\sigma_n, \mathbf{n}) = \frac{1}{2\lambda_{\mathrm{II}}}\sigma_n^2\left(l^4+m^4+n^4-\frac{1}{3}\right)+\frac{1}{2\lambda_{\mathrm{III}}}\sigma_n^2\left(1-\left(l^4+m^4+n^4\right)\right)$$

$$= \sigma_n^2\left[\left(\frac{1}{2\lambda_{\mathrm{II}}}-\frac{1}{2\lambda_{\mathrm{III}}}\right)\left(l^4+m^4+n^4\right)+\frac{1}{2\lambda_{\mathrm{III}}}-\frac{1}{6\lambda_{\mathrm{II}}}\right]. \tag{4.3}$$

Let us observe that there are two initial orientations of the crystal subjected to tension, for which the formula (4.3) obtains a particularly simple form [21]:

- Initial orientation chosen for one of the edges of elementary cube, i.e. [100], [010] or [001].
- Initial orientation taken along the normal to the octahedral plane [111].

For the orientations [100], [010] or [001] we have, respectively, $l=1$, $m=n=0$, $m=1$, $l=n=0$, or $n=1$, $l=m=0$ and the energy of distortion can be expressed by means of tensile stress along one of the cube edges:

$$\Phi_f^{\mathrm{II}}\left(\sigma_{[100]}\right) = \frac{1}{3}\frac{1}{\lambda_{\mathrm{II}}}\sigma_{[100]}^2 = \frac{1}{3}\frac{1}{\lambda_{\mathrm{II}}}\sigma_{[010]}^2 = \frac{1}{3}\frac{1}{\lambda_{\mathrm{II}}}\sigma_{[001]}^2, \quad \Phi_{\mathrm{cr}} = \frac{1}{3}\frac{1}{\lambda_{\mathrm{II}}}Y_2^2, \tag{4.4}$$

while

$$\Phi_f^{\mathrm{III}}\left(\sigma_{[100]}\right) = \Phi_f^{\mathrm{III}}\left(\sigma_{[010]}\right) = \Phi_f^{\mathrm{III}}\left(\sigma_{[001]}\right) = 0. \tag{4.5}$$

On the other hand, for the initial orientation [111] the distortion energy takes the form

$$\Phi_f^{\mathrm{III}}\left(\sigma_{[111]}\right) = \frac{1}{3}\frac{1}{\lambda_{\mathrm{III}}}\sigma_{[111]}^2, \qquad \Phi_{\mathrm{cr}} = \frac{1}{3}\frac{1}{\lambda_{\mathrm{III}}}Y_3^2, \tag{4.6}$$

while

$$\Phi_f^{\mathrm{II}}\left(\sigma_{[111]}\right) = 0. \tag{4.7}$$

It means that in the limit state the ratio of two critical values of tensile stress at yield is determined by Kelvin moduli λ_{II} and λ_{III}

$$\frac{Y_2}{Y_3} = \sqrt{\frac{\lambda_{\mathrm{II}}}{\lambda_{\mathrm{III}}}}. \tag{4.8}$$

Then, the tensile tests of a single crystal along one of the edges of elementary cube and along the initial orientation [111] lead to two deviatoric states, which are energy orthogonal. It can be also proved that these directions correspond to the extremal values of Young modulus (cf. [10]). Due to this we can use one of these tests to measure the yield stress and the other one to verify by means of (4.6) the proposed criterion of energy of distortion.

5. Specification of the criterion for cubic crystals for spectral decomposition of the elasticity tensor C

The second case of possible formulations of energy-based yield condition is related with the elastic energy densities corresponding to three proper elastic states (3.3), as derived in [9, 10]. It is the specification of general criterion (3.1) that was obtained originally by J. Rychlewski from the main energy orthogonal decomposition for cubic symmetry. According to [9] it takes form:

$$\frac{\sigma_1^2}{k_1^2} + \frac{\sigma_2^2}{k_2^2} + \frac{\sigma_3^2}{k_3^2} \leq 1, \tag{5.1}$$

where $\sigma_i^2 = \boldsymbol{\sigma}_i \cdot \boldsymbol{\sigma}_i$, $k_i^2 \equiv 2h_i\lambda_i$, $i = 1, 2, 3$ – no summation for i. In such a case three critical values of limit state (e.g. yield constants) can appear in the limit condition. If $k_i \to \infty$, we say that the i-th state is safe for any state of stress. In the theory of plasticity of isotropic metallic solids it is often assumed that the spherical parts of stress tensors are safe. Such an assumption can be also extended to bulk metallic solids of cubic symmetry, since the hydrostatic state is a proper elastic state. Therefore, sometimes a body of cubic symmetry is called, if we abstract from its crystallographic features, a body of cubic isotropy. It should be mentioned however that for other types of symmetry (anisotropy) the hydrostatic state is not a proper elastic state. If we assume for certain reasons, for simplicity or having experimental justification, that the material is pressure insensitive, we confine at the same time our considerations to certain class of bodies with constraints, which are volumetrically isotropic (cf. [2, 8]). It is also worthwhile to observe that the limit condition (5.1) can be obtained also if we assume that the limit tensor **H** possesses the same symmetry as the compliance tensor **C** (they are coaxial, i.e. they have the same proper subspaces but different proper values).

If the hydrostatic state of stress is safe, we have $k_1 \to \infty$ and the quadratic limit condition (5.1) can be expressed only for two deviatoric states

$$\frac{\sigma_2^2}{k_2^2} + \frac{\sigma_3^2}{k_3^2} = \frac{(\mathbf{m}_1\boldsymbol{\sigma}\mathbf{m}_1)^2 + (\mathbf{m}_2\boldsymbol{\sigma}\mathbf{m}_2)^2 + (\mathbf{m}_3\boldsymbol{\sigma}\mathbf{m}_3)^2 - \frac{1}{3}(\mathrm{tr}\boldsymbol{\sigma})^2}{k_2^2} + \frac{\boldsymbol{\sigma}\cdot\boldsymbol{\sigma} - \left[(\mathbf{m}_1\boldsymbol{\sigma}\mathbf{m}_1)^2 + (\mathbf{m}_2\boldsymbol{\sigma}\mathbf{m}_2)^2 + (\mathbf{m}_3\boldsymbol{\sigma}\mathbf{m}_3)^2\right]}{k_2^2} \leq 1, \tag{5.2}$$

where $k_2^2 \equiv 2h_2\lambda_{\mathrm{II}}$, $k_3^2 \equiv 2h_3\lambda_{\mathrm{III}}$ are the limit constants, which should be determined experimentally, e.g. in tensile tests. The tensile tests for single FCC crystals with different initial orientations have been proposed in [20] to verify experimentally the new yield criterion. Accordingly, the yield stress in tension

along the direction $\mathbf{n} = l\mathbf{m}_1 + m\mathbf{m}_2 + n\mathbf{m}_3$, while the elasticity tensor $\mathbf{C}$ and the limit tensor $\mathbf{H}$ are coaxial for single cubic crystals, was calculated under the assumption that $k_1 \to \infty$

$$Y = \left[-\frac{1}{3k_2^2} + \frac{1}{k_3^2} + \left(\frac{1}{k_2^2} - \frac{1}{k_3^2} \right) (l^4 + m^4 + n^4) \right]^{-1/2}. \tag{5.3}$$

Two limit constants k_2 and k_3 can be determined in the independent tensile tests for a single crystal with initial orientation chosen along one of the edges of elementary cube [100], [010] or [001], what gives $\sigma_{[100]} = \sigma_{[010]} = \sigma_{[001]} = Y_2 = \sqrt{\frac{3}{2}} k_2$, and along the direction $\mathbf{n} = \frac{1}{\sqrt{3}}[111]$, what leads to $\sigma_{[111]} = Y_3 = \sqrt{\frac{3}{2}} k_3$.

6. Specification of the Rychlewski approach for materials of cubic elasticity and orthotropic limit state

In the foregoing discussion there was not necessary to specify the limit tensor $\mathbf{H}$. The limit conditions were derived on the basis of the elasticity tensor $\mathbf{S}$ and compliance tensor $\mathbf{C}$. If we assume that $\mathbf{H}$ is coaxial with $\mathbf{C}$, then the criterion of the form (5.1) can be also obtained

$$\frac{\Phi(\boldsymbol{\sigma}_1)}{h_1} + \frac{\Phi(\boldsymbol{\sigma}_2)}{h_2} + \frac{\Phi(\boldsymbol{\sigma}_3)}{h_3} \leq 1, \tag{6.1}$$

where the Rychlewski moduli $h_i = \Phi_{\mathrm{cr}}(\boldsymbol{\sigma}_i)$, $i = 1, 2, 3$ correspond to critical energy of pertinent proper state.

In the general approach of J. RYCHLEWSKI [2] tensors $\mathbf{C}$ and $\mathbf{H}$ are not interrelated and can possess arbitrary symmetry. In the third case of energy-based limit condition, cubic symmetry of elasticity tensor $\mathbf{C}$ and orthotropy of limit tensor $\mathbf{H}$ is studied. As an example, we can consider a single crystal with the lattice of cubic symmetry in a natural state. According to the Cauchy–Born hypothesis, which says that the lattice vectors deform like "material filaments", an extension along one of the edges of the cell with cubic lattice transforms it into the cell of tetragonal lattice. Such a situation appears also if we consider nanocrystals, where the difference in the interatomic distances in bulk material and strained surface layer results in the change of symmetry from cubic to tetragonal. Similar situation appears in the case of heterostructures composed of layers of cubic symmetry and strained interface of tetragonal symmetry. Therefore, in the elastic regime the bulk material remains cubic and the limit state can appear first in the surface layer or interface, which is of tetragonal symmetry. This is a special case of an orthotropic limit state. In further considerations, we assume that the symmetry axes of the material in elastic range and limit state coincide.

As it was observed in [25], for orthotropy the spherical tensor is not a proper elastic state. However, for the additional constraints $\mathbf{H} \cdot \mathbf{1} = \mathbf{0}$, it becomes the proper state with the eigenvalue equal 0. Such an assumption is often made in order to eliminate the influence of spherical part of stress on plastic yield. In such a case, it can be shown that spectral decomposition of the limit tensor $\mathbf{H}$ takes the form [26]:

$$\mathbf{H} = \frac{1}{K_1}\boldsymbol{\Gamma}_1 + \ldots + \frac{1}{K_6}\boldsymbol{\Gamma}_6, \tag{6.2}$$

where $\boldsymbol{\Gamma}_1, \ldots, \boldsymbol{\Gamma}_6$, are the orthogonal projectors for $\mathbf{H}$. The orthogonal projectors $\boldsymbol{\Gamma}_i$ are defined by proper states $\boldsymbol{\chi}_i$ corresponding to the different eigenvalues K_i of the limit tensor $\mathbf{H}$ that is:

$$\boldsymbol{\Gamma}_1 = \boldsymbol{\chi}_1 \otimes \boldsymbol{\chi}_1, \quad \cdots, \quad \boldsymbol{\Gamma}_6 = \boldsymbol{\chi}_6 \otimes \boldsymbol{\chi}_6. \tag{6.3}$$

Proper states $\boldsymbol{\chi}_i$ of the tensor $\mathbf{H}$ can be expressed as follows

$$\begin{aligned}
\boldsymbol{\chi}_1 &= \frac{1}{\sqrt{3}}\mathbf{I}, \\
\boldsymbol{\chi}_2 &= \cos\psi \mathbf{a}_{\mathrm{II}} + \sin\psi \mathbf{a}_{\mathrm{III}}, \\
\boldsymbol{\chi}_3 &= -\sin\psi \mathbf{a}_{\mathrm{II}} + \cos\psi \mathbf{a}_{\mathrm{III}}, \\
\boldsymbol{\chi}_4 &= \frac{1}{\sqrt{2}}(\mathbf{m}_2 \otimes \boldsymbol{\chi}_3 + \mathbf{m}_3 \otimes \mathbf{m}_2), \\
\boldsymbol{\chi}_5 &= \frac{1}{\sqrt{2}}(\mathbf{m}_1 \otimes \boldsymbol{\chi}_3 + \mathbf{m}_3 \otimes \mathbf{m}_1), \\
\boldsymbol{\chi}_6 &= \frac{1}{\sqrt{2}},
\end{aligned} \tag{6.4}$$

where $(\mathbf{m}_1, \mathbf{m}_2, \mathbf{m}_3)$ denote the unit vectors lying along the edges of the elementary cube, whereas the tensors $\mathbf{a}_{\mathrm{II}}$ and $\mathbf{a}_{\mathrm{III}}$ are defined by the formulae

$$\begin{aligned}
\mathbf{a}_{\mathrm{II}} &= \frac{1}{\sqrt{2}}(\mathbf{m}_1 \otimes \mathbf{m}_1 - \mathbf{m}_2 \otimes \mathbf{m}_2), \\
\mathbf{a}_{\mathrm{III}} &= \frac{1}{\sqrt{6}}(\mathbf{m}_1 \otimes \mathbf{m}_1 + \mathbf{m}_2 \otimes \mathbf{m}_2 - 2\mathbf{m}_3 \otimes \mathbf{m}_3)
\end{aligned} \tag{6.5}$$

and ψ is the strength distributor that depends on the components of the limit tensor $\mathbf{H}$.

From (3.3) and (6.3) it follows that

$$\boldsymbol{\Gamma}_1 = \mathbf{P}_{\mathrm{I}}, \qquad \boldsymbol{\Gamma}_2 + \boldsymbol{\Gamma}_3 = \mathbf{P}_{\mathrm{II}}, \qquad \boldsymbol{\Gamma}_4 + \boldsymbol{\Gamma}_5 + \boldsymbol{\Gamma}_6 = \mathbf{P}_{\mathrm{III}}, \tag{6.6}$$

what results from (3.2) in

$$\mathbf{C} = \frac{1}{\lambda_{\mathrm{I}}}\boldsymbol{\Gamma}_1 + \frac{1}{\lambda_{\mathrm{II}}}(\boldsymbol{\Gamma}_2 + \boldsymbol{\Gamma}_3) + \frac{1}{\lambda_{\mathrm{III}}}(\boldsymbol{\Gamma}_4 + \boldsymbol{\Gamma}_5 + \boldsymbol{\Gamma}_6). \tag{6.7}$$

By comparing (6.2) with (6.7) one comes to the conclusion that, in the considered case, the limit tensor $\mathbf{H}$ is *partially coaxial* with the compliance tensor $\mathbf{C}$, that is *all the proper states of* $\mathbf{H}$ *are the proper states of* $\mathbf{C}$ (but not opposite). It means that the symmetry group of $\mathbf{H}$ is contained in the symmetry group of $\mathbf{C}$.

Let us formulate the Mises-type condition (1.3) for the assumed tensor $\mathbf{H}$ given by (6.2) in the energy-based form (3.1). In order to obtain this form, according to [2], the following eigenvalue problem is to be solved

$$\left(\mathbf{H} - \frac{1}{2h}\mathbf{C}\right) \cdot \boldsymbol{\kappa} = \mathbf{0}. \tag{6.8}$$

Substituting (6.2) and (6.7) into the above formula it is found that

$$\det\left(\mathbf{H} - \frac{1}{2h}\mathbf{C}\right) = 0$$

$$\Updownarrow$$

$$h_1 = \frac{K_1}{2\lambda_{\mathrm{I}}} \to \infty, \quad h_2 = \frac{K_2}{2\lambda_{\mathrm{II}}}, \quad h_3 = \frac{K_3}{2\lambda_{\mathrm{II}}}, \tag{6.9}$$

$$h_4 = \frac{K_4}{2\lambda_{\mathrm{III}}}, \quad h_5 = \frac{K_5}{2\lambda_{\mathrm{III}}}, \quad h_6 = \frac{K_6}{2\lambda_{\mathrm{III}}}$$

and $\boldsymbol{\kappa}_i = \boldsymbol{\chi}_i$ (i = 1,...,6) given in (6.4), so in this case the energy proper states $\boldsymbol{\kappa}_i$ are equal to the proper states of the tensor $\mathbf{H}$. The energy orthogonal stresses $\boldsymbol{\sigma}_i$ are then calculated as

$$\boldsymbol{\sigma}_i = \boldsymbol{\Gamma}_i \cdot \boldsymbol{\sigma} \qquad \text{and} \qquad \boldsymbol{\sigma} = \boldsymbol{\sigma}_1 + \boldsymbol{\sigma}_2 + \ldots + \boldsymbol{\sigma}_6. \tag{6.10}$$

Graphical illustration of the above stress state decomposition for the analysed case of material symmetry is presented in Fig. 1, where the following notation is used:

$$\begin{aligned}
r &= \frac{1}{3}(\sigma_{11} + \sigma_{22} + \sigma_{33}), \\
s &= \frac{1}{2(3+\gamma^2)}[\sigma_{11} + \sigma_{22} - 2\sigma_{33} - \gamma(\sigma_{11} - \sigma_{22})], \\
u &= \frac{1}{2(3+\gamma^2)}[3(\sigma_{11} - \sigma_{22}) + \gamma(\sigma_{11} + \sigma_{22} - 2\sigma_{33})], \\
p &= \sigma_{13}, \qquad q = \sigma_{23}, \qquad v = \sigma_{12}, \qquad \gamma = -\sqrt{3}\cot\psi.
\end{aligned} \tag{6.11}$$

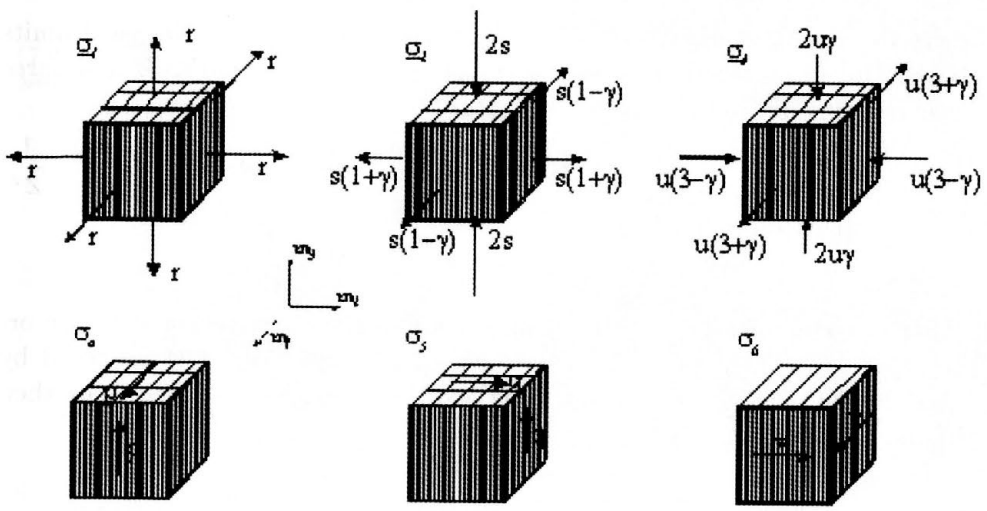

FIG. 1. The energy-orthogonal decomposition of the stress state for the material that has cubic symmetry in the elastic range and becomes orthotropic in the limit state.

Energy-based formulation of the limit criterion for the considered case is therefore due to (3.1) and (6.9) as follows:

$$\boldsymbol{\sigma}\cdot\mathbf{H}\cdot\boldsymbol{\sigma} = \frac{2\lambda_{\mathrm{II}}}{K_2}\Phi(\boldsymbol{\sigma}_2) + \frac{2\lambda_{\mathrm{II}}}{K_3}\Phi(\boldsymbol{\sigma}_3) + \frac{2\lambda_{\mathrm{III}}}{K_4}\Phi(\boldsymbol{\sigma}_4) + \frac{2\lambda_{\mathrm{III}}}{K_5}\Phi(\boldsymbol{\sigma}_5) + \frac{2\lambda_{\mathrm{III}}}{K_6}\Phi(\boldsymbol{\sigma}_6) = 1. \tag{6.12}$$

It should be noted that from (3.6), (4.1) and (6.12) it transpires that

$$\Phi_f^{\mathrm{II}} = \Phi(\boldsymbol{\sigma}_2) + \Phi(\boldsymbol{\sigma}_3) \quad \text{and} \quad \Phi_f^{\mathrm{III}} = \Phi(\boldsymbol{\sigma}_4) + \Phi(\boldsymbol{\sigma}_5) + \Phi(\boldsymbol{\sigma}_6). \tag{6.13}$$

7. An energy interpretation of the Hill yield condition for orthotropic solids

The equation (6.9) enables an energy-based interpretation of the Hill yield condition for plastically incompressible orthotropic solids that exhibit cubic symmetry in the elastic regime. The Hill yield condition for the orthotropic solids is given by the formula [27]:

$$F(\sigma_{22}-\sigma_{33})^2 + G(\sigma_{33}-\sigma_{11})^2 + H(\sigma_{11}-\sigma_{22})^2 + 2N\sigma_{12}^2 + 2M\sigma_{13}^2 + 2L\sigma_{23}^2 = 1, \tag{7.1}$$

where the constants F, G, H, N, M, L can be expressed by the yield limits obtained in three tensile tests along the orthotropy axes, X, Y, Z and three shear tests in the planes of orthotropy R, S, T:

$$2F = \frac{1}{Y^2} + \frac{1}{Z^2} - \frac{1}{X^2}, \quad 2G = \frac{1}{Z^2} + \frac{1}{X^2} - \frac{1}{Y^2}, \quad 2H = \frac{1}{X^2} + \frac{1}{Y^2} - \frac{1}{Z^2},$$

(7.2)

$$2L = \frac{1}{R^2}, \quad 2M = \frac{1}{S^2}, \quad 2N = \frac{1}{T^2}.$$

Stress components σ_{ij} are the components of the stress tensor $\boldsymbol{\sigma}$ in the orthotropy axes. This equation can be rewritten in the form (1.3) proposed by Mises. Eigenvalues of the limit tensor $\mathbf{H}$ and the strength distributor ψ are then obtained as [26]:

$$K_2 = \frac{1}{F + G + H + \frac{1}{2}\sqrt{\Delta_H}}, \qquad K_3 = \frac{1}{F + G + H - \frac{1}{2}\sqrt{\Delta_H}},$$

$$K_4 = \frac{1}{L}, \qquad K_5 = \frac{1}{M}, \qquad K_6 = \frac{1}{N},$$

(7.3)

$$\tan\psi = \frac{F + G - 2H - \sqrt{\Delta_H}}{\sqrt{3}\,(F - G)},$$

$$\Delta_H = 2\left[(H - F)^2 + (H - G)^2 + (F - G)^2\right] \geq 0.$$

Equivalently, due to (7.2) and (7.3) we have

$$\frac{1}{K_2} = \frac{1}{2}\left(\frac{1}{X^2} + \frac{1}{Y^2} + \frac{1}{Z^2}\right) + \frac{1}{2}\left[\left(\frac{1}{X^2} - \frac{1}{Z^2}\right)^2 + \left(\frac{1}{Y^2} - \frac{1}{Z^2}\right)^2 + \left(\frac{1}{Y^2} - \frac{1}{X^2}\right)^2\right]^{1/2},$$

(7.4)

$$\frac{1}{K_3} = \frac{1}{2}\left(\frac{1}{X^2} + \frac{1}{Y^2} + \frac{1}{Z^2}\right) - \frac{1}{2}\left[\left(\frac{1}{X^2} - \frac{1}{Z^2}\right)^2 + \left(\frac{1}{Y^2} - \frac{1}{Z^2}\right)^2 + \left(\frac{1}{Y^2} - \frac{1}{X^2}\right)^2\right]^{1/2},$$

$$K_4 = 2R^2, \qquad K_5 = 2S^2, \qquad K_6 = 2T^2,$$

(7.4) [cont.]

$$\tan\psi = \frac{-\left[2\left[\left(\frac{1}{X^2}-\frac{1}{Z^2}\right)^2+\left(\frac{1}{Y^2}-\frac{1}{Z^2}\right)^2+\left(\frac{1}{Y^2}-\frac{1}{X^2}\right)^2\right]\right]^{1/2}}{\sqrt{3}\left(\frac{1}{Y^2}-\frac{1}{X^2}\right)} - \frac{\frac{1}{Y^2}-\frac{1}{X^2}+\frac{2}{Z^2}}{\sqrt{3}\left(\frac{1}{Y^2}-\frac{1}{X^2}\right)}.$$

The particular case of orthotropy with the additional symmetry of rotations of the angle $\pi/2$ about the axis parallel to $\mathbf{m}_3$ was considered. The results are applied for the analysis of a single cubic crystal which, due to the finite extension along the one of cubic directions, changes symmetry and becomes tetragonal. In such a case we have $F = G$ and $L = M$, or equivalently $X = Y$ and $R = S$, therefore

$$(7.5)\qquad \psi = \frac{\pi}{2}, \quad K_2 = \frac{1}{F+2H}, \quad K_3 = \frac{1}{3F}, \quad K_4 = \frac{1}{L}, \quad K_5 = \frac{1}{N},$$

$$(7.6)\qquad \begin{aligned} \frac{1}{K_2} &= \frac{2+\sqrt{2}}{2}\frac{1}{X^2} + \frac{1-\sqrt{2}}{2}\frac{1}{Z^2}, \\ \frac{1}{K_3} &= \frac{2-\sqrt{2}}{2}\frac{1}{X^2} + \frac{1+\sqrt{2}}{2}\frac{1}{Z^2}, \\ K_4 &= K_5 = 2S^2, \qquad K_6 = 2T^2. \end{aligned}$$

Still tensor $\mathbf{H}$ is partially coaxial with the tensor $\mathbf{C}$, but in this case we have only five uniquely defined energy-orthogonal projectors $\mathbf{\Gamma}'_i$.

$$(7.7)\qquad \mathbf{\Gamma}'_i = \mathbf{\Gamma}_i \quad \text{for} \quad i = 1, \ldots, 3 \quad \text{and} \quad \mathbf{\Gamma}'_4 = \mathbf{\Gamma}_4 + \mathbf{\Gamma}_5, \quad \mathbf{\Gamma}'_5 = \mathbf{\Gamma}_6.$$

The form of energy-orthogonal decomposition (6.10) of the stress state σ for this special case of material symmetry (tetragonal) is shown in Fig. 2. The following notation is used (see (6.11)) for $\gamma = 0$:

$$(7.8)\qquad \begin{aligned} r &= \frac{1}{3}(\sigma_{11}+\sigma_{22}+\sigma_{33}), \quad s = \frac{1}{6}(\sigma_{11}+\sigma_{22}-2\sigma_{33}), \quad u = \frac{1}{2}(\sigma_{11}-\sigma_{22}), \\ p &= \sigma_{13}, \qquad q = \sigma_{23}, \qquad v = \sigma_{12}. \end{aligned}$$

According to (6.2) and (7.6), the limit condition for the material of cubic symmetry in elastic range and tetragonal in limit state can be expressed as follows:

$$(7.9)\qquad \lambda_{\mathrm{II}}\frac{(2+\sqrt{2})Z^2+(1-\sqrt{2})X^2}{X^2Z^2}\Phi(\sigma_2)$$
$$+\lambda_{\mathrm{II}}\frac{(2-\sqrt{2})Z^2+(1+\sqrt{2})X^2}{X^2Z^2}\Phi(\sigma_3)+\frac{\lambda_{\mathrm{III}}}{S^2}\Phi(\sigma_4)+\frac{\lambda_{\mathrm{III}}}{T^2}\Phi(\sigma_5)=1,$$

where, besides the Kelvin elastic moduli λ_{II} and λ_{III}, four limit values are to be determined; in two tensile tests along the edges of the tetragonal unit cell and two shear tests changing the right angles between the edges.

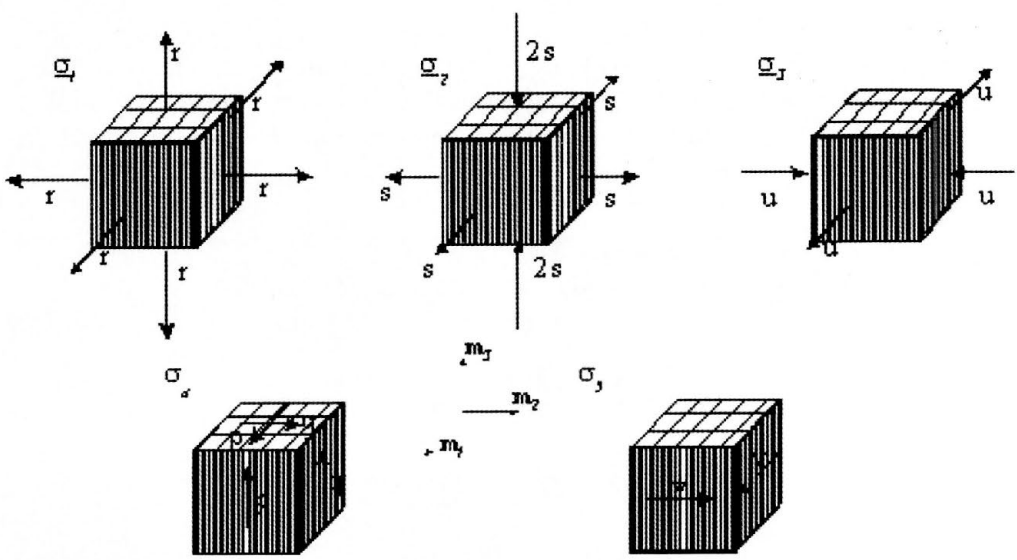

FIG. 2. Energy-orthogonal decomposition of the stress state for the material that has cubic symmetry in the elastic state and becomes tetragonal in the limit state.

8. Discussion of possible experimental verification and conclusions

From the geometry of slip in a FCC single crystal which is subjected to tension in the direction [100], it appears that eight potential slip systems can operate. In such a case we have

$$(8.1)\qquad \sigma_{[100]} = Y_2 = \sqrt{6}\tau_{\mathrm{cr}}.$$

Similar relation holds for tension in the direction [110] corresponding to activation of four potential slip systems, $\sigma_{[110]} = \sqrt{6}\tau_{\mathrm{cr}}$. In the case of tension in

the [111] direction, six potential slip systems exist and the critical stress at yield reads

$$\sigma_{[111]} = Y_3 = \frac{3\sqrt{6}}{2}\tau_{cr}. \tag{8.2}$$

Comparison of the discussed energy-based limit conditions on the example of Cu single crystal leads to the following relations:

- Schmid criterion – $\dfrac{Y_2}{Y_3} = \dfrac{2}{3} \cong 0.67\,, \quad \tau_{cr} = \text{const.}$
- Hypothesis of elastic energy of distortion – $\dfrac{Y_2}{Y_3} = 0.56.$
- Energy-based quadratic condition – $\dfrac{Y_2}{Y_3} = \dfrac{k_2}{k_3}.$

These relations should be verified experimentally. The results of J. DIEHL [28] can be applied to make at least an approximate assessment of the ratio Y_2/Y_3 for Cu single crystals. In [28] (Fig. 12, p. 335) the values of critical resolved shear stress τ_{cr} for different initial orientations of single crystals subjected to tension were given. We calculated the average values of τ_{cr} taken from the neighborhoods of the orientations corresponding to the corners of fundamental triangle of stereographic projection: $(\tau_{cr})^{[001]}_{aver} = 106.67$ [g/mm^2] for [001], $(\tau_{cr})^{[111]}_{aver} = 127.20$ [g/mm^2] for [111] and $(\tau_{cr})^{[110]}_{aver} = 110.25$ [g/mm^2] for [110]. The resulting values of tensile yield strengths are: $Y_2 = \sqrt{6}\,(\tau_{cr})^{[001]}_{aver} = 261.29$ [g/mm^2], $Y_3 = \dfrac{3\sqrt{6}}{2}\,(\tau_{cr})^{[111]}_{aver} = 467.36$ [g/mm^2] and $\sigma_{[110]} = \sqrt{6}\,(\tau_{cr})^{[110]}_{aver} = 270.06$ [g/mm^2], respectively. It is visible that the resulting ratio $Y_2/Y_3 = 0.56$ is close to the value obtained from the hypothesis of elastic energy of distortion. The equality within two digits of accuracy is rather coincidental because the assessment of experimental data is very rough. Nevertheless, rather large discrepancy with the prediction of the ratio $Y_2/Y_3 \cong 0.67$ calculated according to the Schmid criterion should be noted. The test for the direction [110] does not provide so good confirmation. We can observe that due to (4.3) and (4.4), with an account of Kelvin moduli for Cu single crystals $\lambda_{II} = 47$ [GPa], $\lambda_{III} = 150$ [GPa], the theoretical prediction of the ratio $Y_2/\sigma_{[110]} = 1.39$ and the discussed above experimental data provide $Y_2/\sigma_{[110]} = 0.97$. The program of systematic experimental tests is necessary to verify the proposed criteria. The main difficulty lies in accuracy of measurement of yield limit for single crystals.

The proposed energy-based criteria can be applied in mechanics of anisotropic solids, e.g. formulation of yield criteria for metals subjected to shaping operations as well as for polymers and composites. For example, it could provide deeper insight into the description of elastic and plastic anisotropy in sheet metals presented in [29]. The application of spectral decomposition of elasticity tensor

and energy orthogonal stress states proposed by J. Rychlewski for transversely isotropic material, representing fiber reinforced composites, was studied in [30]. Also in the field of nanomechanics the proposed approach can appear helpful filling the gap between the atomistic calculations and continuum mechanics modelling of the behaviour of different kinds of crystalline nanostructures. In such a case the pertinent limit values of elastic energy should be determined from the first principles with use of quantum mechanical theory of the strength of atomic bonds.

Acknowledgment

The State Committee for Scientific Research of Poland (KBN) partly supported this work within the framework of the research project KBN 5 T07A 031 22 and the research project PBZ-KBN-009/T08/1998.

References

1. J. RYCHLEWSKI, *On Hooke's law* [in Russian], PMM, **48**, 420–435, 1984; English translation in Prik. Matem. Mekhan., **48**, 303–314, 1984.

2. J. RYCHLEWSKI, *Elastic energy decomposition and limit criteria* [in Russian], Uspekhi Mekh., Advances in Mech., **7**, 51–80, 1984.

3. J. RYCHLEWSKI, *Unconventional approach to linear elasticity*, Arch. Mech., **47**, 149–171, 1995.

4. J. C. MAXWELL, *Origins of Clerk Maxwell's electric ideas described in familiar letters to William Thompson*, the letter of 18th December 1856, Proc. Cambridge Phil. Soc., **32**, 1936, Part V, also ed. by Sir J. Larmor, Cambridge Univ. Press, 31–33, 1937.

5. M. T. HUBER, *Specific strain work as a measure of material effort – A contribution to the foundations of the theory of material strength* [in Polish], Czasopismo Techniczne, XXII, 1904, Nr. 3., 38–40, Nr. 4., 49–50, Nr. 5., 61–63, Nr. 6., 80–81, Lwów (also: Works, II, 3–20, PWN, Warszawa 1956).

6. H. HENCKY, *Zur Theorie plastischer Deformationen und der hierdurch im Material hervorgerufener Nachspannungen*, ZAMM, **4**, 323–334, 1924.

7. W. T. BURZYŃSKI, *Study upon strength hypotheses* [in Polish], Nakładem Akademii Nauk Technicznych, Lwów, 1928 also: Selected Works, I, PWN, Warszawa, 67–257, 1982.

8. K. KOWALCZYK, J. OSTROWSKA-MACIEJEWSKA, *Energy-based limit conditions for trasversally isotropic solids*, Arch. Mech., **54**, 497–523, 2002.

9. J. OSTROWSKA-MACIEJEWSKA, J. RYCHLEWSKI, *Plane elastic and limit states in anisotropic solids*, Arch. Mech., **40**, 379–368, 1988.

10. J. OSTROWSKA-MACIEJEWSKA, J. RYCHLEWSKI, *Generalized proper states for anisotropic elastic materials*, Arch. Mech., **53**, 501–518, 2001.

11. E. SCHMID, *"Yield point" of crystals. Critical shear stress law*, Proc. Internat. Congr. Appl. Mech., 342–353, Delft 1924.

12. E. SCHMID, W. BOAS, *Kristallplastizität mit besonderer Berücksichtigung der Metalle*, Springer-Verlag, Berlin 1935; English edition: *Plasticity of crystals with special reference to metals*, Hughes, London 1950, reissued by Chapman&Hall, London 1968.

13. A. SEEGER, *Kristallplastizität, Handbuch der Physik*, VII/2, S. FLÜGGE [Ed.], 1–208, Springer-Verlag, Berlin 1958.

14. R. J. ASARO, J. R. RICE, *Strain localization in ductile single crystals*, J. Mech. Phys. Solids, **25**, 309–338, 1977.

15. M. DAO, B. J. LEE, R. J. ASARO, *Non-Schmid effects on the behavior of polycrystals – with applications to Ni_3Al*, Met. Mat. Trans., **27A**, 81–99, 1996.

16. M. F. HORSTEMEYER, M. I. BASKES, A. GODFREY, D. A. HUGHES, *A large deformation atomistic study examining crystal orientation effects on the stress-strain relationship*, Int. J. Plasticity, **18**, 203–229, 2002.

17. J. L. BASSANI, K. ITO, V. VITEK, *Complex macroscopic plastic flow arising from non-planar dislocation core structures*, Mat. Sci. Enging., **A319-321**, 97–101, 2001.

18. K. ITO, V. VITEK, *Atomistic study of non-Schmid effects in the plastic yielding of bcc metals*, Phil. Mag., **A81**, 1387–1407, 2001.

19. R. PHILLIPS, *Crystals, defects and microstructures. Modelling across scales*, Cambridge University Press, Cambridge 2001.

20. K. NALEPKA, R. B. PĘCHERSKI, *Physical foundations of energy-based strength criterion for monocrystals* [in Polish], 311–316, XXX Szkoła Inżynierii Materiałowej, Kraków-Ustroń Jaszowiec, 1–4, X 2002, [Ed.], AGH, Kraków 2002.

21. R. B. PĘCHERSKI, J. OSTROWSKA-MACIEJEWSKA, K. KOWALCZYK *An energy-based criterion of plasticity for FCC single crystals* [in Polish], Rudy Metale, **R46**, 639-644, 2001.

22. W. OLSZAK, W. URBANOWSKI, *The plastic potential in the theory of anisotropic elastic-plastic bodies*, Arch. Mech., **8**, 671–694, 1956.

23. W. OLSZAK, J. OSTROWSKA-MACIEJEWSKA, *The plastic potential in the theory of anisotropic elastic-plastic solids*, Eng. Fracture Mech., **21**, 625–632, 1985.

24. S. SUTCLIFFE, *Spectral decomposition of the elasticity tensor*, J. Appl. Mech., **59**, 762–773, 1992.

25. A. BLINOWSKI, J. OSTROWSKA-MACIEJEWSKA, *On the elastic orthotropy*, Arch. Mech., **48**, 129–141, 1996

26. S. JEMIOŁO, K. KOWALCZYK, *Invariant formulation and spectral decomposition of anisotropic yiled condition of Hill* [in Polish], Prace Naukowe PW, Budownictwo, Zeszyt 133, 87–123, 1999.

27. R. HILL, *The mathematical theory of plasticity*, Oxford at the Clarendon Press, Oxford 1956.

28. J. DIEHL, *Zugverformung von Kupfer-Einkristallen. I. Verfestigungskurven und Oberflächenerscheinungen*, Z. Metallkunde, **47**, 331–343, 1956.

29. CHI-SINGH MAN, *On the correlation of elastic and plastic anisotropy in sheet metals*, J. Elasticity, **39**, 165–173, 1995.

30. P. S. THEOCARIS, T. P. PHILIPPIDIS, *Spectral decomposition of compliance and stiffness fourth-rank tensors suitable for orthotropic materials*, ZAMM, **71**, 161–171, 1991.

Received January 31, 2003; revised version May 29, 2003.

Arch. Mech., **55**, 5–6, pp. 449–479, Warszawa 2003

Finite element analysis and design optimization of rubber components for vibration isolation

WAN-SUL LEE, SUNG-KIE YOUN and BONG-KYU KIM[1]

Department of Mechanical Engineering,
Korea Advanced Institute of Science and Technology,
373-1, Gusung-dong, Yusung-gu, Daejeon, 305-701, Korea
e-mail:skyoun@sorak.kaist.ac.kr

[1] *R&D Division for Hyundai Motor Company & Kia Motor Corporation,*
Jangduk-dong, Whasung-si, Gyunggi-do, 445-706, Korea

A CONSTITUTIVE THEORY, finite element formulation and topology optimization for anti-vibration rubber are presented. Many vibration isolators made of rubbers are operating under small oscillatory load superimposed on large static deformation. A viscoelastic constitutive equation for rubber is proposed considering the influence of large static pre-deformation on the dynamic properties. The proposed model is derived through linearization of Simo's viscoelastic constitutive model and introduction of static deformation correction factor. And then the model is implemented in a finite element code to analyze the behavior of rubber elements under general loading conditions. Dynamic tests are performed in order to verify the model under multiaxial deformation. The computed results by the FEA code are compared with the experimental results and the suggested constitutive equation with static deformation correction factor shows good agreement with the test values. For the stability and low transmissibility of isolation systems, both static and dynamic performance must be concurrently considered in the design process. The continuum-based design sensitivity analyses (DSA) of both the static hyperelastic model and dynamic viscoelastic model are developed. And then the topology optimization methodology is used in order to generate the system layouts considering both the static and dynamic performance.

1. Introduction

MANY RUBBER COMPONENTS, which are used as vibration isolators, experience small oscillatory loads superimposed on large static deformation. Most of dynamic properties of vibration isolators can be described by linearized steady-state harmonic response. Considering nonlinear behavior of rubber under large deformation, it is evident that even linearized dynamic properties depend heavily on prestrain. The accurate constitutive equation that describes rubber under the loading conditions is essential in analyzing the dynamic behavior of rubber and designing the shape of rubber elements.

Morman's model is widely used to describe viscoelastic behavior of rubber that is under small oscillatory loads superimposed on large static deformation [1–5]. Morman derived a viscoelastic constitutive model from the assumption that the time effect and large prestrain effect can be separable. The separability assumption leads to simple relaxation function that is independent of deformation. It is observed in experiments that the separability assumption is applicable to unfilled rubber [1, 6]. In filled rubber, however, the relaxation function is a function of prestrain [6, 7]. Rubber is seldom used as pure gum, because addition of fillers to elastomers improves mechanical properties [8]. Therefore it is very important to consider the effects of prestrain in the constitutive theory of small viscoelastic motion superimposed on large static deformation in many engineering rubber materials [9].

In the previous work [9], the authors have proposed Linearized Simo's Viscoelastic Model (LSVM) with static deformation correction factor as a constitutive equation of rubber that is under small oscillatory loads superimposed on large static deformation. In this constitutive model, the statically pre-deformed configuration has been used as the reference configuration. And static deformation correction factor has been introduced to consider the influence of prestrain on the relaxation function. In the previous work, it has been observed that the proposed model works well under single stress component.

In this work, the proposed model is implemented in a finite element code that enables us to predict the behavior of rubbers for general complex shapes and loading conditions. And dynamic tests are executed in order to verify the proposed constitutive model. Complex stress-state tests are included in the dynamic tests in order to assure the proposed model under multi-axial stress states. The computed results by the FEA code are compared with the experimental results in order to estimate the performance of the model.

Many works for engine mount system of vehicles and aircrafts used two-level design approaches [10]. First step is the system level design in order to decide the mounting location and mount stiffness. In this level, simple spring-damper models are generally used with constant parameters such as dynamic-to-static ratio and loss factor. However these models are too simple to describe the complex behavior of rubber-like materials. Second step is the isolator shape design to get target stiffness decided in the first step. Various optimization approaches [11–13] are applied to the shape design, but they consider the only static hyperelastic behavior of rubber. Most vibration isolators must endure the static loadings due to large gravitational and inertial forces. And also they must be dynamically flexible in order to have small natural frequencies and reduce the transmitting dynamic force from the vibrating systems to the other structures. Therefore in the stiffness and shape design process of the vibration isolators, both static and dynamic behavior of rubber materials must be

simultaneously considered for the structural stability and the vibration isolation.

For the stability and low transmissibility of isolation systems, both static and dynamic performance must be concurrently considered in the design process. Among the various design methods, a topology optimization approach can be applied for the shape design of vibration isolator made of filled rubber. For easier application of the optimization algorithm, two kinds of continuum-based design sensitivity analysis method are developed. Material property design sensitivity analysis of both the hyperelastic constitutive equation and the steady-state viscoelastic one are developed for topology optimization using the mean compliance and adjoint variables. In order to consider simultaneously the static and dynamic behavior of rubber, a proper topology optimization formulations is proposed.

2. Constitutive equation and FE formulation

2.1. Notation

The small deformation superimposed on the large static deformation is depicted in Fig. 1. Let Φ_ξ denote the configuration of the body $\mathscr{B}$ at instant ξ. Configuration $\Phi_{t'}$, Φ_{t_0} and Φ_t refer respectively to the undeformed, the statically deformed and the current configuration. ${}_\xi T(\eta)$ represents a tensor T at time η with respect to a configuration Φ_ξ. For convenience, the following simplified notations are also used:

$$T(\eta) = {}_{t'}T(\eta), \qquad {}_\xi T_0 = {}_\xi T(t_0), \qquad {}_0T(\xi) = {}_{t_0}T(\xi), \qquad {}_\xi T = {}_\xi T(t). \tag{2.1}$$

The deformation gradient and volume preserving deformation gradient tensor are denoted by

$$({}_\xi F(t))_{ij} = \left(\frac{\partial x_i(t)}{\partial X_j(\xi)}\right), \qquad {}_\xi \overline{F} = J^{-1/3}{}_\xi F, \tag{2.2}$$

where J is $\det({}_\xi F)$. Left and right Cauchy–Green tensors that correspond to ${}_\xi \overline{F}$ and ${}_\xi F$ are

$${}_\xi C = {}_\xi F^T {}_\xi F, \qquad {}_\xi \overline{C} = {}_\xi \overline{F}^T {}_\xi \overline{F}, \tag{2.3}$$

$${}_\xi B = {}_\xi F {}_\xi F^T, \qquad {}_\xi \overline{B} = {}_\xi \overline{F} {}_\xi \overline{F}^T \tag{2.4}$$

and Green strains are defined by

$${}_\xi E = \frac{1}{2}\left({}_\xi C - I\right), \qquad {}_\xi \overline{E} = \frac{1}{2}\left({}_\xi \overline{C} - I\right). \tag{2.5}$$

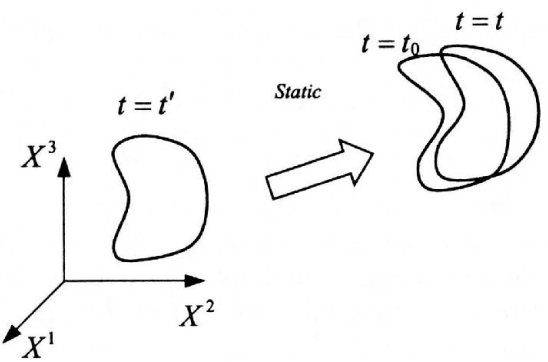

FIG. 1. Large static deformation + small dynamic deformation.

2.2. Linearized Simo's viscoelastic model (LSVM)

Simo proposed a finitely deformable viscoelastic model from the generalization of standard linear solid model [14]. The characteristics of Simo's model are decoupled bulk and deviatoric responses over any range of deformations and linear rate constitutive equation. Simo's nonlinear viscoelastic constitutive model is written as follows:

$$S = JC^{-1}\frac{\partial U}{\partial J} + J^{-2/3}\mathrm{DEV}\left[\left(\frac{\partial \Psi}{\partial \overline{E}}\right)\right] + J^{-2/3}\mathrm{DEV}\left[\int_0^t g(t-\xi)\frac{\partial}{\partial \xi}\mathrm{DEV}\left(\frac{\partial \Psi}{\partial \overline{E}}\right)d\xi\right], \tag{2.6}$$

where $\mathrm{DEV}[\bullet] = (\bullet) - 1/3\,[C : (\bullet)]\; C^{-1}$, U and Ψ are the volumetric and deviatoric parts of the elastic free energy function. From this model, static stress is given as

$$\sigma_0 = P_0 I + \mathrm{dev}\,[\widehat{\sigma}_0], \tag{2.7}$$

where $P_0 = \dfrac{\partial U}{\partial J}$, $\widehat{\sigma}_0 = \dfrac{1}{J}\overline{F}_0\dfrac{\partial \Psi}{\partial \overline{E}}\overline{F}_0^T$ and $\mathrm{dev}\,[\bullet] = (\bullet) - 1/3\,[I : (\bullet)]\,I$. We know from the above equation that static behavior of Simo's model is exactly equal to that of hyperelastic material. The static stress caused by prestrain is determined only by the last state of static deformation. Because of the fading memory hypothesis [15, 16] of the viscoelastic material, the effects of the deformation history are relaxed out. Thus we can assume that viscoelastic effects depend only on the superimposed small vibratory deformation.

A linearized constitutive equation that specifies the behavior of rubber under small oscillatory load superimposed on large static deformation can be derived

from the assumption that the superimposed motion is small. Repeated applications of the chain rule to Eq. (2.6) and the reference configuration transformation yield the relation between the stress increment $\Delta_0 S$ and the superposed strain increment ε.

$$\Delta_0 S = \left(J\frac{\partial^2 U}{\partial J^2} + P\right)\varepsilon_{kk} I - 2P\varepsilon - \frac{2}{3}\left[\operatorname{dev}(\widehat{\sigma}_0)\otimes I + I\otimes\operatorname{dev}(\widehat{\sigma}_0)\right] : \varepsilon + \mathscr{C} : \varepsilon + \int_0^t g(t-\xi)\,\mathscr{C} : \dot{\varepsilon}\,d\xi, \tag{2.8}$$

$$\mathscr{C} = \frac{2}{3}\left(\widehat{\sigma} : I\right)\left(\widehat{I} - \frac{1}{3} I\otimes I\right) + \mathscr{F} - \frac{1}{3}\left[(\mathscr{F} : I)\otimes I + I\otimes(\mathscr{F} : I)\right] + \frac{1}{9}(I : \mathscr{F} : I)\, I\otimes I, \tag{2.9}$$

where $\mathscr{F}_{ijkl} = \dfrac{1}{J}\overline{F}_{iI}\overline{F}_{jJ}\overline{F}_{kK}\overline{F}_{lL}\left(\dfrac{\partial^2\Psi}{\partial\overline{E}^2}\right)_{IJKL}$ and $\widehat{I}$ is the fourth order identity tensor.

Let us suppose that the superimposed deformation is steady-state harmonic such as $\varepsilon = \varepsilon^* e^{i\omega t}$. Then the complex constitutive relation is extracted from Eq. (2.8).

$$\Delta_0 S^* = \left(J\frac{\partial^2 U}{\partial J^2} + P\right)\varepsilon^*_{kk} I - 2P\varepsilon^* - \frac{2}{3}\left[\operatorname{dev}(\widehat{\sigma})\otimes I + I\otimes\operatorname{dev}(\widehat{\sigma})\right] : \varepsilon^* + (1 + i\omega g^*)\ \mathscr{C} : \varepsilon^*, \tag{2.10}$$

where g^* is the Fourier transform of $g(t)$ i.e. $g^*(\omega) = \int_0^\infty g(t)\, e^{-i\omega t} dt$. The relation between g^* and complex shear modulus $G^* = G' + iG''$ is as follows:

$$\omega g^* = \frac{G''}{G_\infty} + \left(1 - \frac{G'}{G_\infty}\right) i. \tag{2.11}$$

2.3. Static deformation correction factor

Thus far it has been assumed that $g(t)$, which represents the time effects, is not affected by static deformation. This separability assumption of time and large prestrain is suitable for the rubbers that do not contain such fillers as carbon black [6, 7]. However, it is known from experiments that $g(t)$ depend

on the static deformation for filled rubber [6]. Unfilled rubber is seldom used for engineering applications, because the addition of fillers improves their mechanical properties [8]. Therefore the influences on $g(t)$ due to the static deformation must be considered in order to develop a realistic viscoelastic constitutive model. In order to describe the non-separability nature of filled rubber, we introduce a static deformation correction factor $c^*(B_0)$ to the constitutive equation. Now we define $\widehat{g}^*$ which is the correction of $1 + i\omega g^*$ in Eq. (2.10).

$$\widehat{g}^* = (1 + i\omega g^*)\, c^*(B_0), \tag{2.12}$$

where $c^*(B_0)$ is a complex-valued function that depends on the static deformation. $\widehat{g}^*$ can also be described as follows using complex shear modulus and $c^*(B_0)$.

$$\widehat{g}^*(\omega, B_0) = \frac{G^*(\omega)}{G_\infty} c^*(B_0) = \left(\frac{G'}{G_\infty} + i\frac{G''}{G_\infty}\right) c^*(B_0) = \frac{\widehat{G}^*}{G_\infty}. \tag{2.13}$$

In the above equation, $\widehat{G}^*$ can be interpreted as an effective complex shear modulus under static deformation. The static deformation correction factor can be expressed by the modulus and argument of c^*,

$$c^*(B_0) = c\, e^{i\theta}. \tag{2.14}$$

To define c^* in a specific form, we need to measure the static deformation that is described by the tensor B_0. It is observed that generalized octahedral shear strain has good performance as a static deformation measure. The generalized octahedral shear strain [17] is defined as

$$\overline{I}_\gamma = \frac{1}{6}\left(2\overline{I}_1^2 - 6\overline{I}_2\right)^{1/2}, \tag{2.15}$$

where $\overline{I}_1$ and $\overline{I}_2$ are the first and second invariants of the right Cauchy–Green tensor $\overline{C}$. $\overline{I}_\gamma$ is an invariant of B_0 and represents the octahedral shear strain under infinitesimal deformation. Since the value of c^* is unity without the static deformation, the following polynomial forms can serve as the static deformation correction factors:

$$c_\gamma^*\left(\overline{I}_\gamma\right) = c_\gamma e^{i\theta_\gamma}, \tag{2.16}$$

$$c_\gamma\left(\overline{I}_\gamma\right) = 1 + z_{\gamma_1}\overline{I}_\gamma + z_{\gamma_2}\overline{I}_{\gamma^2}, \tag{2.17}$$

$$\theta_\gamma\left(\overline{I}_\gamma\right) = {}_\theta z_\gamma \overline{I}_\gamma, \tag{2.18}$$

where z_{γ_1}, z_{γ_2} and ${}_\theta z_\gamma$ are material constants. The material constants can be easily determined by the results of uniaxial tension test.

2.4. Mixed FE formulation of static deformation

For the FEA of a rubber element that is under small steady-state dynamic load superimposed on large static deformation, the static analysis results such as statically deformed shape and static stress state are required. Since rubber can be idealized as a hyperelastic material as mentioned in the previous section, static deformation analysis results can be easily obtained using the techniques that are developed for the FEA of hyperelastic material. In the static analysis, nonlinearity due to large deformation and incompressibility characteristics of rubber should be effectively treated, and so the updated Lagrangian formulation with displacement-pressure mixed method (u/p mixed method) is used in this paper.

The mixed finite element formulation that was proposed by SUSSMAN and BATHE [18] is used in order to analyze the incompressible large deformation problems. In the mixed method, pressure that is defined by $-\sigma_{kk}/3$ is independent of the displacement field and interpolated by its own shape function. The independent pressure variable is denoted by $\widehat{p}$ and the pressure computed from displacement is represented by $\overline{p}$. By definition of pressure and Eq. (2.7), $\overline{p}$ has the following description:

$$\overline{p} = -\frac{\partial U}{\partial J}. \tag{2.19}$$

The stress is composed of the derivatives of the strain energy function that is obtained from the displacement field and the independent pressure field.

$$ {}_0S(t_0) = \sigma(t_0) = \frac{1}{J_0}\mathrm{dev}\left[\overline{F}_0 \frac{\partial \Psi}{\partial \overline{E}} \overline{F}_0^T\right] - \widehat{p}I. \tag{2.20}$$

The governing equations in the u/p mixed method are described by the following weak forms:

$$\int_V \left(\frac{\partial_0 W}{\partial_0 E} - \frac{1}{KJ_0}(\overline{p} - \widehat{p})\frac{\partial \overline{p}}{\partial_0 E}\right) : \delta_0 E \, dV = \int_V {}_0S : \delta_0 E \, dV = \Re, \tag{2.21}$$

$$\int_V \frac{1}{KJ_0}(\overline{p} - \widehat{p})\,\delta\widehat{p}\, dV = 0. \tag{2.22}$$

In the above equations, the first and second equations are respectively the equilibrium equation and pressure constraint between $\widehat{p}$ and $\overline{p}$. $\Re$ and K represent the external virtual work and bulk modulus of rubber, respectively. ${}_0W$ that

is the strain energy per unit volume of statically deformed state is defined as follows:

$$ {}_0W = \frac{\widehat{\Psi}}{J_0} = \frac{1}{J_0}\left(\Psi + U\right). \tag{2.23} $$

In this paper, U and Ψ are described by the Mooney–Rivlin model and the second order polynomial of J. The specific form of the strain energy function is

$$ \Psi = c_1\left(\overline{I}_1 - 3\right) + c_2\left(\overline{I}_2 - 3\right), \tag{2.24} $$

$$ U = \frac{1}{2}K\left(J-1\right)^2, \tag{2.25} $$

where c_1, c_2 and bulk modulus K are the material constants of rubber.

The solution of the governing equations cannot be obtained directly because the equations are nonlinear. Thus we use the Newton–Raphson method in which the linearized governing equations are solved by the iterative technique. The incremental form of the governing equation can be written as follows:

$$ \int_V \delta\varepsilon : \left[\mathscr{D} - \widehat{p}\left(I\otimes I - 2\widehat{I}\right)\right] : \varepsilon \, dV + \int_V \sigma_0 : \Delta\delta_0 E \, dV + \int_V -\Delta\widehat{p}I : \delta\varepsilon \, dV = \Re - \int_V \sigma_0 : \delta\varepsilon \, dV, \tag{2.26} $$

$$ \int_V -\delta\widehat{p}I : \varepsilon dV - \int_V \frac{1}{KJ_0}\delta\widehat{p}\Delta\widehat{p} \, dV = -\int_V \frac{1}{KJ_0}\left(\overline{p}_0 - \widehat{p}_0\right)\delta\widehat{p} \, dV, \tag{2.27} $$

where $\delta\varepsilon_{ij} = \frac{1}{2}\left(\frac{\partial\delta u_i}{\partial x_j} + \frac{\partial\delta u_j}{\partial x_i}\right)$ and $\mathscr{D} = \frac{1}{J_0}\frac{\partial^2\Psi}{\partial_0 E\partial_0 E}$. To solve Eqs. (2.26) and (2.27), the displacement and pressure field are approximated by the shape functions.

$$ u_i = N^I u_i^I, \tag{2.28} $$

$$ \widehat{p} = N_p^I \, \widehat{p}^I. \tag{2.29} $$

In the above equations, N^I is the interpolation function for the displacement and N_p^I is the interpolation function for pressure. u_i^I is the displacement at the I-th node in the i direction and $\widehat{p}^I$ is the I-th pressure degree of freedom. The element used in this study has 27 displacement nodes and 4 pressure degrees

of freedom. The interpolation function for displacement field is the conventional isoparametric shape function that continuously interpolates the field between elements. The pressure field is interpolated by a linear polynomial using element local coordinates and it is discontinuous between elements. Using finite element approximation, the governing incremental equations are converted to the following matrix equation:

$$\begin{bmatrix} K_{UU} & K_{UP} \\ K_{PU} & K_{PP} \end{bmatrix} \begin{Bmatrix} \Delta u \\ \Delta \hat{p} \end{Bmatrix} = \begin{Bmatrix} \mathscr{R} \\ 0 \end{Bmatrix} - \begin{Bmatrix} F_U \\ F_P \end{Bmatrix}, \tag{2.30}$$

where K_{UU}, K_{UP}, K_{PP}, F_U and F_P are defined as follows:

$$(K_{UU})_{mn} = \int \frac{\partial \varepsilon_{ij}}{\partial u_r^I} \left[\mathscr{D} - \hat{p} \left(I \otimes I - 2\hat{I} \right) \right]_{ijkl} \frac{\partial \varepsilon_{kl}}{\partial u_s^J} \, dV + \int \sigma_{ij} \frac{\partial^2 {}_0E_{ij}}{\partial u_r^I \partial u_s^J} \, dV, \tag{2.31}$$

$$(K_{UP})_{mq} = (K_{PU})_{qm} = - \int \frac{\partial N^I}{\partial x_r} N_p^q \, dV, \tag{2.32}$$

$$(K_{PP})_{qt} = - \int \frac{1}{KJ_0} N_p^q N_p^t \, dV, \tag{2.33}$$

$$(F_U)_m = \int \sigma_{ij} \frac{\partial \varepsilon_{ij}}{\partial \mathrm{u}_\mathrm{r}^I} \, dV, \tag{2.34}$$

$$(F_P)_q = \int \frac{1}{KJ_0} (\bar{p} - \hat{p}) \, N_p^q \, dV. \tag{2.35}$$

In the above equations, m and n denote respectively the displacement degree of freedom at the I-th node in direction r and the J-th node in directions in the global matrix.

2.5. FE formulation of steady-state dynamic deformation superposed on large static deformation

The finite element formulation for the dynamic analysis is easily derived through generalization of the static incremental formulation. In the dynamic formulation, the viscoelastic behavior that alters the stress-strain relation and

the inertia effects must be considered. Assuming that the displacement and external force increments which are superimposed on the static deformation are varying in steady-state harmonic manner, the increments are written as follows:

$$\Delta u = \Delta u^* e^{i\omega t}, \quad \Delta \hat{p} = \Delta \hat{p}^* e^{i\omega t}, \quad \Delta \mathscr{R} = \Delta \mathscr{R}^* e^{i\omega t}, \quad \Delta S = \Delta S^* e^{i\omega t}. \tag{2.36}$$

The stress increments are determined by the proposed constitutive equation. Because we use the mixed method in the FEA, the pressures and their increments in the constitutive relations are converted to the independent variables. The stress increments are calculated by

$$\Delta S^* = \mathscr{D}^* : \varepsilon^* - \hat{p}_0 \left(I \otimes I - 2\hat{I} \right) : \varepsilon^* - \Delta \hat{p}^* I, \tag{2.37}$$

where $\mathscr{D}^* = \hat{g}^* \mathscr{C} - 2/3 \left[\operatorname{dev} (\hat{\sigma}_0) \otimes I + I \otimes \operatorname{dev} (\hat{\sigma}_0) \right]$. The inertia effects due to dynamic deformation can be regarded as the body force $\rho \omega^2 \Delta u^*$ by d'Alembert's principle. We can obtain directly the dynamic finite element formulation using the same procedure that is used in the previous static case except for the complex constitutive relation and the inertial body force. The finite element matrix equation for a rubber element subject to steady-state harmonic motion superposed on finite static deformation is

$$\begin{bmatrix} M + K^*_{UU} & K_{UP} \\ K^T_{UP} & K_{PP} \end{bmatrix} \begin{Bmatrix} \Delta u^* \\ \Delta \hat{p}^* \end{Bmatrix} = \begin{Bmatrix} \Delta \mathscr{R}^* \\ 0 \end{Bmatrix}. \tag{2.38}$$

In the above equation, the mass matrix and the dynamic stiffness matrix is written as follows:

$$M_{mn} = -\delta_{rs} \int \rho \omega^2 N^I N^J \, dV, \tag{2.39}$$

$$(K^*_{UU})_{mn} = \int \frac{\partial \varepsilon^*_{ij}}{\partial u^{*I}_r} \left[\mathscr{D}^* - \hat{p}_0 \left(I \otimes I - 2\hat{I} \right) \right]_{ijkl} \frac{\partial \varepsilon^*_{kl}}{\partial u^{*J}_s} \, dV + \int \sigma_{ij} \frac{\partial^2 {}_0 E^*_{ij}}{\partial u^{*I}_r \partial u^{*J}_s} \, dV. \tag{2.40}$$

The dynamic stiffness matrix depends on the static prestress and frequency due to the definition of $\mathscr{D}^*$ and Eq. (2.40). Comparing Eqs. (2.30) and (2.38), we see that the steady-state dynamic finite element equation has the same structure as the incremental equation for static deformation, except that the dynamic equation has the mass matrix and the complex stiffness matrix.

3. Experiment and prediction by the constitutive model

Dynamic tests in which the rubber specimens are subject steady-state harmonic motion superimposed on large static deformation have been executed in order to verify the proposed constitutive model. The tests performed in this work are composed of the uniaxial tension tests and the complex stress-state tests. The coefficients in the proposed model are determined by uniaxial tension test. The determined coefficients are required in FEA of complex stress-state test to specify the constitutive model. In the previous paper [9] it was observed that the proposed model works well under single stress component. In this paper, the complex stress-state test is carried out to verify the model under multi-axial stress state. Varying the size of static deformation, the dynamic stiffness of each specimen is measured and compared with the predicted value that is calculated by FEM using the proposed model. By comparison of the results, we can verify whether the model effectively describes the behavior of rubber subject to the steady-state harmonic motion superposed on finite static deformation.

The tests have been performed at room temperature (26°C) using a servo-hydraulic rubber tester(Instron-5802). To subject the specimen to small dynamic motions superimposed on finite static deformations, experiments are conducted in two steps. Finite prestrain is applied to each specimen with 20 minutes of relaxation time in order to achieve the static equilibrium. After that, the dynamic load is superimposed on the static deformation. The dynamic displacement amplitude is 0.5% with respect to the deformed specimen length. Initial conditioning has been applied 12 hours in advance before the test. For the initial conditioning, each test specimen is exposed to the highest strain and frequency in the test series in order to remove irreversible material structures [19]. The measurement is executed after 50 cycles of initial dynamic loading. When the test is executed using the displacement-control mode, the dynamic displacements and the corresponding dynamic driving forces are measured as the experiment results. And then from these test data, the dynamic modulus and stiffness can be calculated considering the size of specimens.

Table 1. Recipes of specimens.

Ingredient	Content (phr)	Ingredient	Content (phr)	Ingredient	Content (phr)
NR	100	Carbon black GPF	50	Antidegradant	4
ZnO	3	TBBS	1.0		
Stearic acid	1.0	S	1.75		

Table 2. Material constants and the coefficients of static deformation correction factor.

Material constant	Value	Material constant	Value	Material constant	Value
c_1 (MPa)	0.46	ρ (kg/m^3)	1124.7	$_\theta z_\gamma$	-0.0627
c_2 (MPa)	0.08	$z_{\gamma 1}$	-2.841		
G_∞ (MPa)	1.08	$z_{\gamma 2}$	10.81		

The rubber specimens used in this work are made of natural rubber and other ingredients. The recipes and material constants of the rubber are shown in Table 1 and Table 2. Aluminum plates are bonded to both ends of the rubber specimen by quick setting adhesive and each plate is bolted to the test machine. The pictures of specimens used in uniaxial tension test and complex stress-state test are shown in Fig. 2 and Fig. 3.

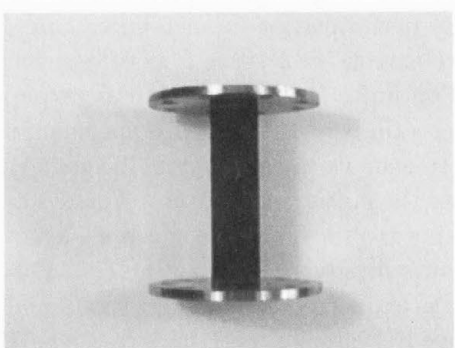

FIG. 2. Tension specimen.

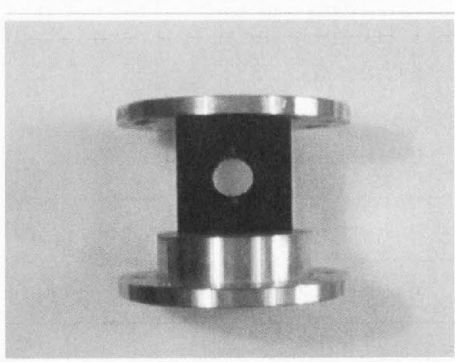

FIG. 3. Complex stress-state specimen.

3.1. Uniaxial tension test

Using the uniaxial tension test, the behavior of rubber under tensile loading conditions can be examined and the performance of the proposed constitutive model can be verified by comparing the test results with the calculated results. As a pre-deformation, the static deformation in the range from 0% ($\lambda = 1$) to 30% ($\lambda = 1.3$) is applied to the specimen. The 0.5% dynamic strain amplitude with respect to the deformed specimen length is superimposed on static deformation in $1 \sim 30$ Hz frequency range. The definition of stretch and dynamic strain is as follows:

$$\lambda = \frac{l}{l_0} = \frac{l_0 + \Delta l_0}{l_0} = 1 + \frac{\Delta l_0}{l_0}, \tag{3.1}$$

$$\varepsilon = \frac{\Delta l}{l}. \tag{3.2}$$

In the above equations, l_0, l, Δl_0 and Δl are respectively, the original length of a specimen in the direction of the test machine axis, length of the specimen after static deformation, static displacement and dynamic displacement amplitude.

As results of the dynamic tension test, storage and loss modulus of the specimen are shown in Fig. 4 and Fig. 5 as a function of vibrating frequency for each static tension case. The well-known near-linear relation between the stiffness and log frequency is observed under different static deformation. We also can observe that the dynamic stiffness is moved vertically with static deformation and conclude that the frequency effect is not influenced by static deformation. In order to

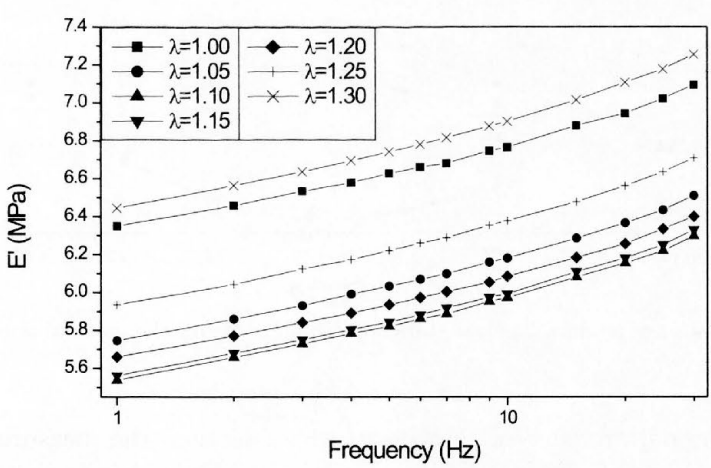

FIG. 4. Storage modulus against frequency at different static stretch for uniaxial tension specimen.

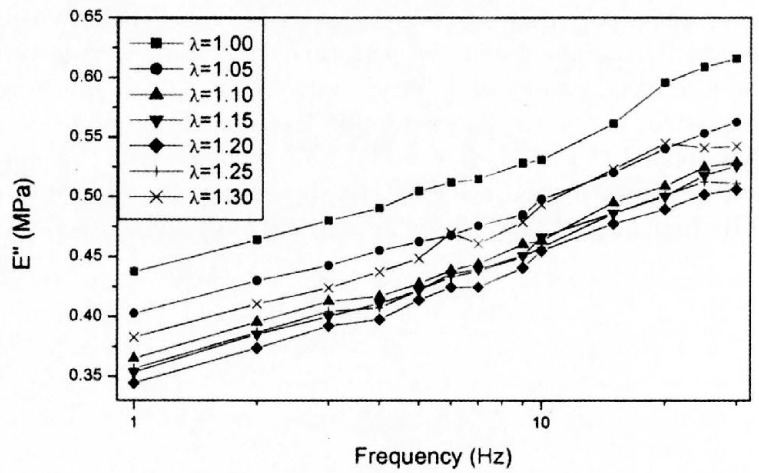

FIG. 5. Loss modulus against frequency at different static stretch for uniaxial tension specimen.

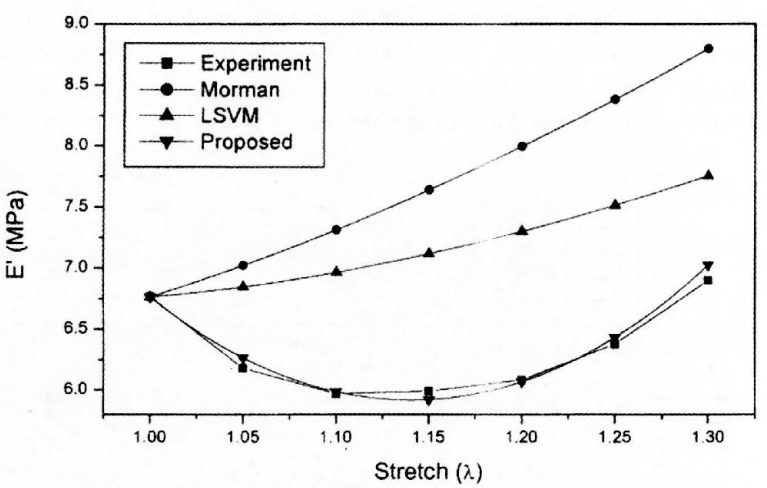

FIG. 6. Storage modulus against static stretch at 10 Hz for the uniaxial tension test.

estimate the performance of the constitutive equation, the measured dynamic modulus and thecalculated ones are plotted at 10 Hz with respect to static deformation in Fig. 6 and Fig. 7. The proposed model successively describes the effects of static deformation. It is observed that the complex Young's modulus

of rubber shows an initial decrease followed by an increase with enlargement of static stretch in the uniaxial tension test. In the uniaxial tension test, Morman's model and LSVM in which static deformation effects are not considered, cannot describe the variation of the modulus by static stretch. The proposed model describes properly the dynamic behavior of the rubber. The constitutive equations in which static deformation effects are not considered tend to predict higher dynamic stiffness than the value measured in the compression test.

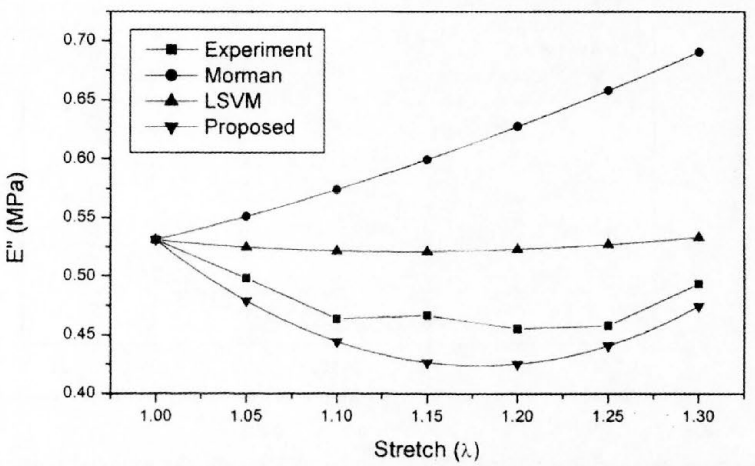

FIG. 7. Loss modulus against frequency at different static stretch for uniaxial tension specimen.

In the prediction of loss modulus, the proposed model anticipates smaller value than the measured result but shows a similar trend. Since the loss moduli are very small compared with the storage modulus and are very sensitive to experimental condition, consistent experiments are difficult to be performed for the loss moduli. The differences between the computed values and the measured ones could be caused by these difficulties. However, the dynamic moduli calculated by the proposed model show the trends of initially decreasing and gradually increasing against the static deformations, as similarly shown in the experimental results.

The storage modulus is plotted with respect to the static deformation at frequencies 5 Hz and 30 Hz in Fig. 8 and Fig. 9. In these figures we can observe that the proposed constitutive model works well at other frequencies. The value of c^* used in the analysis at frequencies 5 Hz and 30 Hz is determined by the uniaxial tension test results at 10 Hz. This means that the static deformation correction factor determined at one frequency is effective at other frequencies in

the tested range. This confirms authors' assumption that c^* is only a function of static deformation.

By the discussion given in this section, the constitutive model proposed in this work efficiently describes the effects of static deformation and shows better performance than the conventional constitutive model in predicting the dynamic behaviors of rubber specimens subject to large static deformations.

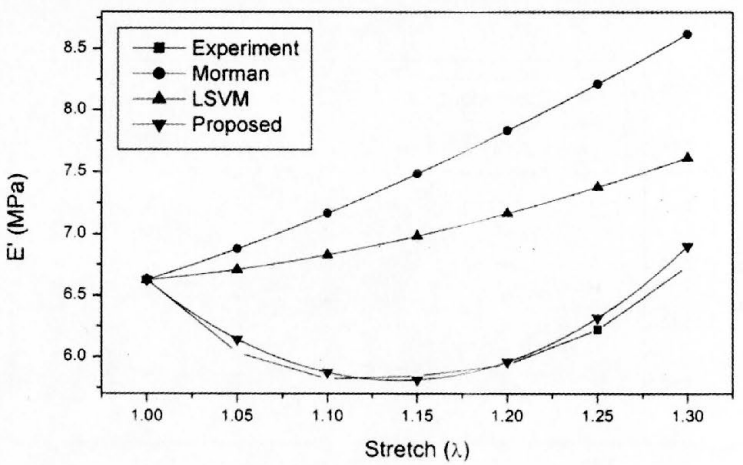

FIG. 8. Storage modulus against static stretch at 5 Hz for the uniaxial tension test.

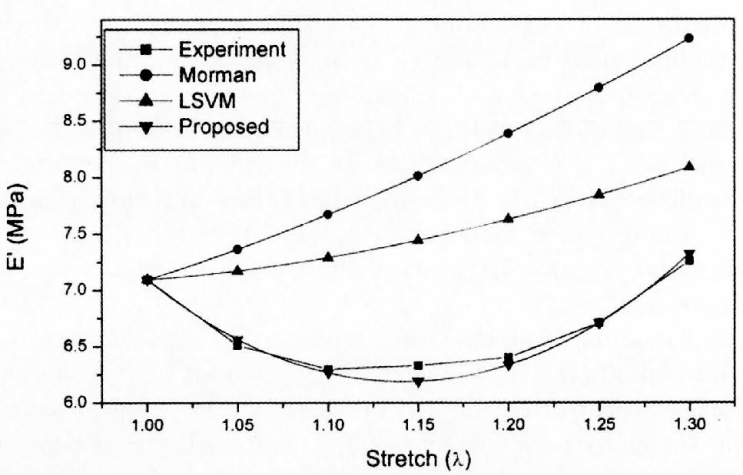

FIG. 9. Storage modulus against static stretch at 30 Hz for the uniaxial tension test.

3.2. Complex stress-state test

Complex stress-state test in which the specimens are under more complicated stress state is used to verify the proposed constitutive model. The specimen used in this test has the shape of a hexahedral block with a central hole and is under intricate stress state when it is deformed as shown in Fig. 10 and Fig. 11. The static deformations are applied to the specimen and the values of deformations are in the range from 15% compression ($\lambda = 0.85$) to 20% tension ($\lambda = 1.2$). The 0.5% dynamic strain amplitude with respect to the deformed specimen length was superimposed on the static deformation over $1 \sim 30$ Hz frequency range. Varying the magnitude of static deformation, the dynamic stiffness defined by the following equation is measured and compared with the computed result:

$$K^* = K' + iK'' = \frac{\Delta F^*}{\Delta l^*}, \tag{3.3}$$

where ΔF^* and Δl^* are the dynamic force and displacement.

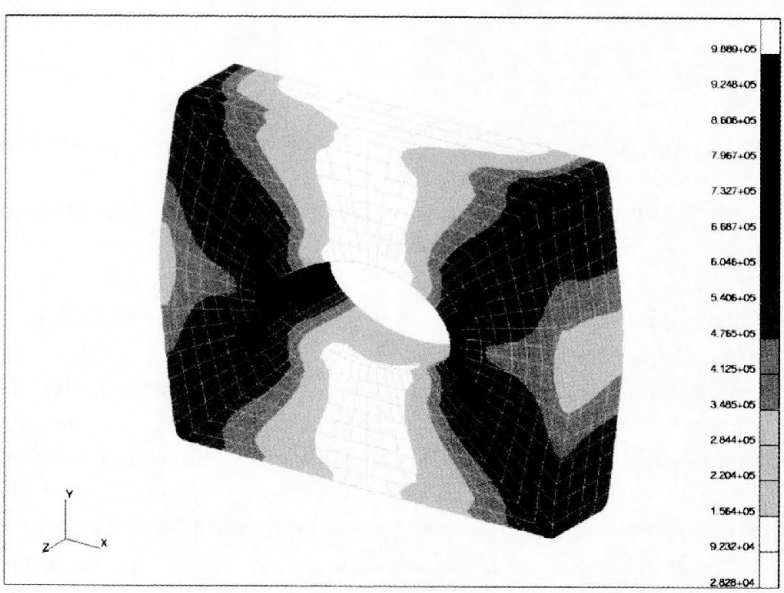

FIG. 10. Static stress distribution for the complex stress specimen (von Mises' stress, $\lambda = 0.85$).

From the results of complex stress-state test, the relations between dynamic stiffness and frequency for each static deformation show the nearlinear relation. This trend is very similar with uniaxial tension test results shown in Fig. 4 and Fig. 5. The dynamic stiffness moves upwards with static compression and

downwards with static tension. The effective cross-sectional area of the specimen increases with the compression and decreases with the tension, as shown in Fig. 10 and Fig. 11.

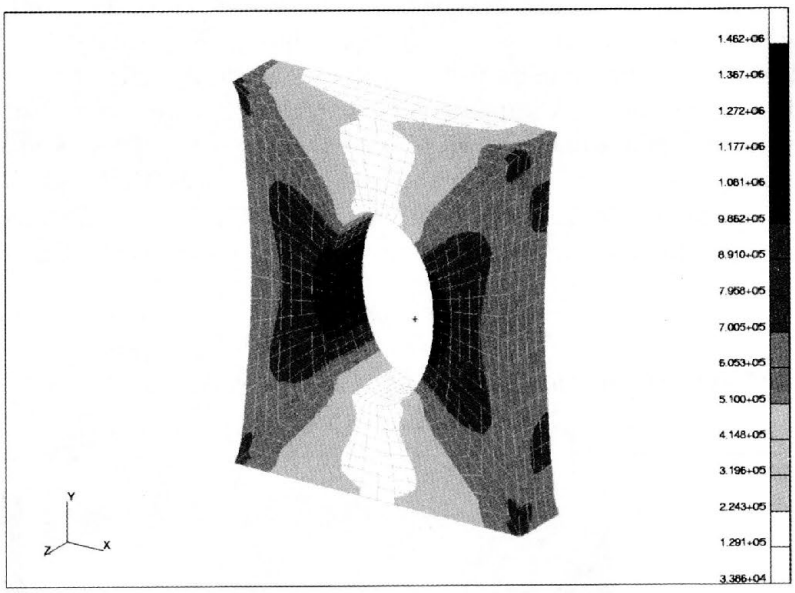

FIG. 11. Static stress distribution for the complex stress specimen (von Mises' stress, $\lambda = 1.20$).

In order to appreciate the performance of the constitutive equation, the measured dynamic stiffness and the calculated one are plotted at 10 Hz with respect to static deformation in Fig. 12 and Fig. 13. The minus sign in the static displacement means that the specimen is compressed by the test machine. It is interesting to notice that the slope of dynamic stiffness curve has a discontinuity at the point with no static deformation. It is clearly observed that the undeformed state is expressed as a local maximum point in the dynamic stiffness plot. It has been shown in uniaxial tension test of the previous section, that the modulus of rubber decreases with static deformation in the vicinity of the undeformed state. The dynamic stiffness of complex stress-state test specimen is decreased by both pre-applied tension and compression pre-deformation. Thus the dynamic test results have a peak when the specimen is under no prestrain. The constitutive equations without static deformation correction factor cannot describe the peak and anticipate higher dynamic stiffness than the experimental value. The proposed model, however, effectively describes the effects of prestrain that cannot be expressed by conventional constitutive models as shown in the

figures. The dynamic stiffness is plotted against the static deformation at 30 Hz in Fig. 14. It is observed that the proposed constitutive model works well at other frequencies. This result confirms the fact that the static deformation correction factor determined at one frequency is also effective at other frequencies in the tested range.

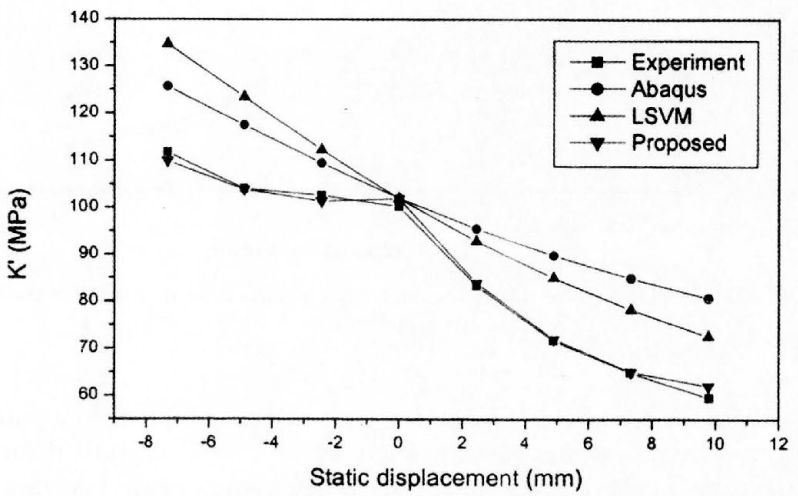

FIG. 12. Real part of complex stiffness against static deformation at 10 Hz for the complex stress specimen.

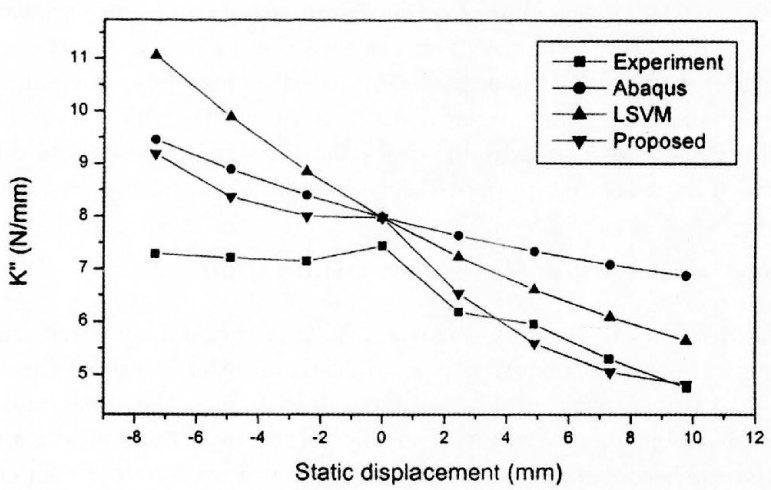

FIG. 13. Imaginary part of complex stiffness against static deformation at 10 Hz for the complex stress specimen.

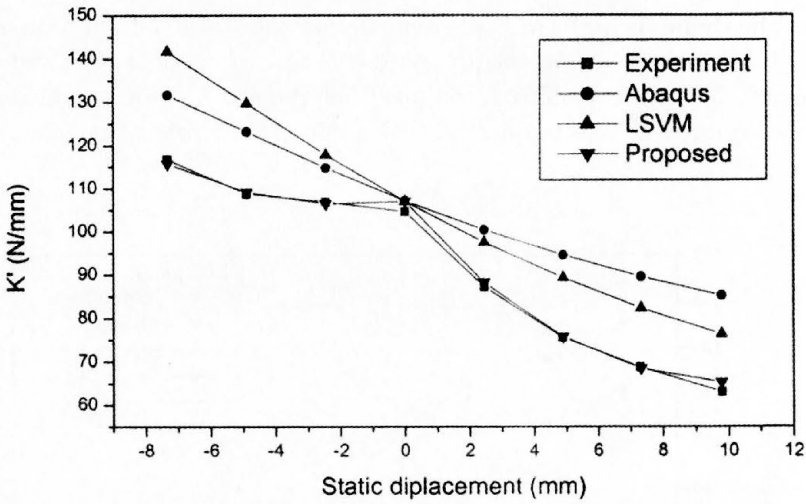

FIG. 14. Real part of complex stiffness against static deformation at 30 Hz for the complex stress specimen.

In prediction of the loss stiffness, the proposed model predicts greater value than the measured result but shows same trend. In case of no static deformation, all constitutive models yield the same value because every model becomes a linear viscoelastic one. The material properties used in the calculation are determined by the uniaxial tension test results. The difference between the computed value and the measured one under no static deformation is caused by material property difference between the test specimens. It is suspected that the material property difference between the specimens comes from curing condition variation during preparation of specimens and the effects caused by adhesive bond between the specimen and fixing plates. There are some experimental difficulties similar to the tension test since imaginary parts of stiffness are very small compared with real part and very sensitive to experimental condition. In spite of these differences, the proposed model shows more precise prediction than the conventional models.

4. Design sensitivity analysis and optimization

In the designs of vibration isolators, both static and dynamic characteristics of rubber must be concurrently considered in order to assure the structural stability and low transmissibility. As mentioned before, the static and dynamic behavior of rubber can be respectively described by a hyperelastic model and a steady-state viscoelastic model. A topology optimization approach can be applied for the shape design of vibration isolator made of filled rubber. For easier application of the optimization algorithm, material property design sensitivity

analyses of both the hyperelastic and viscoelastic constitutive equation are developed for topology optimization using the mean compliance and adjoint variables. In order to consider simultaneously the static and dynamic behavior of rubber, a proper topology optimization formulations should be proposed.

4.1. Design sensitivity analysis of the hyperelastic model

The hyperelastic constitutive equation can be written with the following nonlinear energy form and load linear form:

$$a(r,\bar{r}) = l(\bar{r}), \qquad \forall \bar{r} \in U \times P, \tag{4.1}$$

where U and P are spaces of kinematically admissible virtual displacements and hydrostatic pressure, $r = [u_1, u_2, u_3, p]^T$ is the vector of the displacements and hydrostatic pressure. In this equation, each side can be written with integral terms as follows:

$$a(r,\bar{r}) = \delta\left(\int_V {}_0W + {}_0Q dV\right) = \delta\left(\int_V {}_0W - \frac{1}{2KJ_0}(\bar{p}-\hat{p})^2\, dV\right), \tag{4.2}$$

$$l(\bar{r}) = {}^t\Re = \int_V f\ u\ dV + \int_S T\ u\ dS, \tag{4.3}$$

where ${}_0W$ represents the energy density function. f and T represent the external volumetric and surface forces.

Material property design sensitivity analysis of hyperelastic model was developed [11]. When a structural system with a given design b is in the final equilibrium configuration at time t, the system reaches another equilibrium at time $t + \Delta t$ due to design perturbation $\tau\delta b$.

$$a_{b+\tau\delta b}(r,\bar{r}) = l_{b+\tau\delta b}(\bar{r}), \qquad \forall \bar{r} \in U \times P. \tag{4.4}$$

Since the difference between the final equilibriums of two designs becomes smaller as design perturbation becomes smaller, the first-order variations of the nonlinear energy form and the linear load form with respect to the design variable can be defined as:

$$a'_{\delta b}(r,\bar{r}) = \frac{d}{d\tau} a_{b+\tau\delta b}(\tilde{r},\bar{r})\bigg|_{\tau=0}, \tag{4.5}$$

$$l'_{\delta b}(\bar{r}) = \frac{d}{d\tau} l_{b+\tau\delta b}(\bar{r})\bigg|_{\tau=0}. \tag{4.6}$$

By the chain rule of differentiation, the first order variation of Eq. (4.4) is obtained as:

$$a^*_{\delta b}(r; r', \bar{r}) = l'_{\delta b}(\bar{r}) - a'_{\delta b}(r, \bar{r}). \tag{4.7}$$

Generally, the following static mean compliance can be selected as the static performance measure of the structural system:

$$\psi = \int_V f\, r\, dV. \tag{4.8}$$

If the external force f is independent of the design changes, the first-order variation of the mean compliance is written as follows:

$$\psi' = \int_V f\, r'\, dV. \tag{4.9}$$

Using the adjoint equation, the design sensitivity of static mean compliance is written as:

$$\psi' = -a'_{\delta b}(r,\ r). \tag{4.10}$$

In this equation, the first order variation of energy form with respect to the design variable can be written in terms related to design variables as follows:

$$a'_{\delta b}(r, r) = \int_V \delta\varepsilon : \frac{\partial}{\partial \tau}\Big[\mathscr{D}(b + \tau\delta b)\Big]_{\tau=0} : \varepsilon\, dV + \int_V \frac{\partial}{\partial \tau}\Big[\sigma_0(b + \tau\delta b)\Big]_{\tau=0} : \Delta\delta_0 E\, dV. \tag{4.11}$$

4.2. Design sensitivity analysis of the steady-state viscoelastic model

Introducing the virtual variable, the complex viscoelastic constitutive equation (2.37) is written as the following energy equilibrium equation:

$$a(r^*, \bar{r}^*) = \delta W^* = \Delta\Re^* = l(\bar{r}^*), \qquad \forall \bar{r}^* \in U^* \times P^*, \tag{4.12}$$

where U^* and P^* are spaces of kinematically admissible virtual complex displacements and hydrostatic pressure. The first-order variation of energy equation can be obtained similarly to the static case.

$$a^*_{\delta b}\left(r^*; r^{*'}, \bar{r}^*\right) = l'_{\delta b}(\bar{r}^*) - a'_{\delta b}(r^*, \bar{r}^*). \tag{4.13}$$

In the vibration isolation system, the dynamic performance of the system is the transmissibility from the vibrating systems to the base structures. As shown in Fig. 15 and Fig. 16, the transmissibility of the system has a very similar tendency compared with the dynamic compliance, therefore dynamic compliance can be the dynamic performance measure of structures.

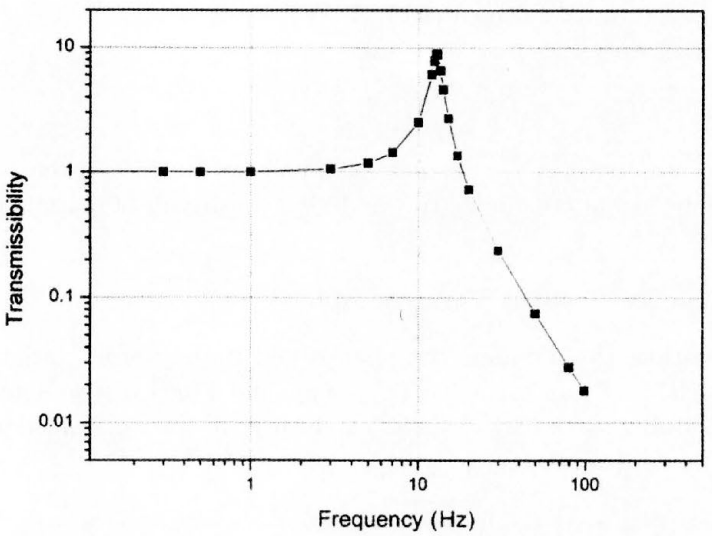

FIG. 15. Transmissibility against vibration frequency.

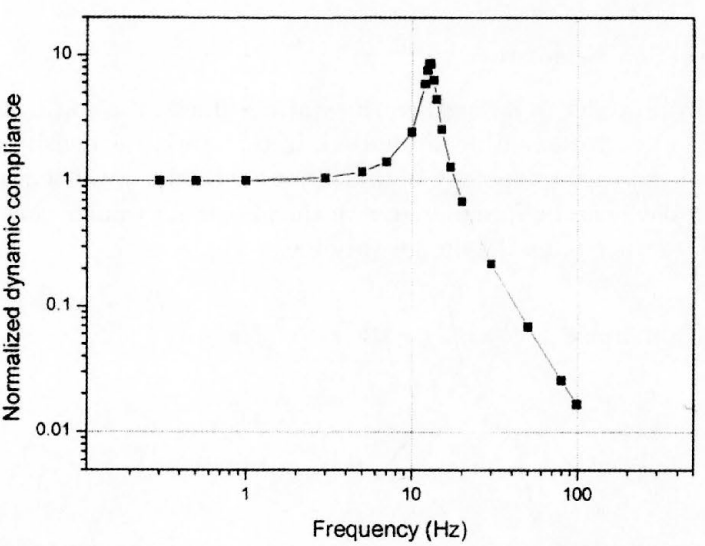

FIG. 16. Normalized dynamic compliance against vibration frequency.

The steady-state dynamic compliance can be defined as:

$$\psi^* = \int_V f^* r^* dV. \tag{4.14}$$

If the vibrating external force f^* is independent of the design changes, the first-order variation is obtained as:

$$\psi^{*'} = \int_V f^* r^{*'} dV. \tag{4.15}$$

The design sensitivity of static mean compliance can be written by using the proper adjoint equation similar to the design sensitivity of static mean compliance,

$$\psi^{*'} = -a'_{\delta b}(r^*, r^*). \tag{4.16}$$

In this equation, the dynamic compliance and its first-order variation are the complex variables defined as $\psi^* = (\psi_1 + i\psi_2)$ and $\delta(\psi^*) = (\delta\psi_1 + i\delta\psi_2)$. Therefore, the following two scalar variables can be used as the real-valued performance measure and its design sensitivity.

$$\|\psi^*\| = \sqrt{\psi_1^2 + \psi_2^2}, \tag{4.17}$$

$$\delta\|\psi^*\| = \frac{1}{2}\left(\psi_1^2 + \psi_2^2\right)^{-1/2}\left(2\psi_1\delta\psi_1 + 2\psi_2\delta\psi_2\right). \tag{4.18}$$

4.3. Optimization formulation

Generally, in order to strengthen the static stiffness, the static mean compliance of the structure should be minimized. In this work, the density distribution approach is used as the topology optimization methodology. The topology optimization problem can be formulated with the maximum volume constraint using the element density η_i as the design variable.

$$\begin{aligned} &\text{minimize} \quad \psi = \int_V f\ r\ dV = \sum_j^{N_f} f_j u_j, \\ &\text{subject to} \quad \int_V \eta dV = \sum_i^{nel} \eta_i V_i^e \le V_{\max}, \qquad 0 \le \eta_i \le 1. \end{aligned} \tag{4.19}$$

In the optimization for transmissibility, we can use the dynamic compliance as the objective function and then the optimization problem can be formulated as

follows. In order to minimize the transmissibility, the dynamic mean compliance should be minimized. The volume constraint must be reversed to minimum value because the structure will become very flexible in view of low force transmission.

$$\begin{aligned} &\text{minimize} \quad \psi = \|\psi^*\| = \left\| \int_V f^* r^* \, dV \right\| = \left\| \sum_j^{N_f} f_i^* u_i^* \right\|, \\ &\text{subject to} \quad \int_V \eta \, dV = \sum_i^{nel} \eta_i V_i^e \geq V_{\min}, \quad 0 \leq \eta_i \leq 1. \end{aligned} \tag{4.20}$$

In order to make an isolator endure the static loadings and reduce the force transmission, the static and dynamic compliance of the structure should be simultaneously considered. Multi-objective optimization can be used for this problem, but the sensitivity differences of static and dynamic compliance cause some difficulties. In this paper, the dynamic compliance is minimized with the maximum static compliance constraint as well as the volume constraint. Such topology optimization problem can be formulated as:

$$\begin{aligned} &\text{minimize} \quad \psi = \|\psi^*\| = \left\| \int_V f^* \, r^* \, dV \right\| = \left\| \sum_j^{N_f} f_i^* u_i^* \right\|; \\ &\text{subject to} \quad h_1 = \int_V f \, r \, dV - C_{\max} = \sum_j^{N_f} f_i u_i - C_{\max} \leq 0, \\ &\qquad h_2 = \int_V \eta \, dV - V_{\max} = \sum_i^{nel} \eta_i V_i^e - V_{\max} \leq 0 \, , \\ &\qquad h_3 = V_{\min} - \int_V \eta \, dV = V_{\min} - \sum_i^{nel} \eta_i V_i^e \leq 0, \\ &\qquad 0 \leq \eta_i \leq 1. \end{aligned} \tag{4.21}$$

As mentioned before, the density distribution approach is selected and the design densities indicating the material existence are used as design variables. In order to assure the existence and uniqueness of a solution, a relaxed and penalized artificial material model is selected. The relation between the elastic modulus and the design density in this artificial material model is represented by the following equation and its characteristics are presented in Fig. 17. As parameter α increases, the relation becomes more penalized.

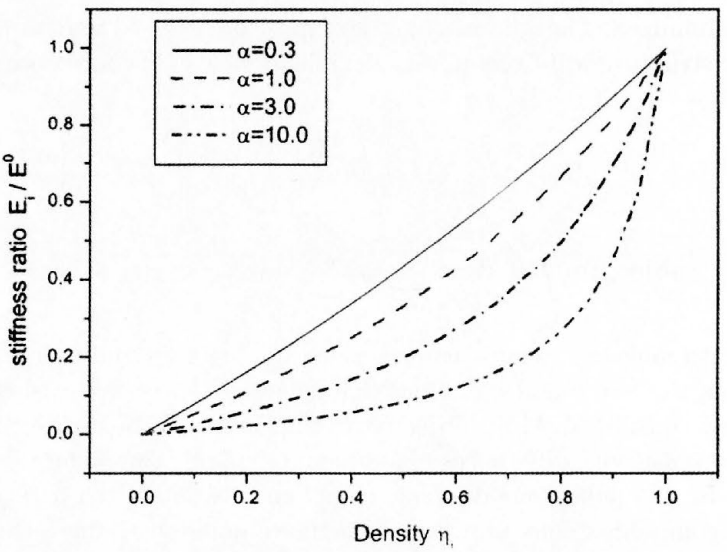

FIG. 17. Characteristics of artificial material model.

$$E_i = \frac{\eta_i}{1 + \alpha(1 - \eta_i)} E_i^0. \tag{4.22}$$

In this work, the three-dimensional quadratic hybrid elements are used in FE analysis for each static and steady-state dynamic problem. The hybrid elements have 27 displacement-nodes and 4 hydrostatic pressure degrees of freedom for the treatment of incompressible or nearly incompressible behavior. Therefore the locking phenomena and checkerboard pattern can be effectively removed. And also the continuation methods for volume and static compliance constraints are used in order to prevent the local minima. A sequentially linear programming (SLP) algorithm is selected as the optimization algorithm, which updates the design variable to improve the performance of structures.

5. Design examples

A simple structure shown in Fig. 18 is selected as a numerical example to demonstrate this approach. A natural rubber filled 70 phr carbon black is applied as the isolator material and steel (ASTM A36) is selected as a non-design mass material. A mass to be isolated is located on the top center surface of rubber. A large static deformation is generated by self-weight of the mass and external vibrating forces are vertically applied to the mass center. The volume constraint for design is set to 50% for all following problems.

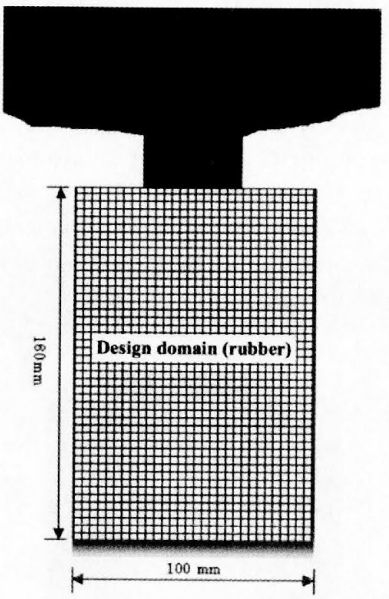

FIG. 18. Schematic diagram of simple structure problem ($t = 10\,\text{mm}$).

At first, the static design result for minimizing the static compliance and obtaining the highest stiffness is shown in Fig. 19. A very stiff structure within the given volume constraint was obtained and this structure is strong enough to endure the large static load. For the design problem to minimize the transmis-

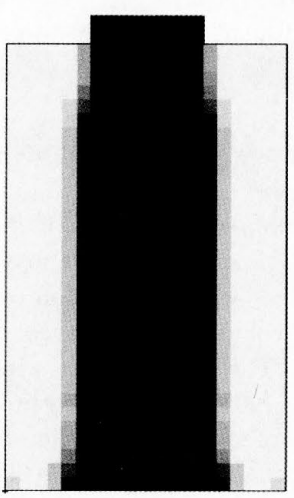

FIG. 19. Maximum static stiffness design of simple structure problem.

sibility for 20 Hz vibrating frequency, a very flexible structure is obtained and shown in Fig. 20. This structure has a very small natural frequency and shows very low transmissibility, however it is too weak to endure the self-weight of the mass. It is obvious that the static stiffness compared to the mass is very small because of a large cavity under the mass. If this design is applied for isolator, very large static deformations may be generated by self-weight of mass and the structure may become unstable due to small disturbances. Therefore it is impossible that the design results considering only the dynamic behavior of rubber could be applied to vibration isolator.

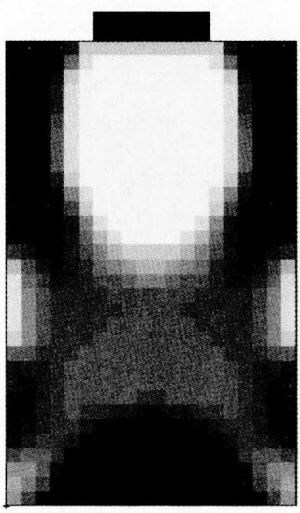

FIG. 20. Minimum transmissibility design of simple structure problem ($f = 20$ Hz).

For this reason, the static and dynamic behavior of rubber must be simultaneously considered in the design process of anti-vibration rubber. A topology optimization process to minimize the dynamic compliance with the static compliance constraint as well as volume constraint is attempted. During iteration of the optimization, structure may become flexible in order to minimize the dynamic compliance and then a large deformation occurs with the element distortions. The continuation of volume and static constraints is applied to avoid this mesh-distortion problem. The design result within 120% static constraint is represented in Fig. 21. The 120% static constraint means that the structure can be deformed within 120% of static deformation of maximum static stiffness design. The obtained result shows a complex truss-like structure. As represented in Table 3, this structure has a sufficient stiffness for static loading by the mass and shows about 20% lower transmissibility compared to the static stiffness de-

sign. On the contrary, the static deformation due to static loading increases by about 20%. We can conclude that the proposed design method is effective for vibration isolator design.

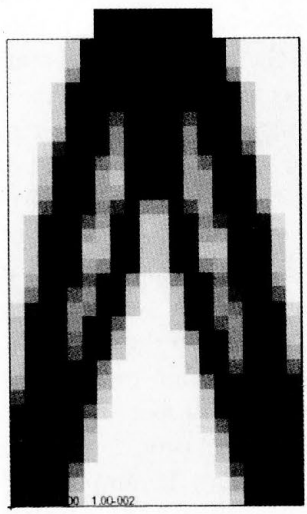

FIG. 21. Simultaneous design result of simple structure problem ($f = 20\,\text{Hz}$, 120% static compliance constraint).

Table 3. Design results of simple structure problem.

Design method	Static design	Dynamic design	Simultaneous design
Static compliance	0.1990635E+00	Not available	0.2401379E+00
Transmissibility	0.1577919E+00	0.2596466E-02	0.1262678E+00
Dynamic compliance	0.1181939E-05	0.1030806E-05	0.1151566E-05

6. Conclusions

A constitutive model, FE formulation and topology optimization for rubber that is under small oscillatory loads superimposed on large static deformation was discussed. The constitutive model was proposed and implemented in a finite element code to calculate the behavior of rubber under complicated loading conditions. Updated Lagrangian formulation with displacement–pressure mixed

method was used to treat the incompressible large deformation problem. Dynamic tests under specified loading conditions were executed in order to verify the proposed constitutive model. Complex stress-state tests are included in the dynamic tests to verify the model under multi-axial stress states. The results computed by the FEA code were compared with the test results to estimate the performance of the model. In the complex stress-state test, it is clearly observed that the undeformed state is expressed as a local maximum point in the dynamic stiffness plot. The proposed model successfully predicts the peak point and its computed results agree well with the experimental ones.

For the stability and low transmissibility of isolation systems, a topology optimization method was proposed considering both the static and dynamic performance. Material property design sensitivity analysis of the hyperelastic model and steady-state viscoelastic one were developed using the mean compliance and adjoint variables. A simple design example was presented and design results showed that the proposed design process could simultaneously consider the static and dynamic behavior of rubber with adequate constitutive models.

The amplitude of dynamic deformation generally affects the dynamic stiffness (Payne effect). It is anticipated that the amplitude effects increase with larger strain amplitude and amplitude variation. As a future work, we are now trying to include the Payne effect in our constitutive equation and consider more realistic loading conditions for the isolator design.

Acknowledgment

This work was supported by grant No.R01-2001-000-00393 from the Basic Research Program of the Korea Science & Engineering Foundation.

References

1. J. I. SULIVAN, K. N. MORMAN and R. A. PETT, *A non-linear viscoelastic characterization of a natural rubber gum vulcanizate*, Rubber Chemistry and Technology, **53**, 805–822, 1980.

2. K. N. MORMAN Jr and J. C. NAGTEGAAL, *Finite element analysis of sinusoida small-amplitude vibrations in deformed viscoelastic solids. Part I: theoretical development*, International Journal For Numerical Methods in Engineering, **19**, 1079–1103, 1983.

3. A. B. ZDUNEK, *Theory and computation of the steady state harmonic response of viscoelastic rubber parts*, Computer Methods in Applied Mechanics and Engineering, **105**, 63–92, 1993.

4. A. B. ZDUNEK, *Determination of material response functions for prestrained rubbers*, Rheologica Acta, **31**, 575–591, 1992.

5. HIBBIT, KARLSSON and SORENSON INC., *ABAQUS theory manual*, Version 5.7. 997.

6. A. VOET and J.C. MORAWSKI, *Dynamic mechanical and electrical properties of vulcanizates at elongations up to sample rupture*, Rubber Chemistry and Technology, **47**, 765–777, 1974.

7. P. MASON, *The viscoelastic behavior of rubber in extension*, Journal of Applied Polymer Science, **1**, 1, 63–69, 1959.

8. O. KRAMER, S. HVIDT and J.D. FERRY, *Dynamic mechanical properties*, [in:] J.E. MARK *et al.* [Ed.] Science and Technology of Rubber, Academic Press, San Diego 1994.

9. B.K. KIM and S.K. YOUN, *A viscoelastic constitutive model of rubber under small oscillatory loads superimposed on large static deformation*, Archive of Applied Mechanics, **71**, 11, 748–763, 2001.

10. Y. YU, N.G. NAGANATHAN and R.V. DUKKIPATI, *A literature review of automotive vehicle engine mounting systems*, Mechanism and Machine Theory, **36**, 123–142, 2001.

11. K.K. CHOI and W. DUAN, *Design sensitivity analysis and shape optimization of structural components with hyperelastic material*, Computer Methods in Applied Mechanics and Engineering, **187**, 219–243, 2000.

12. J.J. KIM and H.Y. KIM, *Shape design of an engine mount by a method of parameter optimization*, Computers and Structures, **65**, 5, 725–731, 1997.

13. S.H. KI and S.M. WANG, *Topology optimization of hyperelastic material*, Proceedings of 4th world congress of structural and multidisciplinary optimization, June 4-8 2001, Dalian, China.

14. J.C. SIMO, *A fully three-dimensional finite-strain viscoelastic damage model: formulation and computational aspects*, Computer Methods in Applied Mechanics and Engineering, **60**, 153–173, 1987.

15. R.M. CHRISTENSEN, *Theory of viscoelasticity*, Academic Press, New York 1982.

16. C. TRUESDELL and W. NOLL, *The nonlinear field theories of mechanics*, [in:] Encyclopedia of Physics, S. FLÜGGE [Ed.], Springer-Verlag, New York 1965.

17. G D. JUNG, S.K. YOUN and B.K. KIM, *A three-dimensional nonlinear viscoelastic constitutive model of solid propellant*, International Journal of Solids and Structures, **37**, 4715–4732, 2000.

18. T. SUSSMAN and K.J. BATHE, *A finite element formulation for nonlinear incompressible elastic and inelastic analysis*, Computers & Structures, **26**, 1/2, 357–409, 1987.

19. R.P. BROWN, *Physical testing of rubber*, Chapman & Hall, London, 3rd [Ed.], 1996.

Received December 5, 2002; revised version July 25, 2003.

Arch. Mech., **55**, 5–6, pp. 481–499, Warszawa 2003

Mesoscopic theory of microcracks

C. PAPENFUSS[1], P. VÁN[2], W. MUSCHIK[3]

[1] *Technische Universität Berlin*
Institut für Mechanik
Straße des 17. Juni
10623 Berlin

[2] *Budapest University of Technology and Economics*
Department of Chemical Physics
1521 Budapest, Budafoki út 8

[3] *Technische Universität Berlin*
Institut für Theoretische Physik
Hardenbergstr. 36
10623 Berlin

THE MESOSCOPIC CONCEPT is a way to deal with complex materials with an internal structure within continuum mechanics. It consists of extending the domain of the balance equations by mesoscopic variables and of introducing a local distribution function of these variables as a statistical element. In our case microcracks are modelled as penny-shaped and are completely characterized by their diameter and the unit normal to the crack surface. Two examples of crack dynamics are given as well as a possible definition of a damage parameter. Orientational order parameters (fabric-alignment tensors) are defined and balance-like dynamic equations for them are derived.

1. A model of microcracks

MACROSCOPIC FAILURE OF BRITTLE materials is initiated by the propagation of microcracks. In a simple model the microcrack is described as a flat, rotationally symmetric surface, a so-called penny-shaped crack. In addition we make here the following simplifying assumptions:

1. The diameter of the cracks is much smaller than the linear dimensions of the continuum element. Under this assumption the cracks can be treated as an internal structure of the continuum element. The cracks are assumed to be small enough so that there is a whole distribution of crack sizes and orientations in the volume element.
2. The cracks are fixed to the material. Therefore their motion is coupled to the motion of representative volume elements.

3. The cracks cannot rotate independently of the material, i.e. if they have a nonzero rotation velocity at all, this rotation velocity is determined by the antisymmetric part of the time derivative of the deformation gradient of the surrounding material and it does *not* depend on crack length and orientation. All cracks within a volume element move and rotate with the same velocity.
4. The number of cracks is fixed, there is no production of cracks, but very short cracks are preexisting in the virgin material.
5. The cracks cannot decrease their area, but can only enlarge, meaning that cracks cannot heal.

To summarize our model, the microcrack is characterized by a unit vector $\mathbf{n}$ representing the orientation of the surface normal and by the radius l of the circular crack surface. These parameters will be taken as the additional variables in the mesoscopic theory.

2. Different approaches to damage mechanics and the mesoscopic concept

There are two principally different possibilities to deal with complex materials within continuum mechanics: the first way is to introduce additional fields depending on position and time. These fields can be any kind of internal variables [1, 2], or damage parameters [3, 4], and damage tensors (fabric tensors) [5, 6]. In damage mechanics such additional macroscopic variables have been introduced in many different cases of materials with internal structure like liquid crystals [7, 8], polymer solutions [9, 10] and others. The other way is a so-called mesoscopic theory. The idea is to enlarge the domain of the field quantities by an additional variable, characterizing the internal degree of freedom connected with the internal structure of the material. Field quantities are introduced, which are defined on an enlarged space $\mathbb{R}^3_x \times \mathbb{R}_t \times M$. The manifold M is given by the set of values the internal degrees of freedom can take. In our case the internal degrees of freedom are the different sizes l and orientations $\mathbf{n}$ of microcracks. We call this way of dealing with the internal structure of complex materials a mesoscopic theory, because it includes more information than a macroscopic theory on $\mathbb{R}^3_x \times \mathbb{R}_t$, but less than a microscopic one on the molecular level. The domain of the mesoscopic field quantities $\mathbb{R}^3_x \times \mathbb{R}_t \times M$ is called the mesoscopic space.

Macroscopic quantities are calculated from mesoscopic ones as averages over crack sizes and crack orientations. The spatial distribution of cracks is not relevant in the sense that the resulting macroscopic quantities are still field quantities depending on position and time. For a treatment of the spatial distribution of cracks and a possible coarsening process see [11].

In contrast to spatial averaging introduced in [12], a nonlocal generalization of the classical Weibull theory, the averages in mesoscopic theory are local in space. They are averages over different microcrack sizes and orientations in a volume element.

Scaling properties [13] are completely out of scope of the whole mesoscopic theory. They result from microscopic statistical considerations. Statistical theories of fracture describe the breakdown of material as a second order phase transition [14, 13], as well as a first order phase transition [15–17].

We will apply now the mesoscopic concept to a damaged material with microcracks. The crack length can take values between a minimal length l_m of the smallest preexisting cracks and a maximal length l_M, which is limited by the linear dimension of the continuum element. The orientation of the unit vector $\mathbf{n}$ can be given by an element of the unit sphere S^2. Therefore in the example of microcracks the manifold M is given by $[l_m, l_M] \times S^2$. The change velocities of the mesoscopic variables $\dot{l}$ and $\mathbf{u} := \dot{\mathbf{n}}$ are defined in such a way that for $\Delta t \to 0$ we have

$$l(t + \Delta t) = l(t) + \dot{l}\Delta t\,, \qquad \mathbf{n}(t + \Delta t) = \mathbf{n}(t) + \mathbf{u}\Delta t \tag{2.1}$$

at later times $t + \Delta t$. The rotation velocity $\mathbf{u}$ and the length change velocity $\dot{l}$ are the components in spherical coordinates of the crack velocity $\mathbf{v}_l$ introduced in [18]. In this previous paper [18] the set of additional mesoscopic variables $\mathbf{n}$ and l was called directional variable.

Beyond the use of additional variables, the mesoscopic concept introduces a statistical element, the so-called mesoscopic distribution function. In our case this is a distribution of crack lengths and orientations in the continuum element at position $\mathbf{x}$ and time t, called here crack distribution function (CDF). The distribution function is the probability density of finding a crack of length l and orientation $\mathbf{n}$ in the continuum element.

3. Mesoscopic balance equations

Now such fields as mass density, momentum density, angular momentum density, and energy density are defined on the mesoscopic space. For distinguishing these fields from the macroscopic ones we add the word "mesoscopic". In addition we introduce the crack number density N as an extensive quantity. The mesoscopic crack number density $N(l, \mathbf{n}, \mathbf{x}, t)$ is the number density, counting only cracks of length l and orientation $\mathbf{n}$. For this crack number density there is a balance equation too, as it is an extensive quantity. The crack number density can be prescribed independently of the mass density, although the motion of cracks is coupled to the motion of surrounding material in our model. Therefore

we distinguish here between the two fields: mass density ρ and number density N, although they have the same equation of motion and were not distinguished in an earlier paper [18].

3.1. Definition of the distribution function

Due to its definition as probability density, the distribution function is the number fraction

$$f(l, \mathbf{n}, \mathbf{x}, t) = \frac{N(l, \mathbf{n}, \mathbf{x}, t)}{N(\mathbf{x}, t)}, \tag{3.1}$$

in volume elements, where the number density $N(\mathbf{x}, t)$ is non-zero. Here $N(\mathbf{x}, t)$ is the macroscopic number density of cracks of any length and orientation. Since the distribution function in Eq. (3.1) is not well defined if $N(\mathbf{x}, t) = 0$, we define in addition that in this case $f(l, \mathbf{n}, \mathbf{x}, t) = 0$. Since there is no creation of cracks in our model, the distribution function will be zero for all times in these volume elements. In all other volume elements with a nonzero crack number it is normalized

$$\int_{l_m}^{l_M} \int_{S^2} f(l, \mathbf{n}, \mathbf{x}, t) l^2 d^2 n dl = 1 . \tag{3.2}$$

3.2. Balance equations of mass, momentum, angular momentum, and energy

For the mesoscopic densities the local balance equations have been derived from the macroscopic global ones [18–21]. The macroscopic balance equations express the fact that the extensive macroscopic quantities within a region G can change due to a flux over the boundary ∂G and due to production and supply within G. This results in the general form of a global balance equation

$$\frac{d}{dt} \int_G \mathbf{X} d^3x d\mathbf{n} l^2 dl = \int_{\partial G} \varphi_{\mathbf{X}}(\cdot) da + \int_G \Sigma_X(\cdot) d^3x d\mathbf{n} l^2 dl . \tag{3.3}$$

A generalized Reynolds transport theorem on the mesoscopic space, analogous to the one in [22], is used to transform the time derivative, and a generalized Gauss theorem is applied. The boundary ∂G of G consists of parts in the position space, in the orientation space, and in the length interval. In regular points of the continuum we get the general form of a local mesoscopic balance equation [18] with the abbreviation $(\cdot) = (l, \mathbf{n}, \mathbf{x}, t)$:

$$\frac{\partial}{\partial t}\mathbf{X}(\cdot) + \nabla_x \cdot [\mathbf{v}(\cdot)\mathbf{X}(\cdot) - \mathbf{S}(\cdot)] + \nabla_n \cdot [\mathbf{u}(\cdot)\mathbf{X}(\cdot) - \mathbf{R}(\cdot)] + \frac{1}{l^2}\frac{\partial}{\partial l}\left(l^2 \dot{l}(\cdot)\mathbf{X}(\cdot) - \mathbf{R}_l(\cdot)\right) = \Sigma(\cdot),$$

where $\mathbf{R}$ and $\mathbf{R}_l$ are the non-convective fluxes over the orientational and length part of the boundary of G, and G is a region in $\mathbb{R}^3 \times S^2 \times [l_m, l_M]$. The derivative with respect to the mesoscopic variable $(l, \mathbf{n})$ is represented in spherical coordinates. In the derivation of the local balance equation it has been supposed that there is no flux over the boundary of the total mesoscopic space:

$$\int_{-\infty}^{\infty} \int_{S^2} \int_{l_m}^{l^M} \nabla \cdot \varphi_{\mathbf{X}}(\cdot) d^3x d\mathbf{n} l^2 dl = 0. \tag{3.4}$$

Otherwise such a non-zero flux term (3.4) could be interpreted as an additional source term on the right-hand side of the equation.

Explicitly we have:

Balance of mass

$$\frac{\partial}{\partial t}\varrho(\cdot) + \nabla_x \cdot \{\varrho(\cdot)\mathbf{v}(\mathbf{x}, t)\} + \nabla_n \cdot \{\varrho(\cdot)\mathbf{u}(\mathbf{x}, t)\} + \frac{1}{l^2}\frac{\partial}{\partial l}\left(l^2 \dot{l}\varrho(\cdot)\right) = 0. \tag{3.5}$$

Balance of momentum

$$\frac{\partial}{\partial t}[\varrho(\cdot)\mathbf{v}(\mathbf{x}, t)] + \nabla_x \cdot \left[\mathbf{v}(\mathbf{x}, t)\varrho(\cdot)\mathbf{v}(\mathbf{x}, t) - \mathbf{t}^\top(\cdot)\right] + \nabla_n \cdot \left[\mathbf{u}(\mathbf{x}, t)\varrho(\cdot)\mathbf{v}(\mathbf{x}, t) - \mathbf{T}^\top(\cdot)\right] + \frac{1}{l^2}\frac{\partial}{\partial l}\left(l^2 \dot{l}\varrho(\cdot)\mathbf{v}(\mathbf{x}, t) - \boldsymbol{\tau}(\cdot)\right) = \varrho(\cdot)\mathbf{f}(\cdot). \tag{3.6}$$

Here $\mathbf{f}(\cdot)$ is the external acceleration density, $\mathbf{t}^\top(\cdot)$ the transposed mesoscopic stress tensor, and $\mathbf{T}^\top(\cdot)$ the transposed stress tensor on orientation space (non-convective momentum flux in orientation space), $\boldsymbol{\tau}(\cdot)$ is the momentum flux vector with respect to the crack length variable. We introduced already the assumption that the material velocity $\mathbf{v}$ and the rotational velocity $\mathbf{u}$ are the same for cracks of all orientations and lengths.

Angular momentum

The balance of angular momentum has to be taken into account as an additional equation independent of the balance of momentum, because there is an

internal angular momentum due to crack rotations. The total angular momentum

$$\mathbf{S}(\mathbf{x},t) := \mathbf{x} \times \mathbf{v}(\mathbf{x},t) + \mathbf{s}(\cdot) \tag{3.7}$$

is the sum of the moment of momentum and the internal angular momentum.

$$\begin{aligned} \frac{\partial}{\partial t}[\varrho(\cdot)\mathbf{S}(\cdot)] + \nabla_x \cdot \left[\mathbf{v}(\mathbf{x},t)\varrho(\cdot)\mathbf{S}(\cdot) - (\mathbf{x} \times \mathbf{T}(\cdot))^\top - \mathbf{\Pi}^\top(\cdot)\right] \\ + \nabla_n \cdot \left[\mathbf{u}(\mathbf{x},t)\varrho(\cdot)\mathbf{S}(\cdot) - (\mathbf{x} \times \boldsymbol{\tau}(\cdot))^\top - \boldsymbol{\pi}^\top(\cdot)\right] \\ + \frac{1}{l^2}\frac{\partial}{\partial l}\left(l^2 \dot{l}\varrho(\cdot)\mathbf{S}(\cdot) - \boldsymbol{\omega}(\cdot)\right) = \varrho(\cdot)\mathbf{x} \times \mathbf{k}(\cdot) + \varrho(\cdot)\mathbf{g}. \end{aligned} \tag{3.8}$$

Here $\mathbf{n} \times \mathbf{g}$ is the vector of couple forces (acting on crack orientation), the tensor $\mathbf{\Pi}$ is the surface torque, and $\boldsymbol{\pi}$ is the analogue with respect to orientation, and ω is the analogue with respect to crack length. These constitutive quantities appear in the non-convective fluxes in the position space, orientation space, and in the length interval, respectively. This equation can be simplified with the assumptions that the material velocity and the rotation velocity depend only on position and time $\mathbf{v}(\mathbf{x},t)$ and $\mathbf{u}(\mathbf{x},t)$.

However, the spin is only relevant, if the model allows for crack rotations independently of the rotations of material elements, and this is not the case in our simplified example dynamics.

Similarly the balance of energy can be given, which is omitted here and can be found in [18]. In all balance equations, in addition to the flux with respect to the position variable, there appear additional flux terms with respect to the additional mesoscopic variables crack orientation and length.

Balance of crack number

In our model the cracks move together with the material element. Therefore their flux is the convective flux, having a part in position space, a part in orientation space, and a part in the length interval. There is no production and no supply of crack number. Therefore we have for the crack number density N:

$$\frac{\partial}{\partial t}N(\cdot) + \nabla_x \cdot \{N(\cdot)\mathbf{v}(\mathbf{x},t)\} + \nabla_n \cdot \{N(\cdot)\mathbf{u}(\mathbf{x},t)\} + \frac{1}{l^2}\frac{\partial}{\partial l}\left(l^2 \dot{l} N(\cdot)\right) = 0. \tag{3.9}$$

In a fixed volume element this crack number density is proportional to the mass density, and therefore these two fields were not distinguished in an earlier paper [18].

We obtain from the mesoscopic balance of crack number density (3.9) a balance of the CDF $f(l, \mathbf{n}, \mathbf{x}, t)$, by inserting its definition (3.1):

$$\begin{aligned}(3.10)\qquad &\frac{\partial}{\partial t} f(l, \mathbf{n}, \mathbf{x}, t) + \nabla_x \cdot (\mathbf{v}(\mathbf{x}, t) f(l, \mathbf{n}, \mathbf{x}, t)) \\ &\quad + \nabla_n \cdot (\mathbf{u}(\mathbf{x}, t) f(l, \mathbf{n}, \mathbf{x}, t)) + \frac{1}{l^2} \frac{\partial}{\partial l} \left(l^2 \dot{l} f(l, \mathbf{n}, \mathbf{x}, t) \right) \\ &\quad = \frac{-f(l, \mathbf{n}, \mathbf{x}, t)}{N(\mathbf{x}, t)} \left(\frac{\partial}{\partial t} + \mathbf{v}(\mathbf{x}, t) \cdot \nabla_x \right) N(\mathbf{x}, t) \\ &\quad = \frac{-f(l, \mathbf{n}, \mathbf{x}, t)}{N(\mathbf{x}, t)} \frac{dN(\mathbf{x}, t)}{dt} = 0.\end{aligned}$$

The right-hand side is equal to zero, as for the co-moving observer the total number of cracks in a volume element does not change in time, as in our model no cracks are created. In our model all cracks in a volume element move with the translational velocity of the volume element $\mathbf{v}(\mathbf{x}, t)$ and rotate with the velocity $\mathbf{u} = \nabla \times \mathbf{v}(\mathbf{x}, t)$. Therefore the first three terms on the left-hand side can be summarized as a co-moving time derivative of the distribution function (the time derivative of an observer moving with the material elements) with the abbreviation d^c/dt:

$$\begin{aligned}(3.11)\qquad &\frac{\partial}{\partial t} f(l, \mathbf{n}, \mathbf{x}, t) + \mathbf{v}(\mathbf{x}, t) \cdot \nabla_x f(l, \mathbf{n}, \mathbf{x}, t) + \mathbf{u}(\mathbf{x}, t) \cdot \nabla_n f(l, \mathbf{n}, \mathbf{x}, t) \\ &\quad = \frac{d^c f(l, \mathbf{n}, \mathbf{x}, t)}{dt}.\end{aligned}$$

If we assume in addition an incompressible motion $\nabla_x \cdot \mathbf{v} = 0$, we end up with the equation of motion for the CDF:

$$(3.12)\qquad \frac{d^c f(l, \mathbf{n}, \mathbf{x}, t)}{dt} + \frac{1}{l^2} \frac{\partial}{\partial l} \left(l^2 \dot{l} f(l, \mathbf{n}, \mathbf{x}, t) \right) = 0.$$

This is not yet a closed differential equation for the CDF as long as no expression for the length change velocity of the crack $\dot{l}$ is given. An example of such a closed equation will be discussed later.

Macroscopic quantities are obtained from mesoscopic ones as averages with the CDF as probability density:

$$(3.13)\qquad A(\mathbf{x}, t) = \int_{l_m}^{l_M} \int_{S^2} A(l, \mathbf{n}, \mathbf{x}, t) f(l, \mathbf{n}, \mathbf{x}, t) d^2 n l^2 dl.$$

Entropy balance

Besides these mesoscopic balances, the entropy balance is necessary for introducing the second law of thermodynamics. Because the production of mesoscopic entropy is not necessarily positive for each crack length and orientation, the entropy balance is only interesting in its macroscopic form

$$\frac{\partial}{\partial t}[\varrho(\mathbf{x},t)\eta(\mathbf{x},t)] + \nabla_x \cdot [\varrho(\mathbf{x},t)\eta(\mathbf{x},t)\mathbf{v}(\mathbf{x},t) + \boldsymbol{\phi}(\mathbf{x},t)] = \varrho(\mathbf{x},t)\sigma(\mathbf{x},t) \tag{3.14}$$

(η = specific entropy density, $\boldsymbol{\phi}$ = entropy flux density, σ = entropy production density). The second law is expressed by the *dissipation inequality*

$$\sigma(\mathbf{x},t) \geq 0. \tag{3.15}$$

The set of balance equations is not a closed system of equations, constitutive equations for mesoscopic quantities are needed. The domain of the constitutive mappings is the state space; here a mesoscopic one. There are the possibilities that the mesoscopic state space includes *only* mesoscopic quantities, or that it includes mesoscopic *and* macroscopic quantities, and there are examples where such mixed state spaces cannot be avoided [23]. (For instance in the case of liquid crystals the macroscopic alignment tensor is included in a mesoscopic state space. This is necessary to account for the orienting mean field of surrounding ordered particles. Otherwise it is not possible to describe the phase transition from the isotropic phase to the ordered liquid crystalline phase) Constitutive equations have to be such that the second law of thermodynamics is fulfilled by any solution of the macroscopic balance equations with the constitutive equations inserted [24]. This requirement restricts the possible constitutive functions.

Finally, even for the exploitation of the dissipation inequality, which is possible only on the macroscopic level, the choice of variables can be motivated by the mesoscopic background [25, 26]. A relevance of these variables could not be guessed from a purely macroscopic theory.

4. Damage parameter and order parameters

4.1. Definition of a damage parameter

The damage parameter is introduced as a macroscopic quantity growing with progressive damage in such a way that it should be possible to relate the change of material properties to the growth of the damage parameter. We define the damage parameter as the fraction of cracks, which have reached a certain length L. The idea is that cracks of this and larger sizes considerably decrease the strength

of the material, and therefore their fraction is a measure of the damage. This idea is related to the slender bar model of KRAJCINOVIC [5] (especially useful in one-dimensional crack problems), where the damage parameter is introduced as the number of "broken bars" in the sample,

$$D(\mathbf{x},t) = \int_L^{\infty} \int_{S^2} f(l,\mathbf{n},\mathbf{x},t) d^2n l^2 dl. \tag{4.1}$$

In this definition of the damage parameter the possibility of cracks of any length ($l_M \to \infty$) is included. This is consistent with many possible laws of crack growth, where the crack does not stop growing.

More sophisticated definitions, taking into account the orientational distribution too, are possible and will be discussed elsewhere. Another measure of damage which could be introduced is the average crack length [27].

4.2. Length order parameters

From the mesoscopic distribution function two different kinds of moment series can be built because of the dependence on crack length and on crack orientation. We can introduce moments of the distribution function with respect to crack length:

$$\int_{l_m}^{l_M} f(l,\mathbf{n},\mathbf{x},t) P_k(l) l^2 dl =: p_k(\mathbf{n},\mathbf{x},t), \tag{4.2}$$

where $P_k(l)$ are polynomials being orthogonal with respect to the measure $l^2 dl$:

$$\int_{l_m}^{l_M} P_i(l) P_j(l) l^2 dl = \delta ij. \tag{4.3}$$

The moments introduced in Eq. (4.2) still depend on crack orientation. Averaging over all orientations gives macroscopic fields, the length order parameters:

$$\pi_k(\mathbf{x},t) = \int_{S^2} P_k(\mathbf{n},\mathbf{x},t) d^2n. \tag{4.4}$$

In the following we will investigate the moments of the distribution function with respect to crack orientation.

4.3. Orientational order parameters

We can introduce the following set of alignment-fabric tensors of successive tensorial order

$$a^{(k)}(\mathbf{x},t) := \int_{l_m}^{l_M}\int_{S^2} f(l,\mathbf{n},\mathbf{x},t)\ \overbrace{\mathbf{n}\circ\ldots\circ\mathbf{n}}^{k}\ l^2 dl d^2n, \tag{4.5}$$

where $\overbrace{\ldots}$ denotes the symmetric irreducible part of a tensor [28]. Renarkable, that only the even order tensors appear in the series because the microcracks are represented by axial vectors, the unit normal to the crack surface, i.e. $\mathbf{n}$ and $-\mathbf{n}$ are not distinguished. Due to this symmetry all odd order moments vanish. The tensors defined above are macroscopic quantities. We want to call them alignment-fabric-tensors. Originally tensorial damage parameters were introduced on a purely statistical ground, without a mesoscopic foundation and were called "fabric tensors of the second kind" in damage mechanics (see KANATANI [6] or KRAJCINOVIC [5]). The alignment-fabric-tensors represent the orientational distribution of microcracks, but do not take into account their lengths. They have to be distinguished from the scalar damage parameter which is a measure of the growth of cracks. These alignnent-fabric tensors form a whole set of internal variables in the sense of thernodynamics.

The alignment-fabric tensors are a measure of the deviation of the crack orientation distribution from isotropy. They are all zero, if all crack orientations are equally probable, and at least some alignment-fabric tensors are nonzero in case of anisotropic distributions. The orientation distribution of cracks and therefore the alignment-fabric tensors become important in the dynamics of the crack distribution. There are usually the specimen geometry and loading conditions rotation symmetric around an axis $\mathbf{d}$ (uniaxial conditions). It is reasonable to assume that also the distribution of crack orientations is rotationally symmetric around the same axis $\mathbf{d}$. Then, for symmetry reasons, all alignment-fabric tensors of different orders can be expressed in terms of scalar orientational order parameters $S^{(k)}$ and the unit vector $\mathbf{d}$ in the following way:

$$a^{(k)} = S^{(k)}\ \overbrace{\mathbf{d}\circ\ldots\circ\mathbf{d}}^{k} \qquad (k=2,4,\ldots), \tag{4.6}$$

where the order parameters $S^{(k)}$ are one in case of total alignment (the microcracks stand parallel) and zero for randomly oriented cracks.

4.4. Equations of motion for the alignment-fabric tensors and for the damage parameter

In general a coupled set of equations of motion for the alignment-fabric tensors of different order can be derived from the differential equation for the crack distribution function by taking moments of this equation, i.e. multiplying with the dyadic product $\underbrace{\mathbf{n} \circ \ldots \circ \mathbf{n}}_{k}$ and integrating over all orientations $\mathbf{n} \in S^2$. This set of equations is analogous to the differential equations for the alignment tensors in liquid crystal theory [19] and will be discussed elsewhere in more detail. In general the equations for the different tensor orders are coupled.

As in our model all cracks in a volume element have the same angular velocity, namely that of the surrounding material, this set of equations simplifies to a set of very special balance type equations without production, and without non-convective flux, which are not coupled:

$$\frac{\partial a^{(k)}}{\partial t} + \mathbf{v}(\mathbf{x}, t) \cdot \nabla a^{(k)} + \frac{1}{2} (\nabla \times \mathbf{v}) \cdot a^{(k)} - \frac{1}{2} a^{(k)} \cdot (\nabla \times \mathbf{v}) = 0, \tag{4.7}$$

$$\text{or} \quad \mathring{\mathbf{a}}^{(k)} = 0 \tag{4.8}$$

for any tensor order k. This special form arises due to the model assumption of a fixed crack number and in addition cracks not moving and rotating independently of the surrounding material. Therefore for an observer co-moving with the material, the orientation distribution and the alignment-fabric tensors do not change. These equations are the equations of motion for the internal variables, which have to be postulated in a purely macroscopic theory. For our simplified crack dynamics the dynamics of the alignment-fabric tensors is not independent of the motion of the material elements. Therefore the change of the alignment tensors in time is not relevant to be considered in our simplified model, as it is completely determined by the motion of the surrounding material. However, the situation is different for other, more complicated crack dynamics. In any case, even if the dynamics of the tensorial damage parameters is not interesting, the orientation distribution itself is relevant, because of the dependence of the effective stress on crack orientation (see below). This effective stress determines the dynamics, as it appears for instance in the Griffith criterion for the onset of growth, and it also appears in the expressions for the length change velocity discussed in the examples below.

Orientation dependence of the effective stress

In an experiment with uniaxial tension σ applied to the sample the stress component σ_n, normal to the crack surface, depends on crack orientation.

Let us assume that in an experiment a uniaxial tension σ is applied along the z-direction. Then the stress component in the direction $\mathbf{n}$, acting on a crack surface with surface unit normal $\mathbf{n}$ is

$$\sigma_{\text{eff}} = \sigma(\mathbf{e}_z \cdot \mathbf{n})^2, \tag{4.9}$$

where $\mathbf{e}_z$ is the unit vector in z-direction. This dependence of the effective stress on crack orientation leads after averaging over all orientations to

$$\begin{aligned} \int_{S^2} \sigma_{\text{eff}} f(l,\mathbf{n},\mathbf{x},t)d^2n &= \int_{S^2} \sigma(\mathbf{e}_z \cdot \mathbf{n})^2 f(l,\mathbf{n},\mathbf{x},t)d^2n \\ &= \left(\int_{S^2} \sigma \left(\mathbf{nn} - \frac{1}{3}\boldsymbol{\delta} \right) f(l,\mathbf{n},\mathbf{x},t)d^2n + \frac{1}{3}\boldsymbol{\delta} \int_{S^2} \sigma f(l,\mathbf{n},\mathbf{x},t)d^2n \right) : \mathbf{e}_z\mathbf{e}_z \\ &= \sigma \left(\mathbf{a} + \frac{1}{3}\boldsymbol{\delta} \right) : \mathbf{e}_z\mathbf{e}_z = \sigma \left(a_{zz} + \frac{1}{3} \right), \end{aligned} \tag{4.10}$$

where a_{zz} is the zz-component of the second order alignment-fabric-tensor $\mathbf{a}$. This dependence of the effective stress on the alignment-fabric-tensor leads to a dependence of the crack dynamics (for instance the critical length) on the orientational order. Thus macroscopic equations of motion of damage parameters depend on the orientational order characterized macroscopically by the alignment-fabric tensors. Hence it would be interesting to study the dynamics of the alignment-fabric-tensors, too.

4.5. Differential equation for the damage parameter

Differentiating the definition of the damage parameter equation (4.1) with respect to time we get the following differential equation for the damage parameter:

$$\begin{aligned} \frac{dD(\mathbf{x},t)}{dt} &= \frac{d}{dt} \int_L^{l_M} \int_{S^2} f(l,\mathbf{n},\mathbf{x},t)d^2n l^2 dl \\ &= \int_L^{l_M} \int_{S^2} \left(\frac{d}{dt} f(l,\mathbf{n},\mathbf{x},t) l^2 + f(l,\mathbf{n},\mathbf{x},t) 2l\dot{l} \right) d^2n dl \end{aligned} \tag{4.11}$$

(4.11) [cont.]
$$= \int_L^{l_M} \int_{S^2} \left(-\frac{\partial}{\partial l} \left(l^2 f(l, \mathbf{n}, \mathbf{x}, t) \dot{l} \right) + f(l, \mathbf{n}, \mathbf{x}, t) 2 l \dot{l} \right) d^2 n dl$$

$$= -\left[l^2 f(l, \mathbf{n}, \mathbf{x}, t) \dot{l} \right]_L^{l_M} + 2 \int_L^{l_M} \int_{S^2} f(l, \mathbf{n}, \mathbf{x}, t) l \dot{l} d^2 n dl.$$

The differential equation for the damage parameter depends on the crack distribution function itself, and therefore also on the initial crack distribution, and it also depends on the dynamical equation for the crack length.

5. Examples of closed differential equations for the distribution function

Some model on the growth velocity of a single crack is needed in order to make a closed differential equation for the length and orientation distribution function out of Eq. (3.10). Two different dynamics of crack extension from the literature will be given here as examples. In the second example we suppose that for a given load not all cracks start growing but only cracks exceeding a certain critical length l_c, which is given by the Griffith criterion. As in many examples of a crack length change dynamics, the cracks do not stop growing but extend infinitely, in all these cases the maximal crack length has to be set to $l_M = \infty$. However, when the cracks become macroscopic their growth dynamics, becomes more complicated (showing for instance branching) than our example dynamics.

5.1. Mott's extension of Griffith's energy criterion including a kinetic crack energy

When the cracks are growing the system has a kinetic energy due to the growth by virtue of the inertia of the material surrounding the separating crack surfaces. This extension of the original Griffith energy concept (see below) by a kinetic energy term goes back to MOTT [29]: A kinetic energy term is added to the sum of the crack surface energy and the elastic deformation energy of the surrounding elastic material, and the crack length is such that the total energy of the system is constant. Two different loading conditions are especially interesting: fixed loading ("dead weight") and "fixed grips" conditions. In both experiments uniaxial symmetry is assumed. In the first case a constant force is applied to the ends of the specimen, leading to a tensile stress. In the second case a fixed displacement is prescribed at the outer boundaries of the specimen. For these two loading conditions, requiring a constant total energy and an argument based on geometrical similarity, the following expressions for the crack length change velocity have been derived ([30] p. 93):

"Dead weight":

$$\dot{l} = \dot{l}_T \left(1 - \frac{l_0}{l}\right), \tag{5.1}$$

where $\dot{l}_T$ is the so-called terminal velocity, not depending on the crack length, but on the applied load σ_{eff}, and therefore on crack orientation. l_0 is the nitial crack length.

"Fixed grips":

$$\dot{l} = \dot{l}_T \left(1 - \frac{l_0}{l}\left(2 - \frac{l_0}{l}\right)\left(\frac{1 + \alpha\dfrac{l^2}{l_0^2}}{(1+\alpha)^2}\right)^{1/2}\right), \tag{5.2}$$

where the parameter α is defined as

$$\alpha = \frac{8\pi l_0^2}{A}. \tag{5.3}$$

It is the ratio of the initial crack area to the surface area A of a cross-section of the specimen. In the "fixed grips" geometry the crack extension might stop again after a certain growth. This can be understood, because of the increase in compliance associated with crack extension in a finite specimen. This leads to a diminishing applied force and decreasing tendency of the crack growth.

From the mesoscopic point of view the growth laws, Eqs. (5.2) as well as (5.1) are mesoscopic constitutive equations relating the length growth velocity $\dot{l}$ to the external load in a material-dependent manner.

In both loading conditions discussed here the crack velocities have been derived for single cracks. If we apply these growth velocities in our differential equation for the length distribution function, Eq. (3.10), this means that we neglect interaction between cracks. However, crack interactions can be taken into account by more sophisticated expressions for the length change velocity.

Inserting the length change velocities of the previous section into the differential equation for the crack distribution function, and integrating over all orientations leads to the following closed differential equations:

"Dead weight":

$$\frac{df(l,\mathbf{x},t)}{dt} = -\frac{1}{l^2}\frac{\partial}{\partial l}\left(l^2 f(l,\mathbf{x},t)\dot{l}_T\left(1 - \frac{l_0}{l}\right)\right). \tag{5.4}$$

The parameter $\dot{l}_T$ depends on the effective load σ_{eff} and therefore on the second order alignment-fabric tensor.

"Fixed grips":

$$\frac{df(l,\mathbf{x},t)}{dt} = -\frac{1}{l^2}\frac{\partial}{\partial l}\left(l^2 f(l,\mathbf{x},t)\dot{l}_T\left(1-\frac{l_0}{l}\left(2-\frac{l_0}{l}\right)\left(\frac{1+\alpha\dfrac{l^2}{l_0^2}}{(1+\alpha)^2}\right)\right)^{1/2}\right), \tag{5.5}$$

5.2. Griffith criterion for the onset of growth

The criterion for the cracks to start growing adopted in the example is the energy criterion introduced originally by GRIFFITH [31]. According to GRIFFITH [31] there is a criticality condition for the crack growth to start, and for cracks larger than a critical length there is a velocity of crack growth $\dot{l}$. From energetic considerations GRIFFITH [31] derived a critical length of cracks with cracks exceeding this length starting to grow. This critical length is given by:

$$l_c = \frac{K}{\sigma_n^2}, \tag{5.6}$$

where K is a material constant, and σ_n is the stress applied perpendicularly to the crack surface. It is assumed that a stress component within the crack plane does not cause the crack growth. For cracks smaller than the critical length l_c the energy necessary to create the crack surface exceeds the energy gain due to release of stresses.

5.3. Rice–Griffith dynamics

A possible crack dynamics, taking into account the criticality condition of Griffith, is derived from a generalization of the Griffith energy criterion on thermodynamic grounds, introducing the Gibbs potential [32], which includes the stress normal to the crack surface and crack length as variables. The resulting crack evolution law has the form

$$\dot{l} = -\alpha + \beta\sigma^2 l \qquad \text{for} \quad l \geq l_c, \tag{5.7}$$

$$\dot{l} = 0 \qquad \text{for} \quad l < l_c \tag{5.8}$$

with material coefficients α, and β. In case of a constant time rate of the applied stress, $\sigma = v_\sigma t$, it results:

$$\dot{l} = -\alpha + \beta v_\sigma^2 l t^2 \qquad \text{for} \quad l \geq l_c, \tag{5.9}$$

$$\dot{l} = 0 \qquad \text{for} \quad l < l_c. \tag{5.10}$$

v_σ is the time derivative of the applied stress normal to the crack surface. The dependence of this normal stress on crack orientation leads to the following orientation dependence of the dynamics:

$$\dot{l} = -\alpha + \beta v_{\sigma\,0}^2 l t^2 (\mathbf{e}_z \cdot \mathbf{n})^4 \quad \text{for} \quad l \geq l_c, \tag{5.11}$$

$$\dot{l} = 0 \qquad \text{for} \quad l < l_c, \tag{5.12}$$

where $v_{\sigma\,0}$ is the change velocity of the stress applied in the z-direction.

After averaging over all orientations, this orientation dependence leads to a dependence on the fourth moment $\int_{S^2} \mathbf{nnnn} f d^2 n$ of the distribution function.

This dynamics also includes a criticality condition for the crack to start growing.

With this model for the length change velocity we end up with the following differential equation for the distribution function:

$$\frac{df(l,\mathbf{n},\mathbf{x},t)}{dt} = -\frac{1}{l^2}\frac{\partial}{\partial l}\left(l^2\left(-\alpha + \beta v_\sigma(\mathbf{n})^2 l t^2\right)\right) \qquad \text{for} \quad l \geq l_c, \tag{5.13}$$

$$\frac{df(l,\mathbf{n},\mathbf{x},t)}{dt} = 0 \qquad \text{for} \quad l < l_c. \tag{5.14}$$

Solutions of this differential equation are discussed in [27].

6. Conclusions

In the mesoscopic description we have introduced mesoscopic fields, defined on an enlarged space including crack size and orientation. Averages over crack sizes and orientations, i.e. macroscopic quantities are calculated with a distribution function f. The differential equation for this distribution function was derived from the mesoscopic balance equations and crack growth law for the single crack. Different crack growth laws from the literature were discussed.

Macroscopic quantities accounting for the progressive damage have been defined as integrals calculated with the distribution function. These are scalar damage parameters, like for instance the average crack length, and fabric-alignment tensors. For these different scalar and tensorial damage parameters equations of

motion have been derived. The time evolution of fabric-alignment tensors will be of special importance under biaxial loading conditions.

The equations of motion for the damage parameters can be compared to the evolution equation in phase field models (or in Landau theory of phase transitions). In phase field models an additional wanted field, the phase field is introduced. The form of the equation of motion, often in the form of a conservation law is postulated [33, 34]. This phase field can be compared to the damage parameter introduced here, and in the non-unilateral case also to the fabric-alignment-tensor. The equation of motion for the damage parameter is of the same type. It is a special form of a balance equation, here with a zero flux term, because spatial inhomogeneities were not taken into account. However, this form of equation of motion has not been postulated here, but derived from mesoscopic considerations, i.e. mesoscopic balance equations.

Acknowledgments

This research was supported by OTKA T034715 and T034603. We thank the DAAD for sponsoring the cooperation between both the Departments of Physics and Chemical Physics of the Technical University of Berlin and the Budapest University of Technology and Economics. Financial support by the VISHAY Company, 95100 Selb, Germany, is gratefully acknowledged.

References

1. W. MUSCHIK, *Internal variables in non-equilibrium thermodynamics,* J. Non-Equilib. Thermodyn., **15**, 1990.
2. G. A. MAUGIN and W. MUSCHIK, *Thermodynamics with internal variables,* J. Non-Equilib. Thermodyn., **19**, 1994.
3. L. M. KACHANOV, *On the time to failure under creep conditions,* Izv. AN SSSR, Otd. Tekhn. Nauk., 8, 1958.
4. G. A. MAUGIN, *The Thermomechanics of Plasticity and Fracture,* Chap. 7, Cambridge University Press, Cambridge 1992.
5. D. KRAJCINOVIC, *Damage mechanics,* Elsevier, Amsterdam, etc., 1996.
6. K. I. KANATANI, *Distribution of directional data and fabric tensors,* International Journal of Engineering Science, **22**, 2, 149–164, 1984.
7. J. L. ERICKSEN, *Anisotropic fluids,* Arch. Rat. Mech. Anal., 4, 1960.
8. F. J. LESLIE, *Some constitutive equations for liquid crystals,* Arch. Rat. Mech. Anal., 28, 1965.
9. S. HESS, *Irreversible thermodynamics of nonequilibrium alignment phenomena in molecular liquids and in liquid crystals,* Z. Naturforsch., **30a**, 728–733, 1975.

10. G. A. MAUGIN and R. DROUOT, *Thermodynamic modelling of polymers in solution*, [in:] AXELRAD and W. MUSCHIK [Eds.], Constitutive Laws and Microstructure, Springer Verlag, 1988.

11. E. A. BRENER, H. MÜLLER-KRUMBHAAR and R. SPATSCHEK, *Coarsening of cracks in a uniaxially strained solid*, Phys. Rev. Let., **86**, 7, 1291–1294, 2001.

12. Z. P. BAŽANT and D. NOVÁK, *Probabilistic nonlocal theory for quasibrittle fracture initiation and size effect. i: theory*, J. Eng. Mech., **126**, 2, 166–174, 2000.

13. S. GLUZMAN and D. SORNETTE, *Self-consistent theory of rupture by progressive diffuse damage*, Physical Review E, **63**, 6, 066129, 11, 2001.

14. J. V. ANDERSEN, D. SORNETTE and K. LEUNG, *Tricritical behaviour in rupture induced by disorder*, Physical Review Letters, **78**, 11, 2140–2143, 1997.

15. R. L. BLUMBERG SELINGER, YHANG-GANG WANG, W. GELBART and A. BEN-SHAUL, *Statistical-themodynamic approach to fracture*, Physical Review A, **43**, 8, 4396–4401, 1991.

16. S. ZAPPERI, P. RAY, H. E. STANLEY and A. VESPIGNANI, *First-order transition in the breakdown of disordered media*, Physical Review Letters, **7**, 8, 1408–1411, 1997.

17. S. ZAPPERI, P. RAY, H. E. STANLEY and A. VESPIGNANI, *Avalanches in breakdown and fracture processes*, Physical Review E, **59**, 5, 5049–5057, 1999.

18. P. VAN, C. PAPENFUSS and W. MUSCHIK, *Mesoscopic dynamics of microcracks*, Physical Review E, **62**, 5, 6206–6215, 2000.

19. S. BLENK, H. EHRENTRAUT, and W. MUSCHIK, *Statistical foundation of macroscopic balances for liquid crystals in alignment tensor formulation*, Physica A, **174**, 119–138, 1991.

20. S. BLENK, H. EHRENTRAUT, and W. MUSCHIK, *Orientation balances for liquid crystals and their representation by alignment tensors*, Mol. Cryst. Liqu. Cryst., **204**, 183–141, 1991.

21. C. PAPENFUSS, *Theory of liquid crystals as an example of mesoscopic continuum mechanics*, Computational Materials Science, **19**, 45–52, 2000.

22. H. EHRENTRAUT, *A unified mesoscopic continuum theory of uniaxial and biaxial liquid crystals*, Wissenschaft und Technik Verlag, Berlin 1996.

23. H. EHRENTRAUT, W. MUSCHIK, and C. PAPENFUSS, *Mesoscopically derived orientation dynamics of liquid crystals*, J. Non-Equilib. Thermodyn., **22**, 285–298, 1997.

24. W. MUSCHIK, *An amendment to the second law of thermodynamics*, J. Non-Equilib. Thermodyn., **21**, 175–192, 1996.

25. S. BLENK, H. EHRENTRAUT, and W. MUSCHIK, *Macroscopic constitutive equations for liquid crystals induced by their mesoscopic orientation distribution*, Int. J. Engng. Sci., **30**, 9, 1127–1143, 1992.

26. S. BLENK and W. MUSCHIK, *Mesoscopic concepts for constitutive equations of nematic liquid crystals in alignment tensor formulation*, ZAMM, **73**, 4–5, T331–T333, 1993.

27. P. VÁN, C. PAPENFUSS, and W. MUSCHIK, *Griffith cracks in the mesoscopic microcrack theory*, published online, Condensed Matter, abstract, cond-mat/0211207; sent to Phys. Rev. E, 2002.

28. H. EHRENTRAUT and W. MUSCHIK, *On symmetric irreducible tensors in d-dimensions*, ARI, 51, 1998.

29. N. F. MOTT, *Brittle fracture in mild steel plates*, Engineering, 165, 1948.

30. B. LAWN. *Fracture of brittle solids*, Cambridge University Press, Cambridge 1993.

31. A. A. GRIFFITH, *The theory of rupture*, Trans. First Intl. Cong. Appl. Mech., Delft 1924.

32. P. VÁN. *Internal thermodynamic variables and failure of microcracked materials*, J. Non-Equilib. Thermodyn., **26**, 2, 167–189, 2001.

33. O. PENROSE and P. C. FIFE, *Thermodynamically consistent models of phase-field type for the kinetics of phase transitions*, Physica D, **43**, 44–62, 1990.

34. L. O. EASTGATE, J. P. SETHNA, M. RAUSCHER, T. CRETEGNY, C. S. CHEN, and C. R. MYERS, *Fracture in mode i using a conserved phase-field model*, Phys. Rev. E, **65**, 3, 2002.

Received December 6, 2002; revised version May 12, 2003.

Arch. Mech., **55**, 5–6, pp. 501–518, Warszawa 2003

Derivation of the normality rule for time-dependent deformation using the principle of maximal rate of entropy production

K. SANTAOJA

Laboratory for Mechanics of Materials,
Helsinki University of Technology,
Otakaari 4, FIN-02150 Espoo, Finland

DERIVATION OF THE normality rule for time-dependent deformation by the principle of the maximal rate of entropy production was carried out. The derivation was made within the framework of thermomechanics with internal variables. Since Ziegler did not cast his principle into an exact mathematical framework, it was done here. A condition for the multiplier in the normality rule (c.f. plasticity multiplier) was derived. If the condition gives a constant value for the multiplier, the specific (complementary) dissipation function was shown to be a homogeneous function. In the case where the value of the multiplier depends on the state variables, the dissipation potential is a non-homogeneous function.

Key words: thermodynamics, thermomechanics, internal variables, dissipation, entropy production, normality rule.

Notations

$\vec{q}$	heat flux vector,
s	specific entropy (entropy per unit mass),
$\dot{s}^{\mathrm{i}}$	specific entropy production rate,
$\dot{s}^{\mathrm{i}}_{\mathrm{con}}$	specific entropy production rate (thermal part),
$\dot{s}^{\mathrm{i}}_{\mathrm{loc}}$	specific entropy production rate (mechanical part),
T	absolute temperature,
$\boldsymbol{\alpha}$	internal state variable (a second-order tensor),
$\boldsymbol{\beta}$	internal force (a second-order tensor),
$\boldsymbol{\varepsilon}$	strain tensor,
$\boldsymbol{\varepsilon}^{\mathrm{i}}$	inelastic strain tensor (irreversible strain tensor),
ρ	density of the material,
$\boldsymbol{\sigma}$	stress tensor,
φ	specific dissipation function (potential),
φ_{loc}	specific dissipation function (mechanical part),
ψ	specific Helmholtz free energy,
$\mathrm{D}/\mathrm{D}t$	material (time) derivative operator,
$\vec{\nabla}$	vector operator del,
$\dot{(\,)}$	material (time) derivative operator,
$\vec{(\,)}$	quantity ( ) is a vector,
	second-order and fourth-order tensors are denoted, by bold letters.

1. Introduction

THE PRESENT PAPER combines the theory of continuum mechanics and thermodynamics and refers to the combination as thermomechanics. There are several dialects of thermodynamics. Here the theory of thermodynamics with internal variables is adopted since it provides an excellent framework within which to evaluate material models.

Basic courses in continuum mechanics already teach students learn that the body has to satisfy the equilibrium equation. They well know that if the equilibrium is not satisfied, the solution is incorrect and therefore has to be dismissed. This is because a solution that does not obey the equilibrium is in contradiction to a basic law of nature. In this case the basic law is the law of balance of momentum. The law of balance of momentum places a restriction on the values of forces and moments.

Corresponding restrictions also exist for a material model. They are the basic laws of thermodynamics, such as first law and second law. The thernodynamical restrictions for constitutive equations are dressed in the form of one inequality called the Clausius–Duhem inequality. If the material model satisfies the Clausius–Duhem inequality, it is not in contradiction to the basic laws of thermomechanics and can therefore be applied. Thermomechanical evaluation of a constitutive cannot prove that the material model is correct. This work is for micromechanical investigation of the material model and experimental work.

In order to prepare a thermomechanical investigation of a material model, the researcher has to write explicit forms for following two functions: the specific Helmholtz free energy ψ (or the specific complementary Helmholtz free energy ψ^c) and the specific dissipation function φ (or the specific complementary dissipation function φ^c or the yield function F). The material model is then obtained from these two functions using state equations and the normality rule. This paper studies the derivation of the normality for time-dependent deformation. The derivation is carried out using the principle of maximal rate of entropy production proposed by ZIEGLER [1, p. 134]. Since Ziegler did not cast his principle into an exact mathematical framework, it is done here. In this paper the normality rule is derived for time-dependent deformation. In the subsequent paper the standard approach of the principle of maximal rate of entropy production is extended for description of time-independent thermoplasticity.

Today when material models within the framework of thermomechanics are studied the normality rule belongs to the standard toolbox. However, usually the principle of maximal rate of entropy production is not used in the derivation of the normality rule. Instead of that the approach by the French school of thermodynamics is adopted. The French school of thermodynamics assumes that there exists a convex scalar-valued dissipation potential which is assumed

to obey the normality rule {see e.g. [2, p. 74]}. Furthermore, some writers have interpreted the work by Ziegler differently from what is done here. HOULSBY and PUZRIN [4, Sec. 4.1], for example, refer to Ziegler's orthogonality condition and therefore their approach deviates from the present one, since the vital part of their derivation is that the dissipation potential is a homogeneous function. SHIZAWA and ZBIB [3, Sec. V.3.1.] refer to the principle of maximal entropy production rate, but do not obtain any condition for the multiplier in the normality rule (c.f. plasticity multiplier) which plays an important role as the present work shows. On the other hand RAJAGOPAL and SRINIVASA [5] make an extensive study on "maximum rate of dissipation criterion", but they do not see the difference between the dissipation, where the terms have the form of force times flux, and the dissipation function whose variables are fluxes only. Furthermore they do not derive the normality rule, but just write it without obtaining a condition for the multiplier in normality rule. There are also writers, see e.g. [6], who just introduce the normality rule and refer to Ziegler.

2. Derivation of the Clausius–Duhem inequality

This section derives the Clausius–Duhem inequality which plays the central role in the thermomechanical verification of the material models and in the derivation of the normality rule.

Verification of a material model starts from the selection of the set of independent variables which describe the process which has to be modelled. When thermomechanics is used two kind of independent variables are present: controllable variables and internal variables. The independent variables present in the basic laws and axioms of thermomechanics are called controllable variables. The other independent variables are called internal variables.

The controllable independent variables for thermomechanical processes in deformable solids are: The strain tensor $\boldsymbol{\varepsilon}$ and the specific entropy s which is a scalar-valued quantity. The strain tensor $\boldsymbol{\varepsilon}$ is a second-order tensor describing both mechanical and thermal deformation.

The internal variables and their form are determined by the material model under consideration. Since the present paper studies time-dependent deformation in general, the inelastic strain tensor $\boldsymbol{\varepsilon}^{\mathrm{i}}$ is one of the internal variables. In order to extend the scope of the this paper more internal variables are introduced. The second-order tensorial quantity $\boldsymbol{\alpha}$ is introduced to represent any number of internal variables, which can be scalars, vectors or tensors of any order. In the theory of visco-plasticity, for example, the variables $\boldsymbol{\alpha}$ are used for description of hardening.

The specific internal energy u is written as:

$$u = u(\boldsymbol{\varepsilon}, \boldsymbol{\varepsilon}^{\mathrm{i}}, \boldsymbol{\alpha}, s, h(\vec{x}))\,, \tag{2.1}$$

where the notation the notation $h(\vec{x})$ indicates that the system V^{b} may be thermodynamically inhomogeneous. This means that, e.g. the material properties for elastic deformation can vary from point to point.

For the sake of simplicity this paper studies material models which (also) model elastic deformation. Thus, the present formulation is for cases where the response of the system consists of elastic and inelastic deformation or pure elastic deformation. This means that the difference $\boldsymbol{\varepsilon} - \boldsymbol{\varepsilon}^{\mathrm{i}}$ belongs to the description of state. Also thermal expansion can be simulated. By neglecting thermodynamically inhomogeneous systems the above assumption reduces Eq. (2.1) to the following form:

$$u = u(\boldsymbol{\varepsilon} - \boldsymbol{\varepsilon}^{\mathrm{i}}, \boldsymbol{\alpha}, s)\,. \tag{2.2}$$

Some writers {see e.g. MAUGIN [7, Sec. 2.3]} replace the difference $\boldsymbol{\varepsilon} - \boldsymbol{\varepsilon}^{\mathrm{i}}$ by the elastic strain tensor $\boldsymbol{\varepsilon}^{\mathrm{e}}$. However, it is not acceptable. Variable $\boldsymbol{\varepsilon}$ is a controllable state variable whereas notation $\boldsymbol{\varepsilon}^{\mathrm{i}}$ refers to an internal state variable. Thermodynamics does not define a difference between a controllable state variable and an internal state variable.

Instead of the specific internal energy u, the state of solids is usualy described by the specific Helmholtz free energy ψ which is a Legendre partial transformation of the specific internal energy u. This is done because writing a material model using the specific internal energy u is very difficult, given that the specific entropy s is an argument of the specific internal energy u. It is very difficult to construct a constitutive model as a function of the specific entropy s. In the formulation of the specific Helmholtz free energy ψ the specific entropy s is replaced by the absolute temperature T. Since the absolute temperature T is a well-known quantity for a human being, writing a material model using the specific Helmholtz free energy ψ is much simpler than doing so with the specific internal energy u.

State functions are obtained as partial derivatives of the specific internal energy u with respect to the state variables. Due to the introduction of the specific Helmholtz free energy ψ state equations take the forms

$$\boldsymbol{\sigma} := \rho \frac{\partial \psi(\ldots)}{\partial(\boldsymbol{\varepsilon} - \boldsymbol{\varepsilon}^{\mathrm{i}})} \qquad \text{and} \qquad \boldsymbol{\beta} := -\rho \frac{\partial \psi(\ldots)}{\partial \boldsymbol{\alpha}} \tag{2.3}$$

and further

$$s = -\frac{\partial \psi(\ldots)}{\partial T}, \qquad \text{where} \qquad \psi = \psi(\boldsymbol{\varepsilon} - \boldsymbol{\varepsilon}^{\mathrm{i}}, \boldsymbol{\alpha}, T)\,. \tag{2.4}$$

In State Equations (2.2) and (2.3) the notation $\boldsymbol{\sigma}$ stands for the stress tensor, $\boldsymbol{\beta}$ is an internal force and ρ is the density.

The principle of conservation of energy, also referred to as the first law of thermodynamics, can be stated as follows: The time rate of change of the sum total of the kinetic energy K and the internal energy U in the body is equal to the sum of the rates of work done by the surface and body loads in producing the deformation (or flow) together with heat energy that may leave or enter the body at a certain rate. Thus the following is obtained:

$$\frac{\mathrm{D}}{\mathrm{D}t}(K+U) = P^{\mathrm{ext}} + Q\,. \tag{2.5}$$

In Basic Law (2.5) P^{ext} is the power input of the external forces and Q is the heat input rate. The local form for the first law of thermodynamics is called the energy equation (in the non-polar case) or the equation of balance of energy. It has the following form:

$$\rho\,\dot{u} = \boldsymbol{\sigma}:\dot{\boldsymbol{\varepsilon}} + \rho r - \vec{\nabla}\cdot\vec{q}, \tag{2.6}$$

where r is the heat source per unit mass and where $\vec{q}$ is the heat flux vector.

The second law of thermodynamics can be written in the form

$$\dot{S} \geq -\oint_{\partial V} \frac{\vec{n}\cdot\vec{q}}{T}\,\mathrm{d}A + \int_V \rho\frac{r}{T}\,\mathrm{d}V\,, \tag{2.7}$$

where $\dot{S}$ is the entropy rate and $\vec{n}$ is the outward unit vector for volume V, the surface of which is denoted by ∂V. The local form of the second law of thermodynamics takes the form

$$\rho\,T\,\dot{s} + \vec{\nabla}\cdot\vec{q} - \frac{\vec{\nabla}T}{T}\cdot\vec{q} - \rho r \geq 0\,. \tag{2.8}$$

The internal energy U and the entropy S are defined by

$$U := \int_V \rho\,u\,\mathrm{d}V \qquad \text{and} \qquad S := \int_V \rho\,s\,\mathrm{d}V\,. \tag{2.9}$$

Combination of the local forms of the first and second law of thermodynamics, i.e. Eqs. (2.6) and (2.8), is called the Clausius–Duhem inequality. For the present set of state variables [see Eq. $(2.4)_2$] it takes the following form:

$$\boldsymbol{\sigma}:\dot{\boldsymbol{\varepsilon}}^{\mathrm{i}} + \boldsymbol{\beta}:\dot{\boldsymbol{\alpha}} - \frac{\vec{\nabla}T}{T}\cdot\vec{q} \geq 0\,. \tag{2.10}$$

Based on the Clausius–Duhem Inequality (2.10) the specific entropy production rate $\dot{s}^{\mathrm{i}}$ is introduced. It is defined by

$$\rho\,T\,\dot{s}^{\mathrm{i}} := \boldsymbol{\sigma}:\dot{\boldsymbol{\varepsilon}}^{\mathrm{i}} + \boldsymbol{\beta}:\dot{\boldsymbol{\alpha}} - \frac{\vec{\nabla}T}{T}\cdot\vec{q} \quad (\geq 0)\,. \tag{2.11}$$

3. Principle of maximal rate of entropy production applied to time-dependent deformation

This section studies the principle of maximal rate of entropy production and derives its consequence: the normality rule. Time-dependent deformation is considered.

The principle of maximal rate of entropy production was first proposed by ZIEGLER [1, p. 134). It should be pointed out that this principle as proposed by ZIEGLER {see e.g. [8, pp. 271 and 272]} is not (yet?) a basic law of physics, contrary to those discussed in the previous section. In Ziegler's own words, the principle of maximal rate of entropy production is quite general ZIEGLER and WEHRLI [9, p. 186]}.

According to ZIEGLER [8, p. 272] the physical foundation of this principle is as follows: From the physical point of view this principle is particularly appealing, since it may be considered as an extension of the second fundamental law. In fact, if a closed system tends towards its state of maximal entropy, it seems reasonable that the rate of entropy increase (the specific entropy production rate) under prescribed forces would take a maximum value, i.e. the system should approach its final state along the fastest (shortest) possible path.

3.1. Normality rule for time-dependent deformation when material model $\varphi = \varphi(\dot{\varepsilon}^{\mathrm{i}}, \alpha, \ldots)$ is expressed by fluxes

Investigation of the expression for the specific entropy production rate $\dot{s}^{\mathrm{i}}$ in Eq. (2.11) shows that $\dot{s}^{\mathrm{i}}$ is dependent upon both forces and fluxes (processes). For example, in the expression $\sigma : \dot{\varepsilon}^{\mathrm{i}}$ the term σ represents the force and $\dot{\varepsilon}^{\mathrm{i}}$ describes the flux. Furthermore, ZIEGLER [1, p. 129] assumes the existence of the specific dissipation function {see also ZIEGLER [8, p. 76]}

$$\varphi = \varphi(\dot{\varepsilon}^{\mathrm{i}}, \dot{\alpha}, \vec{q}; \varepsilon - \varepsilon^{\mathrm{i}}, \alpha, T)\,. \tag{3.1}$$

The concept of the specific dissipation function φ is that in case of an actual process (i.e. when the maximum is present) it contains the same information (except for temperature T) about the state and the process as the specific entropy production rate $\dot{s}^{\mathrm{i}}$, but the arguments of φ are only fluxes $(\dot{\varepsilon}^{\mathrm{i}}, \dot{\alpha}, \vec{q})$ [and state $(\varepsilon - \varepsilon^{\mathrm{i}}, \alpha, T)$], whereas the expression for $\dot{s}^{\mathrm{i}}$ contains also the conjugate variables $[\sigma, \beta, -(\vec{\nabla} T)/T]$. This can be seen in Eqs. (2.11) and (3.1). The specific dissipation function φ is defined by {see ZIEGLER [1, Eq. (4.3)] and [6, Eq. (5.1)]}

$$\text{For an actual process } \varphi := T\dot{s}^{\mathrm{i}} \quad \Rightarrow \quad \frac{1}{T}\varphi - \dot{s}^{\mathrm{i}} = 0\,. \tag{3.2}$$

Ziegler did not cast his above-presented concept into an exact mathematical framework. The author therefore proposes the following formulation for the principle of maximal rate of entropy production:

The process is investigated at a certain state $(\boldsymbol{\varepsilon} - \boldsymbol{\varepsilon}^{\mathrm{i}}, \boldsymbol{\alpha}, T)$ and the values for the fluxes $(\dot{\boldsymbol{\varepsilon}}^{\mathrm{i}}, \dot{\boldsymbol{\alpha}}, \vec{q})$ have to be determined in order to maximise the specific entropy production rate $\dot{s}^{\mathrm{i}}$. The state gives the values for the state functions $[\boldsymbol{\sigma}, \boldsymbol{\beta}, -(\vec{\nabla}T)/T]$ as follows: State Equations (2.13) give the values for the forces $\boldsymbol{\sigma}$ and $\boldsymbol{\beta}$. Since the state $(\boldsymbol{\varepsilon} - \boldsymbol{\varepsilon}^{\mathrm{i}}, \boldsymbol{\alpha}, T)$ is known, the temperature T is known and therefore the state function $-(\vec{\nabla}T)/T$, is also known. Thus, the values for the state functions $[\boldsymbol{\sigma}, \boldsymbol{\beta}, -(\vec{\nabla}T)/T]$ are known.

Based on the above discussion the problem can be expressed in the following way: It is assumed that the state is known, i.e. the set $(\boldsymbol{\varepsilon} - \boldsymbol{\varepsilon}^{\mathrm{i}}, \boldsymbol{\alpha}, T)$ is assumed to be known. This implies that the values for the forces $[\boldsymbol{\sigma}, \boldsymbol{\beta}, -(\vec{\nabla}T)/T]$ are known. The question is, what are the magnitudes of the fluxes $(\dot{\boldsymbol{\varepsilon}}^{\mathrm{i}}, \dot{\boldsymbol{\alpha}}, \vec{q})$ which maximise the specific entropy production rate $\dot{s}^{\mathrm{i}}$? At the same time also Definition $(3.2)_1$ has to be satisfied.

To make the evaluation shorter General Problem (2.11) is not evaluated but the concept by TRUESDELL and NOLL [10, p. 295] is followed by assuming that the specific entropy production rate $\dot{s}^{\mathrm{i}}$ is separable into mechanical and thermal part as follows:

$$\dot{s}^{\mathrm{i}} = \dot{s}^{\mathrm{i}}_{\mathrm{loc}} + \dot{s}^{\mathrm{i}}_{\mathrm{con}} \,. \tag{3.3}$$

Based on Expression (3.3) Eq. (2.11) yields

$$\rho\, T\, \dot{s}^{\mathrm{i}}_{\mathrm{loc}} := \boldsymbol{\sigma} : \dot{\boldsymbol{\varepsilon}}^{\mathrm{i}} + \boldsymbol{\beta} : \dot{\boldsymbol{\alpha}} \qquad (\geq 0) \tag{3.4}$$

and

$$\rho\, T\, \dot{s}^{\mathrm{i}}_{\mathrm{con}} := -\frac{\vec{\nabla}T}{T} \cdot \vec{q} \qquad (\geq 0)\,. \tag{3.5}$$

Quantity $\rho\, T\, \dot{s}^{\mathrm{i}}_{\mathrm{loc}}$ is often called intrinsic dissipation, whereas Quantity $\rho T\, \dot{s}^{\mathrm{i}}_{\mathrm{con}}$ is referred to as thermal dissipation.

Usually Mechanical Problem (3.4) and Thermal Problem (3.5) are studied separately. Since the derivation of the normality rule for a thermal problem follows the same steps that will be taken when the mechanical problem is studied, the thermal problem is not studied here.

Based on the above the principle of maximal rate of entropy production is written in the following mathematical form:

maximise with respect to the fluxes $(\dot{\boldsymbol{\varepsilon}}^{\mathrm{i}}, \dot{\boldsymbol{\alpha}})$

$$\dot{s}^{\mathrm{i}}_{\mathrm{loc}}(\dot{\boldsymbol{\varepsilon}}^{\mathrm{i}}, \dot{\boldsymbol{\alpha}}, \boldsymbol{\sigma}, \boldsymbol{\beta}) = \frac{1}{\rho T}\left(\boldsymbol{\sigma} : \dot{\boldsymbol{\varepsilon}}^{\mathrm{i}} + \boldsymbol{\beta} : \dot{\boldsymbol{\alpha}}\right) \tag{3.6}$$

subject to:

$$\tau_{\mathrm{loc}} = \frac{1}{T}\,\varphi_{\mathrm{loc}}(\dot{\boldsymbol{\varepsilon}}^{\mathrm{i}}, \dot{\boldsymbol{\alpha}}; \boldsymbol{\varepsilon} - \boldsymbol{\varepsilon}^{\mathrm{i}}, \boldsymbol{\alpha}, T) - \dot{s}^{\mathrm{i}}_{\mathrm{loc}}(\dot{\boldsymbol{\varepsilon}}^{\mathrm{i}}, \dot{\boldsymbol{\alpha}}, \boldsymbol{\sigma}, \boldsymbol{\beta}) = 0\,, \tag{3.7}$$

where $\tau_{\text{loc}} = 0$ is a constraint and φ_{loc} is the specific dissipation function for mechanical behaviour. It is worth noting that the specific dissipation function φ is dependent on the fluxes present in the Clausius–Duhem inequality [see Inequality (3.4)] and on the state variables [see Eq. (2.2)]. In this case this means that the function φ_{loc} is dependent on sets $(\dot{\boldsymbol{\varepsilon}}^{\text{i}}, \dot{\boldsymbol{\alpha}})$ and $(\boldsymbol{\varepsilon} - \boldsymbol{\varepsilon}^{\text{i}}, \boldsymbol{\alpha}, T)$. The general maximisation problem (where the specific entropy production rate $\dot{s}^{\text{i}}$ is not separated) follows the above concept.

Both $\dot{s}^{\text{i}}_{\text{loc}}$ and τ_{loc} are assumed to have at least continuous second partial derivatives with respect to the arguments $(\dot{\boldsymbol{\varepsilon}}^{\text{i}}, \dot{\boldsymbol{\alpha}})$. It should be pointed out that also Inequality (3.4) must be satisfied. Applying LUENBERGER [11, p. 225], the first-order sufficient condition for the point $(\dot{\boldsymbol{\varepsilon}}^{\text{i}}, \dot{\boldsymbol{\alpha}})$ to be a local maximum is

$$
\begin{aligned}
&\frac{\partial}{\partial \dot{\boldsymbol{\varepsilon}}^{\text{i}}} \left(\dot{s}^{\text{i}}_{\text{loc}} + \lambda \tau_{\text{loc}}\right) = \mathbf{0}, \\
&\frac{\partial}{\partial \dot{\boldsymbol{\alpha}}} \left(\dot{s}^{\text{i}}_{\text{loc}} + \lambda \tau_{\text{loc}}\right) = \mathbf{0} \qquad \text{and} \quad \tau_{\text{loc}} = 0,
\end{aligned} \tag{3.8}
$$

where λ is the Lagrange multiplier. As mentioned by ARFKEN [12, p. 946] the method based on Lagrange multipliers will fail if in Expressions $(3.8)_1$ and $(3.8)_2$ the coefficients of λ vanish at the extremum. Therefore, also special points where

$$
\frac{\partial \tau_{\text{loc}}}{\partial \dot{\boldsymbol{\varepsilon}}^{\text{i}}} = \mathbf{0} \qquad \text{and} \qquad \frac{\partial \tau_{\text{loc}}}{\partial \dot{\boldsymbol{\alpha}}} = \mathbf{0} \tag{3.9}
$$

must be studied. The above-mentioned coefficients of λ are

$$
\frac{\partial}{\partial \dot{\boldsymbol{\varepsilon}}^{\text{i}}} \tau_{\text{loc}} \qquad \text{and} \qquad \frac{\partial}{\partial \dot{\boldsymbol{\alpha}}} \tau_{\text{loc}} . \tag{3.10}
$$

The above indicates that there are two different cases for evaluation of the local maximum; utilisation of Expressions (3.8) referred to as Case A, and the special case described by Expression (3.9) referred to as Case B.

Starting with Case A:

Substitution of Eqs. (3.5) and (3.6) into Eqs. $(3.8)_1$ gives

$$
\frac{1}{\rho T} \boldsymbol{\sigma} + \lambda \left(\frac{1}{T} \frac{\partial \varphi_{\text{loc}}}{\partial \dot{\boldsymbol{\varepsilon}}^{\text{i}}} - \frac{1}{\rho T} \boldsymbol{\sigma} \right) = \mathbf{0}, \tag{3.11}
$$

which yields to following result:

$$
\boldsymbol{\sigma} = \frac{\lambda}{\lambda - 1} \rho \frac{\partial \varphi_{\text{loc}}}{\partial \dot{\boldsymbol{\varepsilon}}^{\text{i}}} . \tag{3.12}
$$

Similarly Eq. $(3.8)_2$ gives

$$
\boldsymbol{\beta} = \frac{\lambda}{\lambda - 1} \rho \frac{\partial \varphi_{\text{loc}}}{\partial \dot{\boldsymbol{\alpha}}} . \tag{3.13}
$$

By substituting the results in Eqs. (3.12) and (3.13) into Eq. $(3.8)_3$ and reordering the obtained equation, the following result is obtained:

$$\varphi_{\mathrm{loc}}(\dot{\boldsymbol{\varepsilon}}^{\mathrm{i}}, \dot{\boldsymbol{\alpha}}; \boldsymbol{\varepsilon} - \boldsymbol{\varepsilon}^{\mathrm{i}}, \boldsymbol{\alpha}, T) = \frac{\lambda}{\lambda - 1} \left(\frac{\partial \varphi_{\mathrm{loc}}}{\partial \dot{\boldsymbol{\varepsilon}}^{\mathrm{i}}} : \dot{\boldsymbol{\varepsilon}}^{\mathrm{i}} + \frac{\partial \varphi_{\mathrm{loc}}}{\partial \dot{\boldsymbol{\alpha}}} : \dot{\boldsymbol{\alpha}} \right). \tag{3.14}$$

It is worth noting that the value of the Lagrange multiplier λ is dependent on the set $(\boldsymbol{\varepsilon} - \boldsymbol{\varepsilon}^{\mathrm{i}}, \boldsymbol{\alpha}, T)$. This is based on the definition of the maximisation problem, which assumed that the value of the set $(\boldsymbol{\varepsilon} - \boldsymbol{\varepsilon}^{\mathrm{i}}, \boldsymbol{\alpha}, T)$ is known and that the values for the corresponding fluxes $(\dot{\boldsymbol{\varepsilon}}^{\mathrm{i}}, \dot{\boldsymbol{\alpha}})$ have to be determined. This implies that for a certain set $(\boldsymbol{\varepsilon} - \boldsymbol{\varepsilon}^{\mathrm{i}}, \boldsymbol{\alpha}, T)$ a unique value for is obtained. Thus, the following holds: $\lambda = \lambda(\boldsymbol{\varepsilon} - \boldsymbol{\varepsilon}^{\mathrm{i}}, \boldsymbol{\alpha}, T)$.

By extending the definition for homogeneous functions given by e.g. WIDDER [13, pp. 19 and 20] the following is achieved: A function $\phi(x, y, z, u, v)$ is homogeneous of degree ω in variables x , y and z in a region R if, and only if, for x, y and z in R and for every positive value of k the following holds:

$$\phi(k\,x, k\,y, k\,z, u, v) \;:=\; k^{\omega} \phi(x, y, z, u, v)\,. \tag{3.15}$$

Sometimes the definition is assumed to hold for every real k, and if the values of k are restricted to being positive, the function $\phi(x, y, z, u, v)$ is said to be a positive homogeneous function.

Euler's theorem on homogeneous functions {see original form in e.g. WIDDER [13, p. 20]} for the above extended definition reads

$$\omega\, \phi(x, y, z, u, v) = \frac{\partial \phi}{\partial x}\, x + \frac{\partial \phi}{\partial y}\, y + \frac{\partial \phi}{\partial z}\, z\,. \tag{3.16}$$

In the special case that the Lagrange multiplier λ is a constant the extended Euler's theorem for homogeneous functions [Theorem (3.16)] and Result (3.14) indicate that the specific dissipation function φ is a homogeneous function of degree $(\lambda - 1)/\lambda$ in the variables $(\dot{\boldsymbol{\varepsilon}}^{\mathrm{i}}, \dot{\boldsymbol{\alpha}})$.

The following notation is introduced:

$$\mu \;:=\; \frac{\lambda}{\lambda - 1} \qquad \text{which gives} \qquad \lambda = \frac{\mu}{\mu - 1}\,. \tag{3.17}$$

Equation $(3.17)_2$ shows that the multiplier $\mu = \mu(\boldsymbol{\varepsilon} - \boldsymbol{\varepsilon}^{\mathrm{i}}, \boldsymbol{\alpha}, T)$ can be any real number excluding $\mu = 1$. This means that in Case A the dissipation function φ_{loc} cannot be a homogeneous function of $1/\mu = 1$.

Continuing with Case B:

The candidates for the extremum points defined by Eq.(3.9) are investigated next. Substitution of Eq.(3.7) into Eq. $(3.9)_1$ gives

$$\frac{1}{T} \frac{\partial \varphi_{\mathrm{loc}}}{\partial \dot{\boldsymbol{\varepsilon}}^{\mathrm{i}}} - \frac{1}{\rho T}\, \boldsymbol{\sigma} = \mathbf{0}\,, \qquad \text{which gives} \qquad \boldsymbol{\sigma} = \rho\, \frac{\partial \varphi_{\mathrm{loc}}}{\partial \dot{\boldsymbol{\varepsilon}}^{\mathrm{i}}}\,. \tag{3.18}$$

Correspondingly the following is obtained:

$$\boldsymbol{\beta} = \rho \frac{\partial \varphi_{\text{loc}}}{\partial \dot{\boldsymbol{\alpha}}}. \tag{3.19}$$

Instead of Expression (3.14) Case B gives

$$\varphi_{\text{loc}}(\dot{\boldsymbol{\varepsilon}}^{\text{i}}, \dot{\boldsymbol{\alpha}}; \boldsymbol{\varepsilon} - \boldsymbol{\varepsilon}^{\text{i}}, \boldsymbol{\alpha}, T) = \frac{\partial \varphi_{\text{loc}}}{\partial \dot{\boldsymbol{\varepsilon}}^{\text{i}}} : \dot{\boldsymbol{\varepsilon}}^{\text{i}} + \frac{\partial \varphi_{\text{loc}}}{\partial \dot{\boldsymbol{\alpha}}} : \dot{\boldsymbol{\alpha}}. \tag{3.20}$$

Comparison of Eqs. $(3.18)_2$, (3.19) and (3.20) with Eqs. (3.12), (3.13) and (3.14) shows that the special points defined by Case B give the same solution as Case A except that φ_{loc} is a homogeneous function of degree $1 (= 1/\mu)$.

Concluding from Cases A and B the following can be said:

At the start of this chapter the following problem was set: The state is known, which means that the set $(\boldsymbol{\varepsilon} - \boldsymbol{\varepsilon}^{\text{i}}, \boldsymbol{\alpha}, T)$ is known. Due to State Eqs. $(2.3)_1$ and $(2.3)_2$ this implies that the values for the forces $(\boldsymbol{\sigma}, \boldsymbol{\beta})$ are known. The magnitudes of the fluxes $(\dot{\boldsymbol{\varepsilon}}^{\text{i}}, \dot{\boldsymbol{\alpha}})$ have to be determined in order for the specific entropy production rate $\dot{s}^{\text{i}}$ to be maximised. At the same time also Definition $(3.2)_1$ has to be satisfied. The result was as follows:

As a result the following normality rule was achieved:

$$\boldsymbol{\sigma} = \mu \rho \frac{\partial \varphi_{\text{loc}}(\dot{\boldsymbol{\varepsilon}}^{\text{i}}, \dot{\boldsymbol{\alpha}}; \boldsymbol{\varepsilon} - \dot{\boldsymbol{\varepsilon}}^{\text{i}}, \boldsymbol{\alpha}, T)}{\partial \dot{\boldsymbol{\varepsilon}}^{\text{i}}} \tag{3.21}$$

and

$$\boldsymbol{\beta} = \mu \rho \frac{\partial \varphi_{\text{loc}}(\dot{\boldsymbol{\varepsilon}}^{\text{i}}, \dot{\boldsymbol{\alpha}}; \boldsymbol{\varepsilon} - \boldsymbol{\varepsilon}^{\text{i}}, \boldsymbol{\alpha}, T)}{\partial \dot{\boldsymbol{\alpha}}}. \tag{3.22}$$

The specific dissipation function φ_{loc} has to obey the following condition:

$$\varphi_{\text{loc}}(\dot{\boldsymbol{\varepsilon}}^{\text{i}}, \dot{\boldsymbol{\alpha}}; \boldsymbol{\varepsilon} - \boldsymbol{\varepsilon}^{\text{i}}, \boldsymbol{\alpha}, T) = \mu \left(\frac{\partial \varphi_{\text{loc}}}{\partial \dot{\boldsymbol{\varepsilon}}^{\text{i}}} : \dot{\boldsymbol{\varepsilon}}^{\text{i}} + \frac{\partial \varphi_{\text{loc}}}{\partial \dot{\boldsymbol{\alpha}}} : \dot{\boldsymbol{\alpha}} \right). \tag{3.23}$$

The first-order sufficient condition for the point $(\dot{\boldsymbol{\varepsilon}}^{\text{i}}, \dot{\boldsymbol{\alpha}})$ to be a local maximum is that Eqs. (3.21), (3.22) and (3.23) hold. If φ_{loc} is a homogeneous function, according to Eq. (3.23) it is a homogeneous function of degree $1/\mu$. If φ_{loc} is not a homogeneous function, the value for $\mu = \mu(\boldsymbol{\varepsilon} - \boldsymbol{\varepsilon}^{\text{i}}, \boldsymbol{\alpha}, T)$ is obtained from Eq. (3.23).

Equations (3.2), (3.21) and (3.22) show that the specific dissipation function φ_{loc} is a scalar potential, and it is therefore also called the specific dissipation potential.

The second-order both necessary and sufficient conditions for a local maximum lead to matrices so extensive {see LUENBERGER [11, pp. 226 and 227]}

that investigating them is very complicated and it hardly provides any practical results.

However, in practice, when constitutive models are evaluated the explicit form for the specific dissipation function φ_{loc} is assumed and the forces $(\boldsymbol{\sigma}, \boldsymbol{\beta})$ are determined by Normality Rule (3.21) and (3.22).

3.2. Normality rule for time-dependent deformation when material model $\varphi^{\text{c}} = \varphi^{\text{c}}(\boldsymbol{\sigma}, \boldsymbol{\beta}; \ldots)$ is expressed by forces

This section gives the normality rule for time-dependent deformation when the material model is expressed as a function of state functions, i.e. forces instead of the rates of internal variables, i.e. fluxes.

Normality Rule (3.21) and (3.22) assumes that the material model is expressed by the fluxes $(\dot{\boldsymbol{\varepsilon}}^{\text{i}}, \dot{\boldsymbol{\alpha}})$. If the conjugate forces $(\boldsymbol{\sigma}, \boldsymbol{\beta})$ are desired as the arguments of the material model, the specific complementary dissipation function $\varphi^{\text{c}}_{\text{loc}}$ is introduced. It is a Legendre partial transformation of the specific dissipation function φ_{loc}. The transformation is defined by

$$\rho\, \varphi^{\text{c}}_{\text{loc}}(\boldsymbol{\sigma}, \boldsymbol{\beta}\,; \boldsymbol{\varepsilon} - \boldsymbol{\varepsilon}^{\text{i}}, \boldsymbol{\alpha}, T) := \boldsymbol{\sigma} : \dot{\boldsymbol{\varepsilon}}^{\text{i}} + \boldsymbol{\beta} : \dot{\boldsymbol{\alpha}} - \mu\rho\, \varphi_{\text{loc}}(\dot{\boldsymbol{\varepsilon}}^{\text{i}}, \dot{\boldsymbol{\alpha}}; \boldsymbol{\varepsilon} - \boldsymbol{\varepsilon}^{\text{i}}, \boldsymbol{\alpha}, T)\,, \tag{3.24}$$

where the superscript c in notation $\varphi^{\text{c}}_{\text{loc}}$ refers to the complementary function.

Based on Normality Rule (3.21) and (3.22) and Definition (3.24) the coefficient in Expression (A.3) of Appendix A take the values $a = \mu\rho$ and $b = \rho$. Thus, Expression (A.6) of Appendix A gives the following normality rule:

$$\dot{\boldsymbol{\varepsilon}}^{\text{i}} = \rho\, \frac{\partial \varphi^{\text{c}}_{\text{loc}}(\boldsymbol{\sigma}, \boldsymbol{\beta}\,; \boldsymbol{\varepsilon} - \boldsymbol{\varepsilon}^{\text{i}}, \boldsymbol{\alpha}, T)}{\partial \boldsymbol{\sigma}} \tag{3.25}$$

and

$$\dot{\boldsymbol{\alpha}} = \rho\, \frac{\partial \varphi^{\text{c}}_{\text{loc}}(\boldsymbol{\sigma}, \boldsymbol{\beta}\,; \boldsymbol{\varepsilon} - \boldsymbol{\varepsilon}^{\text{i}}, \boldsymbol{\alpha}, T)}{\partial \boldsymbol{\beta}}\,. \tag{3.26}$$

Substitution of Transformation (3.24) and Normality Rules (3.21), (3.22) and (3.25), (3.26) into Expression (3.23) gives

$$\varphi^{\text{c}}_{\text{loc}}(\boldsymbol{\sigma}, \boldsymbol{\beta}\,; \boldsymbol{\varepsilon} - \boldsymbol{\varepsilon}^{\text{i}}, \boldsymbol{\alpha}, T) = (1 - \mu) \left(\frac{\partial \varphi^{\text{c}}_{\text{loc}}}{\partial \boldsymbol{\sigma}} : \boldsymbol{\sigma} + \frac{\partial \varphi^{\text{c}}_{\text{loc}}}{\partial \boldsymbol{\beta}} : \boldsymbol{\beta} \right). \tag{3.27}$$

The first-order sufficient condition for the point $(\boldsymbol{\sigma}, \boldsymbol{\beta})$ to be a local maximum is that Eqs. (3.25), (3.26) and (3.27) hold. If $\varphi^{\text{c}}_{\text{loc}}$ is a homogeneous function, according to Eq. (3.27) it is a homogeneous function of degree $1/(1 - \mu)$. If $\varphi^{\text{c}}_{\text{loc}}$

is not a homogeneous function, the value for $\mu = \mu(\boldsymbol{\varepsilon} - \boldsymbol{\varepsilon}^{\mathrm{i}}, \boldsymbol{\alpha}, T)$ is obtained from Eq. (3.27).

It is worth noting that the specific complementary dissipation function $\varphi^{\mathrm{c}}_{\mathrm{loc}}$ cannot be a homogeneous function of degree 1 in the variables $(\boldsymbol{\sigma}, \boldsymbol{\beta})$, since according to Expression (3.27) in such a case the quantity μ would be zero and Transformation (3.24) would vanish. This means that if the specific complementary dissipation function $\varphi^{\mathrm{c}}_{\mathrm{loc}}$ is a homogeneous function of degree 1, Transformation (3.24) vanishes and it must be replaced by a different transformation. This new transformation is used when time-independent processes are modelled.

Equation (B.17) of Appendix B shows that if the specific dissipation function φ_{loc} is a homogeneous function of degree $1/\mu$ $(\neq 1)$, the specific complementary dissipation function $\varphi^{\mathrm{c}}_{\mathrm{loc}}$ is a homogeneous function of degree $1/(1-\mu)$.

4. Discussion and conclusions

The present paper refers to thermomechanics as a science which is a combination of thermodynamics and continuum mechanics. Since the field of the present work is the evaluation of constitutive equations for solid materials, the application of thermodynamics with internal variables was an obvious choice from the many dialects of thermodynamics.

The topic of this paper is the derivation of the normality rule for time-dependent deformation using the principle of maximal rate of entropy production. This principle is due to ZIEGLER [1, p. 134]. Since Ziegler did not cast his principle into an exact mathematical framework, it is done in this paper. The standard formulation of the principle of maximal rate of entropy production is shown to give a normality that is suitable for material models describing time-dependent processes.

The principle of maximal rate of entropy production is not usually used to obtain the normality rule but instead of that often the approach by the French school of thermodynamics is followed. The French school of thermodynamics assumes that the dissipation potential is a continuous and a convex scalar valued function of the flux variables. It is also non-negative function with a zero value at the origin of the space of the flux variables. According to the French school of thermodynamics, if the dissipation potential satisfies the above-mentioned properties, the normality rule is a sufficient condition for satisfaction of the Clausius–Duhem inequality. The above description is based on LEMAITRE and CHABOCHE [14, Sec. 2.4.3]. The principle of maximal rate of entropy production, however, assumes that real processes follow a path which maximises the entropy production. At the same time the Clausius–Duhem inequality is satisfied. The approach by the French school of thermodynamics is mainly a mathematical construction. Since thermomechanics describes natural events a more physical

background is needed, the author proposes to use the principle of maximal rate of entropy production.

If the state is expressed by the quantities $(\boldsymbol{\varepsilon} - \boldsymbol{\varepsilon}^{\mathrm{i}}, \boldsymbol{\alpha}, T)$ and the material model is given by the specific dissipation function whose variables are the fluxes $(\dot{\boldsymbol{\varepsilon}}^{\mathrm{i}}, \dot{\boldsymbol{\alpha}})$ and the state $(\boldsymbol{\varepsilon} - \boldsymbol{\varepsilon}^{\mathrm{i}}, \boldsymbol{\alpha}, T)$, the mechanical part of the normality rule was shown to take the form

$$\boldsymbol{\sigma} = \mu\rho \frac{\partial \varphi_{\mathrm{loc}}(\dot{\boldsymbol{\varepsilon}}^{\mathrm{i}}, \dot{\boldsymbol{\alpha}}; \boldsymbol{\varepsilon} - \boldsymbol{\varepsilon}^{\mathrm{i}}, \boldsymbol{\alpha}, T)}{\partial \dot{\boldsymbol{\varepsilon}}^{\mathrm{i}}} \quad \text{and} \quad \boldsymbol{\beta} = \mu\rho \frac{\partial \varphi_{\mathrm{loc}}(\dot{\boldsymbol{\varepsilon}}^{\mathrm{i}}, \ldots)}{\partial \dot{\boldsymbol{\alpha}}}. \tag{4.1}$$

It was also shown that the specific dissipation function φ_{loc} has to obey the following condition:

$$\varphi_{\mathrm{loc}}(\dot{\boldsymbol{\varepsilon}}^{\mathrm{i}}, \dot{\boldsymbol{\alpha}}; \boldsymbol{\varepsilon} - \boldsymbol{\varepsilon}^{\mathrm{i}}, \boldsymbol{\alpha}, T) = \mu \left(\frac{\partial \varphi_{\mathrm{loc}}}{\partial \dot{\boldsymbol{\varepsilon}}^{\mathrm{i}}} : \dot{\boldsymbol{\varepsilon}}^{\mathrm{i}} + \frac{\partial \varphi_{\mathrm{loc}}}{\partial \dot{\boldsymbol{\alpha}}} : \dot{\boldsymbol{\alpha}} \right). \tag{4.2}$$

According to Expression (4.2) if φ_{loc} is a homogeneous function, it is a homogeneous function of degree $1/\mu$. If φ_{loc} is not a homogeneous function, the value for $\mu = \mu(\boldsymbol{\varepsilon} - \boldsymbol{\varepsilon}^{\mathrm{i}}, \boldsymbol{\alpha}, T)$ is obtained from Equation (4.2).

In the case where the material model is given by the specific complementary dissipation function whose variables are the forces $(\boldsymbol{\sigma}, \boldsymbol{\beta})$ and the state $(\boldsymbol{\varepsilon} - \boldsymbol{\varepsilon}^{\mathrm{i}}, \boldsymbol{\alpha}, T)$, the specific complementary dissipation function $\varphi^{\mathrm{c}}_{\mathrm{loc}}$ is a Legendre partial transformation of the specific dissipation function φ_{loc}. In this case the mechanical part of the normality rule was shown to take the form

$$\dot{\boldsymbol{\varepsilon}}^{\mathrm{i}} = \rho \frac{\partial \varphi^{\mathrm{c}}_{\mathrm{loc}}(\boldsymbol{\sigma}, \boldsymbol{\beta}; \boldsymbol{\varepsilon} - \boldsymbol{\varepsilon}^{\mathrm{i}}, \boldsymbol{\alpha}, T)}{\partial \boldsymbol{\sigma}} \quad \text{and} \quad \dot{\boldsymbol{\alpha}} = \rho \frac{\partial \varphi^{\mathrm{c}}_{\mathrm{loc}}(\boldsymbol{\sigma}, \ldots)}{\partial \boldsymbol{\beta}}. \tag{4.3}$$

As above a condition for the dissipation potential was obtained. It is

$$\varphi^{\mathrm{c}}_{\mathrm{loc}}(\boldsymbol{\sigma}, \boldsymbol{\beta}; \boldsymbol{\varepsilon} - \boldsymbol{\varepsilon}^{\mathrm{i}}, \boldsymbol{\alpha}, T) = (1 - \mu) \left(\frac{\partial \varphi^{\mathrm{c}}_{\mathrm{loc}}}{\partial \boldsymbol{\sigma}} : \boldsymbol{\sigma} + \frac{\partial \varphi^{\mathrm{c}}_{\mathrm{loc}}}{\partial \boldsymbol{\beta}} : \boldsymbol{\beta} \right). \tag{4.4}$$

According to Expression (4.4) if $\varphi^{\mathrm{c}}_{\mathrm{loc}}$ is a homogeneous function, it is a homogeneous function of degree $1/(1 - \mu)$. If $\varphi^{\mathrm{c}}_{\mathrm{loc}}$ is not a homogeneous function, the value for $\mu = \mu(\boldsymbol{\varepsilon} - \boldsymbol{\varepsilon}^{\mathrm{i}}, \boldsymbol{\alpha}, T)$ is obtained from Equation (4.4).

This paper does not give any examples on the application of thermomechanics for material model verification, but the reader is asked to study, for example, the lecture notes by SANTAOJA [15].

Appendix A. Legendre transformation

The investigation is started with a given scalar-valued function F, which is assumed to be a function of two independent sets of tensorial variables, which

are $\mathbf{u}^1, \ldots, \mathbf{u}^m$ and $\mathbf{w}^1, \ldots, \mathbf{w}^n$, i.e.

$$F = F(\mathbf{u}^1, \ldots, \mathbf{u}^m, \mathbf{w}^1, \ldots, \mathbf{w}^n) . \tag{A.1}$$

The new independent set of second-order tensorial variables $\boldsymbol{\gamma}^1, \ldots, \boldsymbol{\gamma}^m$ is assumed to be defined by

$$\boldsymbol{\gamma}^i := a \frac{\partial F(\mathbf{u}^1, \ldots, \mathbf{u}^m, \mathbf{w}^1, \ldots, \mathbf{w}^n)}{\partial \mathbf{u}^i}, \qquad i = 1, \ldots, m , \tag{A.2}$$

where a is a coefficient independent of $\mathbf{u}^i, \mathbf{w}^j$ and $\boldsymbol{\gamma}^i$ ($i = 1, \ldots, m$ and $j = 1, \ldots, n$). The variables $\mathbf{u}^i$ are called the active variables and the variables $\mathbf{w}^j$ are called the passive variables of the transformation. A new function Ω, called the Lagende partial transformation, is introduced. It is defined by

$$b\, \Omega(\boldsymbol{\gamma}^1, \ldots, \boldsymbol{\gamma}^m, \mathbf{w}^1, \ldots, \mathbf{w}^n) := \sum_{i=1}^{m} \boldsymbol{\gamma}^i : \mathbf{u}^i - a F(\mathbf{u}^1, \ldots, \mathbf{u}^m, \mathbf{w}^1, \ldots, \mathbf{w}^n) . \tag{A.3}$$

The variables $\mathbf{w}^j$ and $\boldsymbol{\gamma}^i$ are given arbitrary variations $\delta\mathbf{w}^j$ and $\delta\boldsymbol{\gamma}^i$. Thus, Eq. (A.3) gives

$$\begin{aligned} \delta\, b\, \Omega(\boldsymbol{\gamma}^1, \ldots, \boldsymbol{\gamma}^m, \mathbf{w}^1, \ldots, \mathbf{w}^n) &= \sum_{i=1}^{m} b \frac{\partial \Omega}{\partial \boldsymbol{\gamma}^i} : \delta\boldsymbol{\gamma}^i + \sum_{j=1}^{n} b \frac{\partial \Omega}{\partial \mathbf{w}^j} : \delta\mathbf{w}^j \\ &= \sum_{i=1}^{m} (\boldsymbol{\gamma}^i : \delta\mathbf{u}^i + \delta\boldsymbol{\gamma}^i : \mathbf{u}^i) - \sum_{i=1}^{m} a \frac{\partial F}{\partial \mathbf{u}^i} : \delta\mathbf{u}^i - \sum_{j=1}^{n} a \frac{\partial F}{\partial \mathbf{w}^j} : \delta\mathbf{w}^j , \end{aligned} \tag{A.4}$$

which yields

$$\begin{aligned} &\sum_{i=1}^{m} b \frac{\partial \Omega}{\partial \boldsymbol{\gamma}^i} : \delta\boldsymbol{\gamma}^i + \sum_{j=1}^{n} b \frac{\partial \Omega}{\partial \mathbf{w}^j} : \delta\mathbf{w}^j \\ &\quad = \sum_{i=1}^{m} \left(\boldsymbol{\gamma}^i - a \frac{\partial F}{\partial \mathbf{u}^i} \right) : \delta\mathbf{u}^i + \sum_{i=1}^{m} \mathbf{u}^i : \delta\boldsymbol{\gamma}^i - \sum_{j=1}^{n} a \frac{\partial F}{\partial \mathbf{w}^j} : \delta\mathbf{w}^j . \end{aligned} \tag{A.5}$$

According to Eq. (A.2) the first term on the right-hand side of Eq. (A.5) vanishes, giving the following equations:

$$\mathbf{u}^i = b \frac{\partial \Omega(\boldsymbol{\gamma}^1, \ldots, \boldsymbol{\gamma}^m, \mathbf{w}^1, \ldots, \mathbf{w}^n)}{\partial \boldsymbol{\gamma}^i}, \qquad i = 1, \ldots, m \tag{A.6}$$

and

$$a\,\frac{\partial F(\mathbf{u}^1,\ldots,\mathbf{u}^m,\mathbf{w}^1,\ldots,\mathbf{w}^n)}{\partial \mathbf{w}^j} = -\,b\,\frac{\partial\,\Omega(\boldsymbol{\gamma}^1,\ldots,\boldsymbol{\gamma}^m,\mathbf{w}^1,\ldots,\mathbf{w}^n)}{\partial \mathbf{w}^j}, \tag{A.7}$$

$$j = 1,\ldots,n.$$

Appendix B. Legendre transformation of a homogeneous function

The Legendre transformation of a homogeneous function is investigated here. It is shown that the Legendre transformation of a homogeneous function is a homogeneous function. This does not hold if the original function is a homogeneous function of degree one.

A scalar-valued function F of m different tensorial variables $\mathbf{u}^1,\ldots,\mathbf{u}^m$ is studied. Function F is expressed as follows:

$$F = F(\mathbf{u}^1,\ldots,\mathbf{u}^m) \tag{B.1}$$

is assumed to be a homogeneous function of degree ω and therefore it satisfies the following definition and equation:

$$F(k\,\mathbf{u}^1,\ldots,k\,\mathbf{u}^m) := k^{\omega}\,F(\mathbf{u}^1,\ldots,\mathbf{u}^m) \tag{B.2}$$

and

$$\omega\,F(\mathbf{u}^1,\ldots,\mathbf{u}^m) = \left(\frac{\partial F}{\partial \mathbf{u}^1}:\mathbf{u}^1 + \ldots + \frac{\partial F}{\partial \mathbf{u}^m}:\mathbf{u}^m\right), \tag{B.3}$$

where k is an arbitrary positive real number {see e.g. WIDDER [13, p. 19 and 20]}.

Next, m second-order tensors $\boldsymbol{\gamma}^i,\ldots\,\boldsymbol{\gamma}^m$ are introduced by defining

$$\boldsymbol{\gamma}^i := a\,\frac{\partial F(\mathbf{u}^1,\ldots,\mathbf{u}^m)}{\partial \mathbf{u}^i}, \qquad i = 1,\ldots,m, \tag{B.4}$$

where a is an arbitrary coefficient independent of both $\mathbf{u}^i$ and $\boldsymbol{\gamma}^i$ $(i = 1,\ldots,m)$.

The Legendre transformation Ω of the function F is defined as in Appendix A, i.e.

$$b\,\Omega(\boldsymbol{\gamma}^1,\ldots,\boldsymbol{\gamma}^m) := \sum_{i=1}^{m} \boldsymbol{\gamma}^i:\mathbf{u}^i - a\,F(\mathbf{u}^1,\ldots,\mathbf{u}^m), \tag{B.5}$$

where the coefficient b does not depend on the tensorial variables $\mathbf{u}^i$ and $\boldsymbol{\gamma}^i$ $(i = 1,\ldots,m)$.

Substitution of Definition (B.4) into Expression (B.3) gives

$$\omega F(\mathbf{u}^1, \ldots, \mathbf{u}^m) = \frac{1}{a} \sum_{i=1}^{m} \boldsymbol{\gamma}^i : \mathbf{u}^i , \tag{B.6}$$

which yields

$$\sum_{i=1}^{m} \boldsymbol{\gamma}^i : \mathbf{u}^i = a\, \omega\, F(\mathbf{u}^1, \ldots, \mathbf{u}^m) . \tag{B.7}$$

Substituting Eq. (B.7) into Legendre Transformation (B.5) gives

$$F(\mathbf{u}^1, \ldots, \mathbf{u}^m) = c\, \Omega(\boldsymbol{\gamma}^1, \ldots, \boldsymbol{\gamma}^m) , \tag{B.8}$$

where the coefficient c is

$$c = \frac{b}{a\,\omega - a} . \tag{B.9}$$

Once again the definition of variables $\boldsymbol{\gamma}^i$ is used. Thus, the variables $\boldsymbol{\gamma}^i$ in Eq. (B.4) are substituted into the arguments of Ω on the right-hand side of Eq. (B.8) and the following equation is obtained:

$$F(\mathbf{u}^1, \ldots, \mathbf{u}^m) = c\, \Omega\left(a\, \frac{\partial F(\mathbf{u}^1, \ldots, \mathbf{u}^m)}{\partial \mathbf{u}^1} , \ldots , a\, \frac{\partial F(\mathbf{u}^1, \ldots, \mathbf{u}^m)}{\partial \mathbf{u}^m} \right) . \tag{B.10}$$

If the variables in Eq. (B.10) were changed by replacing $\mathbf{u}^i$ by $k\,\mathbf{u}^i$, Eq. (B.10) would take the following form:

$$\begin{aligned} &F(k\,\mathbf{u}^1, \ldots, k\,\mathbf{u}^m) \\ &\qquad = c\, \Omega\left(a\, \frac{\partial F(k\,\mathbf{u}^1, \ldots, k\,\mathbf{u}^m)}{\partial (k\,\mathbf{u}^1)} , \ldots , a\, \frac{\partial F(k\,\mathbf{u}^1, \ldots, k\,\mathbf{u}^m)}{\partial (k\,\mathbf{u}^m)} \right) . \end{aligned} \tag{B.11}$$

The definition of a homogeneous function given by Definition (B.2) allows Eq. (B.11) to be written in the form

$$\begin{aligned} &k^{\omega}\, F(\mathbf{u}^1, \ldots, \mathbf{u}^m) \\ &\qquad = c\, \Omega\left(a\, \frac{\partial [k^{\omega}\, F(\mathbf{u}^1, \ldots, \mathbf{u}^m)]}{\partial (k\,\mathbf{u}^1)} , \ldots , a\, \frac{\partial [k^{\omega}\, F(\mathbf{u}^1, \ldots, \mathbf{u}^m)]}{\partial (k\,\mathbf{u}^m)} \right) . \end{aligned} \tag{B.12}$$

For the partial derivatives of the arguments of the Legendre transformation Ω on the right-hand side of Eq. (B.12), the following equations hold:

$$k^{\omega - 1}\, \frac{\partial F(\mathbf{u}^1, \ldots, \mathbf{u}^m)}{\partial \mathbf{u}^i} = \frac{\partial [k^{\omega}\, F(\mathbf{u}^1, \ldots, \mathbf{u}^m)]}{\partial (k\,\mathbf{u}^i)} , \qquad i = 1, \ldots, m . \tag{B.13}$$

Substitution of Definition (B.4) into the left-hand side of Eq. (B.13) yields

$$\frac{1}{a}\, k^{\omega-1}\, \boldsymbol{\gamma}^i = \frac{\partial[k^\omega\, F(\mathbf{u}^1,\ldots,\mathbf{u}^m)]}{\partial(k\,\mathbf{u}^i)}, \qquad i=1,\ldots,m\,. \tag{B.14}$$

Substitution of Eq. (B.8) into the left-hand side of Eq. (B.12) and Eq. (B.14) into the right-hand side of Eq. (B.12) gives the following equality:

$$k^\omega\, \Omega(\boldsymbol{\gamma}^1,\ldots,\boldsymbol{\gamma}^m) = \Omega(k^{\omega-1}\,\boldsymbol{\gamma}^1,\ldots,k^{\omega-1}\,\boldsymbol{\gamma}^m)\,. \tag{B.15}$$

Changing the variables by replacing $k^{\omega-1}$ by t allows Eq. (B.15) to be written in the form

$$t^{\omega/(\omega-1)}\, \Omega(\boldsymbol{\gamma}^1,\ldots,\boldsymbol{\gamma}^m) = \Omega(t\,\boldsymbol{\gamma}^1,\ldots,t\,\boldsymbol{\gamma}^m). \tag{B.16}$$

Equation (B.16) therefore shows the Legendre transformation $\Omega(\boldsymbol{\gamma}^1,\ldots,\boldsymbol{\gamma}^m)$ to be a homogeneous function of degree $\omega/(\omega-1)$, where ω is the degree of the original function F. This does not hold for the case $\omega = 1$, as can be seen in Eqs. (B.9) and (B.16).

If the original function F were a homogeneous function of degree $\mu = 1/\kappa$, the function Ω would be a homogeneous function of degree $1/(1-\mu)$. As above, this does not hold for the case $\mu = 1$.

Acknowledgments

The present study was supported by the RAKE project (Structural Analyses for Nuclear Power Plant Components). The preparation of this paper was funded by the Ministry of Trade and Industry (Finland) and the Technical Research Centre of Finland. Their financial support is greatly appreciated.

References

1. H. ZIEGLER, *Some extremum principles in irreversible thermodynamics with application to continuum mechanics*, [In:] Progress in Solid Mechanics. Vol. IV, I. W. SNEDDON and R. HILL (F.R.S.) [Eds], North-Holland Publishing Company, 93–198, Amsterdam 1963.
2. Q. S. NGUYEN, *Stability and nonlinear solid mechanics*, J. Wiley & Sons, New York 2000.
3. K. SHIZAWA and H. M. ZBIB, *A thermomechanical theory of gradient elastoplasticity with dislocation density tensor. I: Fundamentals*, Internal Journal of Plasticity, **15**, 899–938, 1999.
4. G. T. HOULSBY and A. M. PUZRIN, *A thermomechanical framework for constitutive models for rate-independent dissipative materials*, Internal Journal of Plasticity, **16**, 1017–1047, 2000.

5. K. R. RAJAGOPAL and A. R. SRINIVASA, *Mechanics of the inelastic behaviour of materials. Part II: Inelastic response*, International Journal of Plasticity, **10–11**, 969–995, 1998.

6. P. JUSSILA, *Thermomechanical model for compacted bentonite*, [in:] VIII Suomen Mekaniikkapäivät (VIII Finnish Mechanics Days), Espoo, Finland, June 12–13, 2003. P. RÅBACK, K. SANTAOJA & R. STENBERG [Eds.], Helsinki University of Technology Laboratory of Mechanics of Materials, Research Reports – TKK-LO-36, 509–522.

7. G. A. MAUGIN, *The thermomechanics of plasticity and fracture*, Cambridge University Press, Cambridge 1992.

8. H. ZIEGLER, *An introduction to thermomechanics*, 2nd ed. North-Holland Publishing Company, Amsterdam 1983.

9. H. ZIEGLER and C. WEHRLI, *The derivation of constitutive relations from the free energy and the dissipation function*, [in:] Advances in Applied Mechanics, T. Y. WU and J. W. HUTCHINSON [Eds.], **25**, 183–238, 1987.

10. C. TRUESDELL and W. NOLL, *The nonlinear field theories of mechanics*, [in:] Encyclopedia of Physics, Vol. III/3, S. Flügge [Ed.], Springer-Verlag, Berlin/Heidelberg, 1–602, 1965.

11. D. G. LUENBERGER, *Introduction to linear and nonlinear programming*, Addison-Wesley Publishing Company, Massachusetts 1973.

12. G. ARFKEN, *Mathematical methods for physicists* (3rd ed.), Academic Press Inc., New York 1985.

13. D. V. WIDDER, *Advanced calculus* (2nd ed.), Dover Publications, Inc., New York 1989.

14. J. LEMAITRE and J. L. CHABOCHE, *Mechanics of solid materials*, Cambridge University Press, New-York 1990, [Originally published in French as: Mécanique des matériaux solides, Dunod (and Bordas), Paris 1985].

15. K. SANTAOJA, *Lecture notes on thermomechanics*, Helsinki University of Technology Publications in Mechanics of Materials, TKK-LO-32, Espoo 2001.

Received November 6, 2003.

Arch. Mech., **55**, 5–6, pp. 519–530, Warszawa 2003

Pseudoviscoelastic behavior of TiNi shape memory alloys under stress-controlled subloop loadings

H. TOBUSHI[(1)], M. ENDO[(2)], T. IKAWA[(1)] D. SHIMADA[(1)]

[(1)] *Department of Mechanical Engineering*
Aichi Institute of Technology
1247 Yachigusa, Yagusa-cho, Toyota 470-0392 Japan

[(2)] *Toshiba Ceramics Co., Ltd.*
Nishi-shinjuku 7-5-25, Shinjuku-ku, Tokyo 160-0023 Japan

THE SUPERELASTIC BEHAVIOR of TiNi shape memory alloy under various subloop loadings were investigated. The results obtained can be summarized as follows. (1) In the case of subloop loading under strain-controlled conditions, the reloading curve passes through the unloading-start point. In the case of stress-controlled conditions, the return-point memory does not appear. (2) In the case of subloop loading under stress-controlled conditions, strain increases under constant stress in the loading process and decreases in the unloading process. (3) In the case of subloop loading under stress-controlled conditions, stress decreases under constant strain in the loading process and increases in the unloading process. (4) The above-mentioned behavior concerning the return-point memory and the pseudoviscoelastic behavior similar to creep and stress relaxation, appear according to the martensitic transformation and the reverse transformation based on the variation in stress and temperature.

Key words: Shape memory alloy, superelasticity, subloop, return-point memory, creep, stress relaxation, titanium-nickel alloy, stress control.

1. Introduction

IN SHAPE MEMORY alloys (SMAs), the shape memory effect and superelastic characteristics appear based on the martensitic transformation (MT) [1–7]. In practical applications of SMAs, SMA elements are subjected to various thermomechanical loadings. In order to design SMA elements, the thermomechanical properties of SMAs are important.

Recently it has been reported that the deformation behavior under subloop loadings is different between the strain-controlled condition and the stress-controlled condition [8]. Although the return-point memory appears in the subloop loading under the strain-controlled condition, it does not appear under the stress-controlled condition. In the case of the stress-controlled condition, temperature increases due to the MT in the loading process and decreases due to the reverse

transformation in the unloading process. Both the stress and strain vary based on these variations in temperature, and therefore the return-point memory does not appear in the case of stress-controlled conditions [9]. Recently it has been also reported that creep deformation and stress relaxation appear in SMAs under the subloop loadings [10].

In the present study, the superelastic behavior of TiNi SMAs under various loading conditions are investigated experimentally. The conditions to cause the return-point memory are discussed. The pseudoviscoelastic behavior of creep deformation and stress relaxation under the subloop loadings with the stress-controlled condition is also discussed.

2. Experimental methods

2.1. Materials and specimens

The material tested was a rectilinear Ti–55.4wt%Ni SMA wire, 0.75 mm in diameter, produced by Furukawa Electric Co. Its straightness was shape-memorized through shape-memory processing. This was done by holding the wire rectilinear at 673 K for 60 min followed by cooling in the furnace. The reverse-transformation finish temperature A_f was about 323 K.

2.2. Experimental apparatus

The SMA testing machine was used. The machine was composed of the tensile machine and the heating-cooling device. Displacement was measured by an extensometer with gauge length of 20 mm. Temperature was measured by a thermocouple, 0.1 mm in diameter, which was pressed on the specimen at the central part of the gauge length.

2.3. Experimental procedure

In order to investigate the superelastic properties of the material, the following five kinds of thermomechanical tension tests under various loading conditions were carried out by keeping the ambient temperature $T = 353$ K above A_f constant. Stress and strain were treated in terms of nominal stress and nominal strain, respectively. Therefore the stress-controlled and strain-controlled conditions mean the load-controlled and displacement-controlled conditions, respectively.

1. *Full-loop loading under constant strain rate and stress rate*
   In the tension test, the full-loop loading and unloading were applied under constant strain rate $\dot{\varepsilon}$ and stress rate $\dot{\sigma}$. The MT completes in the loading process and the reverse transformation completes in the unloading process.

2. *Subloop loading under constant strain rate*
Strain rate $\dot{\varepsilon}$ was kept constant during the loading and unloading processes. In the loading process, it was unloaded before the completion of the MT. In the unloading process, it was reloaded before the completion of the reverse transformation. The subloop-loading processes were repeated.

3. *Subloop loading under constant stress rate*
Stress rate $\dot{\sigma}$ was kept constant during the subloop-loading and unloading processes. The subloop-loading processes were repeated.

4. *Subloop loading under constant stress*
Stress was kept constant during the MT in the loading process and during the reverse transformation in the unloading process for a certain duration. Variation in strain was observed under constant stress.

5. *Subloop loading under constant strain*
Strain was kept constant during the MT in the loading process and during the reverse transformation in the unloading process for a certain duration. Variation in stress was observed under constant strain.

3. Experimental results and discussion

3.1. Full-loop superelastic behavior under constant strain rate and stress rate

The stress-strain curves obtained by the tension test under constant strain rate $\dot{\varepsilon}$ and stress rate $\dot{\sigma}$ are shown in Fig. 1. As it can be seen, in the case of $\dot{\varepsilon} = 1\%/\text{min}$, the overshoot occurs at the MT-start point M_S in the loading process and the MT progresses in the region of the upper stress plateau till the MT-end point M_F. In the unloading process, the undershoot occurs at the reverse-transformation start point A_S and the reverse transformation progresses in the region of the lower stress plateau till the end point A_F.

On the other hand, in the case of constant stress rate $\dot{\sigma}$, the overshoot at the point M_S and the undershoot at the point A_S do not appear. Both the MT and the reverse transformation progress with a certain slope of the curve between the points M_s and M_f and between the points A_s and A_f, respectively. The larger is the stress rate, the more steep will be the slope of the curve. The stress-strain curve under constant stress rate is similar to that under high strain rate [11, 12]. If the strain rate is high, the overshoot and undershoot do not appear, and temperature increases due to the MT in the loading process and decreases due to the reverse transformation in the unloading process. The variation in

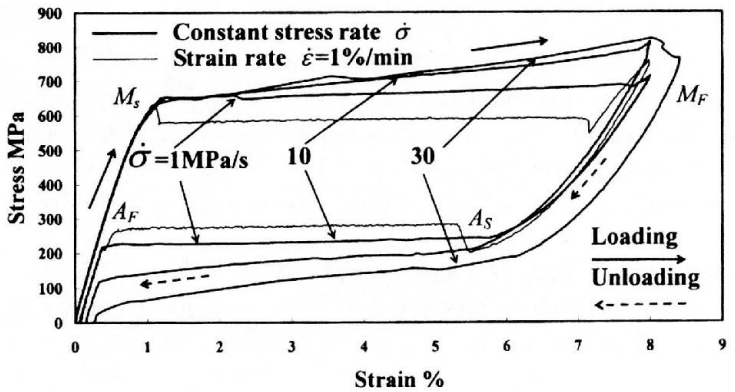

FIG. 1. Stress-strain curves for full-loop loading under constant strain rate $\dot{\varepsilon}$ and stress rate $\dot{\sigma}$.

temperature under constant stress rate is similar to that under high strain rate.

3.2. Subloop superelastic behavior under strain-controlled condition

The stress-strain curves obtained by the subloop loading test under constant strain rate $\dot{\varepsilon} = 1\%/\text{min}$ are shown in Fig. 2. In the test, the process (A_i, B_i and C_i) corresponds to unloading and the process (C_i, D_i and A_{i+1}) to reloading. The process (A_i, B_i) and the process (C_i, D_i) are elastic. The reverse transformation appears in the process (B_i, C_i) and the MT appears in the process (D_i, A_{i+1}). The MT stress decreases under cyclic deformation [13]. Therefore the MT stress plateau during the reloading process (D_i, A_{i+1}) decreases with an increase in the number of cycles N. The reloading curve (C_i, D_i and A_{i+1}) passes through the unloading-start point A_i. Therefore the return-point memory is observed in the case of the strain-controlled condition.

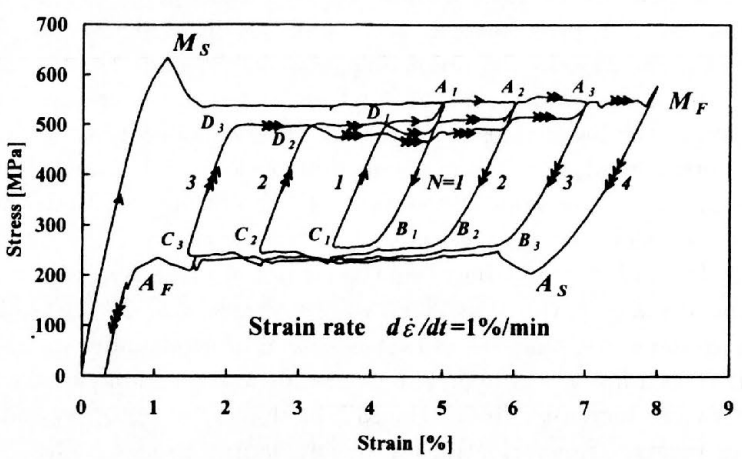

FIG. 2. Stress-strain curves for subloop loading under constant strain rate $\dot{\varepsilon}$.

3.3. Subloop superelastic behavior under stress-controlled condition

1. *Stress-strain curve*

The stress-strain curves obtained by the subloop loading test under constant stress rate $\dot{\sigma}$ are shown in Fig. 3. As it can be seen, strain increases in the early stage of unloading (A_i, B_i) and decreases in the early stage of reloading (D_i, E_i). The variation in strain is lager under low-stress rate.

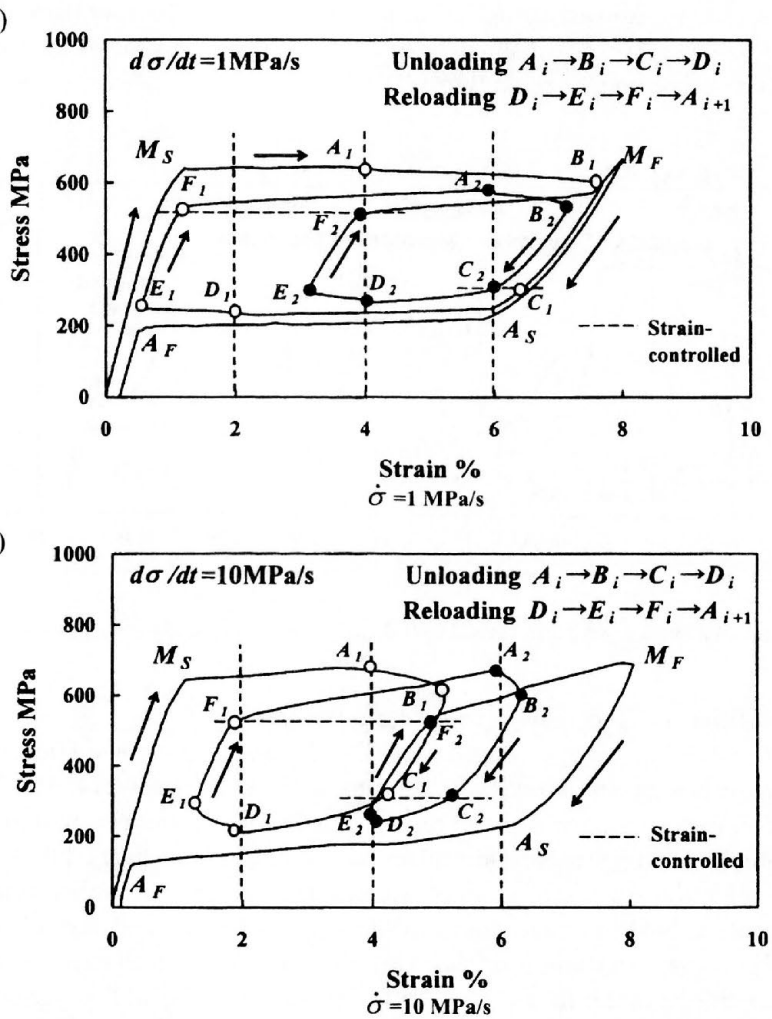

FIG. 3. Stress-strain curves for subloop loading under constant stress rate $\dot{\sigma}$.

These strain behaviors are quite different from those under constant strain rate observed in Fig. 2. In the reloading process, the stress-strain curve does not pass through the unloading-start point A_i. Therefore the return-

point memory which is observed under the strain-controlled condition does not appear under the stress-controlled condition.

2. *Variation in temperature*

The variation in temperature obtained during the subloop loading under $\dot{\sigma} = 1$ MPa/s is shown in Fig. 4. In Fig. 4, the variation in temperature is shown as a function of the accumulated strain path $\Sigma|\Delta L/L|$. As it can be seen, temperature increases due to the MT in the loading process and decreases in the early stage of unloading (A_i, B_i). Temperature decreases due to the reverse transformation in the unloading process and increases in the early stage of reloading (D_i, E_i).

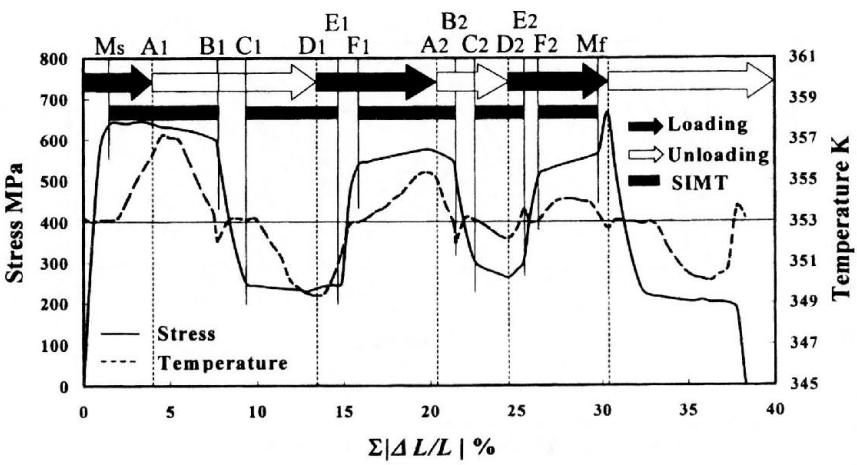

FIG. 4. Variation in temperature for subloop loading under constant stress rate $\dot{\sigma}$=1 MPa/s.

3. *Condition for progress of phase transformation*

The condition for the progress of the MT and the reverse transformation is governed by the kinetics of the phase transformation [14, 15]. The condition for the progress of the phase transformation under subloop loadings is shown on the stress-temperature phase diagram in Fig. 5 [9]. The conditions for the start and finish of the MT and the reverse transformation are expressed by the transformation lines M_S, M_F, A_S and A_F, respectively. Each transformation progresses in the transformation strip between the start line and the finish line. As it can be seen, the MT progresses if the state of stress and temperature varies to the direction in which the volume fraction ξ of the M-phase increases. The reverse transformation progresses if the state varies to the direction in which ξ decreases. Based on this consideration, the MT must progress in the early stage of unloading (A_i, B_i) under constant $\dot{\sigma}$ and strain increases as observed in Fig. 3. The reverse

transformation must progress in the early stage of reloading (D_i, E_i) and strain decreases as observed in Fig. 3.

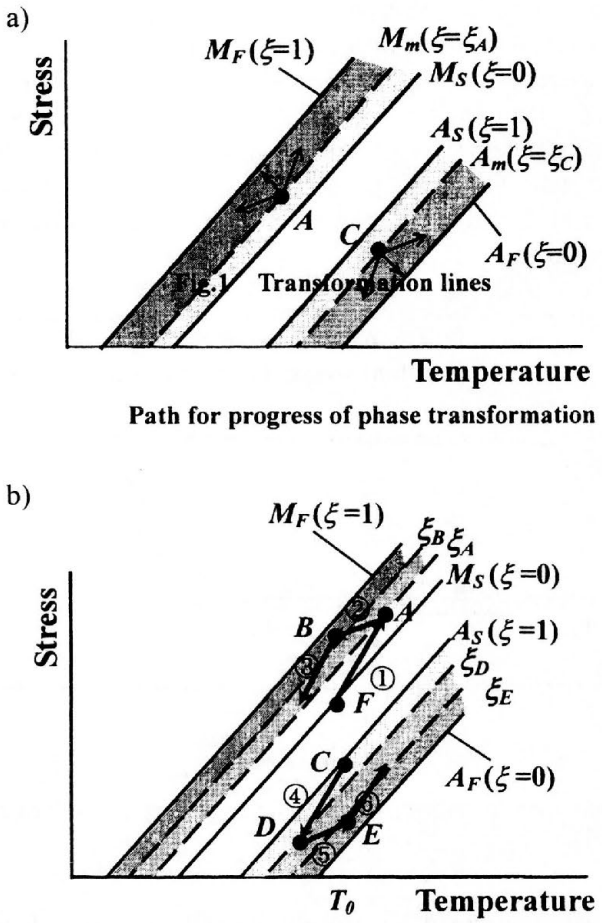

FIG. 5. Conditions for progress of the MT and the reverse transformation under subloop loadings: a) Path for progress of phase transformation, b) Path for progress and stop of phase transformation.

3.4. Strain behavior under constant stress

The stress-strain curve obtained by the subloop loading test under constant stress is shown in Fig. 6. In the loading process (O, A) and the unloading process (B, C), stress rate was 1 MPa/s. Stress was kept constant during the process

(A, M_F) following the point A and during the process (C, A_F) following the point C. The condition of constant stress will correspond to very low stress rate. Therefore, as observed in Figs. 3, 4 and 5, the MT progresses under low stress rate or constant stress due to decrease in temperature, resulting in increase in strain. The reverse transformation also progresses under constant stress due to increase in temperature, resulting in decrease in strain. The increase in strain under constant stress is similar to creep deformation and the decrease in strain under constant stress is similar to creep recovery after unloading which appear in the viscoelastic material. These creep and creep recovery in SMA must appear owing to the MT and the reverse transformation, respectively, based on the variation in temperature.

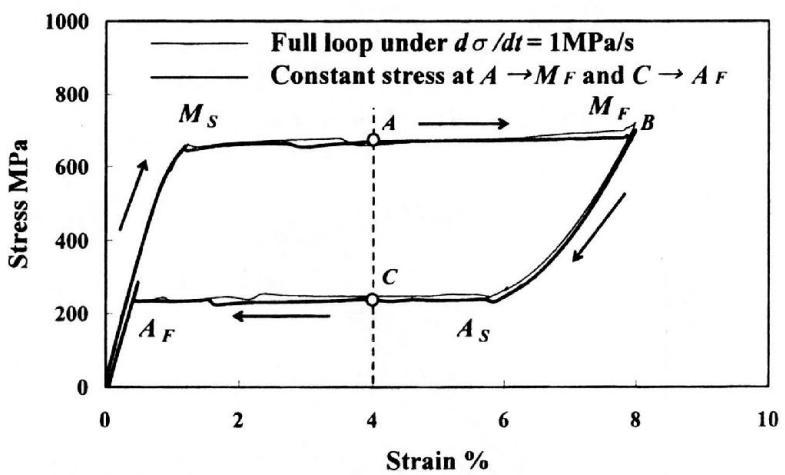

FIG. 6. Stress-strain curves for subloop loading under constant stress during loading and unloading.

As observed above, temperature varies due to the phase transformation during loading and unloading, and temperature returns to the ambient temperature with lapse of time under constant stress, resulting in variation in strain. In order to confirm the strain behavior during variation in temperature under constant stress, the heating-cooling test under constant stress was carried out. The relationship between strain and temperature obtained by the test is shown in Fig. 7. In the test, at first, strain $\varepsilon_0 = 4\%$ at the point A was applied at temperature $T^\circ = 333$ K. Following the loading to the point A and keeping stress $\sigma_0 = 460$ MPa at the point A constant, the specimen was cooled down to $T_l = 303$ K which was followed by heating up to $T_h = 393$ K. The heating and cooling under constant stress were repeated twice. As it can be seen in Fig. 7, strain decreases due to the reverse transformation between A_S and A_F in the heating process. In the

cooling process, strain increases due to the MT between M_S and M_F. Therefore, it is important to note that, even if the ambient temperature is constant in applications of SMAs, creep and creep recovery must appear if the temperature varies based on the phase transformation in the subloop loadings.

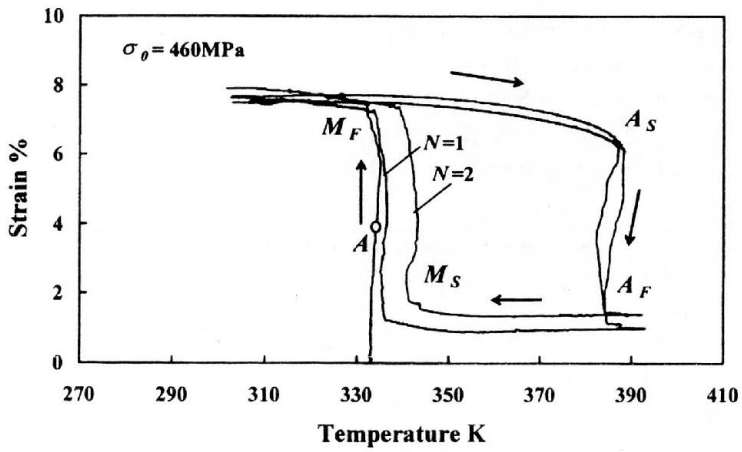

FIG. 7. Variation in strain during heating and cooling under constant stress.

3.5. Stress behavior under constant strain

The stress-strain curve obtained by the subloop loading test under constant strain is shown in Fig. 8. In the loading and unloading processes, stress rate was 30 MPa/s. Strain was kept constant for 10 min during the loading process (A_i, B_i) and during the unloading process (C_i, D_i). As it can be seen in Fig. 8, stress decreases under constant strain during (A_i, B_i) and increases during (C_i, D_i). The decrease in stress and the increase in stress stop on the upper stress plateau and on the lower stress plateau of the stress-strain curve under low strain rate, respectively.

The variations in stress and temperature during the first step of the subloop loading $(O, M_S, A_1$ and $B_1)$ are shown in Fig. 9. In the test, stress rate was constant during loading (O, M_S and A_1) and strain was kept constant during (A_1, B_1). As it can be seen in Fig. 9, temperature increases due to the MT during loading (M_S, A_1). Both the stress and temperature decrease markedly just after keeping the strain constant at the point A_1 and remain constant thereafter till the point B_1. Although temperature varies due to the MT in the early stage under constant strain, temperature approaches the ambient temperature after the early stage. The decrease in stress under constant strain is similar to stress relaxation, and the increase in stress under constant strain is similar to stress recovery after unloading which appear in the viscoelastic material. These stress

relaxation and stress recovery must appear owing to the MT and the reverse transformation, respectively, based on the variation in temperature.

In the experiments of the present study, temperature was controlled to keep the ambient temperature constant. Therefore the variation in temperature of the material depends on the heating and cooling conditions. This means that the variations in stress and strain which appear based on the MT due to the variation in temperature, depend on the size of the SMA elements and the conditions of heat transfer between the SMA elements and atmosphere. Therefore, in order to design the SMA elements, this pseudoelastic behavior must be taken into account in the case of the stress-controlled subloop loadings.

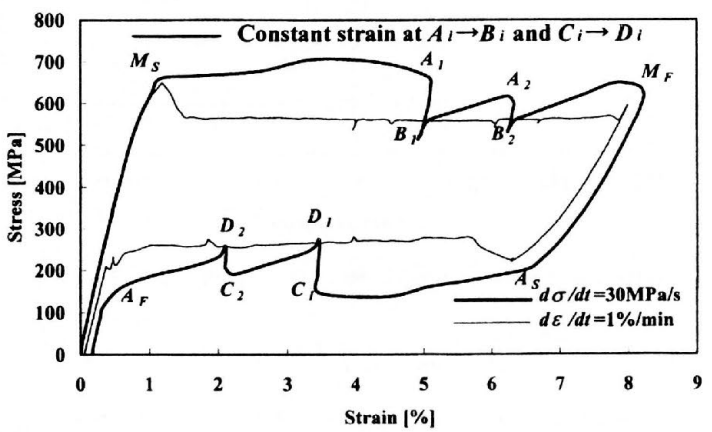

FIG. 8. Stress-strain curves for subloop loading under constant strain during loading and unloading.

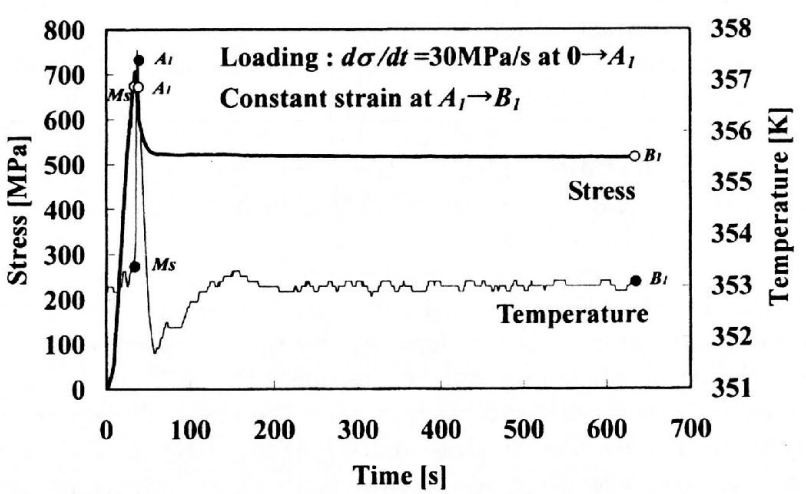

FIG. 9. Variations in stress and temperature during subloop loading with constant strain.

4. Conclusions

The superelastic behavior of TiNi SMA under various subloop loadings has been investigated. The results obtained can be summarized as follows.

1. In the case of subloop loading under strain-controlled conditions, the reloading curve passeses through the unloading-start point. In the case of stress-controlled conditions, the return-point memory does not appear.
2. In the case of subloop loading under stress-controlled conditions, strain increases under constant stress in the loading process and decreases in the unloading process.
3. In the case of subloop loading under stress-controlled conditions, stress decreases under constant strain in the loading process and increases in the unloading process.
4. The above-mentioned behavior concerning the return-point memory and the pseudoviscoelastic behaviors similar to creep and stress relaxation appears according to the MT and the reverse transformation based on the variation in stress and temperature.

Acknowledgments

The experimental work of this study was carried out with the assistance of the students in Aichi Institute of Technology, to whom the authors express their gratitude. The authors are also grateful to the Scientific Research (C) in Grants-in-Aid for Scientific Research by the Japan Society for Promotion of Science for financial support.

References

1. H. FUNAKUBO [Ed.], *Shape memory alloys*, Gordon and Breach Science Pub., 1987.
2. T. W. DUERIG, K. N. MELTON, D. STOCKEL and C. M. WAYMAN [Eds.], *Engineering aspects of shape memory alloys*, Butterworth-Heinemann, 1990.
3. K. OTUKA and C. M. WAYMAN [Eds.], *Shape memory materials*, Cambridge University Press, 1998.
4. T. SABURI [Ed.], *Shape memory materials*, Trans Tech Pub., 2000.
5. B. BRANIECKI and K. TANAKA [Eds.], *Testing and modelling the behaviour of shape memory alloys*, Arch. Mech., **51**, 6, 647–911] 1999.
6. Y. Y. CHU and L. C. ZHAO [Eds.], *Shape memory materials and its applications*, Trans. Tech. Pub., 2002.
7. Q. P. SUN [Ed.], *IUTAM Symposium on mechanics of martensitic phase transformation in solids*, Kluwer Academic Pub., 2002.

8. G. SOCHA, B. RANIECKI and S. MIYAZAKI, *Influence of control parameters on inhomogeneity and the deformation behavior of Ti-51.0at%Ni SMA undergoing martensitic phase transformation at pure tension*, 33rd Solid Mechanics Conference, 369–370, 2000.

9. H. TOBUSHI, K. OKUMURA, M. ENDO and K. TANAKA, *Deformation behavior of TiNi shape-memory alloy under strain- or stress-controlled conditions*, Arch. Mech., **54**, 1, 75–91, 2002.

10. D. HELM and P. HAUPT, *Termomechanical behavior of shape memory alloys*, Smart Structures and Materials 2001, Proc. of SPIE, **4333**, 302–313, 2001.

11. S. P. GADAJ, W. K. NOWACKI and H. TOBUSHI, *Temperature evolution during tensile test of TiNi shape memory alloy*, Arch. Mech., **51**, 6, 649–663, 1999.

12. H. TOBUSHI, K. TANAKA, Y. SHIMENO, W. K. NOWACKI and S. P. GADAJ, *Influence of strain rate on superelastic behaviour of TiNi shape memory alloy*, Proc. Instn. Mech. Engrs., **213**, Part L., 93–102, 1999.

13. H. TOBUSHI, S. YAMADA, T. HACHISUKA, A. IKAI and K. TANAKA, *Thermomechanical properties due to martensitic and R-phase transformation of TiNi shape memory alloy subjected to cyclic loadings*, Smart Mater. Struct., **5**, 788–795, 1996.

14. K. TANAKA, S. KOBAYASHI and Y. SATO, *Thermomechanics of transformation pseudoelasticity and shape memory effect in alloys*, Inter. J. Plasticity, **2**, 59–72, 1986.

15. K. TANAKA, *A thermomechanical sketch of shape memory effets: one-dimensional tensile behavior*, Res Mechanica, **18**, 251–263, 1986.

Received December 2, 2002.

Arch. Mech., **55**, 5–6, pp. 531–553, Warszawa 2003

High-accuracy discretization methods for solid mechanics

A. I. TOLSTYKH, M. V. LIPAVSKII, D. A. SHIROBOKOV

Computing Center of Russian Academy of Sciences
Vavilova str. 40, 119991 Moscow, Russia.
e-mail:tol@ccas.ru

NOVEL HIGH-ACCURACY computational techniques for solid mechanics problems are presented. They include fourth-order and arbitrary-order finite difference methods based on Pade-type differencing formulas and a meshless method which uses radial basis functions in a "finite difference" mode. Some results illustrating high performance of the suggested numerical methods are displayed.

1. Introduction

AT PRESENT, though the finite element method (FEM) is a universally accepted numerical tool in computational solid mechanics, the trend has been observed toward developing alternative techniques in the context of problem-oriented methodologies (for example, for solving problems with large deformations and moving discontinuities). Besides, one can see considerable interest in increasing the accuracy of numerical methods in a broad sense. The merits of high-accuracy methods can be manifested at least in two ways.

First, they may serve as high-resolution tools capable of describing properly fine details of solutions (for example, stress concentrations in small regions).

Second, they can provide engineering accuracy with relatively small numbers of degrees of freedom. As a result, operation counts and hence computational costs dramatically go down (mainly due to reducing by orders of magnitude the operation counts for both direct and iterative solvers of algebraic systems).

In the present paper, novel ideas are presented concerning applications of high-accuracy techniques to solid mechanics. They include:

(i) a finite difference method based on fourth-order compact differencing (CD) operators;

(ii) an arbitrary-order schemes for parallel calculations based on linear combinations of second-order CD operators (multioperators);

(iii) a meshless method which uses radial basis functions in a finite-difference mode.

The above methodologies are aimed at different areas of applications. While (i), (ii) show their peak performance in the case of relatively simple geometries

(for example, in the case of simply shaped plates and shells), using (iii) makes sense if the problem formulations include complicated forms of boundaries or/and an expected solution is that for which meshless methods are preferable.

Though (iii) differs in a significant way from (i) and (ii), both types of techniques, in contrast to the majority of the existing methods for solid mechanics, have in common the strategy of a direct discretization of governing equations rather than following their weak formulations. It makes them compatible when using them in the framework of the domain decomposition approach.

Below, the outlines of the methods followed by estimates of their performance in the case of testing solid mechanics problems are presented.

2. High accuracy schemes based on compact differencing

2.1. Fourth-order method

The well documented second-order difference schemes seem to be not popular in solid mechanics applications since they are approximately as accurate as the simplest FEM methods but they are considerably less flexible. However, recent advances in computational fluid dynamics have shown that high-order schemes can be highly competitive. Among such methods there are the so-called compact schemes which exploit Pade-type differencing formulas which can be viewed as rational functions of difference operators defined at compact stencils.

The simplest compact differencing formulas for the first and second derivatives are due to Collatz and Numerov. Supposing a uniform mesh with the mesh size h, the approximations to the derivatives at each grid point $x_j = jh$ look as

$$
\begin{aligned}
&D_x^{(1)} = (I + \Delta_2/6)^{-1}\,\Delta_0/(2h) = \partial/\partial x - (h^4/180)\,\partial^5/\partial x^5 + O(h^6),\\
&D_x^{(2)} = (I + \Delta_2/12)^{-1}\,\Delta_2/h^2 = \partial^2/\partial x^2 - (h^4/240)\,\partial^6/\partial x^6 + O(h^6),\\
&\Delta_0 f_j = f_{j+1} - f_{j-1}, \qquad \Delta_2 f_j = f_{j+1} - 2f_j + f_{j-1},
\end{aligned}
\tag{2.1}
$$

where I is the unity operator. The above formulas are not only fourth-order approximations, but they also have very small numerical coefficients in their truncation errors thus providing a very high accuracy.

Using Eqs. (2.1) for spatial x, y, z coordinates, one can easily discretize any form of solid mechanics equations. For example, for the biharmonic equation in the Cartesian coordinates describing the Kirchhoff plate, one has

$$B_h w = D_x^{(2)} D_x^{(2)} w + D_y^{(2)} D_y^{(2)} w + 2 D_x^{(2)} D_y^{(2)} w = q,$$

where q is a loading function. To calculate $B_h w$ where w is a known grid function, one needs only to perform several tridiagonal Gauss eliminations. The solutions

of the above equation can be obtained by using the standard iteration procedures. Since B_h is a self-adjoint positive operator in an appropriate Hilbert space, the convergence estimates for preconditioned iterations can be quite favorable. In the case of simply supported plates, it is advantageous to solve the biharmonic equation by sequentially solving two Poisson equations.

As an example of applications, consider a Kirchhoff plate occupying in the (x, y) plane the domain $\Omega: -l \leq x \leq l$, $0 \leq y \leq m$. The flexural rigidity of the plate $D(x, y)$ is supposed to be a sufficiently smooth function of its arguments, the only exception being its possible discontinuity at $x = 0$. It is supposed also that the plate may be strenghthened by a stiffener with the bending and torsional rigidities B and C respectively. Then the z-displacement w of the plate satisfies the biharmonic equation in both subdomains $-l \leq x \leq 0$, $0 \leq y \leq m$ and $0 \leq x \leq l$, $0 \leq y \leq m$ with proper boundary conditions at $\partial\Omega$. At $x=0$, the variational principle [1] gives the following "jump" conditions:

$$
\begin{aligned}
&\left\lceil w \right\rceil = 0, \quad \left\lceil w_{,x} \right\rceil = 0, \quad \left\lceil D(w_{,xx} + \nu w_{,yy}) \right\rceil = -(Cw_{,xy})_{,y}, \\
&\left\lceil \{D(w_{,xx} + \nu w_{,yy})\}_{,x} + 2\{D(1-\nu)w_{,xy}\}_{,y} \right\rceil = -(Bw_{,yy})_{,yy}
\end{aligned} \tag{2.2}
$$

where ν is the Poisson coefficient and for a function $f(x, y)$, $\left\lceil f \right\rceil$ means $f(+0, y) - f(-0, y)$. In the particular case $B = C = 0$, $\lceil D \rceil = 0$, one has the interface conditions for the domain decomposition approach applied to plates with smoothly varying thickness.

Considering as an example the simply supported plate, we discretize the biharmonic equation using the above fourth-order compact differencing operators. To satisfy (2.2), a fifth-order formulas which relate $w_{,x}(-0, y)$ and $w_{,x}(+0, y)$ to w and $w_{,xx}$ at the "left" and "right" nodes respectively were constructed. Using them, a complete set of algebraic equations can be derived. In general, they can be solved by either direct or iterative solvers. The results presented below are obtained by alternately solving the "left" and "right" biharmonic equations.

The results of calculations with the standard-second order and the present fourth-order schemes for the square simply supported plates with a stiffener shown in Fig. 1 are presented in Table 1 for a sinusoidal load.

The bending and torsional rigidity of the stiffener were chosen as $B = 2$ and $C = 2$ respectively. The rigidity of the first plate $D = 1$, (Fig. 1a) was assumed for both sides of the plate while the rigidity of the second plate was set to different values for each side of the plate ($D = 1$, $x < 0$, $D = 2$, $x > 0$, Fig. 1b).

In the Table 1, the L_2 norms of the solution errors δ and the corresponding mesh convergence order k are displayed for several $N \times N$ meshes, the reference "exact" solution being obtained using a very fine mesh.

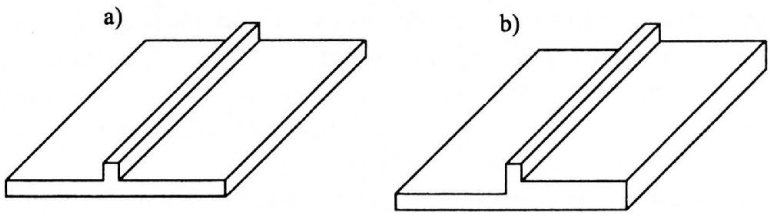

FIG. 1. Plates with stiffeners.

Table 1.

Plate	$D = 1$				$D = 1,\ x < 0;\quad D = 2,\ x > 0$			
Scheme	Second order		Fourth order		Second order		Fourth order	
$N \times N$	δ	k	δ	k	δ	k	δ	k
8×8	6.574e−3		3.532e−5		5.883e−3		4.941e−5	
16×16	1.582e−3	2.06	4.715e−6	2.91	1.395e−3	2.08	5.045e−6	3.29
32×32	3.870e−4	2.03	3.100e−7	3.93	3.386e−4	2.04	3.212e−7	3.97
64×64	9.566e−5	2.02	1.818e−8	4.09	8.339e−5	2.02	1.874e−8	4.10

As it may be seen from the Table 1, the present approach gives the solutions which are by several orders of magnitude more accurate than those obtained by the standard FD method (the latter is approximately as accurate as the FEM with linear elements). From the practical viewpoint, it means dramatic reduction of computational costs. For example, the fourth-order result for the 8×8 mesh is more accurate than the second-order one for 64×64 mesh. Note that the best algebraic solvers for two-dimensional cases give $O(N^2 \log N)$ operation counts.

2.2. Arbitrary-order discretizations

The standard FEM and FD methods (as well as the above described approach) are not able to enjoy in full measure the smoothness (or local smoothness) of exact solutions of many elasticity problems. Generally, they provide mesh-convergence orders which do not exceed the discretizations orders (the so-called "saturation" property). In contrast, accuracies of "saturation-free" methods depend on the numbers of existing exact solution derivatives (an interpolation with nodes chosen as zeroes of Chebyshev polynomials may serve as an example). On some occasions, the convergence can be exponential.

To increase the approximation the orders admitted by exact solutions smoothness, one usually tries to increase the values of some parameters defining the discretizations (for example, polynomial orders of local interpolants). In many cases,

it may complicate the resulting formulas and create some problems when implementing the constructed algorithms. An alternative way was suggested in [2] in the context of the parallel computational fluid dynamics. Its essence is using linear combinations ("multioperators") of special types of basis operators having relatively simple structures to provide theoretically arbitrary-order schemes. Recently [3], the idea was extended to the case of centered discretizations appropriate for solid mechanics equations.

To describe the extension, we return to operators (2.1) and consider without any loss of generality the x-derivatives only. Changing the coefficients $1/6$ and $1/12$ by a parameter c, we obtain one-parametric families $D_x^{(1)}(c)$ and $D_x^{(2)}(c)$ approximating the first and second derivatives with the second (rather than the fourth) order. Fixing now M distinct values of c, $(c = c_1, c_2, \ldots c_M)$, one can define multioperators for the x-derivatives [3]

$$D_M^{(1)} = \sum_{i=1}^{M} \gamma_i D_x^{(1)}(c_i), \qquad D_M^{(2)} = \sum_{i=1}^{M} \bar{\gamma}_i D_x^{(2)}(c_i),$$

where γ_i and $\bar{\gamma}_i$ satisfy the following linear systems:

$$\sum_{j=1}^{M} \gamma_j = 1, \quad \sum_{j=1}^{M} c_j^k \gamma_j = r_k, \quad k = 1, 2, \ldots M-1, \tag{2.3}$$

$$\sum_{j=1}^{M} \bar{\gamma}_j = 1, \quad \sum_{j=1}^{M} c_j^k \bar{\gamma}_j = \bar{r}_k, \quad k = 1, 2, \ldots M-1, \tag{2.4}$$

where r_k and $\bar{r}_k$ are known constants obtainable from the Taylor expansion series for the actions of $D_x^{(1)}(c_i)$ and $D_x^{(2)}(c_i)$ on sufficiently smooth functions projected into the space of grid functions. For example, in the case of $M = 3$, one has $(r_1, r_2) = (1/24, 3/640)$ and $(\bar{r}_1, \bar{r}_2) = (1/6, 1/30)$.

The above systems with the Vandermonde matrices are known to be always uniquely solvable. Moreover, their solutions can be easily obtained in analytical forms.

One can prove the following

THEOREM 1. *Let* $u \in C^{2M}$ *and* $\gamma_1, \gamma_2, \ldots, \gamma_M$, $\bar{\gamma}_1, \bar{\gamma}_2, \ldots, \bar{\gamma}_M$ *denote the solutions of (2.3), (2.4) for* $c_i \neq c_j$, $i \neq j$, $i, j = 1, 2, \ldots, M$. *Then*

$$D_M^{(1)} = \partial/\partial x + O(h^{2M}), \qquad D_M^{(2)} = \partial^2/\partial x^2 + O(h^{2M}).$$

To relax the ill-conditioning property of systems with the Vandermonde matrix when $M \to \infty$, we suppose that c_i are zeroes of the Chebyshev polynomials

for an interval $[c_{\min}, c_{\max}]$. Further limitations on the choice of c_i in the case of second derivatives follow from the requirement that multioperators must be negative definite, thus providing good convergence properties of relevant iterative procedures. For $M=3$, the sufficient conditions can be obtained in an analytical form [3].

Using multioperators for each coordinate, one can discretize any solid mechanics equation. The resulting schemes are especially advantageous when using parallel machines (at least, M processors are needed). In that case, the $2M$-th order admitted by the degree of solutions smoothness is realized by simultaneous and synchronous calculations of actions of basis operators. So the computational costs, when calculating actions of multioperators on a known grid function, turn out to be the same as those in the case of a single basis operator with a simple architecture.

To illustrate possible peak performance of the multioperators method, we consider the following BVP for the Poisson equation

$$\Delta u = -2\pi^2 \sin \pi x \sin \pi y,$$

$$x, y \in \Omega = [0,1] \times [0,1], \quad u|_{\partial\Omega} = 0.$$

Its exact solution is $\sin \pi x \sin \pi y$. The same exact solution can be obtained for the biharmonic equation describing bending of a square plate

$$\Delta\Delta u = 4\pi^4 \sin \pi x \sin \pi y, \quad x, y \in \Omega \tag{2.5}$$

with boundary conditions $u|_{\partial\Omega}=0$; $\partial^2 u/\partial x^2 = 0$ for $x=0, 1$; $\partial^2 u/\partial y^2 = 0$ for $y=0, 1$.

Sixth-order operators $D_M^{(2)}$ corresponding to the x and y coordinates ($M=3$) with proper restrictions imposed on c_1, c_2, c_3 were used to approximate the Laplace operator. In the case of problem (2.5), the biharmonic operator was considered as the square of the Laplace one.

The results for both problems for several meshes are shown in Table 2 ($N \times N$ stands for the number of grid points while k is the estimated mesh-convergence order).

As it may be seen from Table 2, the numerical solution accuracy is very high even if only 4 grid points are placed in each spatial directions. Again, the most important output of using the methodology is the possibility of obtaining an engineering accuracy with a very small number of degrees of freedom since it means computational costs savings up to many orders of magnitude. However, it should be emphasized that the technique exploits the solution smoothness. So its efficiency depends on the quality of meshes in the case of complicated geometries. In that case, one may suggest to use it in the framework of a domain

decomposition by constructing subdomains with "good" and "bad" boundaries. The latter category can be treated by using other methods. In particular, the multioperators method can be combined with the meshless radial basis function technique described in the next section.

Table 2.

Problem	Poisson eq.		Biharmonic eq.	
$N \times N$	δ	k	δ	k
4×4	2.31e−6		4.62e−6	
6×6	3.28e−7	4.81	6.57e−7	4.81
12×12	6.23e−9	5.72	1.24e−8	5.73
24×24	1.01e−10	5.95	2.01e−10	5.95

3. Using meshless interpolants in a finite differencing mode

Recently, considerable attention has been paid in computational solid mechanics to the so-called meshless methods allowing to discretize PDEs using scattered nodes. They have some attractive features. In particular, they do not require structured or unstructured grids thus automatically obviating the difficulties of constructing high quality meshes needed, for example, in the case of the above described technique. Meshless methods are known to greatly simplify the solution procedures in the cases of large deformations, changing geometries etc. Among the first meshless methods, there are generalized finite difference [4] and smooth particle hydrodynamics [5] methods. The majority of existing meshless methods exploit the least squares principle to construct meshless approximations. In these approaches, the approximated functions and their approximations, in general, do not coincide at the nodes. They are used mainly in the framework of the Galerkin method (their extensive review can be found for example in [6]).

Another approach is using radial basis functions (RBF), that is the functions of arguments which are distances between current point and nodes. In contrast to the least squares approximations, RBF interpolants satisfy the interpolation conditions stating that they are equal to the interpolated functions at nodes. It was found that the RBF interpolation procedure has the potential for being very accurate providing in some instances exponential convergence. The overview and the relevant references concerning RBF can be found, for example, in [7].

Unlike the least-squares types methods, RBF applications to PDEs are based mainly on the collocation and boundary elements strategies [8–10]. The merits of the collocation RBF techniques are simplicity of boundary conditions formulations and absence of numerical integration procedures typical for some

meshless Galerkin-type methods. However, serious problems may arise due to the ill-conditioning property of the resulting linear systems. To circumvent the difficulty, some remedies were proposed. They concern locally supported RBF [11–13]; preconditioning [14] and domain decomposition [15].

We consider here another way of using the RBF suggested in [16]. The idea is to define for each node a local set of neighbour nodes ("stencils", following finite differencing terminology), to construct for the set an RBF interpolant and the resulting approximations to derivatives at the node. The approximation formulas can be then used when discretizing the PDE of interest.

The procedure is completely analogous to the finite difference one. It differs from the latter in

(1) using arbitrary spaced nodes instead of grid points,
(2) using RBF instead of polynomials when constructing numerical differentiation formulas.

Comparing with the collocation approach, the governing equations are approximated at each node rather than satisfied at the node. Using local RBF supports greatly relaxes the ill-conditioning limitation. Assuming on good RBF approximation properties, one may expect reasonable high accuracy.

In what follows, the technique is presented in more details.

3.1. RBF approximations to derivatives and RBF schemes

Suppose one has a set $X = \{\mathbf{x}_1, \mathbf{x}_2, \ldots, \mathbf{x}_M\} \subset \Omega$ of nodes in a computational domain Ω. Let $X_j = (\mathbf{x}_1^{(j)}, \mathbf{x}_2^{(j)}, \ldots, \mathbf{x}_{N_j}^{(j)})$, $X_j \subset X$, $\mathbf{x}_j \in X_j$ be a "cloud" of nodes surrounding each node $\mathbf{x}_j$. The node will be referred to as a center of the cloud. Following the finite difference terminology, we shall however use the notion "stencil" instead of cloud.

Suppose further that $u(\mathbf{x})$, $\mathbf{x} \in \Omega$ is a sufficiently smooth function. Denoting $u(\mathbf{x}_i) = u_i$, let us introduce "internal" numbering for a subset X_j: if $\mathbf{x}_i = \mathbf{x}_k^{(j)}$ then $u_i = u_k^{(j)}$ where k is some number from $(1, 2, \ldots, N_j)$.

We construct for each X_j an interpolant

$$s^{(j)}(\mathbf{x}) = \sum_{k=1}^{N_j} c_k^{(j)} \phi(||\mathbf{x} - \mathbf{x}_k^{(j)}||),$$

where $||\cdot||$ is the Euclidean norm, $b_{ki}^{(j)}$ are the entries of the matrix which is inverse of the coefficients matrix $A^{(j)} = \{a_{ik}^j\} = \{\phi(||\mathbf{x}_i - \mathbf{x}_k^{(j)}||\}$ arising from the interpolation conditions $s^{(j)}(\mathbf{x}_k^{(j)}) = u_k^{(j)}$, $k = 1, 2, \ldots, N_j$.

For any linear differential operator D one can construct then the approximate formula $[Du]_j \approx c_k^{(j)}[D\phi(||\mathbf{x} - \mathbf{x}_k^{(j)}||)]_j$ where the notation $[Df]_j = Df|_{\mathbf{x}=\mathbf{x}_j}$

is used. Substituting the expression for $c_k^{(j)}$, one may write finally

$$[Du]_j \approx \sum_{i=1}^{N_j} (c_D)_i^{(j)} u_i^{(j)},$$

$$(3.1) \qquad (c_D)_i^{(j)} = \sum_{k=1}^{N_j} b_{ki}^{(j)} [D\phi(||\mathbf{x} - \mathbf{x}_k^{(j)}||)]_j, \quad j = 1, 2, \ldots, M.$$

The coefficients $(c_D)_i^{(j)}$ depend only on D and the coordinates of the nodes belonging to the j-th stencil. They do not vary during the solution processes (if nodes are not moving) and can be calculated during preprocessing.

In the following, we shall suppose that D is an operator of derivatives with respect to Cartesian coordinates. Then (3.1) may be viewed as usual numerical differentiation formulas written for stencils X_j. Such formulas are used for discretizations of PDEs when each internal node considered as a center leads to algebraic systems with sparse matrices typical for a conventional finite difference method. It is worth noting that it is possible to use "oriented" stencils for skew-symmetric operators, thus introducing an upwinding used in fluid dynamics applications.

Differencing formulas (3.1) can be readily extended to the case when derivatives are specified at data points (for example, near the boundaries where the Neumann boundary conditions are used). In that case we suppose that values $f_i = f(\mathbf{x}_i^{(j)})$ are specified at some nodes of the j-th stencil $\mathbf{x}_1^{(j)}, \mathbf{x}_2^{(j)}, \ldots, \mathbf{x}_p^{(j)}$ while functionals $Df|_{\mathbf{x}=\mathbf{x}_k^{(j)}}$ are given at $\bar{\mathbf{x}}_1^{(j)}, \bar{\mathbf{x}}_2^{(j)}, \ldots, \bar{\mathbf{x}}_q^{(j)}$ where D is a linear operator. It is assumed that $\mathbf{x}_i^{(j)}$ and $\bar{\mathbf{x}}_k^{(j)}$ possibly coincide for certain i and k.

The corresponding RBF interpolant has the form

$$s^{(j)}(\mathbf{x}) = \sum_{k=1}^{p} a_k \phi(||\mathbf{x} - \mathbf{x}_k^{(j)}||) + \sum_{k=1}^{q} b_k D^{(x)} \phi(||\mathbf{x} - \bar{\mathbf{x}}_k^{(j)}||),$$

$$p,\ q < N_j,$$

where (x) indicates the action of D on ϕ as a function of x. Requiring that

$$s^{(j)}(\mathbf{x}_k^{(j)}) = f(\mathbf{x}_k^{(j)}),$$

$$Ds^{(j)}|_{\mathbf{x}=\bar{\mathbf{x}}_k^{(j)}} = Df|_{\mathbf{x}=\bar{\mathbf{x}}_k^{(j)}},$$

one obtains the following linear system:

$$
\begin{pmatrix}
\phi_{11}...\phi_{1p} & D\phi_{11}...D\phi_{1q} \\
\vdots & \vdots \\
\phi_{p1}...\phi_{pp} & D\phi_{p1}...D\phi_{pq} \\
D\phi_{11}...D\phi_{1p} & D^2\phi_{11}...D^2\phi_{1q} \\
\vdots & \vdots \\
D\phi_{q1}...D\phi_{qp} & D^2\phi_{q1}...D^2\phi_{qq}
\end{pmatrix}
\begin{pmatrix} a_1 \\ \vdots \\ a_p \\ b_1 \\ \vdots \\ b_q \end{pmatrix}
=
\begin{pmatrix} f_1 \\ \vdots \\ f_p \\ Df_1 \\ \vdots \\ Df_q \end{pmatrix}, \tag{3.2}
$$

$\phi_{ij} = \phi(||\mathbf{x}_i - \mathbf{x}_j||)$, $D\phi_{ij} = D\phi(||\mathbf{x} - \mathbf{x}_j||)|_{\mathbf{x}=\mathbf{x}_i}$, $D^2\phi_{ij} = D^2\phi(||\mathbf{x} - \mathbf{x}_j||)|_{\mathbf{x}=\mathbf{x}_i}$.

Assuming that matrix (3.2) does not degenerate (this is the case for certain types of ϕ), one can solve the system for coefficients a_k, b_k. Applying operator D to $s(\mathbf{x})$ at a node $\mathbf{x}_j$, one obtains the following generalization of (3.1):

$$
D_\alpha \approx \sum_{k=1}^{p} C_k^{(\alpha)} f_k + \sum_{k=1}^{q} B_k^{(\alpha)} Df_k,
$$

where the coefficients $C_k^{(\alpha)}$ and $B_k^{(\alpha)}$ depend on the coordinates of the nodes forming the j-th stencil while D_α is supposed to be the operator of the αth-order derivative in one direction or another.

It is of interest to estimate the actual accuracy of (3.1) in the cases when D is the operator of the first or second partial derivatives and N_j are reasonably small numbers. Unfortunately, in contrast to the usual FD formulas, the Taylor expansion series are not very efficient here. It is due to degeneration of the coefficient matrix in the limit of vanishing distances between neighbour points.

There are some estimates of the h-convergence in the case of cardinal interpolation [25], when nodes x_j are generated by the Cartesian grid with $N_j = \infty$.

A natural but not a general way to estimate the approximation errors for relatively small N_j is their direct calculation for certain classes of functions. Of course, it gives only some impression concerning the RBF performance in a finite difference mode. The results of the calculations for Hardy multiquadrics (MQ)

$$
\phi(r) = (r^2 + C)^{1/2}, \qquad r^2 = x^2 + y^2, \tag{3.3}
$$

with $C = 1$ are presented in [16]. Figure 2 shows L_2 - norms of errors in the case of the first and second derivatives of $f(x) = \exp(2(x + y))$ when using the stencils indicated herein.

It can be seen from Fig. 2 that the norms can be well presented by the power laws h^p where h is the distance between nodes while $p = 2, 4, 6$ for stencils $1, 2, 3$. For a fixed $h = h_*$, enlarging the stencils increases the accuracy of the derivatives discretization. However, one should not expect that this will continue when the

number of nodes $N_j = K$ in the stencils increases without bound. When $K \to \infty$, the accuracy of the interpolation which provides differencing formulas is expected to tend to that of the cardinal interpolation [26], for $h = h_*$.

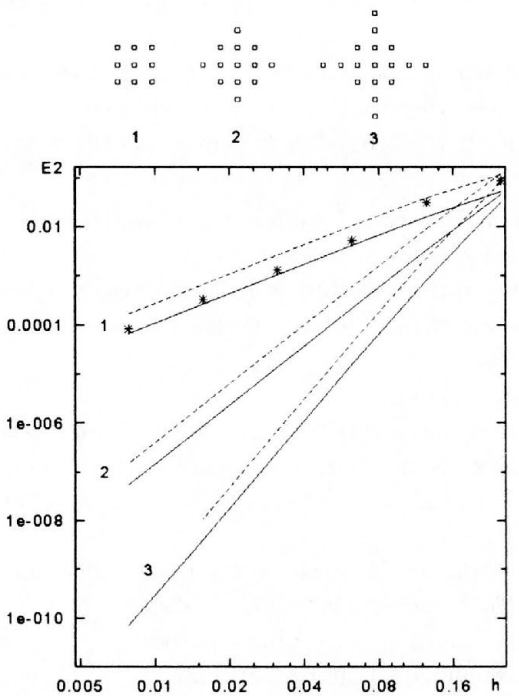

FIG. 2. Mean-root-square errors vs. mesh size and the corresponding RBF stencils. Solid and dashed lines correspond to first and second derivatives respectively.

In the figure, the result obtained with the second-order-accurate centered finite difference formula for the first derivative are also shown (marked by asterisks). They are close to those for the stencil 1.

Discretization at each node of a given PDE can be proceeded in a standard finite difference manner by changing derivatives with their approximations. Assembling then the resulting algebraic equations and using the boundary conditions (which, if needed, can be discretized as well), one obtains a global system for unknown nodal variables.

In the linear case, its matrix is a sparse one and the system can be solved using direct or iterative methods. In the numerical experiments described below the direct nested dissection method [27] was used. It should be noted that condition numbers for "global" systems were found to be quite acceptable. However, though the present technique suggests $N_j \ll N$, ill-conditioning of a system like (3.2) can not be ruled out if N_j is too large or distances between the nodes are

too small. In the calculations, the situation has been encountered only in the h-convergence studies when very small values of h, the characteristic distances between nodes, were used. In those cases, quadro precision arithmetic was exploited. The preconditioning ideas of [14] seems to be quite attractive to deal with such cases.

Summing up, to solve a PDE using the present RBF approach, one should:

(i) Specify the nodes distribution in the considered computational domain;

(ii) For each node x_j considered as a center, specify a stencil with N_j nodes surrounding x_j;

(iii) For each stencil, obtain the "differencing" coefficients (for example $(c_D)_i^{(j)}$ in (3.1)) by solving linear systems;

(iv) Substitute the approximations to derivatives at each node in the PDE and form the resulting "global" system by assembling together the nodal approximations;

(v) Solve the global system.

It should be noted that steps (i)–(iii) can be viewed as a preprocessing procedure once the nodes distributions and stencils are not supposed to be changed during calculations. In nonlinear cases, only steps (iv) and (v) have to be included in iterations.

Since the RBF approach is based on the finite difference principle, the theorem stating that $O(h^k)$ convergence follows from

(i) $O(h^k)$ approximation to governing equations,

(ii) stability of a schemes in the present case.

Unfortunately, it is difficult to prove both properties in a general case of arbitrarily spaced nodes and arbitrary stencils. However, the potential for satisfying (i) and (ii) was discussed in [16] where it was shown that the RBF approximation to the Laplace operator using stencil 1 from Fig. 2 is a negative definite one (the Hilbert space of double-periodic nodal functions with the inner product $(u, v) = h^2 \sum_{i,j} u_{ij} v_{ij}$ where u_{ij} and v_{ij} are defined at grid points $x_i = ih, y_j = jh$ of the Cartesian grid was assumed). As a result, in that case (as well as in the cases of other stencils shown in Fig. 2), very fast convergence was observed when using the simplest iterative procedure for inverting the corresponding L_h operators.

In the calculations described below, h-convergence was always seen at least for the considered ranges of h and all the considered stencils.

Though general RBF methodology is really a meshless one and a random nodes distribution can be used, the most accurate numerical solutions can be expected only if a "proper" distribution is specified depending on the problem to be solved. Moreover, the strategy of choosing stencils in the present approach, as in the finite difference methods, plays an important role.

Since the calculations presented below are aimed mainly at comparisons with other methods, either triangulated or Cartesian meshes were used as nodes distributions. As to step (ii), different strategies were used when specifying stencils.

In the following, the MQ radial basis functions will be considered only. We set $C = 1$ in (3.3) when carrying out the majority of the calculations described below since we are not aware of the existence of a theory giving an optimal choice of C. Of course, judging from the results presented in [17, 18], the solution accuracy is expected to be lower than that for a more successful choice of C.

3.2. Numerical examples

EXAMPLE 1. KIRCHHOFF PLATES

We consider below two cases of the Kirchhoff plates for which exact solutions are available. Their bending is described by the biharmonic equation. In the particular case of simply supported edges, a solution procedure can be reduced to successive solutions of two Poisson equations.

The first case is a square plate problem described by (2.5). The calculations were carried out using seven-points "simple" (or RBF-1) and nineteen-points (or RBF-2) "enlarged" stencils (Fig. 3), the fourth-order technique from Sec. 2 and the FEM method with linear elements. The L_2 norms of errors are displayed in Fig. 4. As it is seen, the "simple" stencils and FEM show second-order mesh convergence while the RBF with "enlarged" stencil and CD method are fourth-order accurate. At the same time, the RBF solutions are more accurate than their counterparts of the same order.

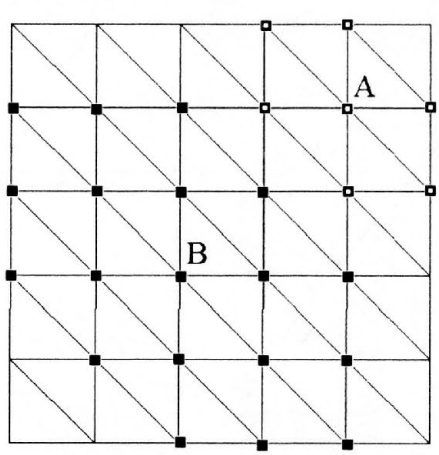

FIG. 3. A triangulated mesh in a square domain. The "simple" stencil for the node A and the "enlarged" stencil for the node B are shown by white and black markers respectively.

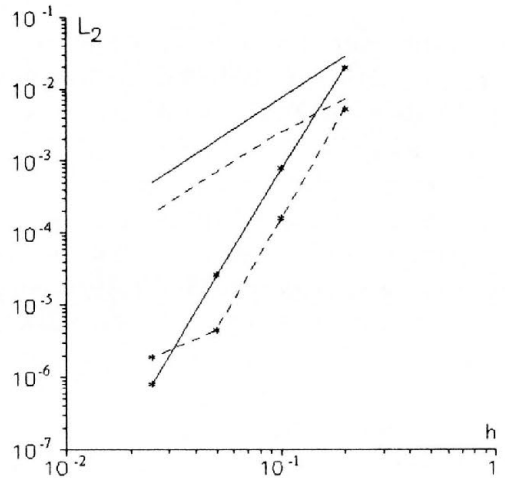

Fig. 4. Mean-root-square errors vs. mesh size for the biharmonic equation in a square domain. Dashed lines without markers and with markers correspond to the RBF "simple" and "enlarged" stencils respectively. Solid lines without markers and with markers correspond to FEM and compact scheme of fourth-order respectively.

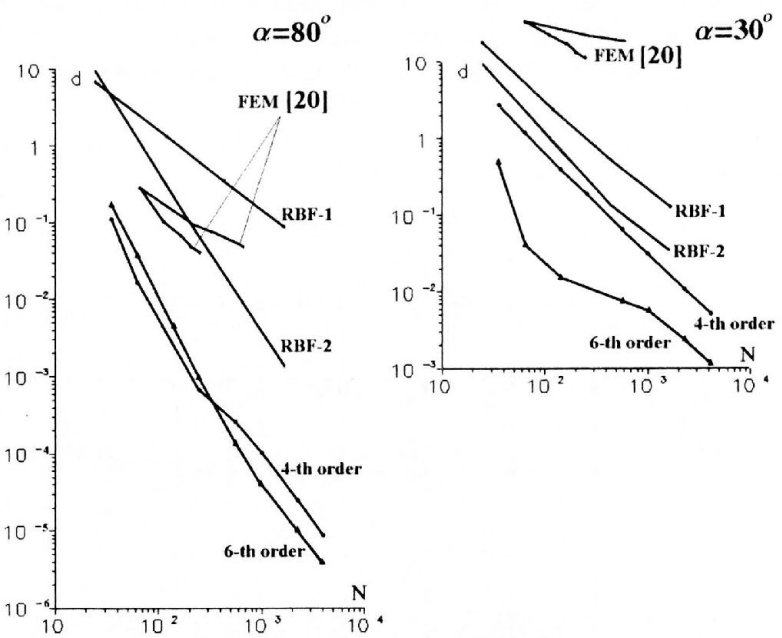

FIG. 5. Relative center displacement error for rhombic plate vs. number of nodes (on percentage basis).

As the next testing example, we consider bending of a simply supported rhombic plate subjected to a uniform load. In that case, there is a singularity of the exact solution which has an adverse effect on the accuracy of numerical methods. The problem is investigated in [20] in the context of performance of several finite element methods. Then the most accurate solutions obtained with 21 degrees of freedom elements using both uniform and non-uniform meshes are compared with the present RBF and CD results.

Figure 5 displays the relative center displacement errors (on a percentage basis) vs. the number of nodes in the computational domain for two values of the rhomb angle. The exact solution considered as a reference one was obtained using the technique described in [21], while the most accurate are the solutions obtained with the fourth-order CD and sixth-order CD-based multioperators schemes. However, the mesh-convergence orders in all cases are not so high as in the previous example. Moreover, the performance of the fourth and sixth-order methods is approximately identical though the latter is slightly more accurate.

EXAMPLE 2. TORSION OF PRISMATIC BARS

According to the elasticity theory, solutions of the bar torsion problems can be obtained by solving the Dirichlet problem for the Poisson equation

$$\triangle\phi = -2, \mathbf{x} \in \Omega, \qquad \phi|_{\partial\Omega} = \mathbf{0},$$

where Ω is a bar cross-section domain. The corresponding stress components can then be expressed in terms of x- and y-derivatives of ϕ. In the case of cross-sections with boundaries which contain "incoming" angles which rounded vertices, it is of interest to predict accurately the stress concentrations near the rounded corners where high gradients are possible (it is known that stresses become singular when the corresponding curvature radii tend to zero).

We consider the geometry of a bar cross-section shown in Fig. 6 which was investigated in [22] using very accurate semi-analytic method. The cross-section is characterized by the radius r of the rounded corner and the "shelf" length A, the "shelf" thickness being assumed to be unity. The asymptotics in the case $r \to 0$ was investigated in [19, 22]. To describe properly the stresses near point C for small r, high-accuracy methods are needed.

The RBF calculations were carried out using triangulated meshes (one of them is shown in Fig. 6). The meshes are defined by numbers M and N of nodes uniformly distributed along the boundary PQ and the boundary RS, respectively. Thus the condensation of nodes near C can be achieved by increasing M.

To compare the solution $K = \text{grad}\,\phi$ in C with the results of [22], the ϕ derivatives were approximated using the third-order four-points formula. The calculations were carried out for three meshes $M=11$, $N=20$; $M=21$, $N=40$ and $M=41$, $N=80$ showed that the difference between the results corresponding to the second and the third meshes could be estimated as 0.2%.

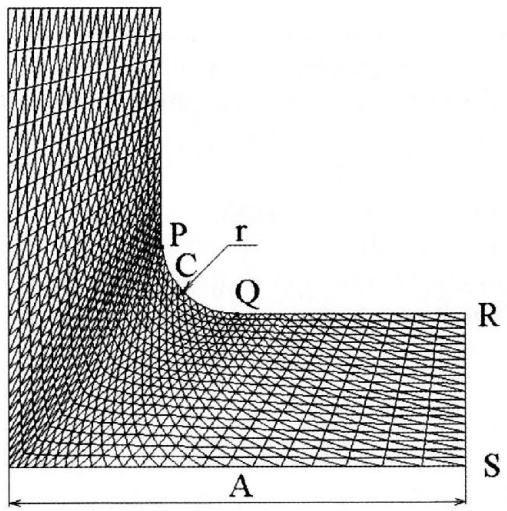

FIG. 6. L-shaped domain with rounded incoming corner.

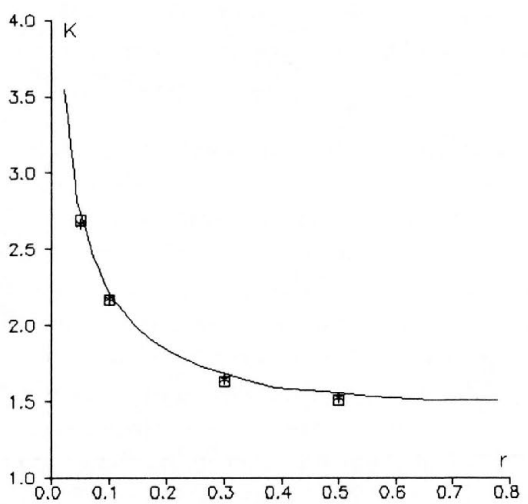

FIG. 7. The stress concentration parameter K vs. radius of the rounding.

Figure 7 displays the K values obtained for $A=3$ and $r=0.5, 0.3, 0.1, 0.05$ using the "simple" stencil defined on the coarsest mesh (markers as squares) and finest mesh (markers as stars), the difference between the values being about 1.2% (an exception is the case $r = 0.05$). The curve depicted in Fig. 7 corresponds to the "almost exact" solution for $A = \infty$. Since the influence of A is quite insignificant in the domain $A > 3$ (the results for $A=3$ and $A=4$ differs by 0.2%), the agreement is rather good.

Another comparison with the solution from [22] is shown in Fig. 8. In the figure, the ratio K/A for the fixed value $r/A = 0.1$ is presented as a function of $1/A$. Again one may see that the present results (markers) agree closely with those from [22] (solid line).

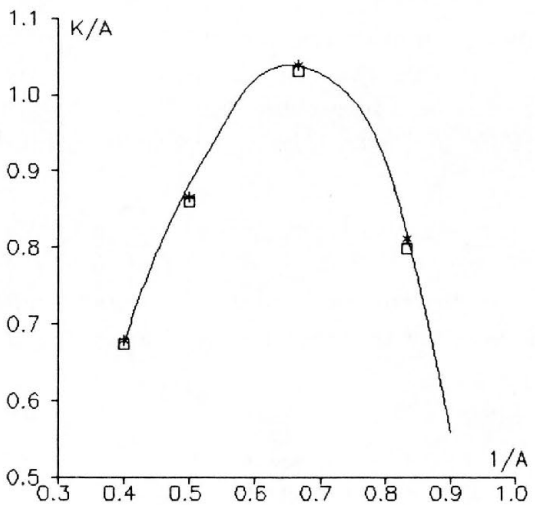

FIG. 8. The parameter K/A vs. $1/A$. The solid line and markers correspond to results from [22] and the present results respectively.

EXAMPLE 3. CANTILEVER BEAM

Consider now the application of the described approach to one of the 2D elasto-statics problems, namely to the cantilever beam problem which is popular when verifying meshless methods (see for example [6], [23]). The governing equations this time are

$$\sigma_{xx,x} + \sigma_{xy,y} = 0, \qquad \sigma_{xy,x} + \sigma_{yy,y} = 0,$$

where, assuming the plane-stress case, $\sigma_{xx} = (u_{,x} + \nu v_{,y})E/(1-\nu^2)$, $\sigma_{xy} = (u_{,y}+v_{,x})E/(2(1-\nu^2))$, $\sigma_{yy} = (v_{,y}+\nu u_{,x})E/(1-\nu^2)$ and u, v are displacements in the x- and y-directions and E is the elasticity modulus. We set $E = 1000$, $\nu = 0.3$ as in [23]. As boundary conditions, the displacements defined by the exact solutions were used. The exact solutions for the cantilever beam problem can be found in [24].

The equations were approximated at nodal points which were distributed in the same manner as those in the above cited publications.

Though an optimal choice of stencils is beyond the scope of the present paper, different strategies of their forming were tried. One of them was as follows. For each center $\mathbf{x}_j$, the stencil was defined as a set of nodes which fall on a domain

S_j : $\mathbf{x}_j \in S_j$ with a prescribed shape of its boundary and a prescribed characteristic length R (the latter was, for example, a circle radius, the edge of a rectangle etc.) or a characteristic area.

In the present case, grid points of regular $M \times N$ meshes were used as nodes. The beam length and width are L=12 and D=2 respectively.

Figure 9 presents L_{uv} solution errors as functions of the mesh size h_x in the x-direction for several stencils with nodes falling on circles, squares, ellipses with the axis length ratio 2 : 1 and rectangles with the aspect ratio 2 : 1, the area of the supports being $20h_x^2$ and $50h_x^2$. The L_{uv} errors are defined as

$$L_{uv} = \left(\sum_i (u_i - u_{ei})^2 + (v_i - v_{ei})^2 / \sum_i u_{ei}^2 + v_{ei}^2 \right)^{1/2},$$

where u_{ei} and v_{ei} are the exact values at a i-th node and the summation is carried out over the nodes of the computational domain.

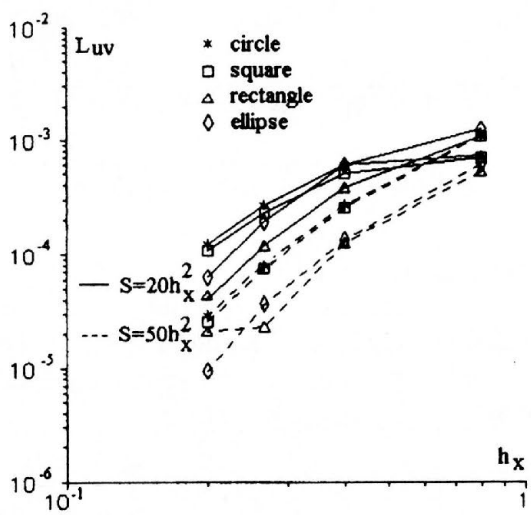

FIG. 9. The cantilever beam problem: relative errors of displacements vs. mesh size h_x for several stencils and areas of supports.

As seen in Fig. 9, the influence of the supports type is not very significant in the present case, the best choice being ellipses. As may be expected, enlarging stencils improves the accuracy and the convergence rate. However, it does not necessary mean that the improvement will continue by including more and more nodes in stencils.

Once the numerical solutions for displacements are obtained, the corresponding stress calculations may be viewed as a postprocessing procedure. A rich vari-

ety of RBF approximations to derivatives using different stencils can be used. In the present particular case, finite difference formulas were found to be effective.

Figure 10 presents the relative errors in the stresses σ_{xx} and σ_{xy} as defined in [23] for the calculations with the elliptical supports.

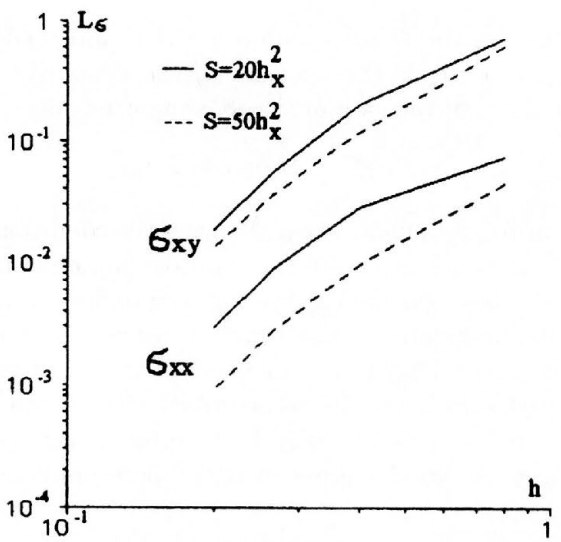

FIG. 10. The cantilever beam problem: relative errors of stresses vs. mesh size h_x for two areas of ellipsis.

EXAMPLE 4. NONLINEAR SHELL DEFORMATIONS

As another example of the present RBF technique application, we consider a nonlinear shell problem described by the Kármán–Föppl equations [28].

Based on the Kirchhoff assumptions, the equations for a plate having thickness h=const read

$$u_{1,xx} + w_{,x}w_{,xx} + 0.5(1+\nu)(u_{2,xy} + w_{,y}w_{,xy}) + 0.5(1-\nu)(u_{1,yy} + w_{,x}w_{,yy}) = 0,$$

$$u_{2,yy} + w_{,y}w_{,yy} + 0.5(1+\nu)(u_{1,xy} + w_{,x}w_{,xy}) + 0.5(1-\nu)(u_{2,xx} + w_{,y}w_{,xx}) = 0,$$

$$D\triangle\triangle w = q + (Eh/(1-\nu^2))\{[u_{1,x} + \nu u_{2,y} + 0.5w_{,x}^2 + 0.5\nu w_{,y}^2]w_{,xx}$$
$$+ [u_{2,y} + \nu u_{1,x} + 0.5w_{,y}^2 + 0.5\nu w_{,x}^2]w_{,yy} + (1-\nu)[u_{1,y} + u_{2,x} + w_{,x}w_{,y}]w_{,xy}\}.$$

In the above equations, u_1, u_2, w are the displacements of a plate middle surface corresponding to the Cartesian coordinates x, y, z respectively. It is supposed that the coordinates origin is at the surface, the axis z being normal to it.

In the following, simply supported edges or clamped edges will be assumed. In both cases, the boundary conditions for the first two equations and the condition for the third equation are

$$u_1|_\Gamma = u_2|_\Gamma = w|_\Gamma = 0.$$

The second condition for the third equation in the clamped edges case has the form $\partial w/\partial n = 0$ where $\partial/\partial n$ is the operator of the derivative in the direction normal to the boundary. In the case of simply supported edges, it reads

$$\triangle w + (1-\nu)k\partial w/\partial n = 0,$$

where k is the curvature of the boundary. By using the condition, one can avoid, as indicated in [29], a manifestation of the Babuska-Saponjan paradox which is an essential difference between the solutions corresponding to round plates and plates with polygonal boundaries with the number of vertices tending to infinity.

In the calculations, grid points of an unstructured triangulated grid were assumed as RBF nodes with the above described RBF-1 and RBF-2 stencils. To discretize the fourth derivatives, the RBF formulas for second derivatives were sequentially applied, special types of RBF operators being used near the boundaries.

As a test problem, consider bending of a round plate with simply supported or clamped edges under uniform loading. Due to the central symmetry, the highly accurate solution can be obtained by solving ordinary differential equations. The solution is used as a reference one. For the triangulated mesh, the number of nodes N along the radial directions were chosen to be $N = 6, 11, 21$.

Table 3. Simply supported edges.

	"simple" stencils			"enlarged" stencils		
Q	$N=6$	$N=11$	$N=21$	$N=6$	$N=11$	$N=21$
L	0.63957	0.67898	0.69090	0.70145	0.69596	0.69532
0.5	0.28053	0.29235	0.29592	0.29971	0.29761	0.29728
1	0.46222	0.47478	0.47869	0.48400	0.48091	0.48030
2	0.68697	0.69773	0.70141	0.70817	0.70407	0.70311
4	0.95080	0.95867	0.96192	0.97005	0.96499	0.96368
6	1.12568	1.13163	1.13459	1.14343	1.13788	1.13638

In Tables 3 and 4, the center displacements of the plate $W = w_{\text{center}}/h$ are presented for various values of the dimensionless load $Q = q(R/h)^4/E$ and the above mentioned values of N, h and R being the plate thickness and the plate radius, respectively. The Poisson coefficient is assumed to be 0.3. For comparison,

the reference solution (column "ref") and the results for the linear case with $Q = 1$ (string "L" in Tables 3) are also included in the tables. It should be noted that the exact solution for the latter case is $W = .695625$.

Table 4. Clamped edges.

	"simple" stencils			"enlarged" stencils			
Q	$N = 6$	$N = 11$	$N = 21$	$N = 6$	$N = 11$	$N = 21$	ref
1	0.15725	0.16459	0.16704	0.16536	0.16744	0.16789	0.16785
2	0.30479	0.31693	0.32094	0.31906	0.32173	0.32234	0.32250
4	0.55499	0.56900	0.57538	0.57537	0.57501	0.57524	0.57625
6	0.75126	0.76252	0.76619	0.77366	0.76824	0.76773	0.76956

As it can be seen, the difference between the RBF and reference solution does not exceed 0.5% for $N = 21$ in the case of the RBF-1 stencil and 0.2% for $N = 11$ in the case of the RBF-2 stencil.

As an example of a more complicated geometry, Fig. 11 presents the dependence "W vs. Q" where W and Q are the above defined variables. The plate boundary is given by $r = R(1 + \cos(6\phi)/5)$ in the polar coordinates (r, ϕ), the nodes distribution being shown in the figure. One can see considerable difference of the results obtained in the frameworks of linear and nonlinear theory.

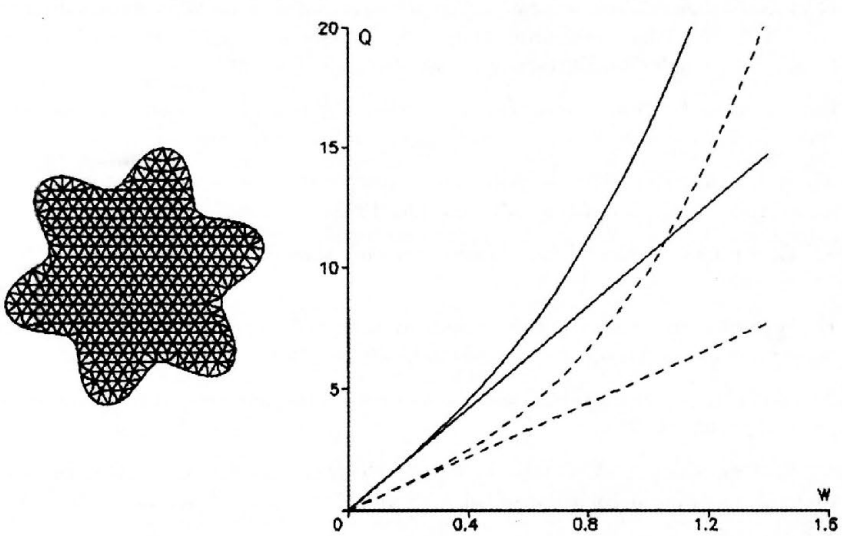

FIG. 11. A mesh for a plate with complicated geometry. Q vs W. Solid and dashed lines correspond to simply supported and clamped edge respectively.

Acknowledgment

This work was supported by INTAS, project N1150 and Russian Fund of basic researches, grant 02-01-00436.

References

1. A. A. SAMARSKII, V. B. ANDREEV, *Finite difference methods for elliptic equations* (in Russian), Izd. Nauka, Moscow 1976.
2. A. I. TOLSTYKH, *Multioperator high-order compact upwind methods for CFD parallel calculations,* [in:] Parallel Computational Fluid Dynamics, D. R. Emerson, A. Ecer, J. Periaux and N. Satofuka [Eds.], 383–390, Elsevier, Amsterdam 1998.
3. A. I. TOLSTYKH, *On prescribed order integro-interpolation schemes,* J. Comput. Math and Math. Phys. (transl. from Russian), to appear in 2002.
4. T. LIZKA, J. ORKITZ, *The finite difference method at arbitrary irregular grids and its application in applied mechanics,* Comput. Struct., **11**, 83–95, 1980.
5. J. J. MONAGHAN, *Why particle methods work,* SIAM J. Sci. Stat. Comput., **3**, 422–433, 1982.
6. T. BELYTCHKO, Y. KRONGAUS, D. ORGAN, M. FLEMING, P. KRYSL, *Meshless methods: An overview and recent developments,* Comp. Meth. Appl. Eng., **139**, 3–47, 1996.
7. E. J. KANSA, R. E. CARLSON, *Radial basis function: a class of grid-free scatterel data approximations,* Comput. Fluid Dynamics J., **3**, 479–496, 1995.
8. G. FASSHAUER, *Solving partial differential equations with collocation with radial basis functions,* [in:] Chamonix proceedings, A. LeMehaute, C. Robut and L. L. Shunaker [Eds.], 1–8, Vanderbilt University Press, Nashville TN 1996.
9. C. FRANKE, R. SCHABACK, *Solving partial differential equations by collocation using radial basis functions,* Appl. Math. Comput., **93**, 73–82, 1998.
10. M. A. ZERROUKAT, *Fast boundary element algorithm for time-dependent potential problems,* Appl. Math. Modelling, **22**, 183–196, 1998.
11. M. D. BUHMANN, *Radial functions on compact support.* Proc. Edinburg Math. Soc., **41**, 33–46, 1998.
12. H. WENDLAND, *Piecewise polynomial, positive definite and compactly supported radial basis functions of minimal degree,* Adv. Comput. Math., **4**, 386–396, 1995.
13. Z. WU, *Compactly supported positive definite radial functions,* Adv. Comput. Math., **4**, 283–292, 1995.
14. R. K. BEATSON, J. B. CHERRIE, C. T. MONAL, *Fast fitting of radial basis functions. Methods based on preconditioned GMRES iteration,* Adv. in Comput. Math., **11**, 253–270, 1999.
15. S. M. WONG, Y. C. HON, T. S. LI, S. L. CHUG, E. J. KANSA, *Multizone decomposition of time dependent problems using the multiquadric scheme,* Comput. Math. Appl., **37**, 23–45, 1999.

16. A. I. TOLSTYKH, *On using RBF-based differencing formulas for unstructured and mixed structured-unstructured grid calculations,* [in:] Proceedings of 16th IMACS World Congress, Lausanne 2000.

17. E. J. KANSA, *Multyquadrics – a scattered data approximation scheme with applications to fluid dynamics – II: Solutions to parabolic, hyperbolic and elliptic partial differential equations*, Comput. Math. Appl., **19**, 147–161, 1990.

18. E. J. KANSA, Y. C. HON, *Circumventing the ill-conditioning problem with multiquadric radial basis functions: Applications to elliptic partial differential equations*, Comput. Math. Appl. **39**, 123–137, 2000.

19. G. I. MARCHUK, V. I. AGOSHKOV, *Introduction to projective-difference methods* (in Russian), Izd. Nauka, Moscow 1981.

20. I. BABUSKA, T. SCAPOLLA, *Benchmark computation and performance evaluation for a rhombic plate bending problem*, Int. J. Num. Meth. Eng., **28**, 155–179, 1989.

21. L. S. D. MORLEY *Skew plates and Structures. International Series of Monographs in Aeronautics*, Macmillan, New York 1963.

22. V. I. VLASOV, D. B. VOLKOV, *Multypole method for solving Poisson equation in domains with rounded angles*, Zh. Vychisl. Mat. Mat. Fiz., **35**, 6, 867–872, 1995.

23. X. ZHANG, K. Z. SONG, M. W. LU, X. LIU, *Meshless methods based on collocation with radial basis functions,* Comput. Mech., **26**, 333–343, 2000.

24. S. P. TIMOSHENKO, S. N. GOODIER, *Theory of elastisity*, McGraw-Hill, New York 1970.

25. W. R. MADYCH, S. A. NELSON, *Error bounds for multiquadric interpolation,* [in:] Approximation theory VI, C. K. CHUI, L. L. SHUMAKER, J. W. WARDS [Eds.], Academic Press, New York 1989.

26. M. D. BUHMANN, *Multivariate cardinal interpolation with radial-basis functions,* Constructive approximations, **6**, 225–255, 1990.

27. A. GEORGE, J. W-H LIU, *Computer Solution of Large Sparse Positive Definite Systems,* Prentice-Hall, New Jercey 1981.

28. E. I. GRIGOLUK, V. I. MAMAI, *Nonlinear deformation of thin-wall construction* [in Russian], Izd. Nauka Fizmatlit, Moscow 1997.

29. V. G. MAZJA, S. A. NAZAROV, *Paradoxes of the solutions of boundary value problem on the smooth domain approximated by polygons,* Izv. Akad. Nauk USSR, Ser. Mat., **50**, 1156–1177, 1986.

Received March 21, 2003; revised version July 1, 2003.

Centre International des Sciences Mecaniques *International Centre for Mechanical Sciences*

International Centre for Mechanical Sciences (CISM)
Preliminary Programme 2004

Multiscale Modelling of Damage and Fracture Processes in Composite Materials T. Sadowski (Lublin, PL)	**May 24–28**
Mesoscale Atmospheric Convection: Research and Operational Forecasting Aspects D. Giaiotti (Udine, I), R. Steinacker (University of Vienna), F. Stel (Udine, I)	**May 31–June 4**
Nonlinear Dynamical Systems in Economics M. Lines (Udine, I)	**June 7–11**
Control of Solids and Structures: Mathematical Modelling and Engineering Applications J.J. Telega (Warsaw, PL), E. Zuazua (Madrid, E)	**June 21–25**
Microsystems Mechanical Design F. De Bona (Udine, I), E. Enikov (Tucson, USA)	**June 28–July 2**
Environmental Stratified Flows V. Armenio (Trieste, I), S. Sarkar (La Jolla, USA)	**July 12–16**
Applied Micromechanics of Porous Materials L. Dormieux (Marne-la-Vallee, F), F. J. Ulm (Cambridge, USA)	**July 19–23**
Surface Waves in Geomechanics: Direct and Inverse Modelling for Soils and Rocks C. Lai (Milan, I), K. Wilmanski (Berlin, D)	**September 6-10**
Advanced Professional Training Course on: Structural Aluminium Connections:Theory, Analysis and Design C.C. Baniatopoulos (Thessaloniki, GR), T. Pekoz (Ithaka, USA)	**September 6–10**
Modelling and Experimentation of Two-Phase Flow V. Bertola (Paris, F)	**September 13–17**

Nonlinear Waves in Fluids: Recent Advances and Modern Applications R. Grimshaw (Loughborough, UK)	**September 20–24**
Nonlinear Dynamics and Chaos for High Volume and Ultra Precision Metal Cutting M. Wiercigroch (Aberdeen, UK)	**September 20-24**
Nonsmooth Mechanics of Solids J. Haslinger (Prague, CZ), G.E. Stavroulakis (Ioannina, GR and Braunschweig, D)	**October 4–8**

For further information please contact:

CISM, Palazzo del Torso, Piazza Garibaldi 18, 33100 Udine (Italy)
Tel. +39 0432 248 511; Fax +39 0432 248 550;
Email: cism@cism.it; WWW: http://www.cism.it

Institute of Fundamental Technological Research
publishes the following periodicals:

Archives of Mechanics — bimonthly (in English)
Archives of Acoustics — quarterly (in English)
Archives of Civil Engineering — quarterly (in English)
Engineering Transactions — quarterly (in English)
Computer Assisted Mechanics and Engineering Sciences — quarterly (in English)
Journal of Technical Physics — quarterly (in English)

Subscription orders for all journals edited by IFTR may be sent directly to:
Editorial Office
Institute of Fundamental Technological Research
Świętokrzyska 21, p. 508
00-049 Warszawa, POLAND